ENHANCEMENT OF POWER SYSTEM STABILITY USING WIDE AREA MEASUREMENT SYSTEM BASED DAMPING CONTROLLER

A Thesis submitted to The University of Manchester for the degree of

Doctor of Philosophy

in the Faculty of Engineering and Physical Sciences

2010

Abdulaziz Almutairi

School of Electrical and Electronic Engineering

TABLE OF CONTENTS

LIST OF FIGURES 6

LIST OF SYMBOLS 10

ABSTRACT 12

DECLARATION 13

COPYRIGHT STATEMENT 14

ACKNOWLEDGMENT 15

1 INTRODUCTION 17

1.1 Background 17

1.2 Overview of WAMS and PMUs 19

1.2.1 Phasor Measurement Units 19

1.2.2 WAMS Structure 20

1.2.3 Applications of PMUs and WAMS 20

1.3 WAMS based Damping Control 22

1.3.1 Control Structure 22

1.3.2 Time Delays 25

1.3.3 Controller Design 26

1.3.4 Input/output Signal Selection 27

1.4 Summary of Past Research in the Area 29

1.5 Aims and Objectives of the Research 31

1.6 Main Contributions of the Thesis 33

1.7 Outline of the Thesis 34

2 POWER SYSTEM MODELLING AND TOOLS FOR ANALYSIS 37

2.1 Introduction 37

2.2 Power System Modelling 37

2.2.1 Synchronous Generator Model 37

2.2.2 Excitation System Model 38

2.2.3 Power System Stabiliser Model 38

2.2.4 Transmission Line Model 40

2.2.5 Transformer Model 40

2.2.6 Load Model 41
2.2.7 Network Model 42
2.2.8 Time Delays 44
2.3 Tools for Analysis 44
2.3.1 Power System Linearisation 44
2.3.2 Modal Analysis 47
2.3.2.1 Eigenvalues and Eigenvectors 47
2.3.2.2 Solution of Differential Equations 48
2.3.2.3 Participation Factors 49
2.3.2.4 Modal Transformation 49
2.3.2.5 Modal Controllability and Observability 50
2.3.2.6 Illustrative Example 51
2.4 Summary 54
3 MODAL LQG CONTROL APPROACH 56
3.1 Introduction 56
3.2 Modal LQG Control 56
3.3 Design of the LQG Controller 58
3.3.1 Standard Formulation 58
3.3.2 Modal Formulation 61
3.3.3 Remarks on the Modal Formulation 62
3.3.3.1 Real Transformation Matrix 62
3.3.3.2 Coordinate Space 63
3.3.3.3 Unstable Power Systems 64
3.3.4 Robustness of the LQG Controller 65
3.3.5 Model Order Reduction 66
3.3.5.1 LQG Control and Order Reduction 66
3.3.5.2 Model Reduction via Balanced Truncation 66
3.3.6 Time Delays 67
3.4 Case Studies 69
3.4.1 Test System 69
3.4.2 Conventional and Modal LQG Design Approaches 70
3.4.2.1 (Conventional) State-based LQR Design 71
3.4.2.2 Modal-based LQR Design 73
3.4.2.3 Transient Performance Analysis of the Closed-loop System ... 74
3.4.3 Reduced Order Modal LQG Controller 79
3.4.3.1 Full Order Based Design 79
3.4.3.2 Reduced Order Based Design 82
3.4.4 Robustness of the Modal LQG Controller 85
3.4.4.1 Robustness to Topological Changes 85
3.4.4.2 Robustness to Changes in Operating Condition 90
3.4.4.3 Robustness to Variations of Time Delays 96

3.4.4.4 Robustness to Loss Failures of Communication Links 102
3.5 Summary 108

4 SELECTION OF INPUT/OUTPUT SIGNALS 110

4.1 Introduction 110
4.2 Multivariable WAMS based Damping Controller 110
4.2.1 Input/Output Signals for Wide-area Controllers 110
4.2.2 Multi-machine Test System 112
4.3 Modal Factors Analysis 112
4.4 The Sequential Orthogonalisation Algorithm 115
4.4.1 The SO Algorithm 116
4.4.1.1 Selection of First Location 116
4.4.1.2 Illustrative Example on Vector Orthogonal Projection 117
4.4.1.3 Selection of Subsequent Locations 120
4.4.1.4 Upper-bound of Condition Number 121
4.4.1.5 Summary of the Algorithm 125
4.4.2 Application of the SO Algorithm to Input/Output Signal Selection 125
4.5 Combined Clustering and Modal Factors Analysis 129
4.5.1 Principal Component Analysis 129
4.5.1.1 Coherency identification using PCA 131
4.5.1.2 Limitations of PCA 134
4.5.2 PCA-based Clustering 137
4.5.2.1 Cluster Analysis 137
4.5.2.2 Illustrative Example on Cluster Analysis 138
4.5.2.3 Coherency Identification using PCA-based Clustering 140
4.5.3 Selection of Input/Output Signals 143
4.6 Comparison of Input/Output Selection Methods 148
4.6.1 Fixed Design of the SWAC 149
4.6.2 Comparisons of the Methods 149
4.7 Summary 155

5 ENHANCEMENT OF MULTI-MACHINE SYSTEM STABILITY 157

5.1 Introduction 157
5.2 Design of the Controller 157
5.3 Assessment of System Stability 163
5.3.1 Small Disturbances 163
5.3.2 Large Disturbances 163
5.3.3 Topological Changes 167
5.3.4 Power Transfer Changes 171

5.3.5 Time Delay Variations 172
5.3.6 Communication Link Failures 179
5.4 Summary 186

6 CONCLUSIONS AND FUTURE WORK 187

6.1 Conclusions 187
6.2 Directions for Future Research 192

7 REFERENCES 195

8 APPENDICES 201

8.1 Appendix A 201
8.1.1 Four-Machine Test System Data 201
8.1.2 New England Test System Data 203
8.2 Appendix B 209
8.2.1 Illustrative Example on Real Modal Transformation 209
8.3 Appendix C 210
8.3.1 Numerical Values of Matrices in Chapter 3 210
8.4 Appendix D 212
8.4.1 System Responses to Small Disturbances 212
8.4.2 System Responses to Large Disturbances (OC-A*i*) 221
8.5 Appendix E 250
8.5.1 Thesis Based Publications 250

Word count: 46,189

LIST OF FIGURES

Figure 1-1: Phasor measurement unit (PMU) [17] ... 19
Figure 1-2: General WAMS structure [21] ... 20
Figure 1-3: Centralised WAMS based control configuration ... 23
Figure 1-4: Quasi-decentralised WAMS based control configuration ... 24
Figure 1-5: Two-level (hierarchical) WAMS based control configuration ... 24
Figure 2-1: Functional block diagram of synchronous generator excitation control system ... 39
Figure 2-2: AVR block diagram ... 39
Figure 2-3: Power system stabiliser block diagram ... 40
Figure 2-4: Equivalent π circuit of a transmission Line ... 40
Figure 2-5: Equivalent π circuit of a transformer ... 41
Figure 2-6: Representation of a multi-machine power system ... 43
Figure 2-7: Reference frame transformation ... 43
Figure 2-8: Time delay function ... 44
Figure 3-1: LQG control system [55] ... 59
Figure 3-2: Standard LQG controller structure [55] ... 60
Figure 3-3: Step response of Padé approximation ... 68
Figure 3-4: Phase response of 1st and 2nd order Padé approximations ... 69
Figure 3-5: 4-machine test system with SWAC ... 70
Figure 3-6: LTR procedure at plant inputs with various values of q ... 75
Figure 3-7: Speed deviation responses for a large disturbance ... 76
Figure 3-8: Active power responses for a large disturbance ... 77
Figure 3-9: Terminal voltage responses for a large disturbance ... 77
Figure 3-10: Voltage phase angle responses (at generator buses) for a large disturbance ... 78
Figure 3-11: Control signals for a large disturbance (using conventional LQG controller) ... 78
Figure 3-12: Wide-area control signals for a large disturbance ... 79
Figure 3-13: Hankel singular values of the 63rd SWAC ... 80
Figure 3-14: Frequency response of full and reduced order LQG controller ... 80
Figure 3-15: Speed deviation responses of the closed-loop system using full and reduced order SWAC. 81
Figure 3-16: Hankel singular value plot of the 47th open-loop model (without time delays) ... 82
Figure 3-17: Open-loop order reduction ... 83
Figure 3-18: Hankel singular value plot of the 26th order controller ... 84
Figure 3-19: Further controller reduction ... 84
Figure 3-20: Speed deviation responses of the closed-loop system with reduced order SWACs ... 85
Figure 3-21: Active power responses (OC-A1) ... 87
Figure 3-22: Active power responses (OC-A2) ... 87
Figure 3-23: Active power responses (OC-A3) ... 88
Figure 3-24: Active power responses (OC-A4) ... 88
Figure 3-25: Active power responses (OC-0) and (OC-A1) ... 89
Figure 3-26: Active power responses (OC-0) and (OC-A2) ... 89

Figure 3-27: Active power responses (OC-B1) ... 91
Figure 3-28: Active power responses (OC-B2) ... 92
Figure 3-29: Active power responses (OC-B3) ... 92
Figure 3-30: Active power responses (OC-B4) ... 93
Figure 3-31: Active power responses (OC-B5) ... 93
Figure 3-32: Active power responses (OC-C1) ... 94
Figure 3-33: Active power responses (OC-C2) ... 94
Figure 3-34: Active power responses (OC-C3) ... 95
Figure 3-35: Active power responses (OC-C4) ... 95
Figure 3-36: Active power responses for different time delays ... 97
Figure 3-37: Speed deviation responses for different time delays ... 97
Figure 3-38: Wide-area control signal for different time delays ... 98
Figure 3-39: Curves of damping ratios of the interarea modes over increasing time delays ... 99
Figure 3-40: Active power responses with maximum time delay (a_2) ... 101
Figure 3-41: Active power responses with maximum time delay (b_2) ... 101
Figure 3-42: Active power responses with maximum time delay (c_2) ... 102
Figure 3-43: Active power responses for different losses of control signals (a) ... 103
Figure 3-44: Active power responses for different losses of control signals (b) ... 104
Figure 3-45: Active power responses for different losses of measurement signals (a) ... 104
Figure 3-46: Active power responses for different losses of measurement signals (b) ... 105
Figure 3-47: Active power responses for different losses of control and measurement signals (a) ... 105
Figure 3-48: Active power responses for different losses of control and measurement signals (b) ... 106
Figure 3-49: Active power responses with alternative measurement signal (a) ... 107
Figure 3-50: Active power responses with alternative measurement signals (b) ... 108
Figure 4-1: Input and output signals of the SWAC ... 112
Figure 4-2: New England test system (NETS) [95] ... 113
Figure 4-3: Projection of *a* onto *b* in 2-dimensional space ... 118
Figure 4-4: Speed deviation responses for 27 large disturbances ... 133
Figure 4-5: Three dimensional scores plot (viewing angle 1) ... 134
Figure 4-6: Three dimensional scores plot (viewing angle 2) ... 135
Figure 4-7: Three dimensional scores plot (viewing angle 3) ... 135
Figure 4-8: Two dimensional scores plot ... 139
Figure 4-9: Dendrogram illustrating the clustering process ... 141
Figure 4-10: Hierarchical clustering using PCA-based cluster analysis ... 142
Figure 4-11: Example of coherent generators ... 143
Figure 4-12: Example of non-coherent generators ... 143
Figure 4-13: Voltage phase angle responses of generator buses for 27 large disturbances ... 145
Figure 4-14: Hierarchical clustering of generators ... 147
Figure 4-15: Voltage angle responses of generators in clusters (G2,G3), (G4,G5) and (G6,G7) ... 147
Figure 4-16: Active power responses for a large disturbance at bus 14 using different I/O signals ... 151
Figure 4-17: Speed deviation responses for a large disturbance at bus 14 using different I/O signals ... 152

Figure 4-18: Active power responses for a large disturbance at bus 14 using different I/O signals (last 10 seconds of simulation) ... 153
Figure 4-19: Speed deviation responses for a large disturbance at bus 14 using different I/O signals (last 10 seconds of simulation) ... 154
Figure 5-1: New England test system with SWAC ... 159
Figure 5-2: Hankel singular value plot of the 124th open-loop model (without time delays) ... 159
Figure 5-3: Open-loop system order reduction ... 160
Figure 5-4: LTR procedure with various values of q ... 161
Figure 5-5: Hankel singular value plot of the 27th order SWAC ... 162
Figure 5-6: Further controller reduction ... 162
Figure 5-7: Active power responses for a small disturbance at generator 1 ... 164
Figure 5-8: Active power responses for a large disturbance at bus 14 ... 165
Figure 5-9: Speed deviation responses for a large disturbance at bus 14 ... 166
Figure 5-10: Control actions for a large disturbance at bus 14 ... 167
Figure 5-11: Active power responses for a large disturbance at bus 14 (OC-A1) ... 170
Figure 5-12: Active power responses for a large disturbance at bus 14 (OC-B4) ... 173
Figure 5-13: Active power responses for a large disturbance at bus 14 (OC-C3) ... 174
Figure 5-14: Active power responses for a large disturbance at bus 14 (OC-D3) ... 175
Figure 5-15: Active power responses for a large disturbance at bus 14 with different (total) time delays ... 176
Figure 5-16: Damping ratios versus time delays ... 177
Figure 5-17: Active power responses for a large disturbance at bus 14 with maximum time delay (c) .. 178
Figure 5-18: Active power responses for large disturbance at bus 14 with communication link failure (case 9) ... 181
Figure 5-19: Active power responses for large disturbance at bus 14 with communication link failure (case 16) ... 182
Figure 5-20: Active power responses for large disturbance at bus 14 with communication link failure (case 17) ... 183
Figure 5-21: Active power responses for large disturbance at bus 14 with communication link failure (case 18) ... 184
Figure 5-22: Active power responses for a large disturbance at bus 14 with alternative measurement signals (case 20) ... 185
Figure 8-1: Mode shape plots (4-machine test system) ... 203
Figure 8-2: Power transfers across the 4-machine test system ... 203
Figure 8-3: Mode shape plots (NETS) ... 207
Figure 8-4: Power transfers across the New England test system ... 208
Figure 8-5: Active power responses for a small disturbance at generator 2 ... 212
Figure 8-6: Active power responses for a small disturbance at generator 3 ... 213
Figure 8-7: Active power responses for a small disturbance at generator 4 ... 214
Figure 8-8: Active power responses for a small disturbance at generator 5 ... 215
Figure 8-9: Active power responses for a small disturbance at generator 6 ... 216
Figure 8-10: Active power responses for a small disturbance at generator 7 ... 217
Figure 8-11: Active power responses for a small disturbance at generator 8 ... 218
Figure 8-12: Active power responses for a small disturbance at generator 9 ... 219

Figure 8-13: Active power responses for a small disturbance at generator 10 220
Figure 8-14: Active power responses for a large disturbance at bus 14 (OC-A2) 221
Figure 8-15: Active power responses for a large disturbance at bus 14 (OC-A3) 222
Figure 8-16: Active power responses for a large disturbance at bus 14 (OC-A4) 223
Figure 8-17: Active power responses for a large disturbance at bus 14 (OC-A5) 224
Figure 8-18: Active power responses for a large disturbance at bus 14 (OC-A6) 225
Figure 8-19: Active power responses for a large disturbance at bus 14 (OC-A7) 226
Figure 8-20: Active power responses for a large disturbance at bus 14 (OC-A8) 227
Figure 8-21: Active power responses for a large disturbance at bus 14 (OC-A9) 228
Figure 8-22: Active power responses for a large disturbance at bus 14 (OC-A10) 229
Figure 8-23: Active power responses for a large disturbance at bus 14 (OC-A11) 230
Figure 8-24: Active power responses for a large disturbance at bus 14 (OC-A12) 231
Figure 8-25: Active power responses for a large disturbance at bus 14 (OC-A13) 232
Figure 8-26: Active power responses for a large disturbance at bus 14 (OC-A14) 233
Figure 8-27: Active power responses for a large disturbance at bus 14 (OC-A15) 234
Figure 8-28: Active power responses for a large disturbance at bus 14 (OC-A16) 235
Figure 8-29: Active power responses for a large disturbance at bus 14 (OC-A17) 236
Figure 8-30: Active power responses for a large disturbance at bus 14 (OC-A18) 237
Figure 8-31: Active power responses for a large disturbance at bus 14 (OC-A19) 238
Figure 8-32: Active power responses for a large disturbance at bus 14 (OC-A20) 239
Figure 8-33: Active power responses for a large disturbance at bus 14 (OC-A21) 240
Figure 8-34: Active power responses for a large disturbance at bus 14 (OC-A22) 241
Figure 8-35: Active power responses for a large disturbance at bus 14 (OC-A23) 242
Figure 8-36: Active power responses for a large disturbance at bus 14 (OC-A24) 243
Figure 8-37: Active power responses for a large disturbance at bus 14 (OC-A25) 244
Figure 8-38: Active power responses for a large disturbance at bus 14 (OC-A26) 245
Figure 8-39: Active power responses for a large disturbance at bus 14 (OC-A27) 246
Figure 8-40: Active power responses for a large disturbance at bus 14 (OC-A28) 247
Figure 8-41: Active power responses for a large disturbance at bus 14 (OC-A29) 248
Figure 8-42: Active power responses for a large disturbance at bus 14 (OC-A30) 249

LIST OF SYMBOLS

Symbol	Description
r_a	Armature resistance
x_d	*d*-axis synchronous reactance
x_q	*q*-axis synchronous reactance
$x_d^{'}$	*d*-axis transient reactance
$x_q^{'}$	*q*-axis transient reactance
$x_d^{''}$	*d*-axis sub-transient reactance
$x_q^{''}$	*q*-axis sub-transient reactance
E_d	*d*-axis voltage
E_q	*q*-axis voltage
$E_d^{'}$	*d*-axis transient voltage
$E_q^{'}$	*q*-axis transient voltage
$E_d^{''}$	*d*-axis sub-transient voltage
$E_q^{''}$	*q*-axis sub-transient voltage
$T_{do}^{'}$	*d*-axis transient open-circuit time constant
$T_{qo}^{'}$	*q*-axis transient open-circuit time constant
$T_{do}^{''}$	*d*-axis sub-transient open-circuit time constant
$T_{qo}^{''}$	*q*-axis sub-transient open-circuit time constant
E_{fd}	Excitation field voltage
i_d	*d*-axis current
i_q	*q*-axis current
P_m	Generator mechanical input power
P_e	Generator electrical output power
H	Generator inertia constant
ω_s	Synchronous speed

$\boldsymbol{\delta}$	Rotor angle
$\boldsymbol{\omega}$	Rotor speed deviation
$\boldsymbol{E_{ref}}$	Excitation system reference voltage
$\boldsymbol{E_t}$	Generator terminal voltage
$\boldsymbol{K_A}$	AVR gain
$\boldsymbol{T_A}$	Excitation system time constant
$\boldsymbol{T_j}$	AVR time constant (*j*=*B*, *C*)
$\boldsymbol{E_{fd-max}}$	Maximum field voltage ceiling
$\boldsymbol{E_{fd-min}}$	Minimum field voltage ceiling
$\boldsymbol{V_{PSS}}$	PSS output signal
$\boldsymbol{K_{PSS}}$	PSS gain
$\boldsymbol{V_{PSS-max}}$	Maximum PSS signal ceiling
$\boldsymbol{V_{PSS-min}}$	Minimum PSS signal ceiling
$\boldsymbol{T_i}$	PSS phase compensation time constant (*i*=1…6)
N_B	Number of PSS phase compensation blocks (N_B=2, 4, or 6)
$\boldsymbol{T_w}$	PSS washout filter time constant
$\boldsymbol{T_{Li}}$	PSS low-pass filter time constant (*i*=1, 2)
$\boldsymbol{Z_{ij}}$	Series impedance of transmission line *i-j*
$\boldsymbol{B_{ij}}$	Charging suseptance of transmission line *i-j*
$\boldsymbol{Z_e}$	Transformer leakage impedance
$\boldsymbol{Y_e}$	Transformer leakage admittance
$\boldsymbol{n_t}$	Off-nominal turns ratio of transformer
τ	Signal transmission time delay
$\boldsymbol{P_1(s)}$	1st order Padé approximation function in Laplace domain
$\boldsymbol{P_2(s)}$	2nd order Padé approximation function in Laplace domain
θ	Bus voltage phase angle
x_{id}	State-variable corresponding to algebraic loop filter for *d*-axis current
x_{iq}	State-variable corresponding to algebraic loop filter for *q*-axis current
$x_{\tau u}$	State-variable corresponding to input channel time delay
$x_{\tau y}$	State-variable corresponding to output channel time delay
$x_{\mathrm{PSS}i}$	State-variable corresponding to PSS *i*
$x_{\mathrm{AVR}i}$	State-variable corresponding to AVR *i*

ABSTRACT

Contemporary power networks are gradually expanding incorporating new sources of electrical energy and power electronic based devices. The major stability issue in large interconnected power systems is the lightly damped interarea oscillations. In the light of growth of their incidents there are increased concerns about the effectiveness of current control devices and control systems in maintaining power system stability.

This thesis presents a Wide Area Measurement System (WAMS) based control scheme to enhance power system stability. The control scheme has a hierarchical (two-level) structure comprising a Supplementary Wide-Area Controller (SWAC) built on top of existing Power System Stabilisers (PSSs). The SWAC's focus is on stabilising the critical interarea oscillations in the system while leaving local modes to be controlled entirely by local PSSs. Both control systems in the two levels work together to maintain system stability. The scheme relies on synchronised measurements supplied by Phasor Measurement Units (PMUs) through the WAMS and the only cost requirement is for the communication infrastructure which is already available, or it will be in the near future.

A novel linear quadratic Gaussian (LQG) control design approach which targets the interarea modes directly is introduced in this thesis. Its features are demonstrated through a comparison with the conventional method commonly used in power system damping applications. The modal LQG approach offers simplicity and flexibility when targeting multiple interarea modes without affecting local modes and local controllers, thus making it highly suitable to hierarchical WAMS based control schemes. Applicability of the approach to large power systems is demonstrated using different scenarios of model order reduction. The design approach incorporates time delays experienced in the transmission of the SWAC's input/output signals. Issues regarding values of time delays and required level of detail in modelling time delays are thoroughly discussed.

Three methods for selection of input/output signals for WAMS based damping controllers are presented and reviewed. The first method uses modal observability/controllability factors. The second method is based on the Sequential Orthogonalisation (SO) algorithm, a tool for the optimal placement of measurement devices. Its application is extended and generalised in this thesis to handle the problem of input/output signal selection. The third method combines clustering techniques and modal factor analysis. The clustering method uses advanced Principal Component Analysis (PCA) where its draw backs and limitations, in the context of power system dynamics' applications, are overcome. The methods for signal selection are compared using both small-signal and transient performance analysis to determine the best optimal set of signals.

Enhancement of power system stability is demonstrated by applying the proposed WAMS based control scheme on the New England test system. The multi-input multi-output (MIMO) WAMS based damping controller uses a reduced set of input/output signals and is designed using the modal LQG approach. Effectiveness of the control scheme is comprehensively assessed using both small-signal and transient performance analysis for different case studies including small and large disturbances, changes in network topology and operating condition, variations in time delays, and failure of communication links.

DECLARATION

No portion of the work referred to in the thesis has been submitted in support of an application for another degree or qualification of this or any other university or other institute of learning.

ACKNOWLEDGMENT

It is a great pleasure to thank everyone who made this thesis possible. Firstly I would like to express my sincere gratitude to my supervisor Prof. Jovica Milanovic for his constant help, guidance and support. His ideas were truly inspirational and he has provided valuable insights as well as guidance throughout the period of this research. His wisdom, knowledge, and commitment to the highest standards inspired and motivated me.

I offer my regards to all of those who supported me in any respect during the completion of the thesis. I would particularly like to thank Dr. Ognjen Marjanovic, Lecturer in Control Systems. The technical discussions we had on control system design were truly useful and inspirational.

I would like also to thank all members of Power Quality and Power System Dynamics group: Soon Kiat Yee, Mustafa Kayikci, Yan Zhang, Ayman Alabduljabbar, Sarat Chandra Vegunta, Jhan Yhee Chan, Samila Mat Zali, Faisal Alhasawi, Muhammad Ali, Manuel Avendano-Mora, Nick Wooley, and Robin Preece. Their efforts have had a positive impact on my overall education.

I wish to thank my friends in Manchester for their help and encouragement. Special thanks to Mohsen Alardhi and Farraj Aldehani. I greatly value their friendship and I deeply appreciate their support.

Last but not least, I would like to express my heart-felt gratitude to my family. None of this would have been possible without the support and patience of my family. They were a constant source of love, concern, encouragement and strength.

To my parents and family

1 INTRODUCTION

1.1 Background

Contemporary power networks are gradually expanding incorporating new sources of electrical energy and power electronic based devices. The increased penetration of renewable generation, largely stochastic and/or intermittent, plays a major role in these expansions. In addition, benefits in terms of economy and reliability increased the tendency for more electric power interconnections in all over the world. Cross-border bulk transfers of electrical power across long distances driven by demands of liberated electricity markets increased the level of stress in the power system operating condition. These stressed conditions could easily lead to onset of stability problems. The major stability issue in large interconnected power systems is the lightly damped interarea oscillations. In the light of growth of interarea incidents [1] there are increased concerns about the effectiveness of current control devices and control systems in maintaining power system stability.

Damping of interarea oscillations, in addition to local modes, is traditionally tackled by installing power system stabilisers (PSSs). Each installed PSS receives a local signal, e.g. generator speed or power, and provides a supplementary signal to the generator excitation system modulated with required phase compensation. The observability of interarea modes in local signals is low, compared to global signals [2], and therefore limits to a certain extent the effectiveness of PSSs in damping multiple interarea oscillations. Conventional PSSs are often tuned based on fixed or limited number of operating conditions and therefore their effectiveness is reduced, compared to that of robust controllers like H_∞ in stabilising the system following changes in system topology or operating condition. In addition, the tuning of PSSs remains largely unaltered despite changes in network topology and the prevailing practice is still to tune PSSs by considering only the local electromechanical modes. As a result, the interarea modes may become insufficiently damped under changing operating conditions and more stressed operation of the system and may even lead to instability.

The increase in application of sophisticated Wide Area Measurement Systems (WAMS) and control devices in power systems around the world resulted in an increased interest in exploring effectiveness of wide-area controllers to damp interarea oscillations. These control schemes rely on Phasor Measurement Unit (PMU) technology and have already shown to be capable of improving significantly the damping of interarea oscillatory modes [2-5]. The only cost requirement in such cases is the communication infrastructure which is either readily available, or will be in the near future.

The enhancement of system stability has been also extensively tackled in the past by using Power Oscillation Damping (POD) controllers installed at Flexible AC Transmission System (FACTS) devices [6-10]. The use of remote signals has shown to increase POD controllers' effectiveness in improving the damping of interarea oscillations. FACTS devices are primarily placed in the network to facilitate steady-state operational flexibility such as power flow (series devices) and dynamic voltage control (shunt devices) [11]. Their locations, and consequently locations of control signals, are decided based on studies considering a large number of power flow scenarios including different network topologies. As a result, enhancement of system stability through POD controllers for FACTS devices, in most cases, usually comes as a bonus. In addition, the feasibility of FACTS devices for damping of interarea oscillations has been constantly questioned due to their high costs [12]. For comparative purposes, it has been shown that the use of multiple global signals in WAMS based damping controllers is more cost effective than installing new control devices [13] for the enhancement of system stability.

1.2 Overview of WAMS and PMUs

1.2.1 Phasor Measurement Units

Developments in time synchronising techniques, coupled with the computer-based measurement technique, have provided the opportunity to measure phasors and phase angle differences in real time [14]. Phasors are the basic tools of alternating current (ac) circuit analysis. They are usually introduced as means of representing steady-state sinusoidal waveforms of fundamental power frequency. Even when a power system is not quite in a steady-state, phasors are useful in describing the behaviour of the system [15].

The PMU is a device which samples voltage and current waveforms of a bus and uses synchronisation signal from the Global Positioning System (GPS) [15, 16]. Figure 1-1 shows functional block diagram of a typical PMU where its measurements are synchronised by the GPS which provides a synchronisation accuracy of (1 μs) of Coordinated Universal Time (UTC). This synchronisation accuracy corresponds to 0.021° for a 60 Hz signal and 0.018° for a 50 Hz signal, at any location on earth [15]. The feature of time-stamping of measurements with high precision enabled to have a coherent picture of the system in real time at control centres. All PMU measurements with the same time-stamp are used to infer the state of the power system at the instant defined by the time-stamp [17].

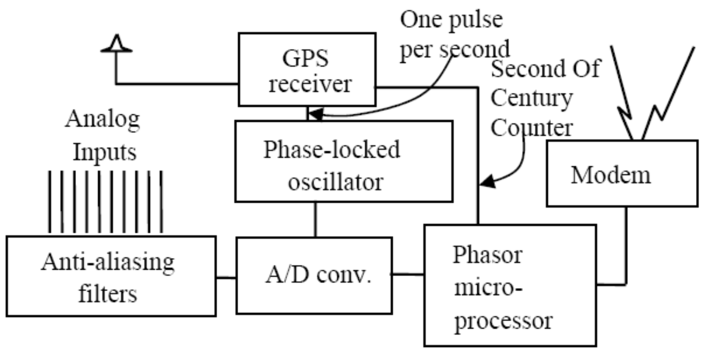

Figure 1-1: Phasor measurement unit (PMU) [17]

The first prototype of the PMU was developed at Virginia Tech in 1988 [15]. Following that, many vendors started commercial manufacturing of PMUs. The IEEE published a standard for synchrophasors for power systems, seven years later, in 1995, [18] and revised versions in 2001 [19] and 2005 [20]. This standard is governing the format of data files created and transmitted by the PMU.

1.2.2 WAMS Structure

The general WAMS structure is shown in Figure 1-2. PMUs are situated in power system substations and provide measurements of time-stamped voltages and currents [17]. From the voltage and current phasors, different applications may compute active and reactive power or other system attributes. The measurements are stored in local data storage devices which can be accessed from remote locations. The phasor data is available for real-time applications in a steady stream as soon as the measurements are made. Phasor information are collected through dispersed PMUs along the network and sent to regional Phasor Data Concentrators (PDCs). The PDC gathers data from PMUs, reject bad data, align the time-stamps, and create coherent record of simultaneously recorded data from a wider part of the power system. Outputs from the PDC are networked to monitoring and control applications [21].

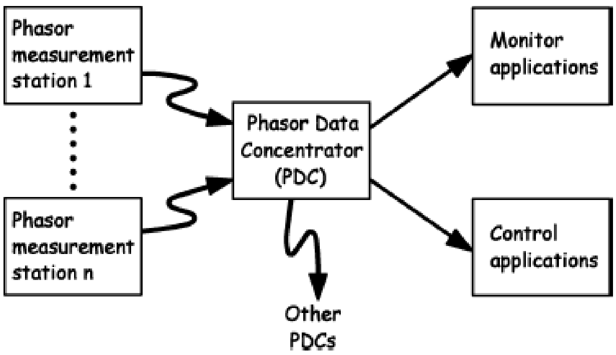

Figure 1-2: General WAMS structure [21]

1.2.3 Applications of PMUs and WAMS

PMU triggered, along with improvements of communication systems, a wide range of application in power systems that were not possible before. This opened the door for many applications that could not be done before such as wide-area monitoring, wide-area protection, wide-area control, etc [22]. The IEEE Committee report on the causes of the 2003 major blackouts addressed the lack of reliable real-time data as one of the major trends in the 2003 blackouts [23]. It recommended WAMS as a potential technology to achieve better knowledge about the actual network condition, timely identification of emergency conditions and possibility of avoiding them, and timely deployment of remedial actions in more controlled fashion [24].

WAMS are additionally useful for efficient operation of deregulated electricity markets because of the requirements for uninhibited exchange of power over long distances and quick changes in the operating conditions. Enhancement to the existing Supervisory Control and Data Acquisition (SCADA) and Emergency Management Systems (EMS) can be done using WAMS [25]. The SCADA/EMS functions are tools that assist the power system/grid operator in his effort to optimise the power system operation, with respect to economy, operational security and robustness, as well as human and material safety. These enhancements are aimed at two key areas: information availability and information interpretation. The operator can have all vital information at his fingertips in an efficient way. For example, with a better analysis tool for voltage instability, the operator can accurately track the power margin across an interface and thus can confidently push the limit of power transfer across that interface [26].

The synchronised measurements technology also led to developments in power system state estimation. A state estimator based on phasor measurements could operate in real-time since the complex voltages used in the algorithm would be measured rather than computed [27]. Therefore, the direct measurement of synchronised positive sequence voltages and currents from the network shifted the emphasis from “state estimation” to “state measurement” [14]. The conventional state estimators are restricted to steady-state applications only, i.e. static estimators. Synchronised phasor measurements provide dynamic synchronous information, i.e. dynamic estimators [15].

Wide-area protection and emergency control systems, using WAMS technology, can also be introduced in the power system to increase the power system transmission capability and/or power system reliability [25, 26]. For example, in [25, 26] several possible design architectures are proposed for the new wide-area protection systems based on PMUs measurements.

Synchronised phasor measurements can further provide simultaneous observations of system oscillations following system disturbances at various sites. This will give a big picture on system dynamics during disturbances and provide sufficient data for validating system models used in computer simulation programs. An example on the use of synchronised measurements for this purpose, i.e. model validation, is given in [22].

One of the important applications of PMUs is the estimation of system security from voltage collapse. Voltage security monitoring system presented in [28] estimates the system security from voltage collapse using PMUs. The use of PMUs for preventing voltage instability is also presented in [29]. PMUs are used as pilot points for the secondary voltage control of power system. This control is performed by decomposing the network into coherent regions and providing each of them with a single PMU.

Installations of PMUs are increasing and many networks started WAMS projects all over the world [30]. Some of the recent examples are the WAMS projects at power systems in Hydro-Quebec [31], the Western Electricity Coordinating Council (WECC) network [32], North America [33], Norway [34], Denmark [35], Brazil [36], Japan [37], China [38], and many more.

1.3 WAMS based Damping Control

Advantages of using synchronised remote signals for damping improvement of interarea oscillations, combined with the availability of these signals through the WAMS, led to an increased interest in applying WAMS based control schemes all over the world. Extensive research has been done to explore the effectiveness and capabilities of the emerging WAMS technology in improving the overall power system stability. For example, research conducted at Hydro-Quebec showed by simulation that wide-area stabilising controllers have a significant potential in improving the dynamic performance of the power system when implemented on few site only [3].

1.3.1 Control Structure

The configuration of WAMS based control schemes can be classified broadly into centralised, quasi-decentralised, and two-level structures. The centralised structure involves a Wide-Area Controller (WAC) controlling the whole power system [39-41]. Input signals to the WAC are coming from pre-selected PMUs and its output signals are sent to excitation systems (represented by AVRs in the figure) of pre-selected generators in the system. The scheme assumes non-existence of PSSs in the system. This is unrealistic as PSSs do exist in real power systems and their function cannot be ignored.

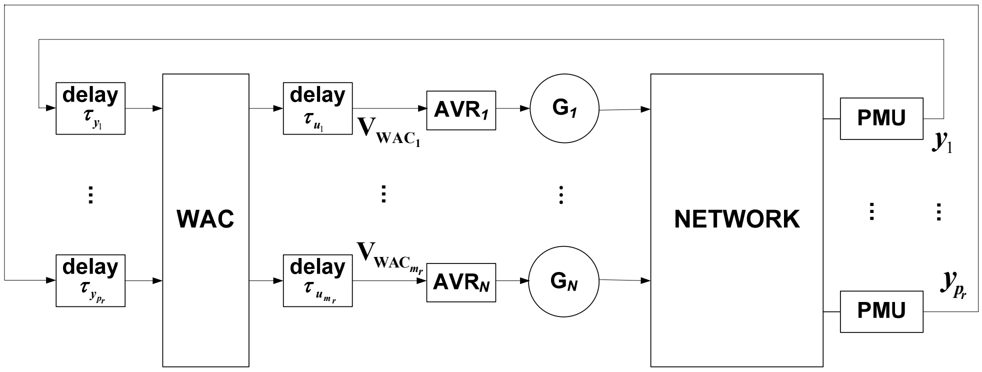

Figure 1-3: Centralised WAMS based control configuration

The quasi-decentralised structure involves remote control loops added to existing decentralised control systems, i.e. PSSs, as shown in Figure 1-4 (reference and terminal voltage signals are not shown for simplicity). Some of the (N) decentralised controllers receive (p_r) delayed remote signals from PMUs dispersed in the network in addition to local signals. The main principle of the structure is to strengthen the effectiveness of decentralised control systems using those remote signals. PSSs have a conventional structure, i.e. lead/lag compensators, in most cases and are designed based on a fixed operating condition. The structure has significant advantages in terms of reliability and operational flexibility [4, 13, 31, 42-44]. When the global signal is lost, then the system will be controlled by decentralised controllers using local signals in the usual way.

The two-level structure of WAMS based control schemes involves adding a second layer of control systems to existing decentralised control systems resulting in a hierarchical configuration as shown in Figure 1-5 [2, 5, 45-49]. Control systems in the first level are fully decentralised and consist mainly of conventional PSSs. PSSs receive local signals, i.e. rotor speed or output power, and add supplementary signals to Automatic Voltage Regulators (AVRs) modulated with required phase compensation (reference and terminal voltage signals are not shown for simplicity). The

Supplementary Wide-Area Controller (SWAC) in the second level receives remote signals, $\left[y_1 \ \ldots \ y_{p_r}\right]$, from ($p_r$) pre-selected PMUs dispersed in the network and provides supplementary damping actions, $\left[\mathrm{V}_{\mathrm{WAC1}} \cdots \mathrm{V}_{\mathrm{WAC}m_r}\right]$, to ($m_r$) pre-selected generators added together with the local control signals from the decentralised controllers in the first level [48]. Decentralised (local) controllers, in the lower level layer ensure the minimum level of system stability and the SWAC in the higher level enhances the overall system stability. Both control systems in the two layers work together to maintain system stability. If local controllers are unable to stabilise the system for certain contingencies the SWAC in the second level can provide additional support. If the SWAC is not functioning, e.g. due to communication link failures, the decentralised layer is still present under these exceptional circumstances thus serving as a fully working backup control system.

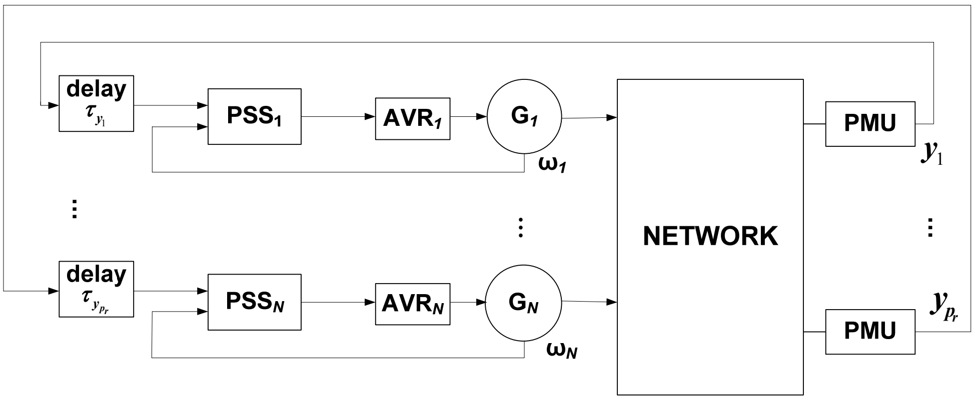

Figure 1-4: Quasi-decentralised WAMS based control configuration

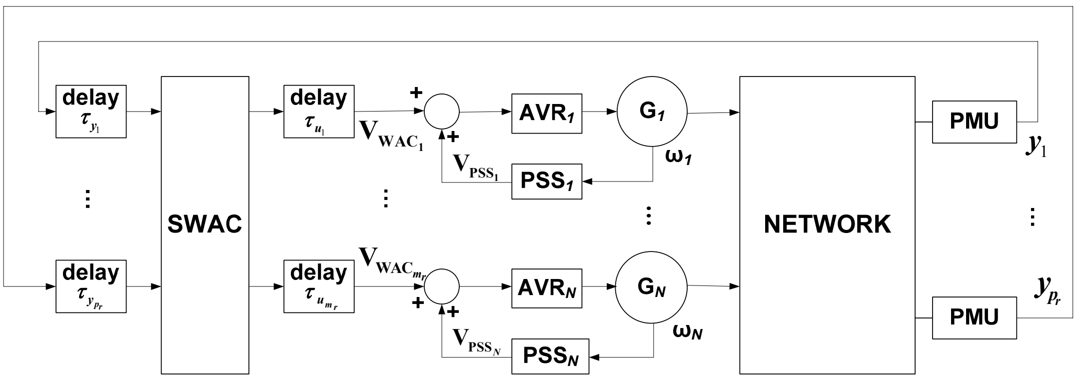

Figure 1-5: Two-level (hierarchical) WAMS based control configuration

1.3.2 Time Delays

In WAMS based control schemes transmitting signals from PMUs to the wide-area controller, through the PDC, and then back to generators involve some time delays. These transmission delays depend primarily on the type of communication link used. Other delays, broadly, include processing and routing of signals at PMUs, PDC(s), and at the wide-area controller. These delays however are small, especially in slow communication links, compared to communication link delays. Time delays can deteriorate effectiveness of the WAMS based damping controllers especially when relatively slow communication link, such as satellite based links, are used [42]. In [39] evaluation of the time delay effect to wide-area power system stabilisers performed using a small gain criterion found that time delay tolerance decreases when the system bandwidth increases. Reference [50] investigates the influence of time delay on power system small signal stability region. It was founds that time delay has significant influence to the boundary of the small signal stability region, especially when the time lag is large.

Different amounts of time delays are reported in the literature for WAMS projects. In the Western Electricity Coordinating Council (WECC) system delays range from approximately 25 ms (one way from PMUs to the wide-area controller) for fibre optics cables to 250 ms for satellite-based links [42]. Reference [51] lists a total estimated time delays for fibre optics communication link in the Nordic power system of 185 ms from PMU to control centre and then to control site. Delays ranging from several milliseconds to 100 ms were reported for the WAMS projects in the Chinese power system [38].

Differences in amounts of delays can be noticed in the proposed WAMS based damping control schemes in the literature. They vary from very short delays of 27.5 ms as in [42], to relatively longer delays of 750 ms as in [52]. Intermediate amount of delays of 100 ms were considered in [13, 39, 53], and of 200 ms in [49]. For a proposed control scheme it is essential to verify the effectiveness of the designed WAMS based damping controller to changes in signal transmission time delays. In addition, due to the wide range of delays encountered in real WAMS it is also essential to demonstrate its validity by considering different amount of delays at the design stage.

In the power system model time delays are represented in Laplace domain as e^{-st}. They are transformed into a rational transfer function for inclusion in the linearised power system model. Padé approximation is a widely used method for modelling of time delays in WAMS based damping applications [13]. The method decreases the real effect of time delays on the control system [53] and with a 2nd order provides good approximation of long delays [49].

1.3.3 Controller Design

Several design methods have been proposed in the past to address the problem of power system damping and control using WAMS technology. The simplest one uses a lead-lag block compensator, similar to the conventional PSS [2, 3]. This wide-area controller is usually designed in a similar way to the conventional PSS, i.e. based on a fixed operating condition of the linearised power system model. H_∞ control [54] has been often used to ensure the robustness of designed wide-area controller in terms of changing operating condition and modelling errors [8, 45, 46]. Despite its clear advantages in terms of robustness, it was found though that it is prone to the pole-zero cancellation between the system plant and the controller when based on the solution of the Algebraic Riccati Equation (ARE) method [55]. In [48] the synthesis of robust H_2/H_∞ controllers is resolved by the Linear Matrix Inequality (LMI) technique [56]. The method relies on the H_∞ optimisation and suffers from the difficulty in selecting the weighting functions [8]. The H_∞ based control schemes typically address the worst-case scenario and are therefore intrinsically conservative when dealing with less severe disturbances and model uncertainties.

The Linear Quadratic Gaussian (LQG) control design has been introduced for WAMS based damping controllers [49, 57]. It is considered to be a cornerstone of the modern optimal control theory and is based on the minimisation of a cost function that penalises states' deviations and actuators' actions during transient periods. The essential idea of the LQG control design is to address the intrinsic compromise between an attempt to minimise the error (state deviations) and an attempt to keep control effort at the minimum. The main advantage of LQG control is its flexibility and usability when specifying the underlying trade-off between state regulation and control action. Advantages of LQG control led to a widespread research in its application for power system damping. Early applications of optimal quadratic control appear in [58-61] where state-feedback controllers are applied to control the excitation and governor systems. In [57, 62-65] an LQG controller, comprising Linear Quadratic Regulator (LQR) and Kalman filter, is used. Adaptive LQG controllers were presented for power system damping in [9, 66]. In [8, 10] a Thyristor Controlled Series Capacitor (TCSC) installed at the power system is equipped with LQG controller to damp interarea oscillations. Reference [67] applies LQG decentralised controller to damp selected electromechanical modes.

Despite the clear advantages of using LQG control for power system damping the design procedure usually is not straightforward. Specific weights on the states in the LQG cost function are derived, in most cases, according to participating factor analysis [68, 69]. The highly participating states being given higher weights and as a result of this ad-hoc procedure [8] the damping of the interarea modes is improved [10, 49, 57, 66]. The cost function weightings imposed on these highly participating states however do not directly address the critical interarea modes. In addition, for power systems with multiple lightly damped interarea modes those difficulties in the tuning process are magnified and the design stage becomes complex.

1.3.4 Input/output Signal Selection

The WAMS based damping controller depends primarily on the synchronised measurements transmitted from PMUs through the WAMS. Due to the costs associated with the installations of PMUs, communication infrastructure costs in particular, their number should be minimised. The same constraint applies equally to number of used wide-area control signals sent to generators' exciters. Their number should be minimised in order to reduce the associated communication infrastructure costs and also to reduce complexity of the overall control system. Effectiveness of the WAMS based damping controller is highly affected by the observability/controllability information carried by its input/output signals, respectively, about the modes of interest. The used sets of reduced measurement and control signals therefore should provide as much as possible enough observability/controllability information, respectively, about the modes of interest to increase the effectiveness of the controller.

Extensive research in the power system literature has been done in the past two decades to tackle the problem of optimal placement of PMUs. The vast majority of placement methods aim to maximise the observability information, from state-estimation perspective, to improve the state estimation of the system [17]. In the context of WAMS based control schemes placement of PMUs aims to maximise the observability information, from stability perspective, about the critical electromechanical modes in the system, i.e. the lightly damped interarea modes. Inputs to the WAMS based damping controller are the synchronised measurements taken from the optimally placed PMUs in the network.

An early work on the optimal placement of measurement devices to maximise their coverage of interarea oscillations was introduced in [70]. GPS-based monitoring devices, angle transducers, are placed optimally so as to maximise their sensitivity to the lightly damped interarea modes while minimising their sensitivity to the more heavily damped local modes. The methodology uses modal observability factors of the electromechanical modes and accounts for correlation (redundancy) of information about the interarea oscillations of concern. The placement procedure is done sequentially such that redundancy of observability information is minimised and the optimal set of PMUs gives the greatest coverage of the various interarea modes as possible. Research conducted at Hydro-Quebec allowed a minimum number of PMUs to be optimally placed using this method on the system in order to collectively maximise the amount of dynamic information contained in the wide-area measurements [3].

The most common method of input/output signal selection for wide-area controllers is based on modal controllability/observability factors, respectively [2, 3, 5, 48, 71]. For each individual mode of interest the measurement signal with highest modal observability, among all candidate measurements, is selected as input signal to the wide-area controller. Similarly for each individual mode of interest the control signal with highest modal controllability, among all candidate control signals, is selected as output signal from the wide-area controller. In this widely used method, number of modes of interest decides the maximum number of input/output signals.

Coherency of generators [72] has been used in [13], combined with good knowledge of the system, for the selection of the remote input signal used for the controller. Coherency is also applied for the selection of input signals for frequency-input wide-area controllers in a large scale power system [3]. The system is divided into 9 coherent areas and the modal observability of the average frequency signals, from each of the 9 areas, are compared. Individual signals from each area having the maximum modal observability are further compared and the frequency signal with the highest modal observability is selected as input to the wide-area controller. The two-steps procedure is repeated for each individual interarea mode. The process considers all coherent areas in the system in the final hierarchical wide-area control system.

A time domain coherency identification method has been introduced in [73] using Principal Component Analysis (PCA). System responses, e.g. generator rotor angle variation, following a disturbance can be transformed using the PCA to uncorrelated variables. The required system response can be provided by PMUs through the WAMS. Coherent groups of generators are then identified by the visual inspection of three dimensional plots representing the response of each generator in the system. The PCA method is fast and identifies coherent generators without any model information thus making it suitable for very large networks analysis. The method does not need linearisation and modal information, e.g. eigen-analysis results, of the system as it relies only on PMUs measurements. Therefore it can be regarded as an effective tool for the identification of coherent generators. Visual inspection of the PCA results however could lead to inaccurate clustering of generators, mainly due to human judgment and the viewing angle. Furthermore, visual inspection of the results is limited to three principal components which, in some cases, might not be sufficient for adequate capturing of original data variation in the PCA decomposition; thus leading to inaccurate results. Coherency identification generally needs to be performed quickly and visual inspection obviously cannot meet this requirement.

1.4 Summary of Past Research in the Area

Different structure of WAMS based control schemes are proposed in the literature. The centralised structure [39, 40, 44] ignores the existence of PSSs in the power system and therefore seems unrealistic. The quasi-decentralised and hierarchical structures have significant advantages in terms of reliability and operational flexibility. They comply with real power systems and the only cost requirement is, mainly, the cost of communication infrastructure. The quasi-decentralised structures involve conventional PSSs with extra remote signals to increase their effectiveness in maintaining the system stability [4, 13, 31, 42, 43]. The structure of PSSs however is changed and therefore limits the application of this type of control scheme to large extent. In fact many utilities are reluctant to change the structures of existing PSSs. The hierarchical structure has the advantage of keeping local controllers as they are, and only remote feedback loops are built on top of them [2, 5, 45-49]. The wide-area controller in the higher level focuses on stabilising the critical interarea oscillations and the decentralised controllers in the lower level focus on maintaining the adequate level of system stability. Both control systems in the two levels are working together to ensure the stability of the system.

In WAMS based control schemes signals transmitted from PMUs to the wide-area controller, through the PDC, and then back to generators involve some time delays. These transmission delays depend primarily on the type of communication link used. Time delays can deteriorate effectiveness of the WAMS [39]. Different amounts of time delays have been reported in the literature for WAMS projects [38, 42, 51]. Differences in amounts of delays can be noticed also in the WAMS based damping control schemes proposed in the literature [13, 39, 42, 49, 52, 53]. In the power system model time delays are represented in Laplace domain and are transformed into a rational transfer function. Padé approximation is widely used for modelling of time delays in WAMS based damping applications as it decreases the real effect of time delays on the control system [13, 49, 53].

The controller's design plays a major role in focusing the control effort towards damping improvement of certain modes in the system. Several control design methods are applied in the proposed schemes ranging from conventional structures of PSSs [2, 3], i.e. lead/lag compensator, to more advanced robust control like H_2/H_∞ [45-48] and LQG [49, 57]. The LQG control has the advantage of flexibility and usability when specifying the underlying trade-off between state regulation and control action. The main difficulty in LQG control design is when handling multiple interarea modes simultaneously. The LQG controller's tuning process becomes complex and depends primarily on participation factors analysis [68, 69].

WAMS based damping controllers use reduced number of input/output signals to reduce the communication infrastructure costs and also to reduce the complexity of the overall control system. Input signals to the controller are synchronised measurements taken at optimally placed PMUs in the network. Optimal placement of PMUs has been extensively researched from the state estimation perspective [17]. PMUs placed to maximise the coverage of interarea oscillations has been introduced in [70] while considering the sensitivity to the local modes.

The effectiveness of the wide-area controller increases when its input/output signals carry the maximum observability/controllability, respectively, information about the critical interarea modes of interest. The most common used method to select input/output signals uses the individual modal observability/controllability factors, respectively, for each mode of interest [2, 3, 5, 48, 71]. Coherency also has been used for signal selection [13] and for big systems it was combined with modal factors [3] to reduce the number of controller's signals.

An effective tool for coherency identification uses principal component analysis applied to system responses following disturbances [73]. The method is fast and identifies coherent generators with any model information and relies only on PMU measurements. The method however depends on visual inspection of 3-D plots, in most cases, which may lead to inaccurate results mainly due to human judgement and the viewing angle.

1.5 Aims and Objectives of the Research

Currently most utilities are reluctant to install control loops on top of existing local controllers. The major concern is about possible interference with functionality of existing local controllers (PSSs in particular).

The main aim of this research is therefore to propose a WAMS based control scheme considering this issue. The hierarchical control structure should comply with current practices in real power systems and enable the PSSs to continue in maintaining system stability as before. The added Supplementary Wide-Area Controller (SWAC) in the higher level should enhance the system stability by focusing only on the critical interarea oscillations. If the SWAC is controlling the whole power system then the control scheme becomes centralised. An important aim of the research is therefore to analyse the effect of the SWAC on local modes and also on local controllers.

In order to achieve the above aims the research has the following objectives:

- The controller design plays a major role in directing its control effort towards enhancement of system stability and effects on other modes and decentralised controllers. The first objective of the research is to enhance the LQG control method such that the designed SWAC focuses only on stabilising the critical interarea modes and leaves other modes unaffected.

- The second objective is to simplify the design process without using participation factors analysis. Effectiveness of designed LQG controller has to be ensured over wide range of operating conditions. The design methodology should be compared with the conventional LQG design method on a small and large test systems [74, 75] to verify its performance.
- Amounts of signal transmission time delays reported in the literature are different for different WAMS projects. The third objective of the research is that the controller design methodology should be applicable for any amount of time delay. The SWAC as a WAMS based damping controller should be assessed for possible variations in signal transmission time delay along with communication link failures.
- In real WAMS based control schemes, the SWAC uses a reduced set of input/output signals. Different methods are introduced in the literature for signal selection. The most common method uses modal observability/controllability factors for each individual mode of interest. For large power systems, signals are reduced using coherency combined with modal factors analysis. The PCA coherency identification method can be used to partition the network into coherent areas. The method however depends on visual inspection of 3-D plots, in most cases, which may lead to inaccurate results. The fourth objective of the research is to overcome drawbacks and limitations of the PCA method for fast and accurate identification of coherent generators. In the context of input/output signal selection for the SWAC, the research should enhance the PCA method to cluster candidate signals into different groups and then use the modal factors analysis to select the best signal from each group.
- The SO algorithm, as an effective tool for the optimal placement of PMUs, can be also used for the selection of input/output signals. The fifth objective of the research is to generalise the application of the SO algorithm to the selection of optimal input/output signals for the SWAC. The research should also compare the different signal selection methods to determine the best choice of signals which increase the effectiveness of the SWAC.

- The final objective of the research is to apply a hierarchical WAMS based control scheme on a relatively large power system. The multi-machine power system to be used is the New England Test System (NETS) modified in this thesis such that is has multiple interarea modes. Input/output signals of the SWAC should be determined by comparing different selections from different methods. The research objective is to demonstrate the benefits of using WAMS based damping controllers in enhancing the system stability. The demonstration of proposed control scheme should be done using comprehensive small-signal and transient performance analysis over wide range of operating conditions involving different network topologies and power transfers. Effectiveness of the WAMS based damping controller should be verified for variations in time delays and communication link failures.

1.6 Main Contributions of the Thesis

The main contributions of the thesis are summarised as follows (the cited papers in parentheses are listed in Appendix E):

- Modelling of multi-machine power system in the Matlab/Simulink environment. This includes incorporation of PMU measurements (phasors) and time delays of WAMS communication links in the model in addition to application of analysis, design, and assessment tools for small and large disturbance analysis.
- Development of suitable test systems, by modification of the existing ones, in order to have multiple interarea modes for the thorough demonstration of proposed methodologies in the thesis. This is achieved by comprehensive load flow studies, small-signal stability analysis, and robustness analysis to changing operating conditions for different case studies (papers E1-E3).
- Generalisation of the SO algorithm to tackle the problem of input/output signal selection for WAMS based damping controllers. This includes a thorough representation of the algorithm with examples illustrating the mathematical principles applied (paper E6).
- Critical review of the Principal Component Analysis (PCA) coherency identification method with emphasis on its features and drawbacks (paper E4).

- Development of new technique to overcome limitations and drawbacks of the PCA coherency identification method using cluster analysis. Advantages of applying the novel PCA-based clustering method to coherency identification are also addressed thoroughly (paper E4).
- Application of the combined PCA-based clustering method with modal factors analysis to select reduced sets of input/output signals for wide-area controllers (papers E5 and E7).
- Comparison of methodologies for selection of input/output signals for wide-area controllers through the optimal placement of PMUs and comparison of the effectiveness of resulting controllers (papers E5 and E7).
- Critical review of LQG application to power system damping including exposing difficulties at the deign stage when handling multiple interarea modes. Effect on other modes, local modes in particular, is discussed in the context of hierarchical WAMS based damping control (paper E1).
- Development of a novel modal LQG design approach which enables adding damping only to certain modes in the system while keeping other modes unaffected. Characteristic features of the approach, in terms of design simplicity and high suitability to hierarchical WAMS based control schemes, are also addressed (paper E1).
- Comprehensive assessment of the designed WAMS based damping controller using the modal LQG approach under different scenarios of model order reduction, changing operating conditions, variations in signal transmission time delays, and failures in communication links (papers E2 and E3).
- Demonstration of potential enhancement of multi-machine power system stability using multi-input multi-output (MIMO) WAMS based damping controller with reduced set of input/output signals designed using the modal LQG approach (paper E3).

1.7 Outline of the Thesis

Chapter 1: Introduction addresses stability issues of modern interconnected power systems. Overview of WAMS and PMUs and their applications then follows. The WAMS based control schemes are then described in terms of structure, time delays, controller design, and input/output signal selection. Summary of past research is presented along with aims and contributions of this thesis.

Chapter 2: Power System Modelling and Tools for Analysis describes in brief models of the main components of the power system. This includes synchronous generators, excitation control systems, Power System Stabilisers (PSSs), transmission lines, transformers, system loads, and the electrical network. Models of time delays encountered in the transmission of synchronised measurements are then described. Following this, linearised power system model is described mathematically through modal analysis. Its characteristics are presented through defining parameters such as: eigenvalues, right and left eigenvectors, participation factors, modal controllability and observability, and residues.

Chapter 3: Modal LQG Control Approach introduces a novel design approach to linear quadratic Gaussian (LQG) control. The approach enables direct damping of multiple interarea oscillations by the LQG controller while leaving other modes unaffected. The modal LQG approach is compared with the standard, conventional, LQG design method to demonstrate its design simplicity, effectiveness, applicability to large systems, and suitability to WAMS based control schemes. Signal transmission time delays are incorporated in the design approach. Effectiveness of the WAMS based damping controller designed using the modal LQG approach is verified on different case studies using both small-signal and transient performance analysis.

Chapter 4: Selection of Input/Output Signals introduces different methods for the selection of input/output signals for WAMS based damping controllers. The first method is based on modal observability/controllability factors analysis. The second method is based on the Sequential Orthgonalisation (SO) algorithm generalised in this thesis for the selection of both optimal input and output signals. The third method is based on combined clustering and modal factors analysis. The clustering of generators' measurements is done using a novel Principal Component Analysis (PCA) based cluster analysis technique. Each method is presented and applied to a multi-machine power system to select sets of reduced input/output signals. Results of the methods are assessed and compared using both small-signal and transient performance analysis.

Chapter 5: Enhancement of Multi-Machine System Stability presents a WAMS based control scheme for damping of multiple interarea oscillations. Optimal set of input/output signals is used for the WAMS based damping controller. The multi-input multi-output (MIMO) damping controller is designed using the modal LQG control approach. Effectiveness of the controller in enhancing the system stability is demonstrated using both small-signal and transient performance analysis on different case studies.

Chapter 6: Conclusions and Future Work presents the main conclusions of the research work presented in the thesis. Proposals for future work are presented based on the various techniques and methodologies implemented in the thesis.

2 POWER SYSTEM MODELLING AND TOOLS FOR ANALYSIS

2.1 Introduction

This chapter briefly describes models of the main components of the power system. This includes synchronous generators, excitation control systems, Power System Stabilisers (PSSs), transmission lines, transformers, system loads, and the electrical network. Models of time delays encountered in the transmission of synchronised measurements are then described. Following this, linearised power system model is described mathematically through modal analysis. Its characteristics are presented through defining parameters such as: eigenvalues, right and left eigenvectors, participation factors, modal controllability and observability, and residues.

2.2 Power System Modelling

2.2.1 Synchronous Generator Model

The synchronous generator model used in this study is the 5^{th} order model [76]. The model differential equations are as follows

$$pE_q^{''} = \frac{1}{T_{do}^{''}}\left\{E_q^{'} - E_q^{''} - i_d\left(x_d^{'} - x_d^{''}\right)\right\} + pE_q^{'} \tag{2.1}$$

$$pE_d^{''} = \frac{1}{T_{qo}^{''}}\left\{-E_d^{''} + i_q\left(x_q - x_q^{''}\right)\right\} \tag{2.2}$$

$$pE_q^{'} = \frac{1}{T_{do}^{'}}\left\{E_{fd} - E_q^{'} - i_d\left(x_d - x_d^{'}\right)\right\} \tag{2.3}$$

$$p\omega = \frac{1}{2H}\left(P_m - P_e\right) \tag{2.4}$$

$$p\delta = \omega_s\left(\omega - 1\right) \tag{2.5}$$

where $p=d/dt$ and ω_s is the synchronous speed. The algebraic equations describing stator d-axis voltage, q-axis voltage, stator terminal voltage, and generator electrical real power are as follows, respectively

$$E_d = E_d^{''} - r_a i_d + x_q^{''} i_q \tag{2.6}$$

$$E_q = E_q^{''} - r_a i_q - x_d^{''} i_d \tag{2.7}$$

$$E_t = \sqrt{E_d^2 + E_q^2} \tag{2.8}$$

$$P_e = E_d i_d + E_q i_q \tag{2.9}$$

2.2.2 Excitation System Model

The basic function of an excitation system is to provide direct current to the synchronous machine field winding [74]. In addition, the excitation system controls, through the Automatic Voltage Regulator (AVR), the field voltage and thereby the field current. The control functions include the control of voltage and reactive power flow, and the enhancement of system stability. Excitation system can be DC, AC, and static. Different types and models of excitation systems are listed in [77]. Figure 2-1 shows the functional block diagram of a synchronous generator excitation control system. The AVR block diagram used in this work is shown in Figure 2-2.

2.2.3 Power System Stabiliser Model

The main function of a PSS is to add damping to the generator rotor oscillations by controlling its excitation [74]. This is achieved by modulating the generator excitation so as to develop a component of electrical torque in phase with rotor speed deviations. The PSS adds appropriate phase compensation to account for phase lag between the exciter input and the electrical torque. This is performed by adding a supplementary PSS signal to the AVR summation input along with terminal and reference voltages. The PSS block diagram is shown in Figure 2-3. Shaft speed, real power, and terminal frequency are among the commonly used input signals to the PSS [78].

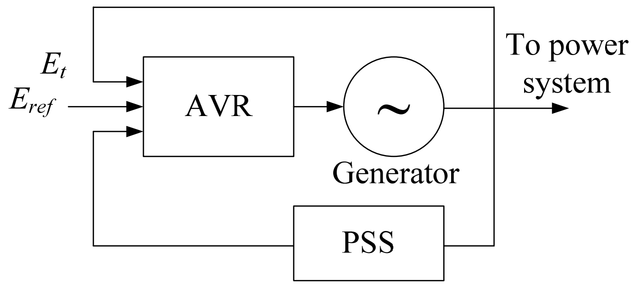

Figure 2-1: Functional block diagram of synchronous generator excitation control system

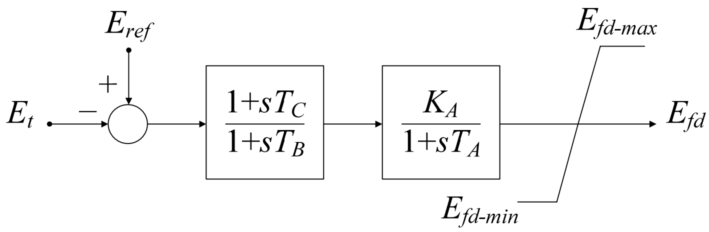

Figure 2-2: AVR block diagram

In this work, the rotor speed deviation is used as the input signal to the PSS. The phase compensation blocks, usually 2 to 3 first order blocks, provide the appropriate phase lead characteristics to compensate for the phase lag between the exciter input and the generator rotor speed. The PSS gain, K_{PSS}, is used for amplification and its value is set for maximum amount of damping. The blocks of signal washout, a high-pass filter, and low-pass filter are used to allow signals associated with rotor oscillations to pass unchanged. In addition, the washout block is used to prevent steady changes in speed from modifying the generator terminal voltage. The output of the stabiliser must be limited to prevent damping signals from saturating the excitation system and thereby defeating the voltage regulation function [78]. The positive output limit of the stabiliser is set at a relatively large value in the range of 0.1 to 0.2 pu. This allows a high level of contribution from the PSS during large swings. The negative output limit of the stabiliser, usually in the range of -0.05 to -0.1 pu, is to allow sufficient control range while providing satisfactory transient response and also to prevent unit trip in case of PSS output being held at the negative limit because of a failure of the stabiliser.

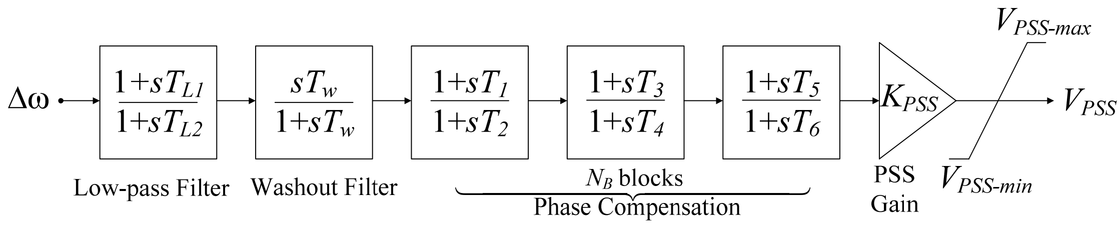

Figure 2-3: Power system stabiliser block diagram

2.2.4 Transmission Line Model

Transmission lines are modelled using the well-known π equivalent circuit shown in Figure 2-4 bellow where $\boldsymbol{Z_{ij}}$ represents the series impedance of the line and $\frac{\boldsymbol{B_{ij}}}{2}$ represents half of the total line charging susceptance at each node. It is assumed that lines are not too long so that the use of lumped parameters in equivalent model is justified.

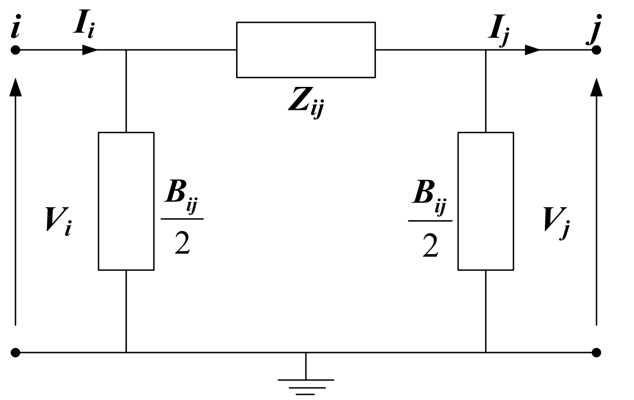

Figure 2-4: Equivalent π circuit of a transmission Line

2.2.5 Transformer Model

Transformers are modelled using the equivalent π circuit shown in Figure 2-5 bellow where $\boldsymbol{Y_e}=1/\boldsymbol{Z_e}$, $\boldsymbol{c}=1/\boldsymbol{n}$, $\boldsymbol{Z_e}$ is the transformer leakage impedance and $\boldsymbol{n}$, a complex quantity, is the off-nominal turns ratio.

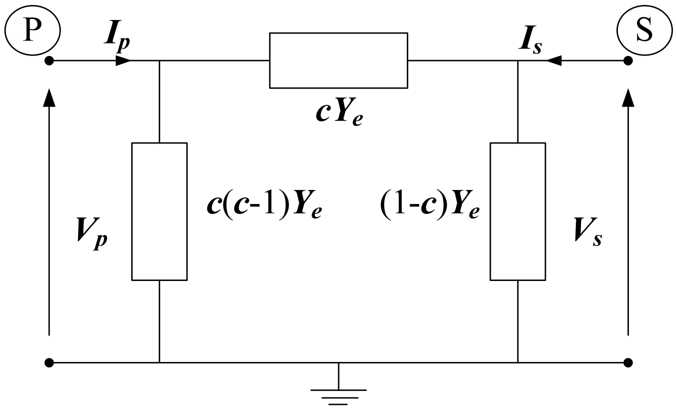

Figure 2-5: Equivalent π circuit of a transformer

2.2.6 Load Model

Power system loads models are classified into two broad categories: static models and dynamic models [74]. A static load model expresses the characteristics of the load at any instant of time as algebraic functions of the bus voltage magnitude and frequency at that instant. When the response of loads to voltage and frequency changes is fast, the steady-state of the response is reached very quickly and the use of static models is justified. Voltage dependency of load can be described by an exponential model as follows

$$\boldsymbol{P} = \boldsymbol{P}_0 \left(\frac{\boldsymbol{V}}{\boldsymbol{V}_0} \right)^{a}, \ \boldsymbol{Q} = \boldsymbol{Q}_0 \left(\frac{\boldsymbol{V}}{\boldsymbol{V}_0} \right)^{b} \tag{2.10}$$

where the subscript 0 identifies the values of the respective variable at the initial operating condition. The parameters of this model are the exponents *a* and *b*. With these exponents equal to 0, 1, or 2, the model represents constant power, constant current, or constant impedance characteristics, respectively. The load model used in this work is the constant impedance model and represented by a constant shunt admittance connected to the bus as follows

$$\boldsymbol{Y}_{load} = \frac{\boldsymbol{P}_0 - j\boldsymbol{Q}_0}{\left|\boldsymbol{V}_0\right|^2} \tag{2.11}$$

The load representation can have a significant impact on analysis results [79]. For example, system voltages are normally depressed during the first angular swing following a disturbance. The power consumed by the loads during this period will affect the generation-load power imbalance and thereby affect the magnitude of the angular excursion and the first swing stability of the system. Another effect is in the case of interarea modes of oscillation occurring in the modelled system. The presence of these oscillations often results in significant variations in voltage and local frequency. In such cases, the load voltage and frequency characteristics may have significant impact on the damping of the oscillations. Ref. [80] gives examples of the effect of load representation in power system stability studies.

The chosen load model in this work, the constant impedance model, is however not critical in this particular work as the main emphasis is to propose a methodology of power system wide-area control. Nevertheless, the representation of loads using the constant impedance model is considered adequate in stability studies [81]. Load modelling effects, especially those associated with induction motors, however must be included in further detailed studies.

2.2.7 Network Model

The interlinked transmission lines, transformers, and constant impedance loads are combined to model the whole network by forming the nodal network equation [82] as follows

$$\begin{bmatrix} \boldsymbol{I}_n \\ \boldsymbol{I}_r \end{bmatrix} = \begin{bmatrix} \boldsymbol{Y}_{nn} & \boldsymbol{Y}_{nr} \\ \boldsymbol{Y}_{rn} & \boldsymbol{Y}_{rr} \end{bmatrix} \begin{bmatrix} \boldsymbol{V}_n \\ \boldsymbol{V}_r \end{bmatrix} \tag{2.12}$$

where the subscript n is used to denote generator nodes and the subscript r is used for the remaining nodes. The current injection for the remaining nodes $\boldsymbol{I}_r$ is zero. Therefore, by expanding (2.12) and applying the matrix partial inversion [81] the current injection at generator nodes is found as follows

$$\boldsymbol{I}_n = \boldsymbol{Y}_{red}\boldsymbol{V}_n = \left(\boldsymbol{Y}_{nn} - \boldsymbol{Y}_{nr}\boldsymbol{Y}_{rr}^{-1}\boldsymbol{Y}_{rn}\right)\boldsymbol{V}_n \tag{2.13}$$

Figure 2-6 shows the representation of a multi-machine power system with n generators and the reduced nodal admittance matrix. Voltages at the remaining nodes can be calculated as follows

$$\boldsymbol{V}_r = \left(-\boldsymbol{Y}_{rr}^{-1}\boldsymbol{Y}_{rn}\right)\boldsymbol{V}_n \tag{2.14}$$

A coordinate transformation is applied between each individual machine model (d-q) reference frame, which rotates with its rotor, and the network (D-Q) common reference frame, which rotates at synchronous speed. Figure 2-7 and equations (2.15) and (2.16) show the reference frame transformation for voltages. Reference frame transformation for currents is applied similarly.

$$\begin{bmatrix} V_D \\ V_Q \end{bmatrix} = \begin{bmatrix} \sin\delta & \cos\delta \\ -\cos\delta & \sin\delta \end{bmatrix} \begin{bmatrix} V_d \\ V_q \end{bmatrix} \tag{2.15}$$

$$\begin{bmatrix} V_d \\ V_q \end{bmatrix} = \begin{bmatrix} \sin\delta & -\cos\delta \\ \cos\delta & \sin\delta \end{bmatrix} \begin{bmatrix} V_D \\ V_Q \end{bmatrix} \tag{2.16}$$

For transient performance analysis, a three phase fault is applied at a bus i by modifying the pre-fault bus admittance matrix to a large value, say 10^6, as follows [74]

$$Y(i,i) = 10^6 \tag{2.17}$$

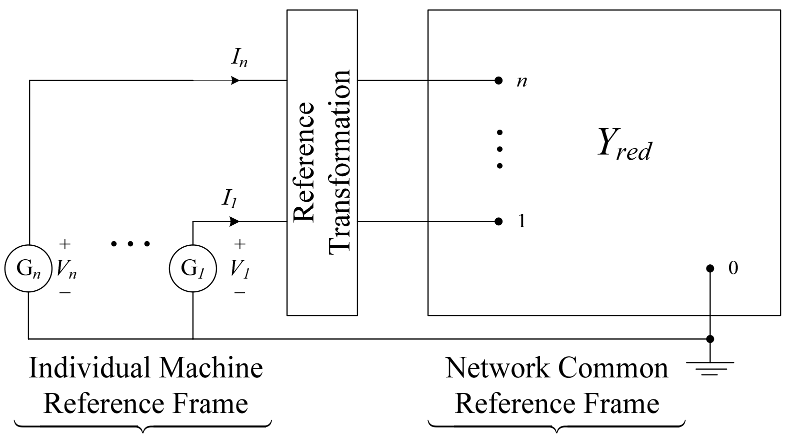

Figure 2-6: Representation of a multi-machine power system

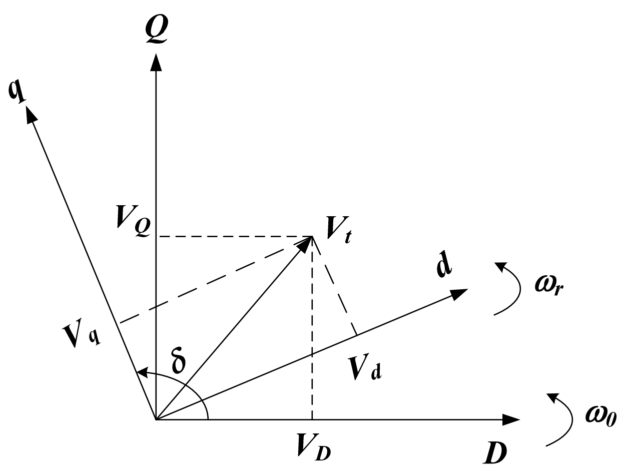

Figure 2-7: Reference frame transformation

2.2.8 Time Delays

In Wide Area Measurement Systems (WAMS) transmission of signals from Phasor Measurement Units (PMUs) to Phasor Data Concentrators (PDCs) involves time delays. Figure 2-8 shows the mathematical representation of time delay function in both time and Laplace domains. The Laplace domain function $\boldsymbol{T}(\boldsymbol{s}) = \boldsymbol{e}^{-\tau s}$ is transformed into a rational function for inclusion in the linearised power system model. Padé approximation is a widely used method in WAMS based damping application for modelling of time delays [13, 49, 53]. The Padé approximation of time delays is given by [83]

$$\boldsymbol{P}(\boldsymbol{s}) = \sum_{j=0}^{l} \frac{(l+k-j)!\,l!\,(-\boldsymbol{\tau s})^j}{j!\,(l-j)!} \Bigg/ \sum_{j=0}^{k} \frac{(l+k-j)!\,k!\,(\boldsymbol{\tau s})^j}{j!\,(k-j)!} \tag{2.18}$$

where l and k refer to the order of the approximation.

$$\boxed{\boldsymbol{T}(t-\tau)} \longrightarrow \boxed{\boldsymbol{T}(\boldsymbol{s})=\boldsymbol{e}^{-\tau s}}$$

Time domain Laplace domain

Figure 2-8: Time delay function

2.3 Tools for Analysis

2.3.1 Power System Linearisation

The power system can be modelled using sets of non-linear Differential-Algebraic Equations (DAEs). The set of differential equations describes the dynamic behaviour of the system and can be represented compactly in vector-matrix format as follows

$$\dot{\boldsymbol{x}} = \boldsymbol{f}(\boldsymbol{x}, \boldsymbol{u}) \tag{2.19}$$

where

$$\dot{\boldsymbol{x}} = [\dot{\boldsymbol{x}}_1 \quad \dot{\boldsymbol{x}}_2 \quad \dots \quad \dot{\boldsymbol{x}}_n]^T, \ \boldsymbol{x} = [\boldsymbol{x}_1 \quad \boldsymbol{x}_2 \quad \dots \quad \boldsymbol{x}_n]^T$$
$$\boldsymbol{u} = [\boldsymbol{u}_1 \quad \boldsymbol{u}_2 \quad \dots \quad \boldsymbol{u}_m]^T, \ \boldsymbol{f} = [\boldsymbol{f}_1 \quad \boldsymbol{f}_2 \quad \dots \quad \boldsymbol{f}_n]^T$$

and n is the order of the system, m is the number of inputs, $\boldsymbol{x}$ is the state vector with its entries as state variables, $\boldsymbol{u}$ is the vector of inputs to the system, and $\boldsymbol{f}$ is a vector of n first order nonlinear ordinary differential equations. Output variables which can be observed on the system may be expressed in terms of the state variables and the input variables as follows

$$\boldsymbol{y} = \boldsymbol{g}(\boldsymbol{x}, \boldsymbol{u}) \tag{2.20}$$

where

$$\boldsymbol{y} = \begin{bmatrix} \boldsymbol{y}_1 & \boldsymbol{y}_2 & \cdots & \boldsymbol{y}_p \end{bmatrix}^T, \; \boldsymbol{g} = \begin{bmatrix} \boldsymbol{g}_1 & \boldsymbol{g}_2 & \cdots & \boldsymbol{g}_p \end{bmatrix}^T$$

and p is the number of outputs, $\boldsymbol{y}$ is the vector of outputs, and $\boldsymbol{g}$ is a vector of nonlinear functions relating state and input variables to output variables.

The derivatives $(\dot{\boldsymbol{x}}_1, \dot{\boldsymbol{x}}_2, \ldots, \dot{\boldsymbol{x}}_n)$ are simultaneously zero at equilibrium points where all the variables are constant and unvarying with time. The system in this case is in steady state and (2.19) is written as

$$\dot{\boldsymbol{x}}_0 = \boldsymbol{f}(\boldsymbol{x}_0, \boldsymbol{u}_0) = 0 \tag{2.21}$$

where $\boldsymbol{x}_0$ and $\boldsymbol{u}_0$ are the state and input vectors, respectively, at to the equilibrium point. Assume the system is perturbed from its equilibrium point by small deviations of the following form

$$\boldsymbol{x} = \boldsymbol{x}_0 + \Delta\boldsymbol{x}, \; \boldsymbol{u} = \boldsymbol{u}_0 + \Delta\boldsymbol{u} \tag{2.22}$$

where the prefix Δ denotes a small deviation, then (2.19) is written as

$$\dot{\boldsymbol{x}} = \dot{\boldsymbol{x}}_0 + \Delta\dot{\boldsymbol{x}} = \boldsymbol{f}\left[(\boldsymbol{x}_0 + \Delta\boldsymbol{x}), (\boldsymbol{u}_0 + \Delta\boldsymbol{u})\right] \tag{2.23}$$

which can be expressed in terms of Taylor's series expansion, truncated to first order, as follows

$$\begin{aligned} \dot{\boldsymbol{x}}_i &= \dot{\boldsymbol{x}}_{i0} + \Delta\dot{\boldsymbol{x}}_i = \boldsymbol{f}_i\left[(\boldsymbol{x}_0 + \Delta\boldsymbol{x}), (\boldsymbol{u}_0 + \Delta\boldsymbol{u})\right] \\ &= \boldsymbol{f}_i(\boldsymbol{x}_0, \boldsymbol{u}_0) + \left(\frac{\partial \boldsymbol{f}_i}{\partial \boldsymbol{x}_1}\Delta\boldsymbol{x}_1 + \cdots + \frac{\partial \boldsymbol{f}_i}{\partial \boldsymbol{x}_n}\Delta\boldsymbol{x}_n\right) + \left(\frac{\partial \boldsymbol{f}_i}{\partial \boldsymbol{u}_1}\Delta\boldsymbol{u}_1 + \cdots + \frac{\partial \boldsymbol{f}_i}{\partial \boldsymbol{u}_m}\Delta\boldsymbol{u}_m\right) \end{aligned} \tag{2.24}$$

Since $\dot{\boldsymbol{x}}_{i0} = \boldsymbol{f}_i(\boldsymbol{x}_0, \boldsymbol{u}_0)$, (2.24) is written as

$$\Delta \dot{\boldsymbol{x}}_i = \left(\frac{\partial \boldsymbol{f}_i}{\partial \boldsymbol{x}_1} \Delta \boldsymbol{x}_1 + \cdots + \frac{\partial \boldsymbol{f}_i}{\partial \boldsymbol{x}_n} \Delta \boldsymbol{x}_n \right) + \left(\frac{\partial \boldsymbol{f}_i}{\partial \boldsymbol{u}_1} \Delta \boldsymbol{u}_1 + \cdots + \frac{\partial \boldsymbol{f}_i}{\partial \boldsymbol{u}_m} \Delta \boldsymbol{u}_m \right) \tag{2.25}$$

with i=1,2,…,n. Similarly, (2.20) is written as

$$\Delta \boldsymbol{y}_j = \left(\frac{\partial \boldsymbol{g}_j}{\partial \boldsymbol{x}_1} \Delta \boldsymbol{x}_1 + \cdots + \frac{\partial \boldsymbol{g}_j}{\partial \boldsymbol{x}_n} \Delta \boldsymbol{x}_n \right) + \left(\frac{\partial \boldsymbol{g}_j}{\partial \boldsymbol{u}_1} \Delta \boldsymbol{u}_1 + \cdots + \frac{\partial \boldsymbol{g}_j}{\partial \boldsymbol{u}_m} \Delta \boldsymbol{u}_m \right) \tag{2.26}$$

with j=1,2,…,p. The linearised form, in state-space representation, of the nonlinear equations (2.19) and (2.20) to small perturbations from the equilibrium point is therefore expressed as

$$\Delta \dot{\boldsymbol{x}} = \boldsymbol{A} \Delta \boldsymbol{x} + \boldsymbol{B} \Delta \boldsymbol{u} \tag{2.27}$$

$$\Delta \boldsymbol{y} = \boldsymbol{C} \Delta \boldsymbol{x} + \boldsymbol{D} \Delta \boldsymbol{u} \tag{2.28}$$

where

$$\begin{gathered} \boldsymbol{A} = \begin{bmatrix} \frac{\partial \boldsymbol{f}_1}{\partial \boldsymbol{x}_1} & \cdots & \frac{\partial \boldsymbol{f}_1}{\partial \boldsymbol{x}_n} \\ \vdots & \cdots & \vdots \\ \frac{\partial \boldsymbol{f}_n}{\partial \boldsymbol{x}_1} & \cdots & \frac{\partial \boldsymbol{f}_n}{\partial \boldsymbol{x}_n} \end{bmatrix}, \boldsymbol{B} = \begin{bmatrix} \frac{\partial \boldsymbol{f}_1}{\partial \boldsymbol{u}_1} & \cdots & \frac{\partial \boldsymbol{f}_1}{\partial \boldsymbol{u}_m} \\ \vdots & \cdots & \vdots \\ \frac{\partial \boldsymbol{f}_n}{\partial \boldsymbol{u}_1} & \cdots & \frac{\partial \boldsymbol{f}_n}{\partial \boldsymbol{u}_m} \end{bmatrix} \\ \boldsymbol{C} = \begin{bmatrix} \frac{\partial \boldsymbol{g}_1}{\partial \boldsymbol{x}_1} & \cdots & \frac{\partial \boldsymbol{g}_1}{\partial \boldsymbol{x}_n} \\ \vdots & \cdots & \vdots \\ \frac{\partial \boldsymbol{g}_p}{\partial \boldsymbol{x}_1} & \cdots & \frac{\partial \boldsymbol{g}_p}{\partial \boldsymbol{x}_n} \end{bmatrix}, \boldsymbol{D} = \begin{bmatrix} \frac{\partial \boldsymbol{g}_1}{\partial \boldsymbol{u}_1} & \cdots & \frac{\partial \boldsymbol{g}_1}{\partial \boldsymbol{u}_m} \\ \vdots & \cdots & \vdots \\ \frac{\partial \boldsymbol{g}_p}{\partial \boldsymbol{u}_1} & \cdots & \frac{\partial \boldsymbol{g}_p}{\partial \boldsymbol{u}_m} \end{bmatrix} \end{gathered} \tag{2.29}$$

and $\Delta \boldsymbol{x}$ is the system state vector of dimension n, $\Delta \boldsymbol{y}$ is the output vector of dimension p, $\Delta \boldsymbol{u}$ is the input vector of dimension m, $\boldsymbol{A}$ is the state or plant matrix of size $n \times n$, $\boldsymbol{B}$ is the control or input matrix of size $n \times m$, $\boldsymbol{C}$ is the observation (output) matrix of size $p \times n$, and $\boldsymbol{D}$ is the feed-forward matrix of size $p \times m$.

The transfer function representation of the linearised system, assuming zero initial conditions, can be obtained by taking the Laplace transform of (2.27) and (2.28) and is as follows

$$\boldsymbol{G}(\boldsymbol{s}) = \frac{\Delta \boldsymbol{y}(\boldsymbol{s})}{\Delta \boldsymbol{u}(\boldsymbol{s})} = \boldsymbol{C}(\boldsymbol{sI} - \boldsymbol{A})^{-1} \boldsymbol{B} + \boldsymbol{D} = \boldsymbol{C} \frac{\operatorname{adj}(\boldsymbol{sI} - \boldsymbol{A})}{\det(\boldsymbol{sI} - \boldsymbol{A})} \boldsymbol{B} + \boldsymbol{D} \tag{2.30}$$

where $\det\left(s\boldsymbol{I} - \boldsymbol{A}\right)$ is the characteristic polynomial of matrix $\boldsymbol{A}$. Its roots are the eigenvalues of the system.

2.3.2 Modal Analysis

2.3.2.1 Eigenvalues and Eigenvectors

The eigenvalues of the $\boldsymbol{A}$ matrix are given by the values of the scalar parameter λ for which there exist non-trivial solutions to the equation

$$\boldsymbol{A}\phi = \lambda\phi \tag{2.31}$$

where ϕ is an $n\times 1$ vector. For any eigenvalue λ_i, the n-column vector ϕ which satisfies Equation (2.31) is called the *right eigenvector* of $\boldsymbol{A}$ associated with the eigenvalue λ_i. Therefore, we have

$$\boldsymbol{A}\phi_{\boldsymbol{i}} = \lambda_{\boldsymbol{i}}\phi_{\boldsymbol{i}} \quad , i=1, 2, \ldots, n \tag{2.32}$$

$$\phi_i = \begin{bmatrix} \phi_{1i} & \phi_{2i} & \cdots & \phi_{ni} \end{bmatrix}^T \tag{2.33}$$

Right eigenvector associated with a mode accounts for the mode shape. It defines the relative distribution of the mode through the system dynamic states. It has the same dimensions as the state variable and therefore is unit dependent. Each component of the right eigenvector contains information about the observability of the associated mode in the state variable corresponding to that component.

Similar to (2.32), the n-row vector ψ_i which satisfies

$$\psi_{\boldsymbol{i}}\boldsymbol{A} = \lambda_{\boldsymbol{i}}\psi_{\boldsymbol{i}} \quad , i=1, 2, \ldots, n \tag{2.34}$$

$$\psi_{\boldsymbol{i}} = \begin{bmatrix} \psi_{i1} & \psi_{i2} & \cdots & \psi_{\boldsymbol{in}} \end{bmatrix} \tag{2.35}$$

is called the *left eigenvector* associated with the eigenvalue λ_i. Left eigenvector associated with a mode gives the distribution of the states within a mode. It has a direct effect on the amplitude of a mode excited by a specific input. Each component of the left eigenvector contains information about the controllability of the associated mode using the state variables corresponding to that component.

The left and right eigenvectors corresponding to different eigenvalues are orthogonal. In other words, if λ_i is not equal to λ_j, then

$$\phi_i \psi_j = 0 \quad , i \neq j \tag{2.36}$$

However, in the case of eigenvectors corresponding to the same eigenvalue,

$$\phi_i \psi_i = C_i \tag{2.37}$$

where C_i is a non-zero constant. It is a common practice to normalise these vectors so that

$$\phi_i \psi_i = 1 \tag{2.38}$$

The modal matrices $\mathbf{\Phi}$ and $\mathbf{\Psi}$ of right and left eigenvectors are formed from their individual corresponding vectors as follows

$$\mathbf{\Phi} = \begin{bmatrix} \phi_1 & \phi_2 & \cdots & \phi_n \end{bmatrix} \tag{2.39}$$

$$\mathbf{\Psi} = \begin{bmatrix} \psi_1^T & \psi_2^T & \cdots & \psi_n^T \end{bmatrix}^T \tag{2.40}$$

$$\mathbf{\Psi\Phi} = \mathbf{I}, \; \mathbf{\Psi} = \mathbf{\Phi}^{-1} \tag{2.41}$$

2.3.2.2 Solution of Differential Equations

Assuming zero input, the solution of each individual differential equation in (2.27) in terms of the eigenvalues, and left and right eigenvectors is given by [74]

$$\Delta x_j(t) = \sum_{i=1}^{n} \phi_{ji} c_i e^{\lambda_i t} \tag{2.42}$$

where $c_i = \psi_i \Delta x(0)$ is a scalar product that represents the magnitude of the excitation of the *i*th mode resulting from the initial conditions. Therefore the free motion, or initial condition, response is given by a linear combination of *n* dynamic modes corresponding to the *n* eigenvalues of the state matrix. As a result, the stability of the linear system is determined by the eigenvalues. A real eigenvalue, corresponding to a non-oscillatory mode, with a negative value represents a decaying mode. Its magnitude determines how fast the decay is. A positive real eigenvalue represents a mode with increasing amplitude. Complex eigenvalues, which occur in conjugate pairs, correspond to oscillatory modes and are given by

$$\lambda = \sigma \pm j\omega \tag{2.43}$$

The real component gives the damping and the complex component gives the frequency of oscillation in rad/s. A negative real part represents a damped oscillation whereas a positive real part represents oscillation of increasing amplitude. To determine the rate of decay of the amplitude of the oscillation, a damping ratio is calculated using

$$\zeta = \frac{-\sigma}{\sqrt{\sigma^2 + \omega^2}} \tag{2.44}$$

2.3.2.3 Participation Factors

The concept of *participation factor* was developed in [68] initially to measure the degree of participation of a state variable in a mode. The participation factor for the *j*th state in the *i*th mode is calculated as follows

$$p_{ji} = \phi_{ji}\psi_{ij} \tag{2.45}$$

where ϕ_{ji} is the *j*th entry of the *i*th right eigenvector and ψ_{ij} is the *j*th entry of the *i*th left eigenvector. The right eigenvector element, ϕ_{ji}, measures the activity of the *j*th state in the *i*th mode and the left eigenvector element, ψ_{ij}, weighs the contribution of this activity to the mode and thus the participation factor p_{ji} measures the net participation of the *j*th state in the *i*th mode. By using the left eigenvectors, the participation factors can be seen as right eigenvectors weighted by left eigenvectors. The participation factor is in fact a measure of the sensitivity of the *i*th eigenvalue to a change in the *j*th diagonal element of the ***A*** matrix. The participation factors are dimensionless and are associated exclusively with the mode. Since they deal only with state variables and do not include inputs and outputs, their use for PSS siting is considered necessary but not sufficient [1].

If the participation vector is defined as the vector containing all the participation factors for the *i*th mode, i.e. $\mathbf{p}_i = \begin{bmatrix} p_{1i} & p_{2i} & \cdots & p_{ni} \end{bmatrix}$, then the participation matrix ***P*** is formed as follows

$$\boldsymbol{P} = \begin{bmatrix} \mathbf{p}_1 & \mathbf{p}_2 & \cdots & \mathbf{p}_n \end{bmatrix} \tag{2.46}$$

2.3.2.4 Modal Transformation

The linearised system model shown in (2.27) and (2.28) is described by state variables; i.e. state-space representation. The rate of change of each state variable, assuming zero input, is a linear combination of all the state variables. In other words, the state variables are cross-coupled. Another description of the linearised system can be made using uncoupled modal variables. This can be achieved by using a modal transformation, using the matrix of right eigenvector, between the state variables and the modal variables as follows

$$\Delta \boldsymbol{x} = \boldsymbol{\Phi z} \tag{2.47}$$

where $\boldsymbol{z}$ is vector of modal variables. Substituting the above expression for $\Delta \boldsymbol{x}$ in the equations (2.27) and (2.28), we obtain

$$\dot{\boldsymbol{z}} = \boldsymbol{F z} + \boldsymbol{G}\Delta \boldsymbol{u} \tag{2.48}$$

$$\Delta \boldsymbol{y} = \boldsymbol{H z} + \boldsymbol{D}\Delta \boldsymbol{u} \tag{2.49}$$

where

$$\boldsymbol{F} = \boldsymbol{\Phi}^{-1}\boldsymbol{A\Phi} \tag{2.50}$$

$$\boldsymbol{G} = \boldsymbol{\Phi}^{-1}\boldsymbol{B} = \boldsymbol{\Psi B} \tag{2.51}$$

$$\boldsymbol{H} = \boldsymbol{C\Phi} \tag{2.52}$$

The matrix $\boldsymbol{F}$ is a diagonal matrix, whose diagonal elements are the eigenvalues of $\boldsymbol{A}$. Assuming zero input, free motion, equation (2.48) represents n uncoupled first-order differential equations:

$$\dot{z}_i = \lambda_i z_i \quad , i\text{=}1, 2, \ldots, n \tag{2.53}$$

and their solution with respect to time is

$$z_i(t) = z_i(0)e^{\lambda_i t} \tag{2.54}$$

2.3.2.5 Modal Controllability and Observability

The modal-space description of linearised system model in (2.48) and (2.49) has the feature of describing the system through decoupled modal variables. In (2.48), if the ith row of matrix $\boldsymbol{G}$ is zero, the inputs have no effect on the ith mode. The entries of matrix $\boldsymbol{G}$ are the modal controllability factors defined as

$$f_{C_i}(k) = \psi_i \boldsymbol{b}_k \quad , k\text{=}1, 2, \ldots, m \tag{2.55}$$

where k refers to system inputs, i refers to system modes, and m is the number of system inputs. The $\boldsymbol{G}$ matrix is referred to as the *mode controllability matrix* [74].

In (2.49), the ith column of the matrix $\boldsymbol{H}$ determines whether or not the modal variable z_i contributes to the formation of the outputs. If the ith column is zero, then the ith mode is unobservable from outputs. The entries of the matrix $\boldsymbol{H}$ are the modal observability factors defined as

$$f_{O_i}\left(l\right) = \boldsymbol{c}_l \phi_i \quad , l = 1, 2, \ldots, p \tag{2.56}$$

where l refers to system outputs, i refers to system modes, and p is the number of system outputs. The $\boldsymbol{H}$ matrix is referred to as the *mode observability matrix* [74].

If the modal transformation is applied to the transfer function representation given by (2.30), assuming zero feed-forward matrix $\boldsymbol{D}$, and if $\boldsymbol{G}\left(\boldsymbol{s}\right)$ is expanded in partial fractions, then (2.30) becomes

$$\boldsymbol{G}\left(\boldsymbol{s}\right) = \boldsymbol{C\Phi}\left(\boldsymbol{sI} - \boldsymbol{\Phi}^{-1}\boldsymbol{A\Phi}\right)^{-1}\boldsymbol{\Psi B} = \boldsymbol{H}\left(\boldsymbol{sI} - \boldsymbol{F}\right)^{-1}\boldsymbol{G} = \sum_{i=1}^{n}\frac{\boldsymbol{R}_i}{\boldsymbol{s} - \lambda_i} \tag{2.57}$$

where $\boldsymbol{R}_i$ are the open-loop residues of the system transfer function. The feed-forward matrix $\boldsymbol{D}$ is assumed zero since it has no effect on system modes and to simplify the analysis. The residues are related to the controllability and observability factors as follows [84]

$$\boldsymbol{R}_i\left(k,l\right) = f_{O_i}\left(l\right) f_{C_i}\left(k\right) = \left(\boldsymbol{c}_l \phi_i\right)\left(\psi_i \boldsymbol{b}_k\right) \tag{2.58}$$

where i refers to system modes, k refers to system inputs, and l refers to system outputs. A multi-input multi-output (MIMO) linear system with n eigenvalues, m inputs, and p outputs, has n matrices of residues with dimension $m \times p$.

2.3.2.6 Illustrative Example

Consider the following linear system described in the state-space representation as in (2.27)-(2.28):

$$\dot{\boldsymbol{x}} = \boldsymbol{Ax} + \boldsymbol{Bu} \Rightarrow \begin{bmatrix} \dot{x}_1 \\ \dot{x}_2 \\ \dot{x}_3 \end{bmatrix} = \begin{bmatrix} 0 & 0 & -195 \\ 1 & 0 & -71 \\ 0 & 1 & -5 \end{bmatrix}\begin{bmatrix} x_1 \\ x_2 \\ x_3 \end{bmatrix} + \begin{bmatrix} 1 & 1.5 \\ 0 & 0.6 \\ 0 & 0 \end{bmatrix}\begin{bmatrix} u_1 \\ u_2 \end{bmatrix}$$

$$\boldsymbol{y} = \boldsymbol{Cx} + \boldsymbol{Du} \Rightarrow \begin{bmatrix} y_1 \\ y_2 \\ y_3 \end{bmatrix} = \begin{bmatrix} 1 & -1 & 9 \\ 0 & 0 & 2 \\ -1 & 4 & 0 \end{bmatrix}\begin{bmatrix} x_1 \\ x_2 \\ x_3 \end{bmatrix} + \begin{bmatrix} 0 & 0 \\ 0 & 0 \\ 0 & 0 \end{bmatrix}\begin{bmatrix} u_1 \\ u_2 \end{bmatrix}$$

The matrix of transfer functions is

$$\begin{bmatrix} \boldsymbol{G}_{1,1}(\boldsymbol{s}) = \dfrac{\boldsymbol{y}_1(\boldsymbol{s})}{\boldsymbol{u}_1(\boldsymbol{s})} & \boldsymbol{G}_{2,1}(\boldsymbol{s}) = \dfrac{\boldsymbol{y}_1(\boldsymbol{s})}{\boldsymbol{u}_2(\boldsymbol{s})} \\ \boldsymbol{G}_{1,2}(\boldsymbol{s}) = \dfrac{\boldsymbol{y}_2(\boldsymbol{s})}{\boldsymbol{u}_1(\boldsymbol{s})} & \boldsymbol{G}_{2,2}(\boldsymbol{s}) = \dfrac{\boldsymbol{y}_2(\boldsymbol{s})}{\boldsymbol{u}_2(\boldsymbol{s})} \\ \boldsymbol{G}_{1,3}(\boldsymbol{s}) = \dfrac{\boldsymbol{y}_3(\boldsymbol{s})}{\boldsymbol{u}_1(\boldsymbol{s})} & \boldsymbol{G}_{2,3}(\boldsymbol{s}) = \dfrac{\boldsymbol{y}_3(\boldsymbol{s})}{\boldsymbol{u}_2(\boldsymbol{s})} \end{bmatrix}^{\boldsymbol{T}} = \begin{bmatrix} \dfrac{\boldsymbol{s}^2+4\boldsymbol{s}+75}{\boldsymbol{s}^3+5\boldsymbol{s}^2+71\boldsymbol{s}+195} & \dfrac{0.9\boldsymbol{s}^2+8.4\boldsymbol{s}-4.5}{\boldsymbol{s}^3+5\boldsymbol{s}^2+71\boldsymbol{s}+195} \\ \dfrac{2}{\boldsymbol{s}^3+5\boldsymbol{s}^2+71\boldsymbol{s}+195} & \dfrac{1.2\boldsymbol{s}+3}{\boldsymbol{s}^3+5\boldsymbol{s}^2+71\boldsymbol{s}+195} \\ \dfrac{-\boldsymbol{s}^2-\boldsymbol{s}-51}{\boldsymbol{s}^3+5\boldsymbol{s}^2+71\boldsymbol{s}+195} & \dfrac{0.9\boldsymbol{s}^2+10.5\boldsymbol{s}+40.5}{\boldsymbol{s}^3+5\boldsymbol{s}^2+71\boldsymbol{s}+195} \end{bmatrix}^{\boldsymbol{T}}$$

The characteristic polynomial is $\left(\boldsymbol{s}^3+5\boldsymbol{s}^2+71\boldsymbol{s}+195\right)$ and its roots are the eigenvalues of the system. The eigenvalues are λ_1=-3, which corresponds to a non-oscillatory mode, and the complex conjugate pair (λ_2,λ_3)=($-1\pm j8$) which corresponds to an oscillatory mode. The matrix of right eigenvectors is

$$\boldsymbol{\Phi} = \left[\phi_1 \mid \phi_2 \mid \phi_3\right]$$

$$= \begin{array}{c} \\ x_1 \\ x_2 \\ x_3 \end{array} \begin{array}{c} \begin{array}{ccc} \lambda_1 & \lambda_2 & \lambda_3 \end{array} \\ \left[\begin{array}{c|c|c} 1 & 0.7198+\mathrm{j}0.2802 & 0.7198-\mathrm{j}0.2802 \\ 0.0308 & 0.2855+\mathrm{j}0.0091 & 0.2855-\mathrm{j}0.0091 \\ 0.0154 & 0.0152-\mathrm{j}0.0281 & 0.0152+\mathrm{j}0.0281 \end{array}\right] \end{array}$$

Note that eigenvector corresponding to the non-oscillatory mode has real elements while eigenvectors corresponding to the oscillatory mode have complex elements and are in complex conjugate pairs. The matrix of left eigenvectors is

$$\boldsymbol{\Psi} = \left[\psi_1^T \mid \psi_2^T \mid \psi_3^T\right]^T$$

$$= \begin{array}{c} \\ \lambda_1 \\ \lambda_2 \\ \lambda_3 \end{array} \begin{array}{c} \begin{array}{ccc} x_1 & x_2 & x_3 \end{array} \\ \left[\begin{array}{ccc} 0.9559 & -2.8676 & 8.6029 \\ \hline -0.0588-\mathrm{j}0.2299 & 1.8982-\mathrm{j}0.2409 & 0.0288+\mathrm{j}15.4262 \\ \hline -0.0588+\mathrm{j}0.2299 & 1.8982+\mathrm{j}0.2409 & 0.0288-\mathrm{j}15.4262 \end{array}\right] \end{array}$$

The matrix of participation factors is

$$\boldsymbol{P} = \left[\mathbf{p}_1 \quad \mathbf{p}_2 \quad \mathbf{p}_3\right]$$

$$= \begin{array}{c} \\ x_1 \\ x_2 \\ x_3 \end{array} \begin{array}{c} \begin{array}{ccc} \lambda_1 & \lambda_2 & \lambda_3 \end{array} \\ \left[\begin{array}{c|c|c} 0.9559 & 0.0221-\mathrm{j}0.182 & 0.0221+\mathrm{j}0.182 \\ -0.0882 & 0.5441-\mathrm{j}0.0515 & 0.5441+\mathrm{j}0.0515 \\ 0.1324 & 0.4338+\mathrm{j}0.2335 & 0.4338-\mathrm{j}0.2335 \end{array}\right] \end{array}$$

Note that the sum of the entries of each column is 1. This is due to the normalisation between right and left eigenvectors as in (2.38). It is common in modal analysis studies to normalise each vector of participation factors to highest element, for a better visualisation of the analysis results, as follows

$$\boldsymbol{P} = \begin{array}{c} \\ x_1 \\ x_2 \\ x_3 \end{array} \begin{array}{c} \begin{array}{ccc} \lambda_1 & \lambda_2 & \lambda_3 \end{array} \\ \left[\begin{array}{c|c|c} 1 & 0.0715 - j0.3277 & 0.0715 + j0.3277 \\ -0.0923 & 1 & 1 \\ 0.1385 & 0.75 + j0.5 & 0.75 - j0.5 \end{array}\right] \end{array}$$

The normalised participation factors in phasor form are

$$\boldsymbol{P} = \begin{array}{c} \\ x_1 \\ x_2 \\ x_3 \end{array} \begin{array}{c} \begin{array}{ccc} \lambda_1 & \lambda_2 & \lambda_3 \end{array} \\ \begin{bmatrix} |1|\angle 0^\circ & |0.3354|\angle -77.7^\circ & |0.3354|\angle 77.7^\circ \\ |0.0923|\angle 180^\circ & |1|\angle 0^\circ & |1|\angle 0^\circ \\ |0.1385|\angle 0^\circ & |0.9014|\angle 33.7^\circ & |0.9014|\angle -33.7^\circ \end{bmatrix} \end{array}$$

The first state has the highest participation in the first mode. For the second mode, the second state has the highest participation. The system in modal-space representation, calculated as in (2.50)-(2.52), is

$$\dot{\boldsymbol{z}} = \boldsymbol{F}\boldsymbol{z} + \boldsymbol{G}\boldsymbol{u}$$

$$\begin{bmatrix} \dot{z}_1 \\ \dot{z}_2 \\ \dot{z}_3 \end{bmatrix} = \begin{bmatrix} -3 & 0 & 0 \\ 0 & -1 + \boldsymbol{j}8 & 0 \\ 0 & 0 & -1 - \boldsymbol{j}8 \end{bmatrix} \begin{bmatrix} z_1 \\ z_2 \\ z_3 \end{bmatrix} + \begin{bmatrix} 0.9559 & -0.2868 \\ -0.0588 - \boldsymbol{j}0.2299 & 1.0506 - \boldsymbol{j}0.4894 \\ -0.0588 + \boldsymbol{j}0.2299 & 1.0506 + \boldsymbol{j}0.4894 \end{bmatrix} \begin{bmatrix} \boldsymbol{u}_1 \\ \boldsymbol{u}_2 \end{bmatrix}$$

$$\boldsymbol{y} = \boldsymbol{H}\boldsymbol{z} + \boldsymbol{D}\boldsymbol{u}$$

$$\begin{bmatrix} \boldsymbol{y}_1 \\ \boldsymbol{y}_2 \\ \boldsymbol{y}_3 \end{bmatrix} = \begin{bmatrix} 1.1077 & 0.5710 + \boldsymbol{j}0.0182 & 0.5710 - \boldsymbol{j}0.0182 \\ 0.0308 & 0.0304 - \boldsymbol{j}0.0562 & 0.0304 + \boldsymbol{j}0.0562 \\ -0.8769 & 0.4222 - \boldsymbol{j}0.2437 & 0.4222 + \boldsymbol{j}0.2437 \end{bmatrix} \begin{bmatrix} z_1 \\ z_2 \\ z_3 \end{bmatrix} + \begin{bmatrix} 0 & 0 \\ 0 & 0 \\ 0 & 0 \end{bmatrix} \begin{bmatrix} \boldsymbol{u}_1 \\ \boldsymbol{u}_2 \end{bmatrix}$$

The entries of the mode controllability matrix $\boldsymbol{G}$ are the modal controllability factors. The matrix of controllability factors, in phasor form, is

$$\begin{bmatrix} f_{C_1}(1) & f_{C_1}(2) \\ f_{C_2}(1) & f_{C_2}(2) \\ f_{C_3}(1) & f_{C_3}(2) \end{bmatrix} = \begin{array}{c} \\ \lambda_1 \\ \lambda_2 \\ \lambda_3 \end{array} \begin{array}{c} \begin{array}{cc} u_1 & u_2 \end{array} \\ \begin{bmatrix} |0.9559|\angle 0^\circ & |0.2868|\angle 180^\circ \\ |0.2373|\angle -104.4^\circ & |1.159|\angle -25^\circ \\ |0.2373|\angle 104.4^\circ & |1.159|\angle 25^\circ \end{bmatrix} \end{array}$$

The first input has the highest controllability of the first mode and the second input has the highest controllability of the second mode. The entries of the mode observability matrix ***H*** are the modal observability factors. The matrix of modal observability factors, in phasor form, is

$$\begin{bmatrix} f_{O_1}(1) & f_{O_2}(1) & f_{O_3}(1) \\ f_{O_1}(2) & f_{O_2}(2) & f_{O_3}(2) \\ f_{O_1}(3) & f_{O_2}(3) & f_{O_3}(3) \end{bmatrix} = \begin{array}{c|ccc} & \lambda_1 & \lambda_2 & \lambda_3 \\ \hline y_1 & |1.1077|\angle 0^\circ & |0.5713|\angle 1.8^\circ & |0.5713|\angle -1.8^\circ \\ y_2 & |0.0308|\angle 0^\circ & |0.0639|\angle -61.6^\circ & |0.0639|\angle 61.6^\circ \\ y_3 & |0.8769|\angle 180^\circ & |0.4875|\angle -30^\circ & |0.4875|\angle 30^\circ \end{array}$$

The first output has the highest observability about the first and second mode. Residues, in phasor form, of the multi-input multi-output transfer function, arranged for each mode, are

$$\left\{ \begin{array}{c} \boldsymbol{R}_i(k,l) \\ \hline \boldsymbol{R}_i(k,l) \\ \hline \boldsymbol{R}_i(k,l) \end{array} \right\} = \left\{ \begin{array}{c} \begin{bmatrix} \boldsymbol{R}_1(1,1) & \boldsymbol{R}_1(1,2) & \boldsymbol{R}_1(1,3) \\ \boldsymbol{R}_1(2,1) & \boldsymbol{R}_1(2,2) & \boldsymbol{R}_1(2,3) \end{bmatrix} \\ \hline \begin{bmatrix} \boldsymbol{R}_2(1,1) & \boldsymbol{R}_2(1,2) & \boldsymbol{R}_2(1,3) \\ \boldsymbol{R}_2(2,1) & \boldsymbol{R}_2(2,2) & \boldsymbol{R}_2(2,3) \end{bmatrix} \\ \hline \begin{bmatrix} \boldsymbol{R}_3(1,1) & \boldsymbol{R}_3(1,2) & \boldsymbol{R}_3(1,3) \\ \boldsymbol{R}_3(2,1) & \boldsymbol{R}_3(2,2) & \boldsymbol{R}_3(2,3) \end{bmatrix} \end{array} \right\}$$

$$= \left\{ \begin{array}{c} \begin{bmatrix} |1.0588|\angle 0^\circ & |0.0294|\angle 0^\circ & |0.8382|\angle 180^\circ \\ |0.3176|\angle 180^\circ & |0.0088|\angle 180^\circ & |0.2515|\angle 0^\circ \end{bmatrix} \\ \hline \begin{bmatrix} |0.1356|\angle -102.5^\circ & |0.0152|\angle -165.9^\circ & |0.1157|\angle -134.4^\circ \\ |0.6621|\angle -23.1^\circ & |0.074|\angle -86.6^\circ & |0.565|\angle -55.0^\circ \end{bmatrix} \\ \hline \begin{bmatrix} |0.1356|\angle 102.5^\circ & |0.0152|\angle 165.9^\circ & |0.1157|\angle 134.4^\circ \\ |0.6621|\angle 23.1^\circ & |0.074|\angle 86.6^\circ & |0.565|\angle 55.0^\circ \end{bmatrix} \end{array} \right\}$$

where *i* refers to system modes, *k* refers to system inputs, and *l* refers to system outputs. The highest residue for the first mode is $R_1(1,1)$. Therefore the best feedback control loop to stabilise the first mode is from the first system output to the first system input. For the second mode the best control loop is from the first output to the second input.

2.4 Summary

Models of different components comprising the power system are briefly presented in this chapter. In this work, the whole power system, along with its components, is modelled in Matlab and Simulink environment. This is due to the flexibility offered in modelling each component and interlinking all components to form the simulated power system. In addition, Matlab has the required mathematical tools for load flow calculation, linearisation of the power system, modal analysis calculations, simulating small and large disturbances, and performing multivariable control design.

Modal analysis of linearised power system model was introduced. Physical interpretation of the system model eigenvalues in the context of power system stability was explained. Importance of the use of right eigenvectors, left eigenvectors, and participation factors in small signal stability studies was addressed. Modal factors of observability and controllability are commonly used in power system stability studies for the selection of controller's input and output signals. The modal analysis techniques presented in this chapter will be applied in studies carried out in this thesis.

3 MODAL LQG CONTROL APPROACH

3.1 Introduction

This chapter presents a design approach to linear quadratic Gaussian (LQG) control that makes it highly suitable for wide-area damping applications. The approach enables direct damping of multiple interarea oscillations by the supplementary wide-area controller (SWAC) while leaving other modes to be controlled entirely by local PSSs. The modal LQG approach is compared with the standard, conventional, LQG design method to demonstrate its design simplicity, effectiveness, applicability to large systems, and suitability to wide-area power system damping applications. Signal transmission time delays are incorporated in the design approach. Effectiveness of the SWAC designed using the modal LQG approach is verified on different case studies using both small-signal and transient performance analysis.

3.2 Modal LQG Control

Linear quadratic Gaussian (LQG) control is considered to be a cornerstone of the modern optimal control theory. It is based on the minimisation of a quadratic cost function that penalises states' deviations and actuators' actions during transient periods.

The essential idea of the LQG control design is to address the intrinsic compromise between an attempt to minimise error, i.e. state deviations, and an attempt to keep control effort at the minimum. This is done by varying weights on system states and control inputs in the cost function. The main advantage of LQG control, therefore, is its flexibility and usability when specifying the underlying trade-off between state regulation and control action.

In power system damping applications, specific weightings on the states in the LQG cost function are derived, in most cases, according to the participation factor analysis for the modes of interest with the highly participating states being given higher weightings [8, 10, 49, 67]. However, the cost function weightings imposed on these highly participating states *indirectly* address the modes of interest. In addition, the weighting process becomes more complex when multiple modes are addressed in the cost function. Damping is not added to the addressed modes only; other modes in the system, local modes in particular, are affected.

The time response of a state variable of a linear, or linearised, system with zero input is given by a linear combination of n dynamic modes corresponding to n eigenvalues λ_i of the system state matrix $\boldsymbol{A}$ [74]

$$\Delta \boldsymbol{x}_j(\boldsymbol{t}) = \sum_{\boldsymbol{i}=1}^{\boldsymbol{n}} \phi_{ji} \boldsymbol{c}_i \boldsymbol{e}^{\lambda_i \boldsymbol{t}} \tag{3.1}$$

where $\boldsymbol{c}_i = \psi_i \Delta \boldsymbol{x}(0)$ represents the magnitude of the excitation of the ith mode $\boldsymbol{e}^{\lambda_i t}$ resulting from initial conditions, ϕ_{ji} is the jth element of the ith right eigenvector, and $\boldsymbol{\psi}_i$ is the ith left eigenvector. These modes, electromechanical oscillatory modes in particular, determine the system time response and are crucial for determining system behaviour during and after disturbances. They are typically located in the frequency range of 0.1-2.5 Hz [74] and easily identifiable using modal analysis [68]. In the context of LQG control design, the cost function therefore, should be formulated in terms of the underlying system modes rather than internal state variables in order to directly address damping of those modes of interest. The LQG cost function can be reformulated using a transformation matrix that provides mapping between state and modal coordinate systems [85]. Using such transformation the cost function can be expressed in terms of system modal variables, directly associated with system modes, rather than internal state variables. In this way, damping of system modes can be *directly* addressed during the LQG controller design.

The idea of formulating control problem in terms of the system modes as state variables has been extensively used in the field of vibration control and is known as independent mode-space control [86, 87]. In the mentioned approach, the *n*th order mechanical system is partitioned into *n/2* decoupled 2nd order sub-systems. Unlike the independent mode-space control, the *novel approach* proposed in this thesis does not partition the system into sub-systems. It expresses the controller's cost function in terms of system modal variables that are directly associated with the modes.

3.3 Design of the LQG Controller

3.3.1 Standard Formulation

Consider a following linearised state-space plant (power system) model [85]

$$\dot{\boldsymbol{x}} = \boldsymbol{A}\boldsymbol{x} + \boldsymbol{B}\boldsymbol{u} + \Gamma\boldsymbol{w} \tag{3.2}$$

$$\boldsymbol{y} = \boldsymbol{C}\boldsymbol{x} + \boldsymbol{v} \tag{3.3}$$

where $\boldsymbol{w}$ is process noise and $\boldsymbol{v}$ is measurement (sensor) noise. They are usually assumed to be uncorrelated zero-mean Gaussian stochastic processes with constant power spectral density matrices $\boldsymbol{W}$ and $\boldsymbol{V}$, respectively. Number of system states is n, number of system inputs is m, and number of system outputs is p. The linear quadratic regulator (LQR) control problem is to devise a feedback control law, which minimises the following cost function

$$\boldsymbol{J}_K = \lim_{T\to\infty} \boldsymbol{E}\left\{\int_0^T \left(\boldsymbol{x}^T\boldsymbol{Q}\boldsymbol{x} + \boldsymbol{u}^T\boldsymbol{R}\boldsymbol{u}\right)\mathrm{d}\boldsymbol{t}\right\} \tag{3.4}$$

where $\boldsymbol{Q}$ and $\boldsymbol{R}$ are appropriately chosen weighting matrices such that $\boldsymbol{Q} = \boldsymbol{Q}^{\mathrm{T}} \geq 0$ and $\boldsymbol{R} = \boldsymbol{R}^T > 0$. The $\boldsymbol{Q}$ and $\boldsymbol{R}$ matrices are, in most cases, set as diagonal. The values of the diagonal elements of $\boldsymbol{Q}$ are set in order to penalise the corresponding states when deviating from their steady-states values. The values of the diagonal elements of $\boldsymbol{R}$ are set in order to penalise the corresponding system inputs (i.e. controller's outputs) from high actions. (*Note*: It is the ratio between the sizes of $\boldsymbol{Q}$ and $\boldsymbol{R}$ that matters rather than their absolute values. For example, when $\boldsymbol{Q}$ and $\boldsymbol{R}$ are chosen as diagonal matrices, the selection of 100 for the diagonal entries of $\boldsymbol{Q}$ and 1 for the diagonal entries of $\boldsymbol{R}$ result in the identical controller to that obtained using values of 0.1 for the diagonal entries of $\boldsymbol{Q}$ and 0.001 for the diagonal entries of $\boldsymbol{R}$).

The solution of the LQR problem can be written in terms of the standard state feedback law

$$\boldsymbol{u}(\boldsymbol{t}) = -\boldsymbol{K}\boldsymbol{x}(\boldsymbol{t}) \tag{3.5}$$

where

$$\boldsymbol{K} = \boldsymbol{R}^{-1}\boldsymbol{B}^{\boldsymbol{T}}\boldsymbol{X} \tag{3.6}$$

is a constant state feedback matrix and $\boldsymbol{X} = \boldsymbol{X}^{\boldsymbol{T}} \geq 0$ is the unique positive semi-definite solution of the algebraic Riccati equation (ARE),

$$\boldsymbol{A}^{\boldsymbol{T}}\boldsymbol{X} + \boldsymbol{X}\boldsymbol{A} - \boldsymbol{X}\boldsymbol{B}\boldsymbol{R}^{-1}\boldsymbol{B}^{\boldsymbol{T}}\boldsymbol{X} + \boldsymbol{Q} = 0 \tag{3.7}$$

The closed-loop dynamics of the state feedback control loop are described by

$$\dot{\boldsymbol{x}} = \boldsymbol{A}\boldsymbol{x} - \boldsymbol{B}\boldsymbol{K}\boldsymbol{x} + \Gamma\boldsymbol{w} \tag{3.8}$$

System states in (3.5) are assumed to be measureable; which is not realistic in power systems. To solve this issue an estimate $\hat{\boldsymbol{x}}$ of the states $\boldsymbol{x}$ could be used, see Figure 3-1, and the feedback control law becomes,

$$\boldsymbol{u}(\boldsymbol{t}) = -\boldsymbol{K}\hat{\boldsymbol{x}}(\boldsymbol{t}) \tag{3.9}$$

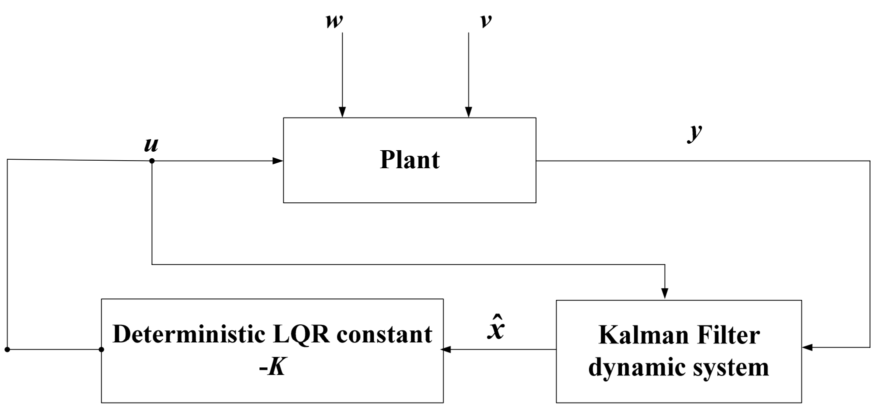

Figure 3-1: LQG control system [55]

The most commonly used state-estimator is Kalman filter, shown in Figure 3-2, described by the following

$$\dot{\hat{x}}(t) = A\hat{x} + Bu + L(y - C\hat{x}) + Lv \tag{3.10}$$

where L is a constant estimation error feedback matrix. The optimal choice of L which minimises $E\left\{\left[x-\hat{x}\right]^T\left[x-\hat{x}\right]\right\}$ is designed using the following cost function

$$J_L = \lim_{T\to\infty} E\left\{\int_0^T \left(x^T W x + u^T V u\right)\mathrm{d}t\right\} \tag{3.11}$$

and is given by

$$L = \Sigma C^T V^{-1} \tag{3.12}$$

where $\Sigma = \Sigma^T \geq 0$ is the unique positive semi-definite solution of the ARE,

$$\Sigma A^T + A\Sigma - \Sigma C^T V^{-1} C\Sigma + W = 0 \tag{3.13}$$

The LQG control problem is solved using the *Separation Principle*, which consists of determining the optimal control to a deterministic LQR problem and finding the optimal estimate $\hat{x}$ of the state x, given by Kalman Filter. The weighting matrices Q, R, W, and V are the tuning parameters of the LQG controller, selected by controller designer in order to obtain satisfactory closed-loop response. The Q and R matrices are used when designing LQR controller state feedback matrix given by (3.4), while the W and V matrices correspond to the Kalman filter design given by (3.11).

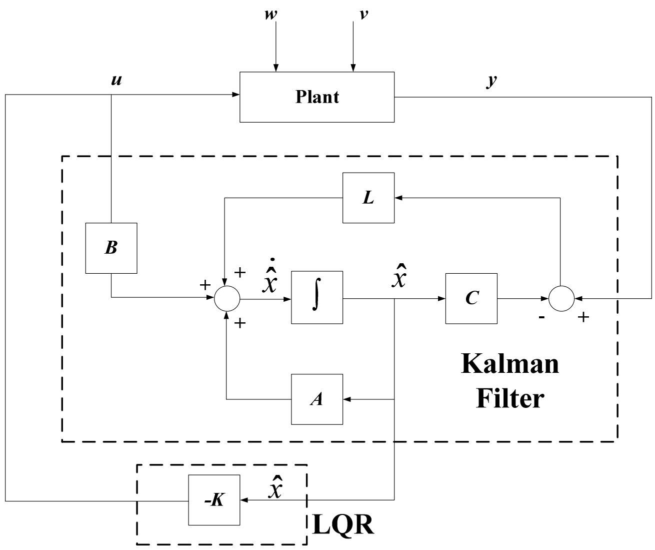

Figure 3-2: Standard LQG controller structure [55]

The closed-loop dynamics with the LQG controller are described by

$$\frac{d}{dt}\begin{bmatrix} x \\ \hat{x} \end{bmatrix} = \begin{bmatrix} A & -BK \\ LC & A-LC-BK \end{bmatrix}\begin{bmatrix} x \\ \hat{x} \end{bmatrix} + \begin{bmatrix} \Gamma w \\ Lv \end{bmatrix} \tag{3.14}$$

which can be re-written as

$$\frac{d}{dt}\begin{bmatrix} x \\ x-\hat{x} \end{bmatrix} = \begin{bmatrix} A-BK & BK \\ 0 & A-LC \end{bmatrix}\begin{bmatrix} x \\ x-\hat{x} \end{bmatrix} + \begin{bmatrix} \Gamma w \\ \Gamma w - Lv \end{bmatrix} \tag{3.15}$$

This shows that that the closed-loop poles are simply the union of the poles of the deterministic LQR system, i.e. eigenvalues of $(A-BK)$, and the poles of Kalman filter, i.e. eigenvalues of $(A-LC)$ [55]. The LQG controller, in the feedback loop from y to u, described in state-space representation is given by

$$\begin{bmatrix} A_C & B_C \\ C_C & D_C \end{bmatrix} = \begin{bmatrix} A-BK-LC & L \\ -K & 0 \end{bmatrix} \tag{3.16}$$

and it is of the same order as the plant, i.e. $n_C=n$.

3.3.2 Modal Formulation

The LQR cost function (3.4) can be formulated in terms of any variable, e.g. system outputs or modal variables, provided that they can be expressed as linear combination of the states [85]. Consider a linear mapping between the modal variables z, directly associated with system modes ($e^{\lambda_i t}$ where i=1… n), and the state variables x,

$$z(t) = Mx(t) \tag{3.17}$$

Then the LQR cost function, expressed in terms of the new modal variables, becomes

$$J_{K_m} = \lim_{T\to\infty} E\left\{\int_0^T \left(z^T Q_m z + u^T R u\right)\mathrm{d}t\right\} \tag{3.18}$$

where $Q_m = Q_m^T \geq 0$, and Q_m is the weighting matrix corresponding to system modal variables z. The term $\left(z^T Q_m z\right)$ in (3.18) is equivalent to $\left(x^T Q x\right)$ in (3.4) as shown below

$$z^T Q_m z = (Mx)^T Q_m (Mx) = x^T\left(M^T Q_m M\right)x = x^T Q x \tag{3.19}$$

and the original cost function, in the state-space, can be reformulated as follows

$$\boldsymbol{J}_{\boldsymbol{K}_x} = \lim_{T\to\infty} \boldsymbol{E}\left\{\int_0^T \left(\boldsymbol{x}^T\left(\boldsymbol{M}^T\boldsymbol{Q}_m\boldsymbol{M}\right)\boldsymbol{x} + \boldsymbol{u}^T\boldsymbol{R}\boldsymbol{u}\right)\mathrm{d}\boldsymbol{t}\right\} \tag{3.20}$$

If $\boldsymbol{Q}_m$ is selected as a diagonal matrix ($\boldsymbol{Q}_m = diag.\left[\boldsymbol{q}_{m_i}\right]$, where i=1…n), then each diagonal entry is directly associated with a modal variable $\boldsymbol{z}_i$ and hence with the corresponding mode $\boldsymbol{e}^{\lambda_i t}$. Higher value of a modal weight corresponds to higher effort by the controller to stabilise the corresponding mode. In order to focus on adding damping to the modes of interest only, those will be given some weights in $\boldsymbol{Q}_m$ while the other modes' weights are set to zeros. In this way, control effort of the designed LQR is directed towards only the modes of interest by shifting them to the left in the complex plane while keeping locations of other modes unaltered.

3.3.3 Remarks on the Modal Formulation

3.3.3.1 Real Transformation Matrix

Standard procedure of obtaining the transformation matrix that relates modal and state variables is to utilise the matrix of right eigenvectors associated with the state matrix $\boldsymbol{A}$. However, the underlying assumption for the modal formulation is that the mapping matrix $\boldsymbol{M}$ is real. The method of obtaining the transformation matrix $\boldsymbol{M}$ by using such a complex matrix of right eigenvectors therefore cannot be used. Instead, matrix $\boldsymbol{M}$ is obtained using the *Real Schur Decomposition* [88]. The Real Schur decomposition method produces a real transformation matrix $\boldsymbol{U}$, with dimensions the same as of $\boldsymbol{A}$, which transforms the $\boldsymbol{A}$ matrix into

$$\boldsymbol{A}_m = \boldsymbol{U}^{-1}\boldsymbol{A}\boldsymbol{U} \tag{3.21}$$

$$\boldsymbol{A}_m = diag.\left\{\left[\lambda_1,\cdots,\lambda_{n_r}\right],\begin{bmatrix}\sigma_1 & \omega_1\\ -\omega_1 & \sigma_1\end{bmatrix}\cdots\begin{bmatrix}\sigma_{n_c} & \omega_{n_c}\\ -\omega_{n_c} & \sigma_{n_c}\end{bmatrix}\right\} \tag{3.22}$$

where $\left\{\lambda_1\cdots\lambda_{n_r}\right\}$ are the real eigenvalues, the (2×2) block diagonals $\left\{\begin{bmatrix}\sigma_1 & \omega_1\\ -\omega_1 & \sigma_1\end{bmatrix}\cdots\begin{bmatrix}\sigma_{n_c} & \omega_{n_c}\\ -\omega_{n_c} & \sigma_{n_c}\end{bmatrix}\right\}$ correspond to the complex pairs of eigenvalues$\left(\lambda_i = \sigma_i \pm \boldsymbol{j}\omega_i\right)$, and the total number of eigenvalues is $n = n_r + n_c$. Note that the diagonal entries and the (2×2) block diagonals can be ordered differently from the order shown in (3.22).

The transformation matrix $\boldsymbol{U}$ relates state and modal variables as follows

$$\boldsymbol{x} = \boldsymbol{U}\boldsymbol{z} \Leftrightarrow \boldsymbol{z} = \boldsymbol{U}^{-1}\boldsymbol{x} \tag{3.23}$$

where

$$\boldsymbol{M} = \boldsymbol{U}^{-1} \tag{3.24}$$

The state-space representation of the linear (or linearised) system is transformed into decoupled modal-space form (with real matrices) as follows,

$$\dot{\boldsymbol{z}} = \boldsymbol{A}_{\boldsymbol{m}}\boldsymbol{z} + \boldsymbol{B}_{\boldsymbol{m}}\boldsymbol{u} + \Gamma\boldsymbol{w} \tag{3.25}$$

$$\boldsymbol{y} = \boldsymbol{C}_{\boldsymbol{m}}\boldsymbol{x} + \boldsymbol{v} \tag{3.26}$$

where $\boldsymbol{A}_{\boldsymbol{m}}$ is as in (3.21), and

$$\boldsymbol{B}_{\boldsymbol{m}} = \boldsymbol{U}^{-1}\boldsymbol{B} \tag{3.27}$$

$$\boldsymbol{C}_{\boldsymbol{m}} = \boldsymbol{C}\boldsymbol{U} \tag{3.28}$$

An illustrative example on the real modal transformation procedure is given in Appendix B.

3.3.3.2 Coordinate Space

The LQR gain matrix $\boldsymbol{K}$, using the cost function formulation in (3.20), is calculated by solving the associated ARE using the $(\boldsymbol{A}, \boldsymbol{B}, \boldsymbol{C})$ matrices of the state-space representation (3.2)-(3.3). It can be calculated alternatively using the cost function formulation (3.18) by solving the associated ARE using the real $(\boldsymbol{A}_{\boldsymbol{m}}, \boldsymbol{B}_{\boldsymbol{m}}, \boldsymbol{C}_{\boldsymbol{m}})$ matrices of the modal-space representation (3.25)-(3.26). Both modal formulations however use the modal weighting matrix $\boldsymbol{Q}_{\boldsymbol{m}}$ and therefore produce the same final representation of the modal LQG controller in (3.16). Nevertheless, in either of the two modal formulations, Kalman filter gain should be calculated using the same coordinate space used at the LQR design stage.

The LQR gain computed based on cost function (3.18) formulated in the modal-space coordinates is

$$\boldsymbol{K}_{\boldsymbol{m}} = \boldsymbol{R}^{-1}\boldsymbol{B}_{\boldsymbol{m}}^{\boldsymbol{T}}\boldsymbol{X}_{\boldsymbol{m}} \tag{3.29}$$

where $\boldsymbol{X}_m$ is the solution of the ARE

$$\boldsymbol{A}_m^T \boldsymbol{X}_m + \boldsymbol{X}_m \boldsymbol{A}_m - \boldsymbol{X}_m \boldsymbol{B}_m \boldsymbol{R}^{-1} \boldsymbol{B}_m^T \boldsymbol{X}_m + \boldsymbol{Q}_m = 0 \tag{3.30}$$

Recall that $\boldsymbol{M} = \boldsymbol{U}^{-1}$ and hence $\boldsymbol{A}_m = \boldsymbol{MAM}^{-1}$, $\boldsymbol{B}_m = \boldsymbol{MB}$, and $\boldsymbol{C}_m = \boldsymbol{CM}^{-1}$, then (3.30) becomes

$$\left(\boldsymbol{MAM}^{-1}\right)^T \boldsymbol{X}_m + \boldsymbol{X}_m \left(\boldsymbol{MAM}^{-1}\right) - \boldsymbol{X}_m \left(\boldsymbol{MB}\right) \boldsymbol{R}^{-1} \left(\boldsymbol{MB}\right)^T \boldsymbol{X}_m + \boldsymbol{Q}_m = 0 \tag{3.31}$$

$$\Rightarrow \left(\boldsymbol{M}^T\right)^{-1} \boldsymbol{A}^T \boldsymbol{M}^T \boldsymbol{X}_m + \boldsymbol{X}_m \boldsymbol{MAM}^{-1} - \boldsymbol{X}_m \boldsymbol{MBR}^{-1} \boldsymbol{B}^T \boldsymbol{M}^T \boldsymbol{X}_m + \boldsymbol{Q}_m = 0 \tag{3.32}$$

The multiplication ($\boldsymbol{M}^T$×(3.32)×$\boldsymbol{M}$) will give

$$\begin{aligned} &\cancel{\boldsymbol{M}^T} \cancel{\left(\boldsymbol{M}^T\right)^{-1}} \boldsymbol{A}^T \left(\boldsymbol{M}^T \boldsymbol{X}_m \boldsymbol{M}\right) + \left(\boldsymbol{M}^T \boldsymbol{X}_m \boldsymbol{M}\right) \boldsymbol{A} \cancel{\boldsymbol{M}^{-1}} \cancel{\boldsymbol{M}} \\ &- \left(\boldsymbol{M}^T \boldsymbol{X}_m \boldsymbol{M}\right) \boldsymbol{BR}^{-1} \boldsymbol{B}^T \left(\boldsymbol{M}^T \boldsymbol{X}_m \boldsymbol{M}\right) + \left(\boldsymbol{M}^T \boldsymbol{Q}_m \boldsymbol{M}\right) = 0 \end{aligned} \tag{3.33}$$

$$\Rightarrow \boldsymbol{A}^T \boldsymbol{X} + \boldsymbol{XA} - \boldsymbol{XBR}^{-1} \boldsymbol{B}^T \boldsymbol{X} + \boldsymbol{Q} = 0 \tag{3.34}$$

which is the same as (3.7) where $\boldsymbol{X} = \left(\boldsymbol{M}^T \boldsymbol{X}_m \boldsymbol{M}\right)$ and $\boldsymbol{Q} = \left(\boldsymbol{M}^T \boldsymbol{Q}_m \boldsymbol{M}\right)$. Therefore, the cost function in (3.18) formulated in the modal-space coordinates has the same ARE as the cost function (3.20) formulated in the state-space coordinates.

The feedback control law in the state and modal space coordinates are identical indicated by (3.35) and (3.36), respectively.

$$\begin{aligned} \boldsymbol{u}(\boldsymbol{t}) &= -\boldsymbol{K}\hat{\boldsymbol{x}}(\boldsymbol{t}) \\ &= -\boldsymbol{R}^{-1} \boldsymbol{B}^T \boldsymbol{X}\hat{\boldsymbol{x}}(\boldsymbol{t}) \\ &= -\boldsymbol{R}^{-1} \boldsymbol{B}^T \left(\boldsymbol{M}^T \boldsymbol{X}_m \boldsymbol{M}\right) \hat{\boldsymbol{x}}(\boldsymbol{t}) \end{aligned} \tag{3.35}$$

$$\begin{aligned} \boldsymbol{u}(\boldsymbol{t}) &= -\boldsymbol{K}_m \hat{\boldsymbol{z}}(\boldsymbol{t}) \\ &= -\boldsymbol{R}^{-1} \boldsymbol{B}_m^T \boldsymbol{X}_m \hat{\boldsymbol{z}}(\boldsymbol{t}) \\ &= -\boldsymbol{R}^{-1} \boldsymbol{B}^T \left(\boldsymbol{M}^T \boldsymbol{X}_m \boldsymbol{M}\right) \hat{\boldsymbol{x}}(\boldsymbol{t}) \end{aligned} \tag{3.36}$$

3.3.3.3 Unstable Power Systems

The shifting of the targeted modes (i.e. modes of interest) towards the left in the complex plane, using the modal LQG controller, holds only when all other modes are stable. If some of the other modes are unstable, then the priority of the control effort is to stabilise the unstable mode(s) first [89]. In this case damping is added to both, the targeted modes and the other unstable modes. When some or all of the targeted modes are unstable, then the damping is added only to the targeted modes and other modes are not affected. In the context of hierarchical WAMS based power system control applications, the modes of interest tackled by the SWAC are usually the lightly damped interarea modes. If these interarea modes are unstable, especially in the post fault conditions frequently encountered in power systems, then the modal LQG approach still applies and the modal LQG controller will stabilise them without affecting the other (stable) modes in the system. In real power systems local modes are stable and adequately damped by local PSSs. Note that the SWAC is built on top of the existing PSSs to enhance the overall stability of the system. Applicability of the modal LQG control approach under these circumstances however will be verified for various case studies in the sequel.

3.3.4 Robustness of the LQG Controller

Both the LQR and Kalman filter loops have good individual robustness properties [55, 85]. However, when the loops are combined together, to form the LQG controller, individual robustness properties are lost [90]. A widely used method to recover these robustness properties is the loop transfer recovery (LTR) procedure at either plant input or output [91, 92]. Recovery at the plant input is used in this study. The LQR is designed first with required specification, i.e. adding damping to the lightly damped interarea modes. Then, Kalman filter is synthesised such that the loop transfer function $\boldsymbol{K_{LQG}}(\boldsymbol{s})\boldsymbol{G}(\boldsymbol{s})$, where $\boldsymbol{G}(\boldsymbol{s})$ is the plant transfer function and $\boldsymbol{K_{LQG}}(\boldsymbol{s})$ is the LQG controller transfer function, approaches the LQR loop transfer function $\boldsymbol{K_{LQR}}(\boldsymbol{s}) = \boldsymbol{K}(\boldsymbol{sI} - \boldsymbol{A})^{-1}\boldsymbol{B}$. The tuning parameters of Kalman filter are calculated as follows

$$\boldsymbol{W} = \Gamma \boldsymbol{W_o} \Gamma^{\boldsymbol{T}} + \boldsymbol{qB}\Theta\boldsymbol{B^T} \tag{3.37}$$

$$\boldsymbol{V} = \boldsymbol{V_o} \tag{3.38}$$

where $\boldsymbol{W_o}$ and $\boldsymbol{V_o}$ refer to the nominal model, and Θ is any positive definite matrix. The second term in (3.37) refers to noises coming directly through the inputs. Full recovery of robustness is achieved as $\boldsymbol{q} \to \infty$. Care should be taken though, as full recovery would lead to excessive high gains and therefore would make the LQG controller too sensitive to small perturbations in the system. For non-minimum phase systems, which is a common case in power systems, only partial recovery of robustness can be achieved [55].

3.3.5 Model Order Reduction

3.3.5.1 LQG Control and Order Reduction

The order of designed LQG controller is typically at least equal to that of the plant and is even higher with the inclusion of time delays. The control law therefore may be too complex with regards to practical implementation and simpler designs are sought [55]. A detailed and complete model of the system, especially for cases of large scale power systems, might not be easily available; due to computing capabilities, availability of full data… etc. An approximation of the power system model, therefore, is used in these cases to design the LQG controller. In addition, the use of a reduced order power system model reduces numeric ill-condition problems that may exist when solving the AREs at the design stage. The LQG controller order can be reduced in several ways: by reducing the order of the plant model prior to controller design, by reducing the controller model order at the final stage, or by doing both.

In case of plant and/or controller model reduction, number of state estimates $\hat{\boldsymbol{x}}$ is not equal to the number of states $\boldsymbol{x}$ of the full plant model. In this case (3.14) cannot be transformed into (3.15) and the resulting closed-loop poles are not the exact union of the LQR system and Kalman filter poles. Effectiveness of the modal LQG controller, therefore, should be assessed under these circumstances of model order reduction.

3.3.5.2 Model Reduction via Balanced Truncation

A reduced model $\boldsymbol{G_r}$ is said to represent a good approximation of the full order model $\boldsymbol{G}$ if the infinity norm of their difference $\left\|\boldsymbol{G}-\boldsymbol{G_r}\right\|_\infty$ is sufficiently small [55]. This can be done by removing the states that have little effect on the system input-output behaviour. The contribution of individual states can be computed using Hankel singular values of balanced realisation [93]. A balanced realisation is an asymptotically stable minimal realisation in which the controllability and observability gramians are equal and diagonal [55]. Consider the following Lyapunov equations

$$\boldsymbol{A}\boldsymbol{P_C} + \boldsymbol{P_C}\boldsymbol{A}^{\boldsymbol{T}} + \boldsymbol{B}\boldsymbol{B}^{\boldsymbol{T}} = 0 \tag{3.39}$$

$$\boldsymbol{A}^T \boldsymbol{P_O} + \boldsymbol{P_O} \boldsymbol{A} + \boldsymbol{C}^T \boldsymbol{C} = 0 \tag{3.40}$$

where $\boldsymbol{P_C}$ and $\boldsymbol{P_O}$ are the controllability and observability gramians, respectively, defined by

$$\boldsymbol{P_C} \triangleq \int_0^\infty \boldsymbol{e}^{\boldsymbol{A}t} \boldsymbol{B}\boldsymbol{B}^T \boldsymbol{e}^{\boldsymbol{A}^T t} \boldsymbol{dt} \tag{3.41}$$

$$\boldsymbol{P_O} \triangleq \int_0^\infty \boldsymbol{e}^{\boldsymbol{A}^T t} \boldsymbol{C}^T \boldsymbol{C} \boldsymbol{e}^{\boldsymbol{A}t} \boldsymbol{dt} \tag{3.42}$$

If $\boldsymbol{P_C} = \boldsymbol{P_O} = diag.(\sigma_1, \sigma_2, \ldots, \sigma_n) \triangleq \Lambda$, where $\boldsymbol{\sigma}_1 \geq \boldsymbol{\sigma}_2 \geq \cdots \geq \boldsymbol{\sigma}_n > 0$ then the realisation $(\boldsymbol{A}, \boldsymbol{B}, \boldsymbol{C}, \boldsymbol{D})$ is called *balanced*. The $\boldsymbol{\sigma}_i$ are the ordered Hankel singular values of $\boldsymbol{G}(\boldsymbol{s})$, defined as $\sigma_i \triangleq \sqrt{eig.(\boldsymbol{P_C P_O})}$. The value of each $\boldsymbol{\sigma}_i$ is associated with a state $\boldsymbol{x}_i$ of the balanced system. The size of $\boldsymbol{\sigma}_i$ is a relative measure of the contribution that $\boldsymbol{x}_i$ makes to the input-output behaviour of the system. Therefore, if $\boldsymbol{\sigma}_1 \gg \boldsymbol{\sigma}_2$, then the state $\boldsymbol{x}_1$ affects the input-output behaviour much more than $\boldsymbol{x}_2$. The balanced truncation reduction method [94] is used in this study. The least contributing states to the system input-output behaviour, determined using Hankel singular values, are discarded to achieve required model order reduction.

3.3.6 Time Delays

Transmitting signals from PMUs to the SWAC and from the SWAC to generators involve some time delays. These time delays depend primarily on the type of communication link used and could vary from 25 ms (one way) for fibre optic based links to 250 ms for satellite based links [42]. Additionally, the processing and routing of signals at both PMUs and the SWAC also involve time delays. These delays, however, are small (especially in slow communication links) compared to communication link delays, and can be neglected without loss of generality. Time delays in general can reduce effectiveness of the SWAC especially when relatively slow communication link, such as satellite based links, are used [42]. Therefore, they should be taken into account at the design stage of the SWAC.

In this study time delays are modelled in Laplace domain, as $\boldsymbol{e}^{-s\tau}$ and then transformed into a rational transfer function for inclusion in the linearised power system model. Padé approximation is a widely used method in WAMS based damping application for modelling of time delays [13, 49, 53]. The 1st and 2nd order Padé approximation are given, respectively, as follows [83]

$$P_1(s) = \frac{-\tau s + 2}{\tau s + 2} \tag{3.43}$$

$$P_2(s) = \frac{\tau^2 s^2 - 6\tau s + 12}{\tau^2 s^2 + 6\tau s + 12} \tag{3.44}$$

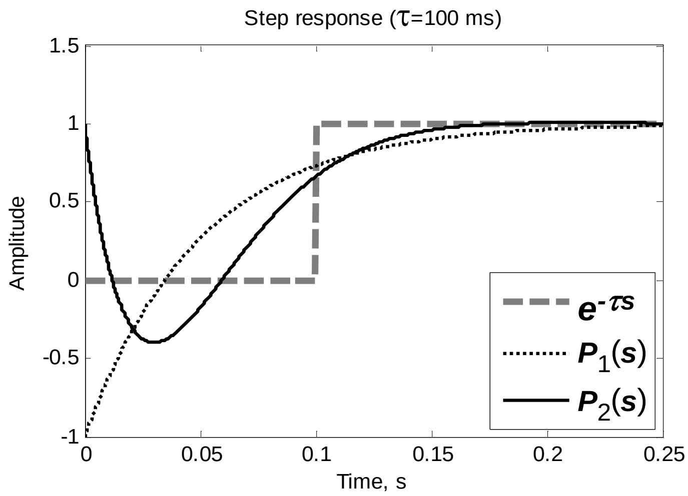

Figure 3-3: Step response of Padé approximation

Figure 3-3 shows step response of 1st and 2nd order Padé approximations for 100 ms time delay, and compares them with the exact response of the time delay. The 1st order Padé approximation has the advantage, over the 2nd order approximation, of reducing the overall order of the designed controller. However, its accuracy is reduced for cases of long time delays. Figure 3-4 shows the phase response of 1st and 2nd order Padé approximations and compares them with the exact response of the time delay (Note: the Padé approximation has unit gain at all frequencies). The figure shows the phase response at, approximately, the typical frequency range of electromechanical modes, i.e. 0.1-2 Hz (equivalently 0.6-12.6 rad/s). The figure compares the phase responses of 1st and 2nd order Padé approximations for different time delays ranging from 25 ms (for fibre optic based links) to 250 ms (for satellite based links). It can be seen from the figure that the 1st order Padé approximation provides good accuracy in modelling short time delays, i.e. 25 ms. For longer time delays greater than 100 ms its accuracy is reduced. The 2nd order Padé approximation on the other hand provides better accuracy for time delays up to 250 ms. The 2nd order Pade approximation therefore is more accurate for modelling time delays, especially when slow communication links are in place, than the 1st order approximation.

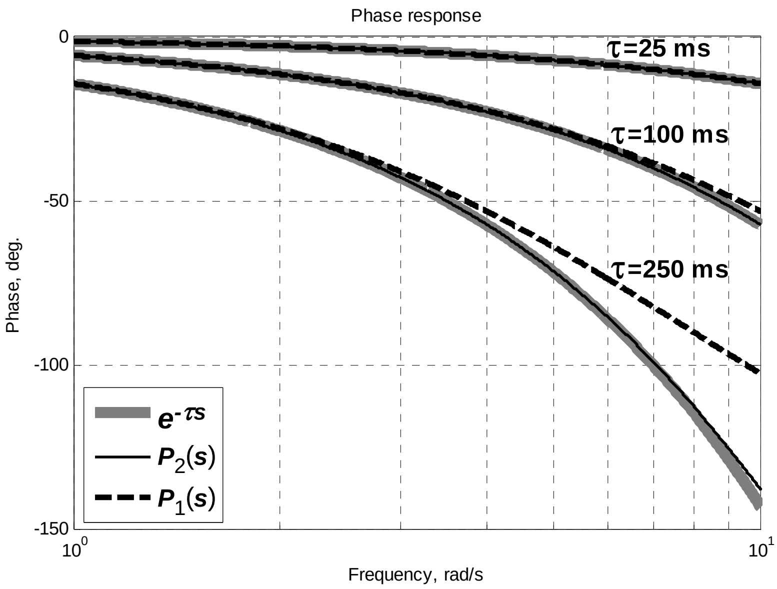

Figure 3-4: Phase response of 1st and 2nd order Padé approximations

3.4 Case Studies

3.4.1 Test System

The modal LQG deign approach is demonstrated on the 4-machine test system [74] shown in Figure 3-5. All generators in the system are equipped with PSSs (PSS parameters are as in [74]). The network is modified such that the resulting electromechanical modes are two interarea modes and one local mode. This was deliberately done for a better demonstration of key properties of the proposed design approach when handling multiple interarea modes. Full system data and modifications made to the network are given in Appendix A. The nominal operating condition comprises power transfers of (200 MW) across corridor 8-9 and (383 MW) across corridor 8-7 (power transfers across the network are shown in Appendix A). Transient performance of the system is assessed through a large disturbance represented by a 100 ms, self-clearing, three-phase fault at bus 8 in all case studies.

Input signals to the SWAC are voltage phase angles of each generator bus. This type of type of signal is selected because of its direct measurement by PMUs, no calculation or estimation is required, and for its high correlation with active power [16]. Input/output (I/O) signals of the SWAC are commonly selected based on their observability/controllability, respectively, of the modes of interest. Due to the small size of the test system and for the purpose of illustrating the proposed control design approach thoroughly, the I/O signals are selected from and to all generators in the system. The SWAC therefore has 4 inputs and 4 outputs. Output signals of the SWAC are passed through a ±0.1 limiter, similar to PSSs [78].

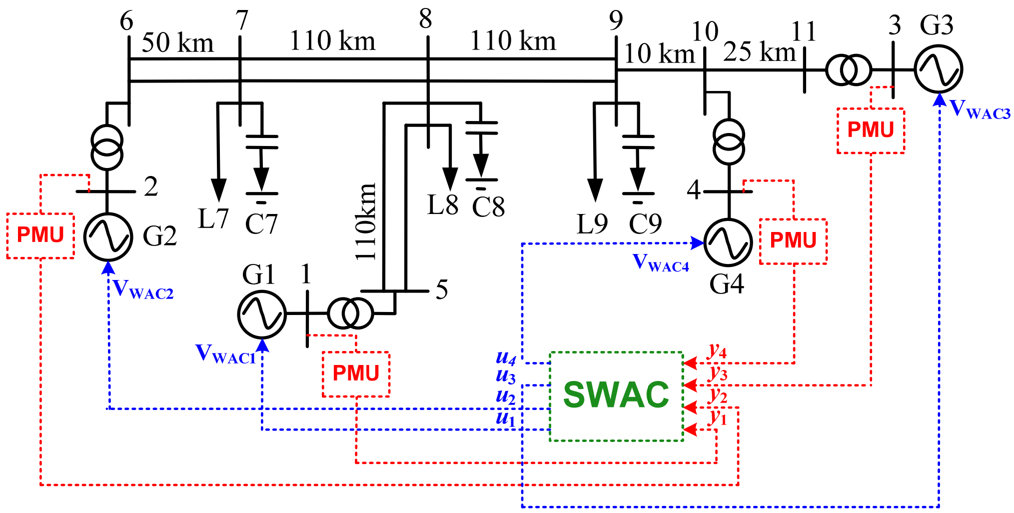

Figure 3-5: 4-machine test system with SWAC

Time delays are set to 100 ms for one way transmission, i.e. 200 ms in total for round-trip communication. They are assumed to be fixed and identical for all channels. The fibre optics communication links are assumed to be in place. Time delays are modelled using the 2nd order Padé approximation.

3.4.2 Conventional and Modal LQG Design Approaches

The 4-machine test system was modelled and linearised using Matlab/Simulink software. The order of linearised power system model, with PSSs only, is 47. The modelled time delays, using 2nd order Padé approximation, have a total of 16 states. The order of the complete open-loop power system model used for controller design, with time delays included is therefore 63. The electromechanical modes of the open-loop system and corresponding damping ratios are listed in Table 3-1. The participating states are shown in descending order according to their magnitudes. Reference generator in the model is generator 1 (G1). The modes targeted by the SWAC are modes 1 and 2.

Table 3-1: Electromechanical modes of the open-loop system

Mode no.	Mode [1/s , rad/s]	ζ [%]	f [Hz]	Mode shape	Highest participating states	Mode type
1	-0.14±j4.49	3.08	0.71	(G1,G2) vs. (G3,G4)	(δ_3, ω_3, ω_2, δ_4, ω_1, ω_4, δ_2)	interarea
2	-0.14±j4.99	2.75	0.79	G1 vs. (G2,G3,G4)	(δ_2, ω_2, ω_1)	interarea
3	-0.39±j6.90	5.65	1.10	G3 vs. G4	(ω_4, δ_4, ω_3, δ_3)	local

3.4.2.1 (Conventional) State-based LQR Design

The LQR is designed using the standard formulation of the cost function given by (3.4). The weighting matrix corresponding to control effort $\boldsymbol{R}$ is set to a 4×4 identity matrix. The weighting matrix $\boldsymbol{Q}$ is constructed as a diagonal $n \times n$ matrix with diagonal entries $\begin{bmatrix} \boldsymbol{q}_{x_1} & \cdots & \boldsymbol{q}_{x_n} \end{bmatrix}$. Each of them is associated directly to a state variable. The LQR gain $\boldsymbol{K}$ is then calculated by solving the associated ARE. The closed-loop eigenvalues associated with the LQR, according to the Separation Principle, will be the eigenvalues of ($\boldsymbol{A}$-$\boldsymbol{BK}$). To address a particular mode in the cost function, non-zero weights are assigned to the states which participate highly in that mode while zero weights are assigned to the other states. In this indirect way, damping is added to the addressed mode. Table 3-2 lists the electromechanical modes of the resulting LQR loops, eig.($\boldsymbol{A}$-$\boldsymbol{BK}$), for different weights assigned to the diagonal entries in $\boldsymbol{Q}$ corresponding to relevant electromechanical states $\left[\boldsymbol{q}_{\omega_1} \mid \boldsymbol{q}_{\delta_2} \;\; \boldsymbol{q}_{\omega_2} \mid \boldsymbol{q}_{\delta_3} \;\; \boldsymbol{q}_{\omega_3} \mid \boldsymbol{q}_{\delta_4} \;\; \boldsymbol{q}_{\omega_4}\right]$ determined based on participation factor analysis results shown in Table 3-1 . All other states are assigned zero weights.

To address only mode 2 non-zero weights are assigned based on participation factor analysis, see rows (1-2) in Table 3-2, to diagonal entries corresponding to the highly participating states, i.e. $\left(\boldsymbol{q}_{\omega_1} \;\; \boldsymbol{q}_{\delta_2} \;\; \boldsymbol{q}_{\omega_2}\right)$. It can be seen (Table 3-2) that its damping ratio improves with the increase in assigned weights. Mode 3 is kept unaltered and the damping ratio of mode 1 increased slightly. This is because the selected states participate, to a lesser extent though, in mode 1 as well. The frequency of mode 2 also increases noticeably when the weights are increased.

To address only mode 1, all electromechanical states should be assigned with non-zero weights. Note that modes 2 and 3 have some common participating states with mode 1 as shown in Table 3-1. Rows (3-4) in Table 3-2 clearly show that mode 1 cannot be addressed individually without affecting the other two modes. In fact some other non-electromechanical modes were also affected. Table 3-3 lists other affected modes, in addition to the affected electromechanical modes 2-3, for the weightings used in row (3) of Table 3-2. Those other modes are affected as a result of assigning weights to states which are participating in them.

Table 3-2: Closed-loop electromechanical modes corresponding to the LQR loop for different state weightings

no.	State weights $\left[q_{\omega_1} \vert q_{\delta_2}\ q_{\omega_2} \vert q_{\delta_3}\ q_{\omega_3} \vert q_{\delta_4}\ q_{\omega_4}\right]$	Mode 1 [1/s , rad/s]	ζ_1 [%]	Mode 2 [1/s , rad/s]	ζ_2 [%]	Mode 3 [1/s , rad/s]	ζ_3 [%]
-	Open-loop system	-0.14±j4.49	3.08	-0.14±j4.99	2.75	-0.39±j6.90	5.65
1	$[0.1 \vert 0.1\ 0.1 \vert 0\ 0 \vert 0\ 0]$	-0.15±j4.49	3.39	-0.72±j5.14	13.88	-0.39±j6.90	5.65
2	$[1 \vert 1\ 1 \vert 0\ 0 \vert 0\ 0]$	-0.16±j4.49	3.48	-1.67±j5.77	27.74	-0.39±j6.90	5.65
3	$[0.1 \vert 0.1\ 0.1 \vert 0.1\ 0.1 \vert 0.1\ 0.1]$	-0.73±j4.69	15.33	-0.87±j5.18	16.57	-0.56±j6.94	8.11
4	$[1 \vert 1\ 1 \vert 1\ 1 \vert 1\ 1]$	-1.54±j5.30	27.86	-1.96±j5.99	31.08	-1.23±j7.19	16.91
5	$[0 \vert 0\ 0 \vert 0.1\ 0.1 \vert 0.1\ 0.1]$	-0.78±j4.89	15.67	-0.36±j4.84	7.35	-0.56±j6.94	8.11
6	$[0 \vert 0\ 0 \vert 1\ 1 \vert 1\ 1]$	-1.86±j5.73	30.93	-0.31±j4.82	6.52	-1.24±j7.19	16.92
7	$[2 \vert 2\ 2 \vert 1\ 1 \vert 1\ 1]$	-1.69±j5.38	30.04	-2.16±j6.25	32.71	-1.23±j7.19	16.90

To address only mode 3, non-zero weights are assigned to its participating states, i.e. $\left(q_{\delta_3}\quad q_{\omega_3}\quad q_{\delta_4}\quad q_{\omega_4}\right)$. These states also participate in mode 1. Rows (5-6) in Table 3-2 show that the damping ratios of all three modes increased even though the intention was to address mode 3 only. Notice that the damping ratio of mode 1 increased even more than that of mode 3.

The last design case in the table lists the closed-loop electromechanical modes when using a blending of state weights that result in target damping ratio in the range of 30% for both mode 1 and 2. This design base-case will be used for comparisons with SWAC designed using the modal LQG approach in the sequel.

Previous analysis shows that when using the conventional LQR design method, the tuning process to address one particular mode is not a straightforward procedure. In some cases other modes get affected as well. The whole design procedure becomes more complicated when addressing multiple modes. It is shown clearly that the two interarea modes cannot be addressed without affecting the local mode. Furthermore, in order to achieve higher improvement in the damping ratios of the addressed modes, by assigning higher state weights, the frequency of those modes will change considerably.

Table 3-3: Other modes affected by the conventional LQG controller

Open-loop location		Closed-loop location	
Mode [1/s , rad/s]	**ζ [%]**	**Mode [1/s , rad/s]**	**ζ [%]**
-0.94±j0.89	72.50	-1.44±j0.48	94.89
-0.82±j0.87	68.73	-1.16±j0.74	84.36
-0.49±j0.67	58.88	-0.77±j0.68	74.89

3.4.2.2 Modal-based LQR Design

The open-loop system model is transformed to the modal canonical form using the Real Schur Decomposition with the resulting transformation matrix $\boldsymbol{M}$ relating the original states variables and the decoupled modal variables. The matrix $\boldsymbol{R}$ is set to a 4×4 identity matrix. The modal weighting matrix $\boldsymbol{Q_m}$ is constructed as a diagonal matrix where each diagonal entry represents the weight associated with the corresponding modal variables, and hence the corresponding mode. Modal weights in $\boldsymbol{Q_m}$ were all set to zeros except for the ones corresponding to the addressed electromechanical mode(s). Table 3-4 lists the closed-loop electromechanical modes, corresponding to the LQR loop, for different weightings used to formulate the cost function (3.20). It can be seen from rows (1-3) in the table that when modal weights are assigned to a particular mode, its damping ratio is increased. Other un-addressed electromechanical modes remained unaltered. All other eigenvalues of the closed- loop system also remained the same as in the case of the open-loop system. Row 3 in the table shows that even the local mode can be addressed individually without affecting the two interarea modes. The table also shows that multiple modes, modes 1 and 2 in row 4, can be addressed simultaneously together without affecting the local mode. Increasing the weights assigned to the addressed modes leads to a direct increase in their damping ratios. The last row in Table 3-4 lists the closed-loop electromechanical modes when using a blending of modal weights for the target damping ratios in the range of 30% for both interarea modes.

Notice that the modal LQG approach offers design flexibility to achieve an *exact* target damping ratios for the addressed modes. Numerical values for matrix $\boldsymbol{Q_m}$ are given in Appendix C (for case 5 in Table 3-4).

Table 3-4: Closed-loop electromechanical modes corresponding to the LQR loop for different modal weightings

no.	Target mode(s)	Modal weights $\left[q_{m_1} \mid q_{m_2} \mid q_{m_3}\right]$	Mode 1 [1/s , rad/s]	ζ_1 [%]	Mode 2 [1/s , rad/s]	ζ_2 [%]	Mode 3 [1/s , rad/s]	ζ_3 [%]
-	-	Open-loop system	-0.14±j4.49	3.08	-0.14±j4.99	2.75	-0.39±j6.90	5.65
1	mode 1	$[0.1 \mid 0 \mid 0]$	-1.01±j4.49	21.90	-0.14±j4.99	2.75	-0.39±j6.90	5.65
2	mode 2	$[0 \mid 0.1 \mid 0]$	-0.14±j4.49	3.08	-0.88±j4.99	17.40	-0.39±j6.90	5.65
3	mode 3	$[0 \mid 0 \mid 1]$	-1.01±j4.49	3.08	-0.14±j4.99	2.75	-0.57±j6.90	8.19
4	modes 1 & 2	$[0.1 \mid 0.1 \mid 0]$	-1.01±j4.51	21.79	-0.87±j4.96	17.20	-0.39±j6.90	5.65
5	modes 1 & 2	$[0.2236 \mid 0.3725 \mid 0]$	-1.43±j4.56	30.04	-1.70±j4.90	32.71	-0.39±j6.90	5.65

Comparison between the last rows of Table 3-2 and Table 3-4 shows clearly that the modal LQG design approach leads to improvement in damping ratio for the modes of interest without affecting any other mode in the system. In addition, the frequency of the addressed modes is not changing considerably as in the case when conventional LQG design method was used. The resulting LQR gain matrix is given in Table 8-13 in Appendix C for the two approaches. The table shows that the modal LQG approach reduces the resulting LQR gains.

3.4.2.3 Transient Performance Analysis of the Closed-loop System

Kalman filter is synthesised to recover robustness of the LQR transfer function in the base-case for designed, modal and conventional, LQRs at plant inputs using tuning parameters $\boldsymbol{W}$ and $\boldsymbol{V}$ calculated as in (3.37) and (3.38). The following values of parameters were used.

$$\boldsymbol{V_o} = 10^{-3} \times \boldsymbol{I}_{p\times p},\ \Gamma = \boldsymbol{I}_{n\times n},\ \boldsymbol{W_o} = 10^{-3} \times \boldsymbol{I}_{n\times n}, \Theta = 10^{-3} \times \boldsymbol{I}_{m\times m} \tag{3.45}$$

The high quality of measurements supplied by PMUs is depicted by choosing a low measurement noise covariance $\boldsymbol{V_o}$ [8]. Figure 3-6 illustrates the LTR procedure, depicting the largest singular value of the compared transfer functions $\boldsymbol{K_{LQR}}(\boldsymbol{s})$ and $\boldsymbol{K_{LQG}}(\boldsymbol{s})\boldsymbol{G}(\boldsymbol{s})$, at plant inputs with various values of $\boldsymbol{q}$. The compromise between the best partial recovery of robustness (at the frequency range of the modes of interest) and

Kalman filter gains was found with ***q*** =10.

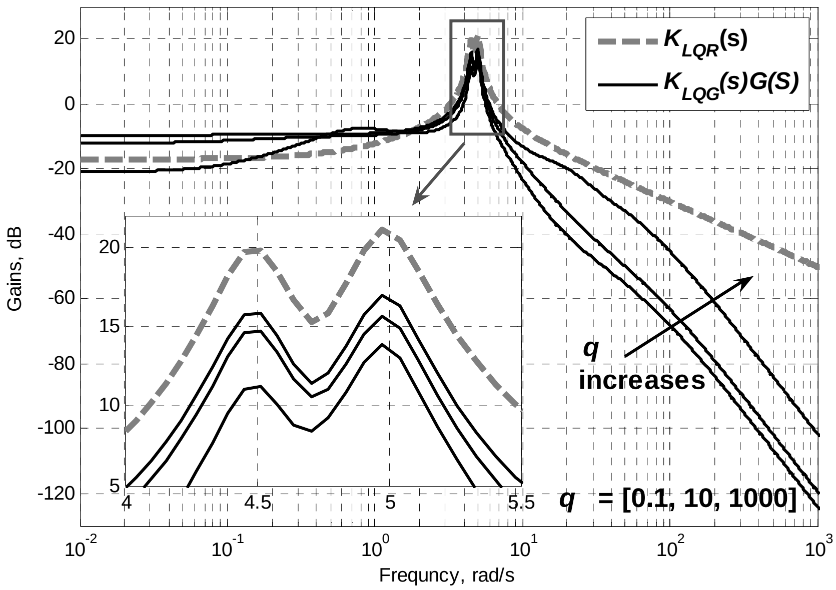

Figure 3-6: LTR procedure at plant inputs with various values of *q*

The system was subjected to a large disturbance consisting of 100 ms self-clearing three-phase fault at bus 8. Responses of speed deviation, active power, terminal voltage, and voltage phase angle at generator buses are shown, respectively, in Figure 3-7, Figure 3-8, Figure 3-9, and Figure 3-10. The figures compare the responses of the closed-loop system (with PSSs and SWAC) using the modal and conventional LQG controllers, in addition to the open-loop system (with PSS only). It can be seen from the figures that both LQG controllers improve the transient performance of the system.

The closed-loop control signals from PSS ($\mathbf{V_{PSS}}$) and the SWAC ($\mathbf{V_{WAC}}$) are shown in Figure 3-11 when using the conventional LQG controller. Note the 200ms time lag due to transmission delays between the actions of local PSS and the SWAC. It can be seen from the figure that the magnitude of the wide-area control signal, coming from the conventional LQG controller, is much higher than the magnitude of the local PSS control signal. It reaches the upper and lower limits (±0.1) during the first swing indicating that saturation of control action has been reached. The wide-area control signals of the conventional and modal LQG controllers are compared in Figure 3-12. It can be seen that the magnitude of the control signal of the conventional LQG controller is much larger than that of the modal LQG controller. This is due to the LQR design stage, using the conventional LQG design method, which resulted in adding damping not only to three electromechanical modes but also to some other system modes.

Stabilisation of these extra modes (note that the targeted modes were only the two interarea modes) led to higher control efforts in case of large disturbance. The modal LQG controller, on the other hand, is directed towards adding damping only to two modes of interest and such resulting in a smaller overall control effort. It can be seen also from the figure that the frequency of the conventional LQG control signal is higher than that of the modal LQG controller. This is due to the rise in frequency of the electromechanical modes resulting from the LQR design stage (see the last row in Table 3-2). The control signal of the modal LQG controller, on the other hand, has the frequency close to the frequencies of the two addressed interarea modes (see the last row in Table 3-4).

Table 3-5 presents a summarised comparison, based on the results of small-signal and transient performance analysis discussed above, between the conventional and modal LQG controller. The comparison clearly shows advantages of using the modal LQG design approach for the supplementary wide-area controller over the conventional method. The feature of leaving other modes unaltered, particularly, makes the modal approach highly suitable for hierarchical wide-area control structures.

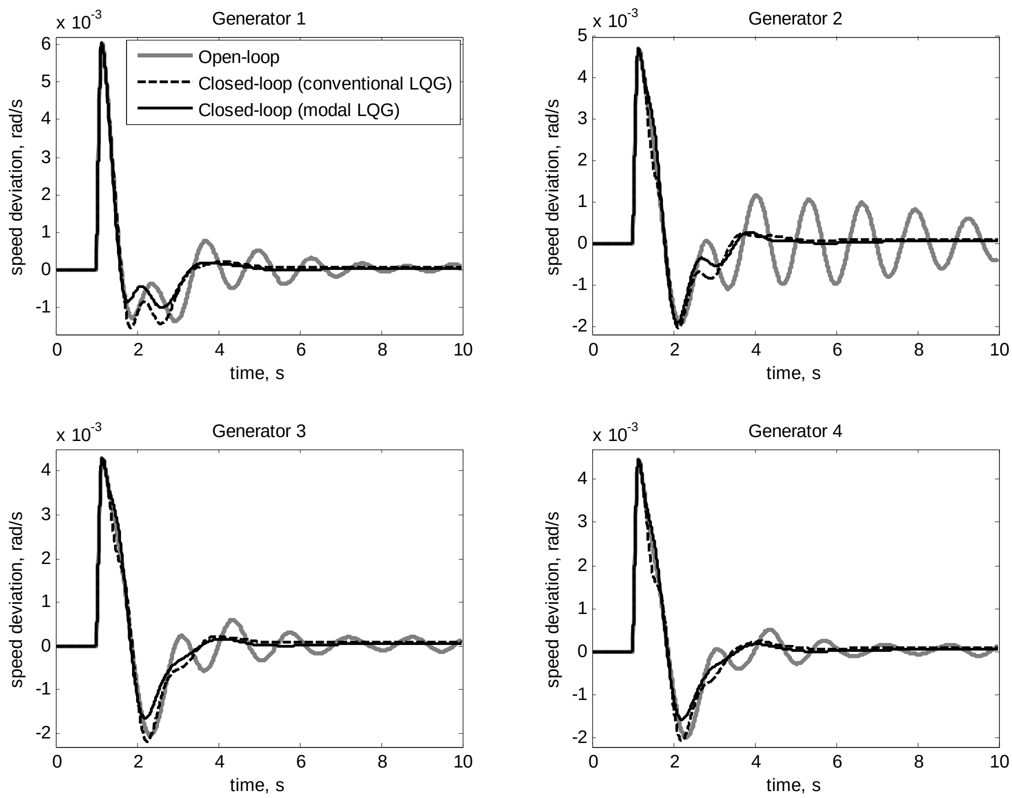

Figure 3-7: Speed deviation responses for a large disturbance

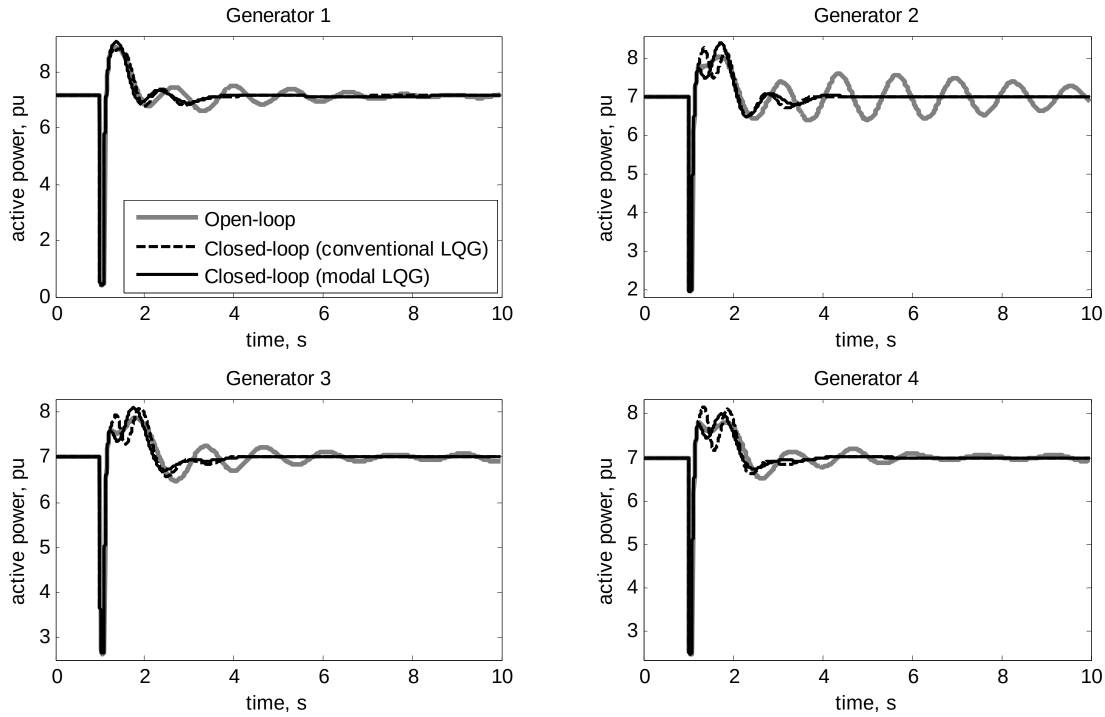

Figure 3-8: Active power responses for a large disturbance

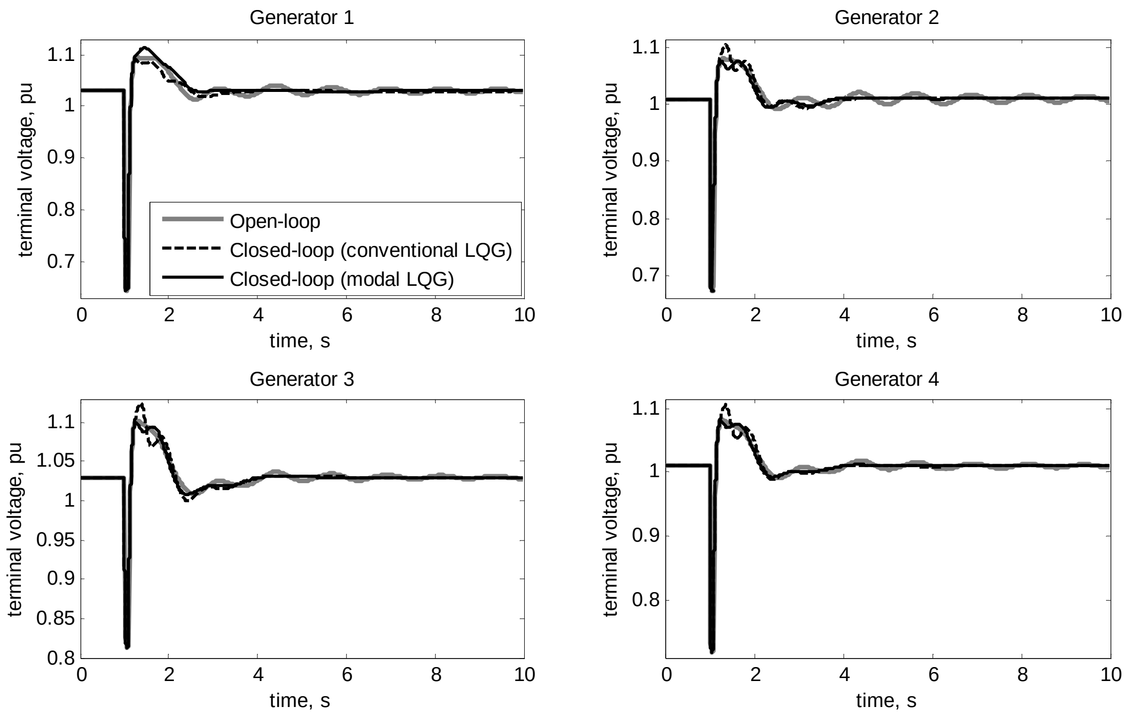

Figure 3-9: Terminal voltage responses for a large disturbance

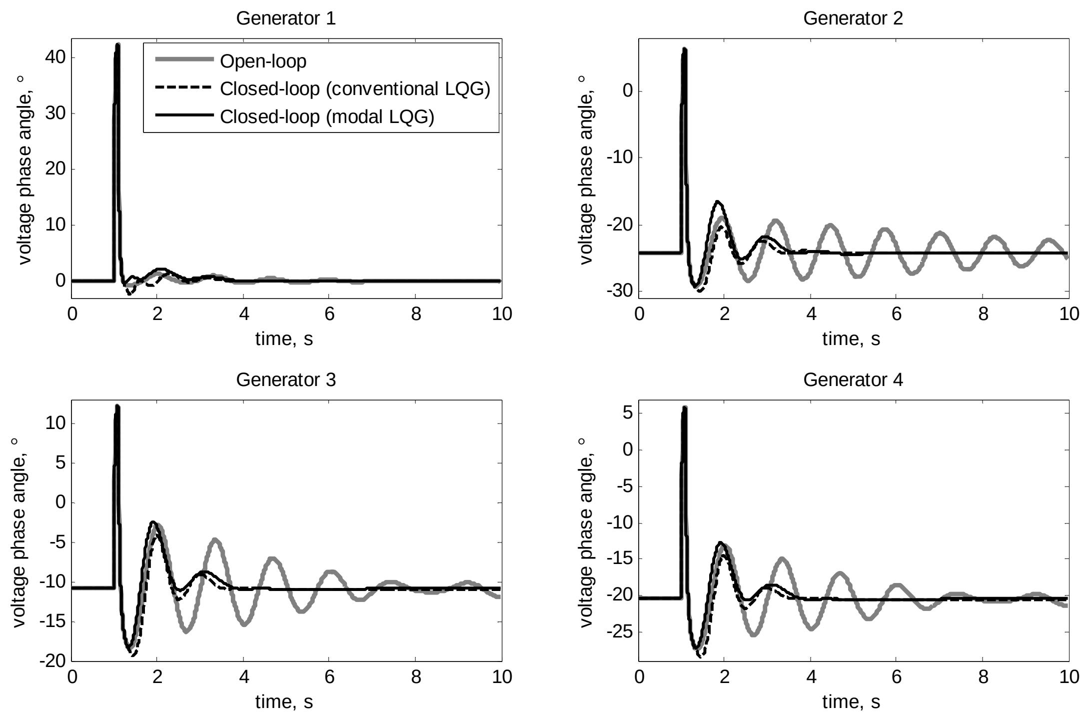

Figure 3-10: Voltage phase angle responses (at generator buses) for a large disturbance

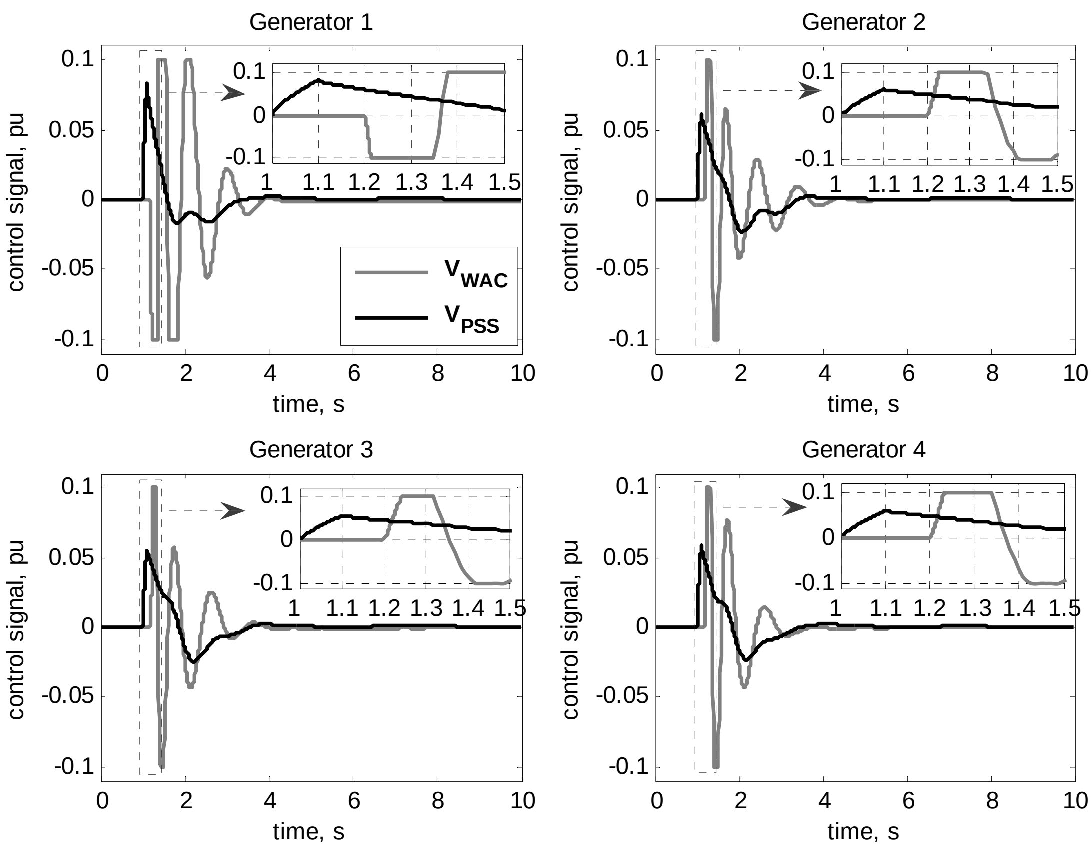

Figure 3-11: Control signals for a large disturbance (using conventional LQG controller)

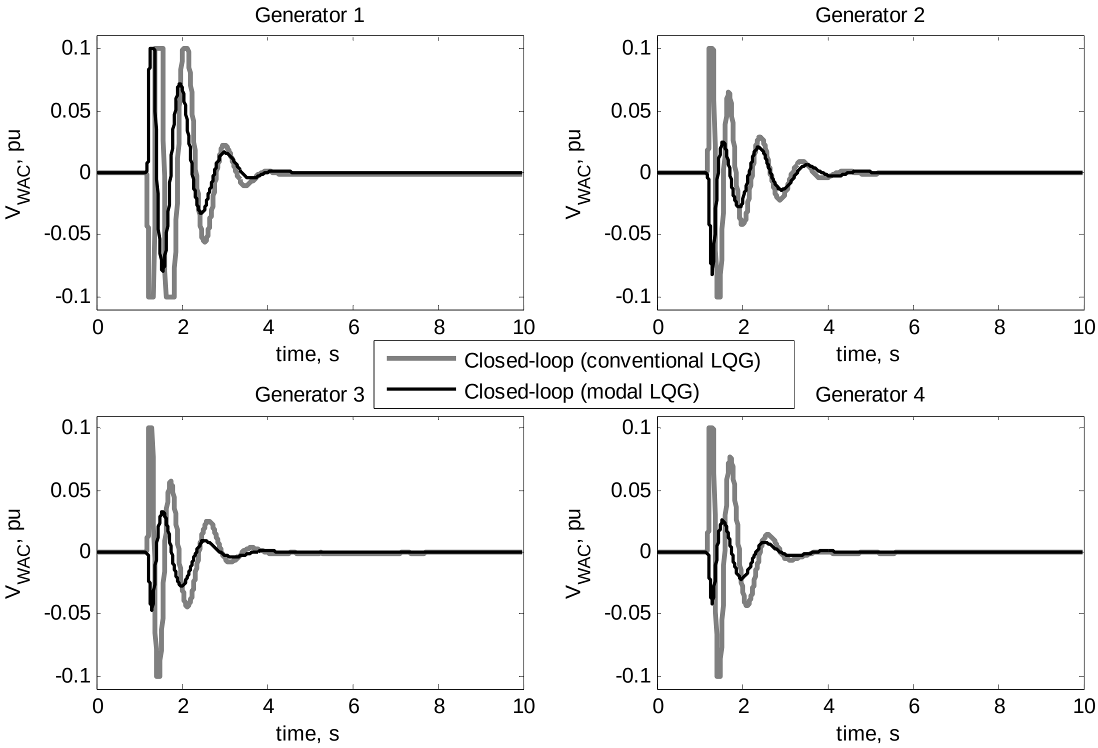

Figure 3-12: Wide-area control signals for a large disturbance

Table 3-5: Summarised comparison between conventional and modal LQG design methods

Feature	Conventional LQG design method	Modal LQG design approach
Participation factor analysis	essentially needed	not needed
Procedure of addressing multiple modes	complex	simple
Ability to obtain exact target damping ratio	hard (if possible)	easy (by fine tuning of weights)
LQR tuning process	time consuming	straightforward
Effect on other modes	some are affected	all are unaffected
Frequency (of targeted modes)	changes considerably	almost the same
Control efforts	high magnitudes	low magnitudes

3.4.3 Reduced Order Modal LQG Controller

3.4.3.1 Full Order Based Design

The result above showed good performance achieved by the SWAC designed using the modal LQG approach. The constructed 63^{rd} order SWAC, designed based on the full 63rd order open-loop system model, is reduced using the balanced truncation method [94]. Figure 3-13 shows the Hankel singular values of the designed SWAC (*Note*: the first Hankel singular value is infinity) where it can be seen that the first 5 states, of the balanced realisation, contribute the most to the controller input/output behaviour. A comparison of the frequency response, i.e. singular value plot (for the largest singular value), between the full 63rd order and reduced 5th order SWAC is shown in Figure 3-14 where it can be seen that good approximation is achieved in the frequency range of the electromechanical modes.

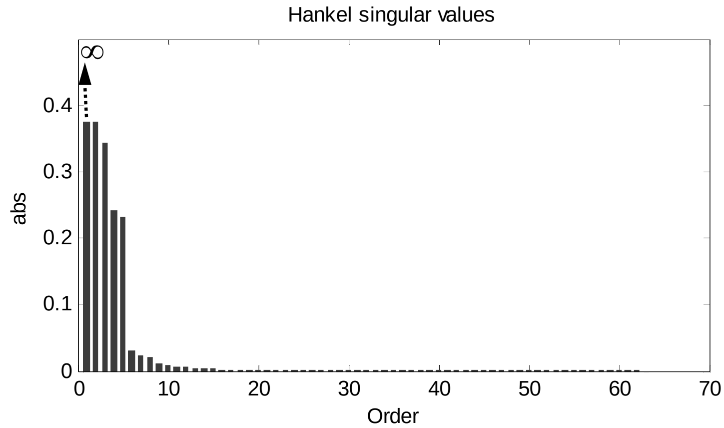

Figure 3-13: Hankel singular values of the 63rd SWAC
(the first Hankel singular value is infinity)

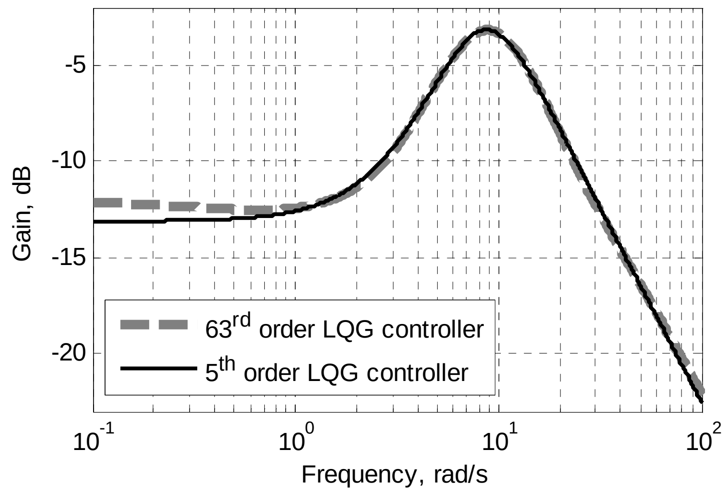

Figure 3-14: Frequency response of full and reduced order LQG controller

Table 3-6 lists the closed-loop electromechanical modes using the full and reduced order SWACs. It can be seen that the damping ratios of the two interarea modes didn't change when using the reduced order SWAC and the local mode remained unaltered from its location in the open-loop system. It can be seen also that the frequency of mode 2 is changed as a result of controller reduction. The closed-loop transient responses, to the same large disturbance applied in the previous section, using full and reduced order SWACs are compared in Figure 3-15. It can be seen that good performance is achieved using the 5th order reduced SWAC. The figure shows also that the small change in frequency of mode 2, resulting from controller reduction, didn't reduce the transient performance of the reduced order SWAC.

Table 3-6: Closed-loop electromechanical modes using full and reduced order SWACs

SWAC's Order	Mode 1 [1/s , rad/s]	ζ_1 [%]	Mode 2 [1/s , rad/s]	ζ_2 [%]	Mode 3 [1/s , rad/s]	ζ_3 [%]
63rd	-1.43±j4.56	30.04	-1.70±j4.90	32.71	-0.39±j6.90	5.65
5th	-1.41±j4.63	29.11	-1.78±j5.30	31.91	-0.39±j6.90	5.65

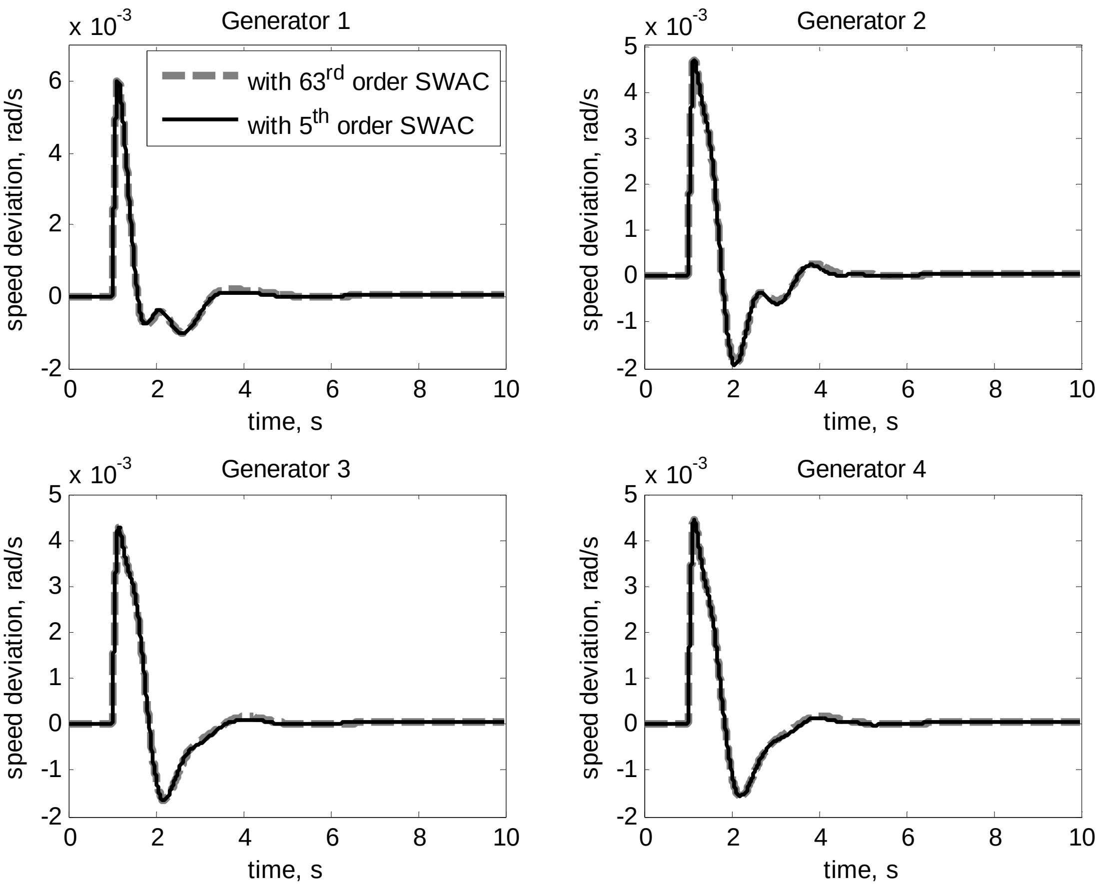

Figure 3-15: Speed deviation responses of the closed-loop system using full and reduced order SWAC

3.4.3.2 Reduced Order Based Design

The modal LQG controller can be designed based on a reduced order open-loop system model. Reduced open-loop model should provide adequate approximation of the full order model especially in the frequency range of the modes of interest. In addition, the modes of interest should be retained in the reduced open-loop model. Since other modes, including local modes, are not tackled by the modal LQG controller, retaining them in the reduced model is not necessary; provided that an adequate approximation still exist.

The Hankel singular values of the 47^{th} order linearised power system model, without time delays, are shown in Figure 3-16. It can be seen from the figure that the first 5-10 states contribute the most the system input/output behaviour. Figure 3-17 shows a comparison of the frequency response (the first singular value plot is shown) of the full 47^{th} order model with the reduced 10^{th} and 5^{th} order models. It can be seen that reduction to 10^{th} order gives good approximation of the 47^{th} order model better than a reduction to 5^{th} order. Table 3-7 lists the electromechanical modes for the full and reduced order models. It can be seen that the interarea modes are retained with good accuracy when using a 10^{th} order model. A further reduction to 5^{th} order model results in loss of accuracy in preserved interarea modes. The 10^{th} order reduced open-loop model therefore is used to design the LQG controller.

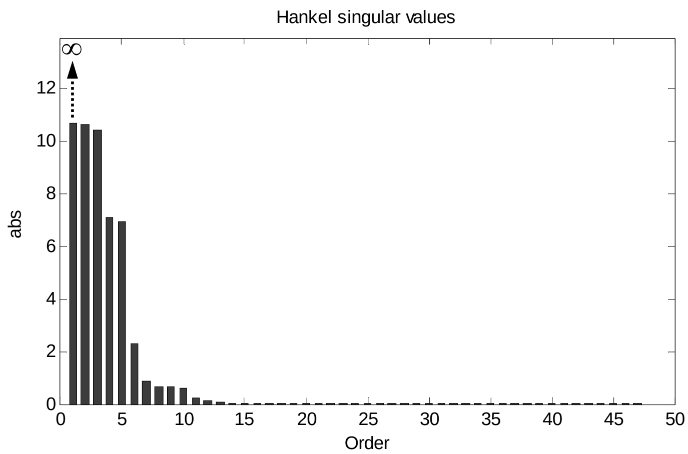

Figure 3-16: Hankel singular value plot of the 47^{th} open-loop model (without time delays) (the first Hankel singular value is infinity)

Models of input/output signal transmission delays (total of 16 states), using 2^{nd} order Padé approximation, are then added to 10^{th} order reduced model. The LQR is designed based on the 26th order model, incorporating time delays, by assigning modal weights to the two interarea modes and zero weights to other modes; similar to the full order open-loop model case. Target damping ratios are the same as for full order based design, i.e. 30.04% and 32.71% for modes 1 and 2, respectively. Table 3-8 lists the resulting electromechanical modes of the LQR system where it can be seen that exact target damping ratios are obtained by fine tuning of modal weights.

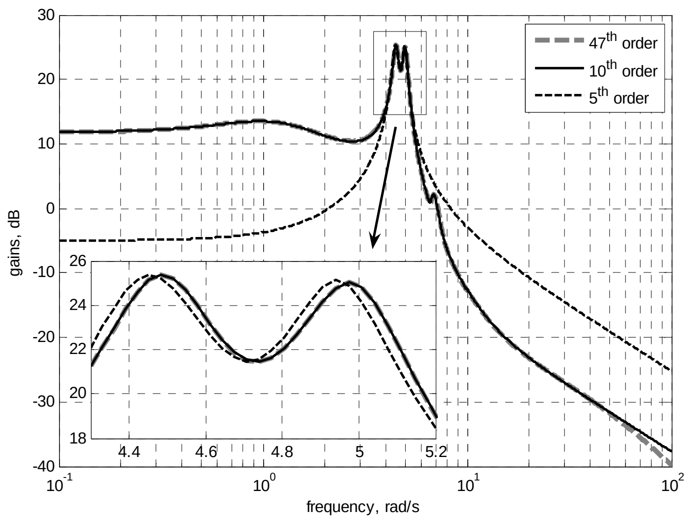

Figure 3-17: Open-loop order reduction

Table 3-7: Electromechanical modes of the full and reduced order open-loop models (mode 3 is not retained in the 5th order reduced model)

Order	Mode 1 [1/s , rad/s]	ζ_1 [%]	Mode 2 [1/s , rad/s]	ζ_2 [%]	Mode 3 [1/s , rad/s]	ζ_3 [%]
47th	-0.14±j4.49	3.08	-0.14±j4.99	2.75	-0.39±j6.90	5.65
10th	-0.14±j4.49	3.10	-0.14±j4.99	2.76	-0.39±j6.85	5.64
5th	-0.15±j4.45	3.29	-0.13-±j4.94	2.65	-	-

Table 3-8: Electromechanical modes of the LQR system (designed based on reduced order open-loop model)

Modal Weights $\left[q_{m_1} \mid q_{m_2} \mid q_{m_3}\right]$	Mode 1 [1/s , rad/s]	ζ_1 [%]	Mode 2 [1/s , rad/s]	ζ_2 [%]	Mode 3 [1/s , rad/s]	ζ_3 [%]
$\left[0.2235 \mid 0.2857 \mid 0\right]$	-1.44±j4.56	30.04	-1.70±j4.90	32.71	-0.39±j6.85	5.64

Kalman filter synthesis then follows, done similar to the full order based design case using same the LTR procedure, and the resulting closed-loop electromechanical modes are listed in Table 3-9. It can be seen that the damping ratios of the addressed modes are close to the target damping ratios and the local mode, mode 3, is kept unaltered from its location in the open-loop system. Figure 3-18 shows the Hankel singular values of the 26th order SWAC, designed based on reduced order open-loop model where it can be seen that a further reduction could be done to the controller. Figure 3-19 and Table 3-9 show that good approximation is achieved using a 5th order reduced SWAC. Closed-loop transient responses shown in Figure 3-20, for the same large disturbance applied in the previous section, also show that good performance is achieved using reduced 5th order SWAC.

Table 3-9: Closed-loop electromechanical modes with different reduced SWACs

Order	Mode #1 [1/s , rad/s]	ζ_1 [%]	Mode #2 [1/s , rad/s]	ζ_2 [%]	Mode #3 [1/s , rad/s]	ζ_3 [%]
26th	-1.35±j4.53	28.47	-1.58±j4.92	30.62	-0.39±j6.90	5.65
5th	-1.37±j4.66	28.21	-1.58±j5.12	29.43	-0.39±j6.90	5.65

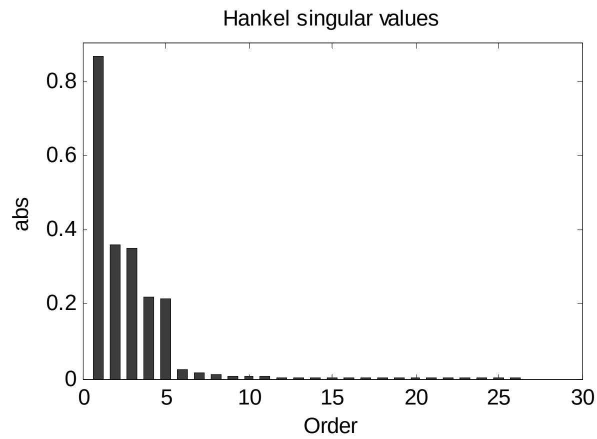

Figure 3-18: Hankel singular value plot of the 26th order controller

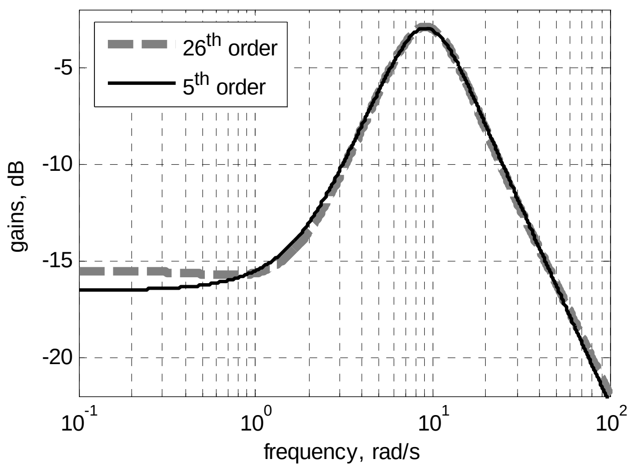

Figure 3-19: Further controller reduction

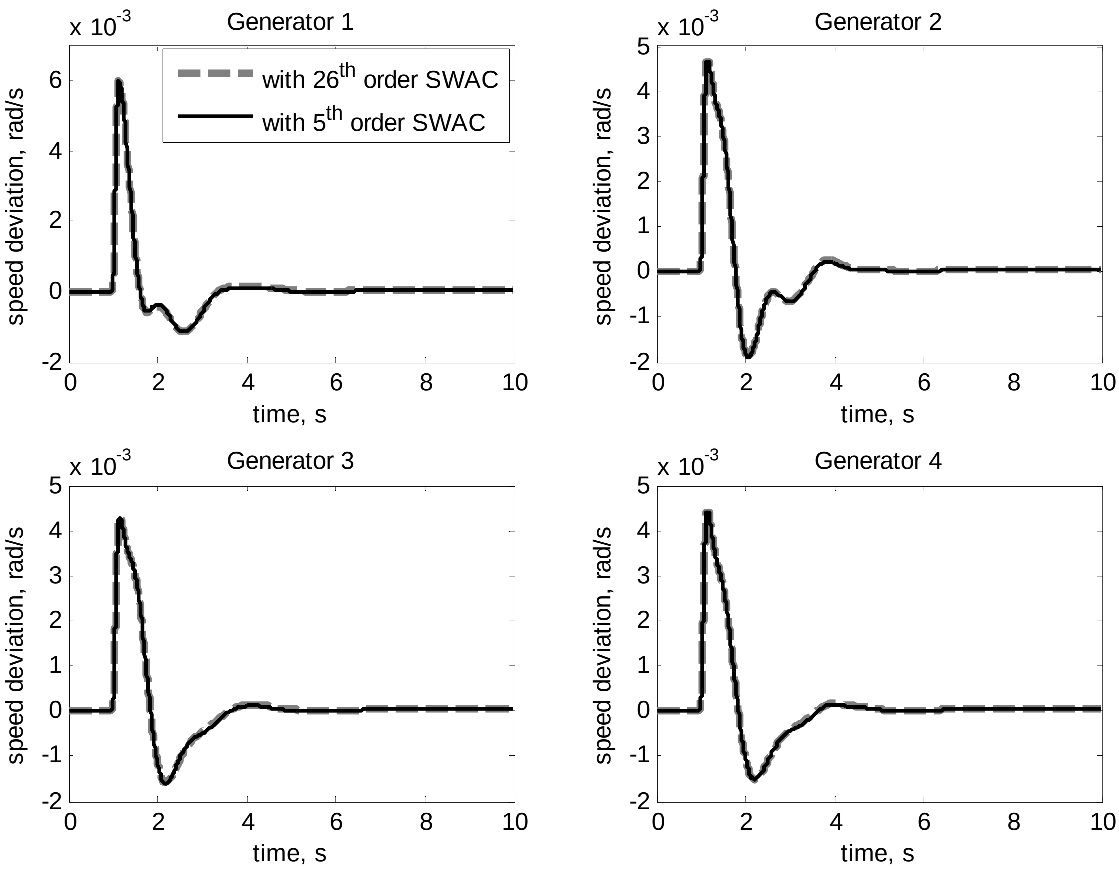

Figure 3-20: Speed deviation responses of the closed-loop system with reduced order SWACs

3.4.4 Robustness of the Modal LQG Controller

Robustness of the SWAC designed using the modal LQG approach is assessed for different operational scenarios including topological changes in the network, changes in the operating condition, variations in signal transmission time delays, and failures of communication links. Performance of the SWAC under these scenarios is assessed using both small-signal and transient performance analysis. In addition, the closed-loop system (with PSSs and SWAC) is compared with the open-loop system (with PSSs only). The closed-loop system used in the comparisons is formed using the 5th order reduced SWAC, designed based on 10th order reduced open-loop model. Numerical values of the used 5th order reduced SWAC, in state-space representation, are given in Appendix C.

3.4.4.1 Robustness to Topological Changes

The modal LQG controller was designed by considering that all transmission lines are in service. Robustness of the controller is assessed for cases when the topology of the network is changed because of outages of some transmission lines; due to scheduled maintenance, tripping by protection systems, etc. The open-loop and closed-loop systems are compared for different outages, each including outage of one parallel line, in the network. Table 3-10 lists the resulting frequency and damping ratios of the electromechanical modes for different line outages. The table shows that the SWAC improves the damping ratios for the two interarea modes at the new network topologies without affecting the local mode. The SWAC also stabilises the unstable interarea modes with adequate damping ratios while the local PSSs alone couldn't. It can be seen also that the frequency of mode 1 in the closed-loop system is reduced in most of the listed cases. This is due to the change in network topology and design of the SWAC assuming that all transmission lines are in service.

Table 3-10: Electromechanical modes for different line outages

Operating condition	**Parallel line outage**	**Open-loop (with PSSs only)**						**Closed-loop (with PSSs and SWAC)**					
		f_1 [Hz]	ζ_1 [%]	f_2 [Hz]	ζ_2 [%]	f_3 [Hz]	ζ_3 [%]	f_1 [Hz]	ζ_1 [%]	f_2 [Hz]	ζ_2 [%]	f_3 [Hz	ζ_3 [%]
OC-0	none	0.71	3.08	0.79	2.75	1.10	5.65	0.74	28.21	0.81	29.43	1.10	5.65
OC-A1	7-8	0.66	6.17	0.73	0.81	1.09	5.61	0.56	44.97	0.75	31.19	1.09	5.60
OC-A2	8-9	0.61	3.04	0.79	3.00	1.09	5.64	0.42	74.81	0.78	28.02	1.09	5.63
OC-A3	6-7	0.64	2.04	0.74	0.71	1.09	5.61	0.56	30.14	0.75	33.42	1.09	5.60
OC-A4	5-8	0.59	-1.79	0.77	4.12	1.12	5.70	0.38	12.25	0.79	25.98	1.12	5.69

Active power responses to the large disturbance shown in (Figure 3-21 - Figure 3-24), for each of listed operating conditions in Table 3-10, confirm the robustness of the SWAC. The figures also show that the SWAC effectively damps out the oscillations even though with reduction in frequency of mode 1.

Figure 3-25 and Figure 3-26 show the closed-loop active power responses for operating conditions (OC-A1) and (OC-A2), respectively, compared with the closed-loop responses for the nominal operating condition (OC-0). The effect of high damping ratio of mode 1, i.e. 44.97% for OC-A1 and 74.81% for OC-A2 in Table 3-10, for these two operating conditions can be seen in these figures.

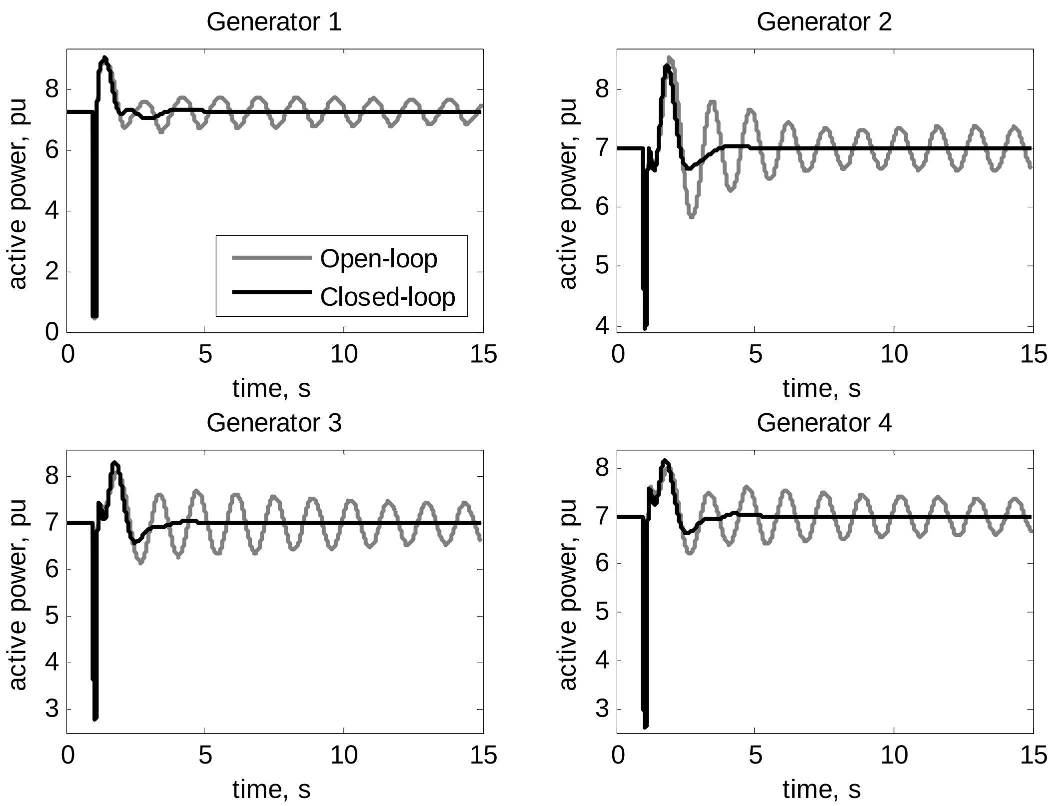

Figure 3-21: Active power responses (OC-A1)

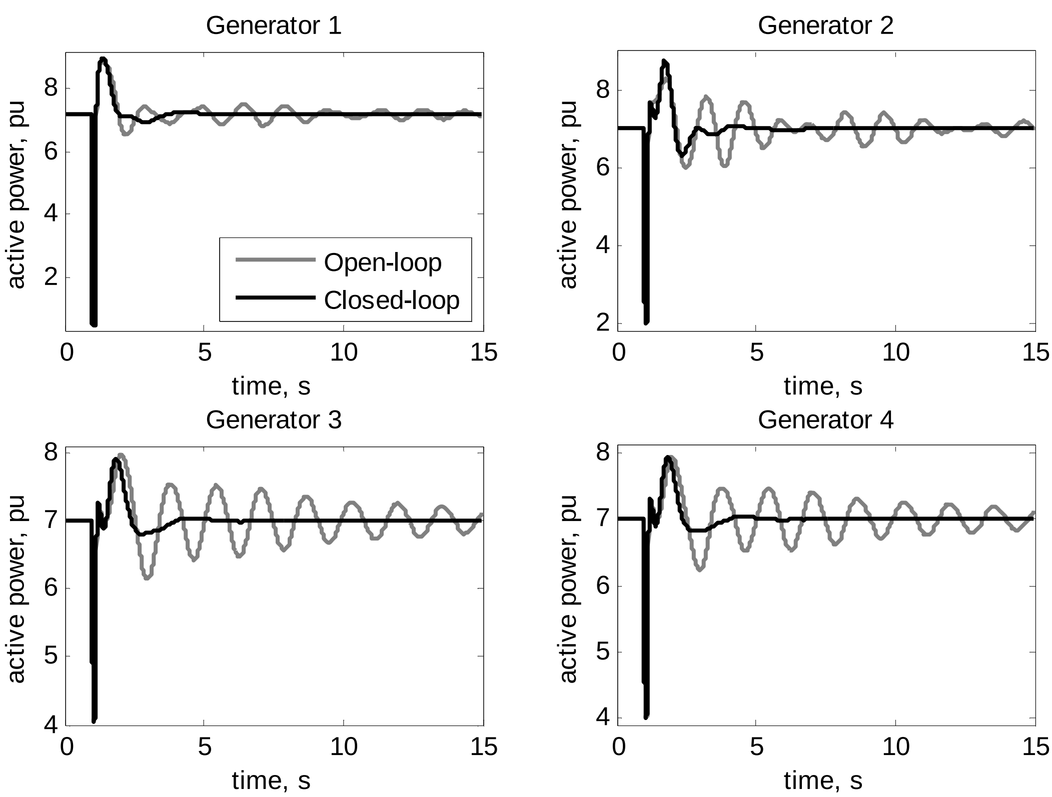

Figure 3-22: Active power responses (OC-A2)

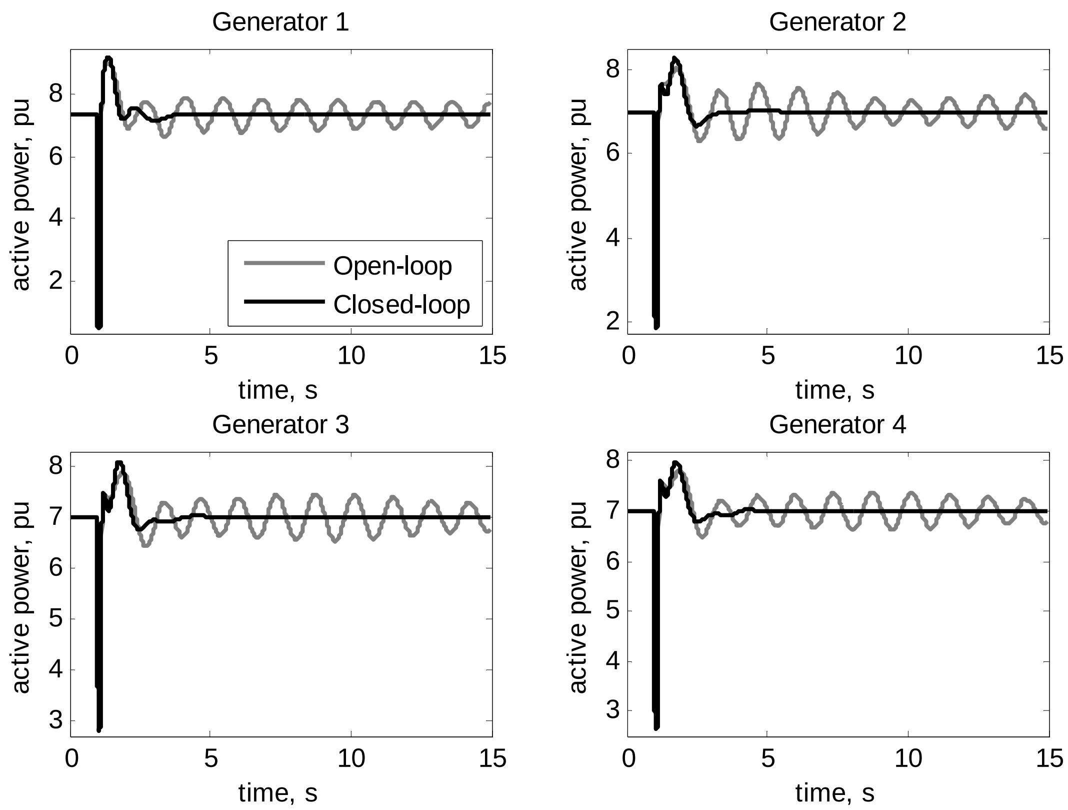

Figure 3-23: Active power responses (OC-A3)

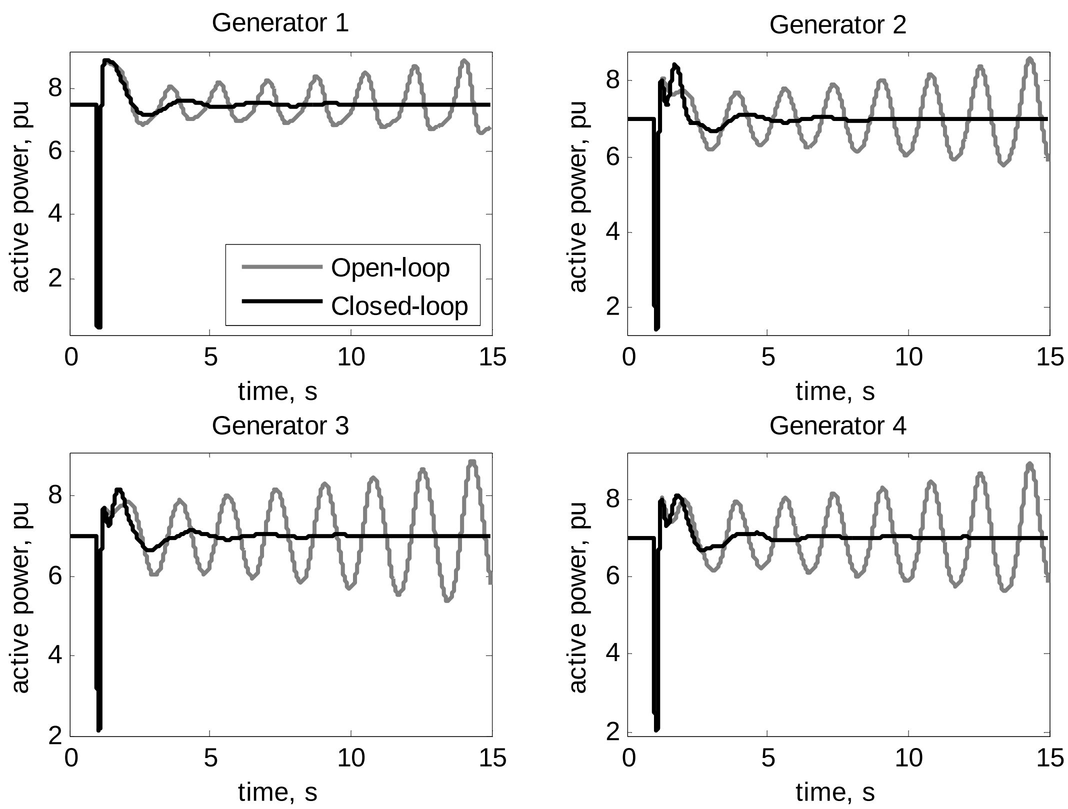

Figure 3-24: Active power responses (OC-A4)

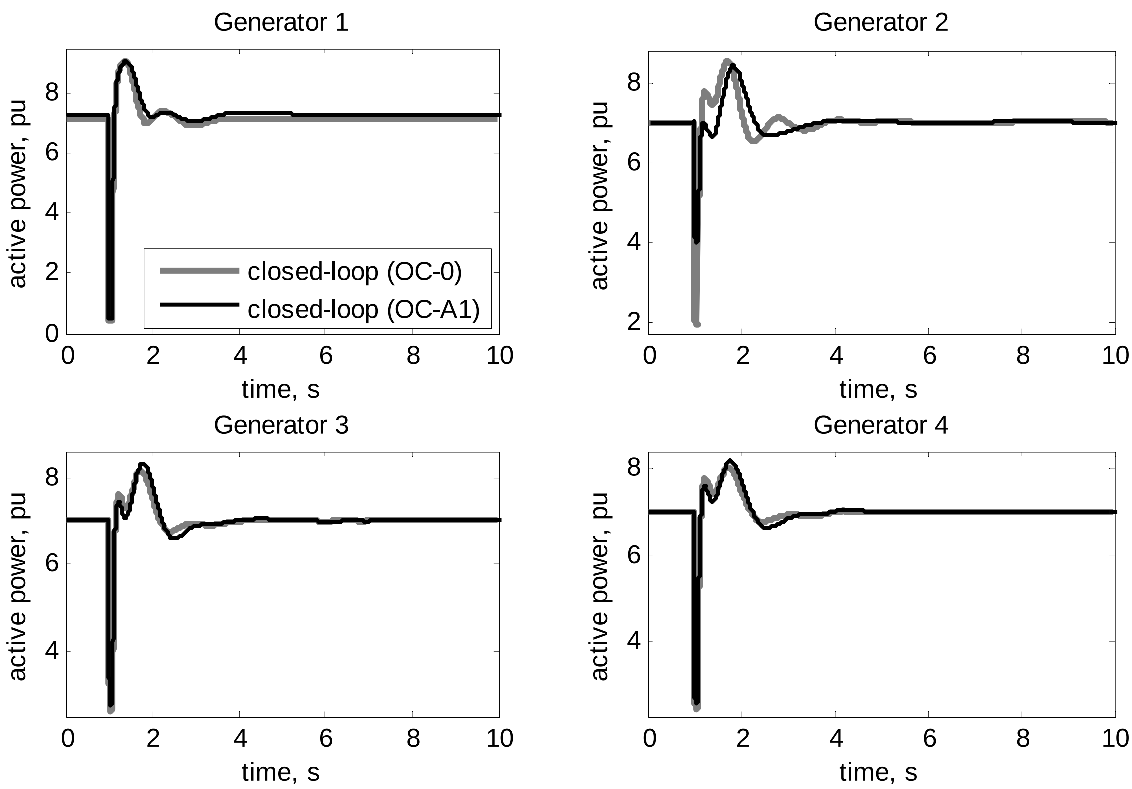

Figure 3-25: Active power responses (OC-0) and (OC-A1)

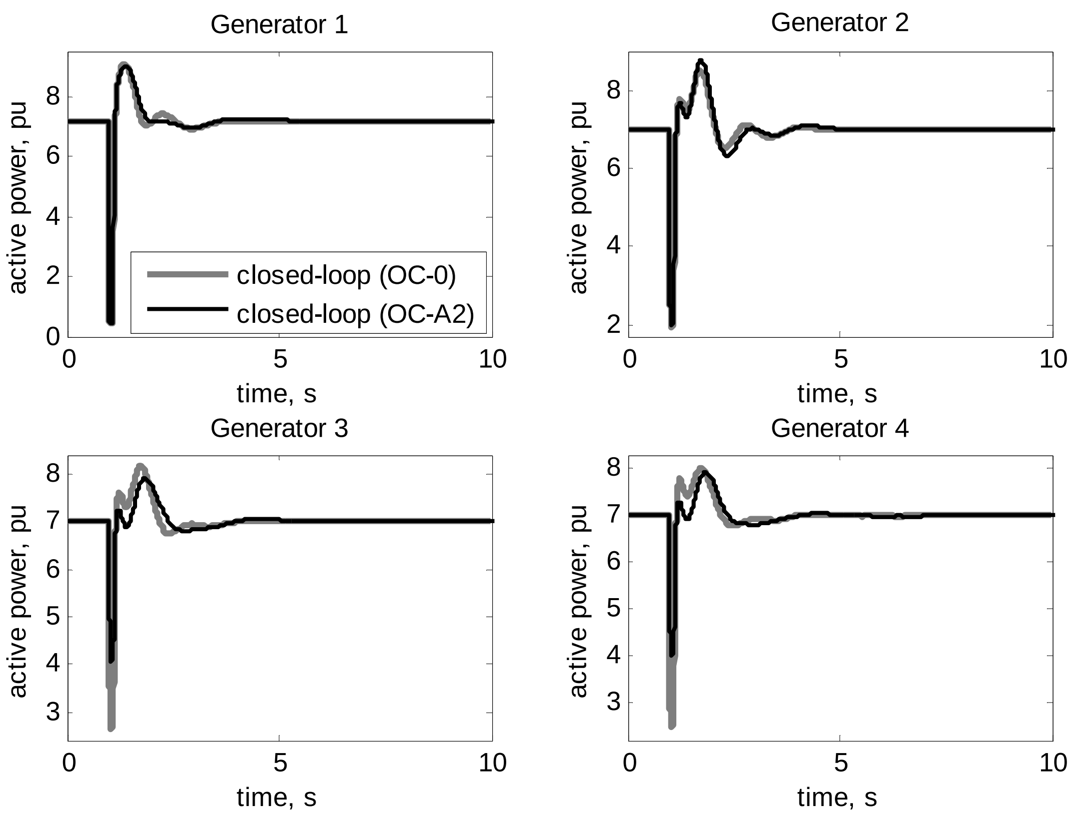

Figure 3-26: Active power responses (OC-0) and (OC-A2)

3.4.4.2 Robustness to Changes in Operating Condition

Table 3-11 lists the resulting frequency and damping ratios of the electromechanical modes for different increases in power transfer across corridor 8-7. This was done by increasing the output active power of generator 1 and decreasing that of generator 2 by the same amount (output active power of both generators 3 and 4 is kept as in the nominal operating condition). It can be seen from the table that the damping ratio of mode 1 decreases at operating conditions (OC-B1 and OC-B2), in the open-loop system, and then increases at (OC-B3, OC-B4, and OC-B5). The decrease in damping ratio of mode 1 at (OC-B1 and OC-B2) is due to the high participation of generator 1 in that mode combined with the increase in its output power. The increase in damping ratio of mode 1 at (OC-B3, OC-B4, and OC-B5) is due to the high participation of generator 2 in that mode (much higher than the rest of generators) combined with decrease in its output power at these operating conditions.

Improvement in the damping ratios for the interarea modes at the new operating conditions without affecting the local mode can be seen in the Table 3-11. As the power transfer increases, mode 2 becomes unstable using PSSs only. The SWAC sufficiently stabilises that mode for heavy power transfers. Active power responses to the large disturbance shown in (Figure 3-27 - Figure 3-31), for different power transfers, confirm the listed results in Table 3-11.

Table 3-12 lists the resulting frequency and damping ratios of the electromechanical modes for different increases in power transfer across corridor 8-9. As in the previous tables the SWAC improves the damping of the two interarea modes while not affecting the local mode. Mode 1 becomes unstable, using PSSs only, as the power transfer increases and the SWAC stabilises it effectively. The SWAC is further assessed using transient performance analysis as shown in (Figure 3-32 - Figure 3-35). Transient simulations confirm the robustness of the SWAC in addition to the listed results in Table 3-12.

Reduction in frequencies of mode 2 and mode 1 (in the closed-loop system) can be seen from Table 3-11 and Table 3-12, respectively, as power transfer is increased. This is due to the design of the SWAC based on a fixed operating condition. Transient performance analysis results (shown in Figure 3-27 - Figure 3-35), however, show that the SWAC effectively damps out the oscillations even though with reduction in frequencies of closed-loop interarea modes.

Table 3-11: Electromechanical modes for different power transfers across corridor 8-7

Operating condition	Power transfer increase across corridor 8-7	Open-loop (with PSSs only)						Closed-loop (with PSSs and SWAC)					
		f_1 [Hz]	ζ_1 [%]	f_2 [Hz]	ζ_2 [%]	f_3 [Hz]	ζ_3 [%]	f_1 [Hz]	ζ_1 [%]	f_2 [Hz]	ζ_2 [%]	f_3 [Hz	ζ_3 [%]
OC-B1	10 %	0.71	2.95	0.77	2.37	1.10	5.63	0.75	26.11	0.76	31.79	1.10	5.63
OC-B2	20 %	0.72	2.14	0.74	2.29	1.09	5.62	0.73	24.44	0.71	34.00	1.09	5.60
OC-B3	30 %	0.72	4.61	0.70	-1.59	1.09	5.59	0.69	27.87	0.65	30.21	1.09	5.57
OC-B4	40 %	0.71	5.27	0.66	-4.57	1.08	5.56	0.69	28.65	0.55	21.65	1.08	5.54
OC-B5	50 %	0.69	5.43	0.61	-8.64	1.08	5.51	0.68	28.84	0.49	6.71	1.08	5.48

Table 3-12: Electromechanical modes for different power transfers across corridor 8-9

Operating condition	Power transfer increase across corridor 8-9	Open-loop (with PSSs only)						Closed-loop (with PSSs and SWAC)					
		f_1 [Hz]	ζ_1 [%]	f_2 [Hz]	ζ_2 [%]	f_3 [Hz]	ζ_3 [%]	f_1 [Hz]	ζ_1 [%]	f_2 [Hz]	ζ_2 [%]	f_3 [Hz	ζ_3 [%]
OC-C1	25 %	0.71	2.65	0.77	2.26	1.09	5.82	0.74	27.04	0.75	31.72	1.09	5.81
OC-C2	50 %	0.70	0.87	0.75	2.63	1.08	5.99	0.68	32.00	0.73	27.75	1.08	5.97
OC-C3	75 %	0.67	-2.54	0.74	3.74	1.07	6.15	0.56	26.61	0.73	28.17	1.07	6.13
OC-C4	100 %	0.62	-7.11	0.73	4.46	1.05	6.28	0.50	10.30	0.72	28.53	1.05	6.26

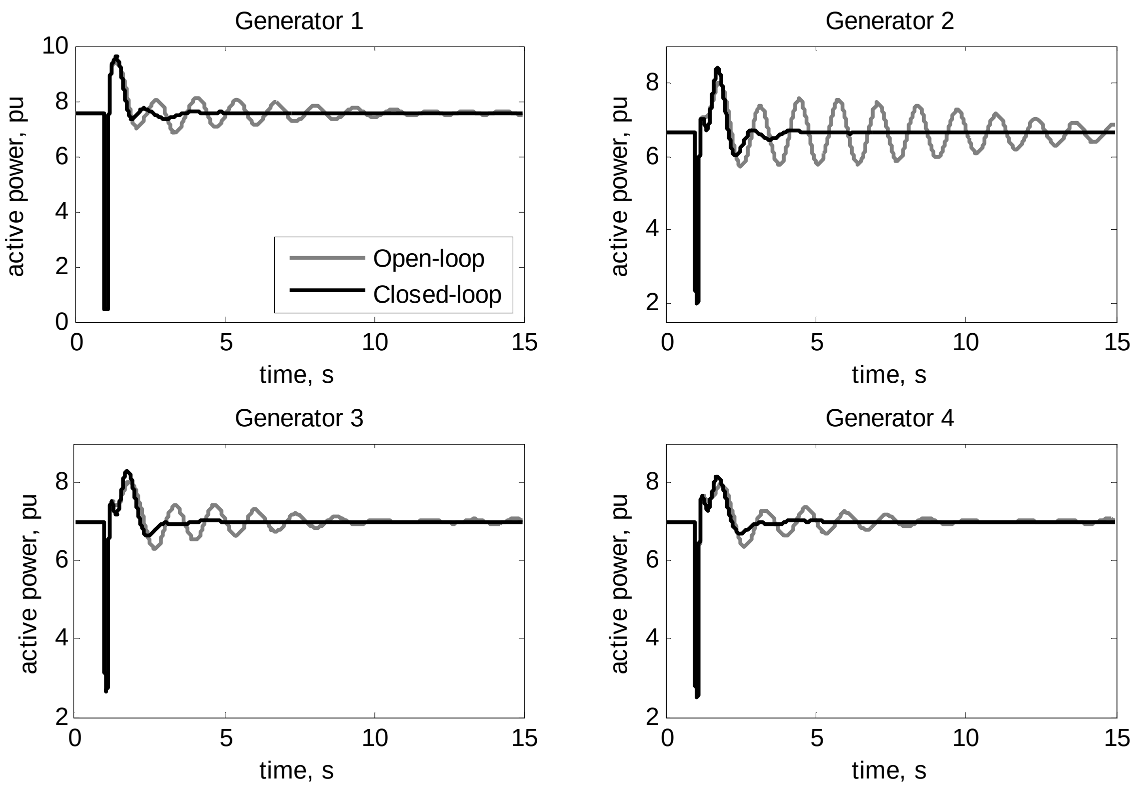

Figure 3-27: Active power responses (OC-B1)

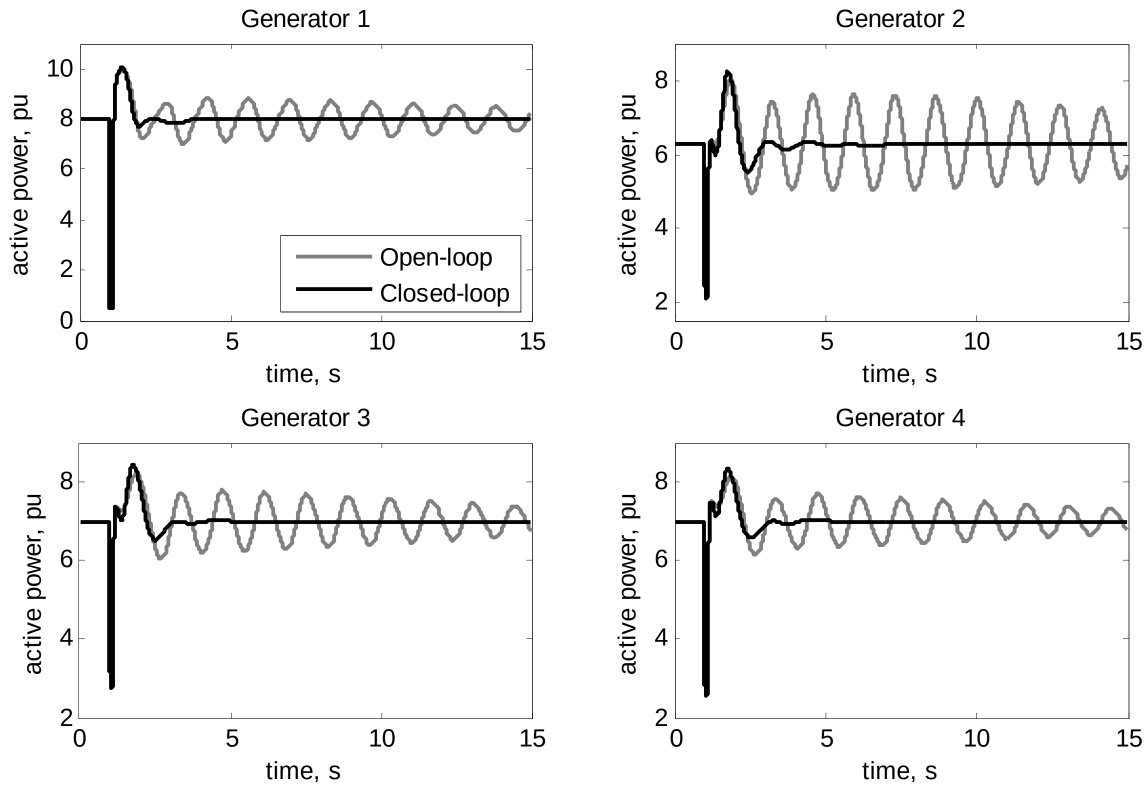

Figure 3-28: Active power responses (OC-B2)

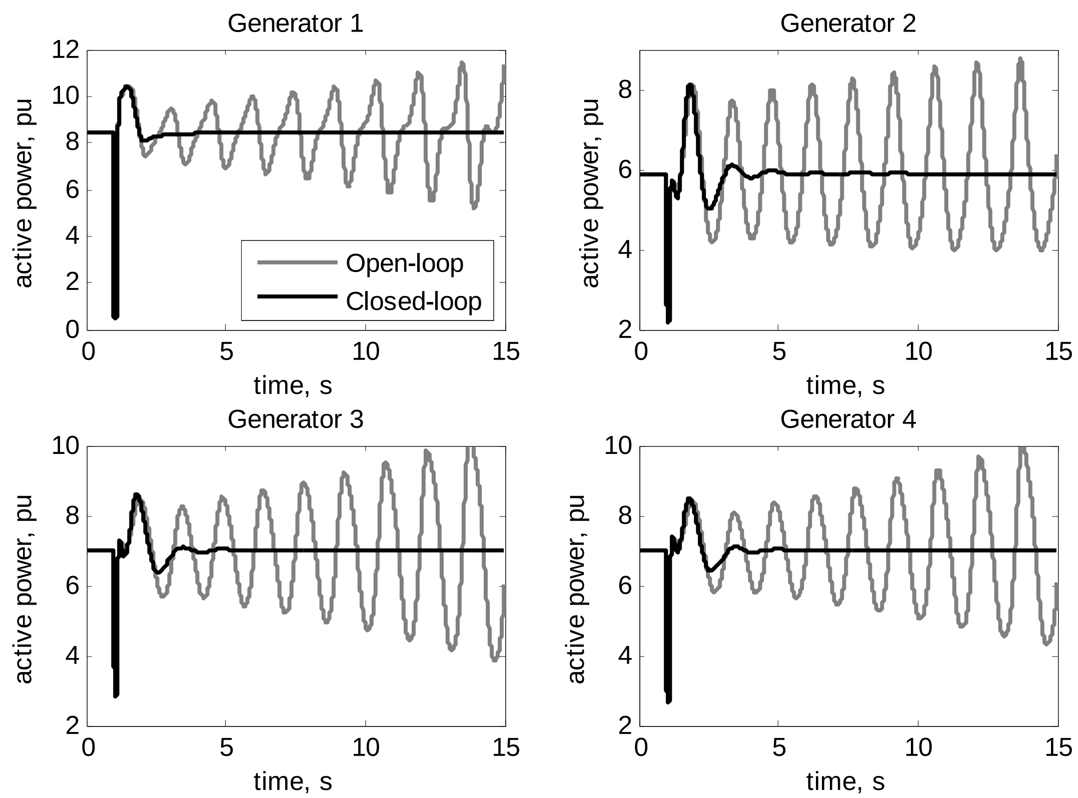

Figure 3-29: Active power responses (OC-B3)

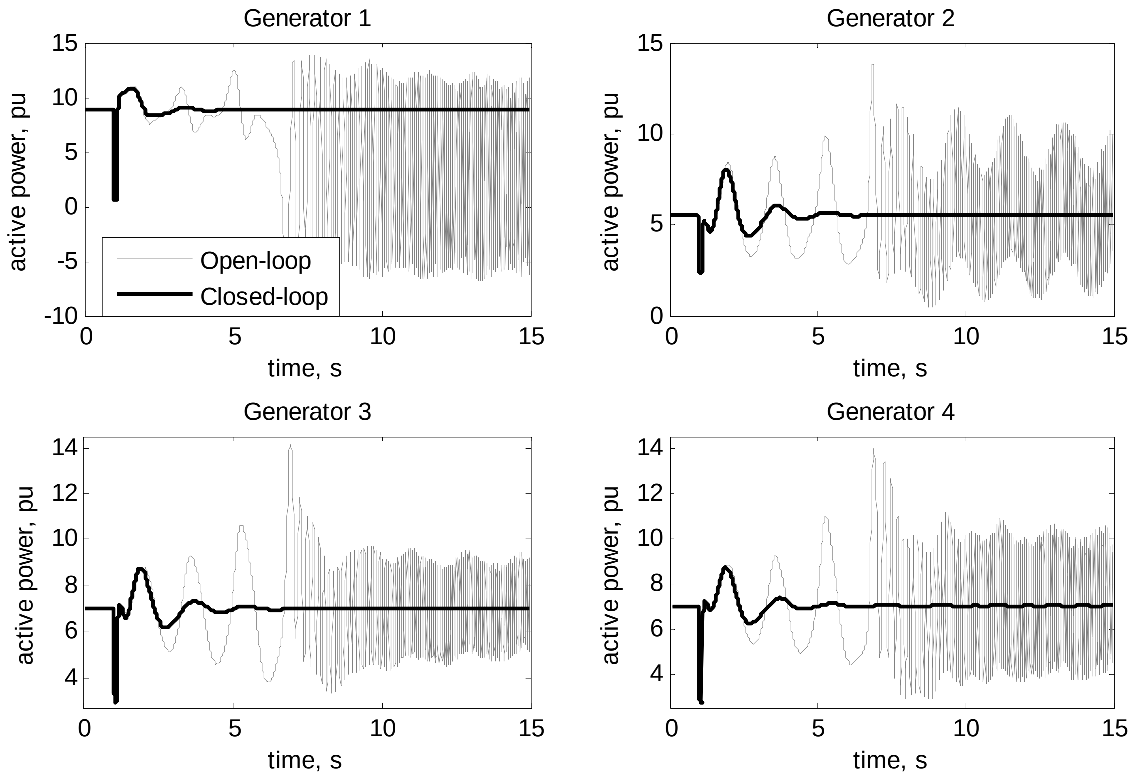

Figure 3-30: Active power responses (OC-B4)
(loss of synchronism in the open-loop system occurs at t≈7s)

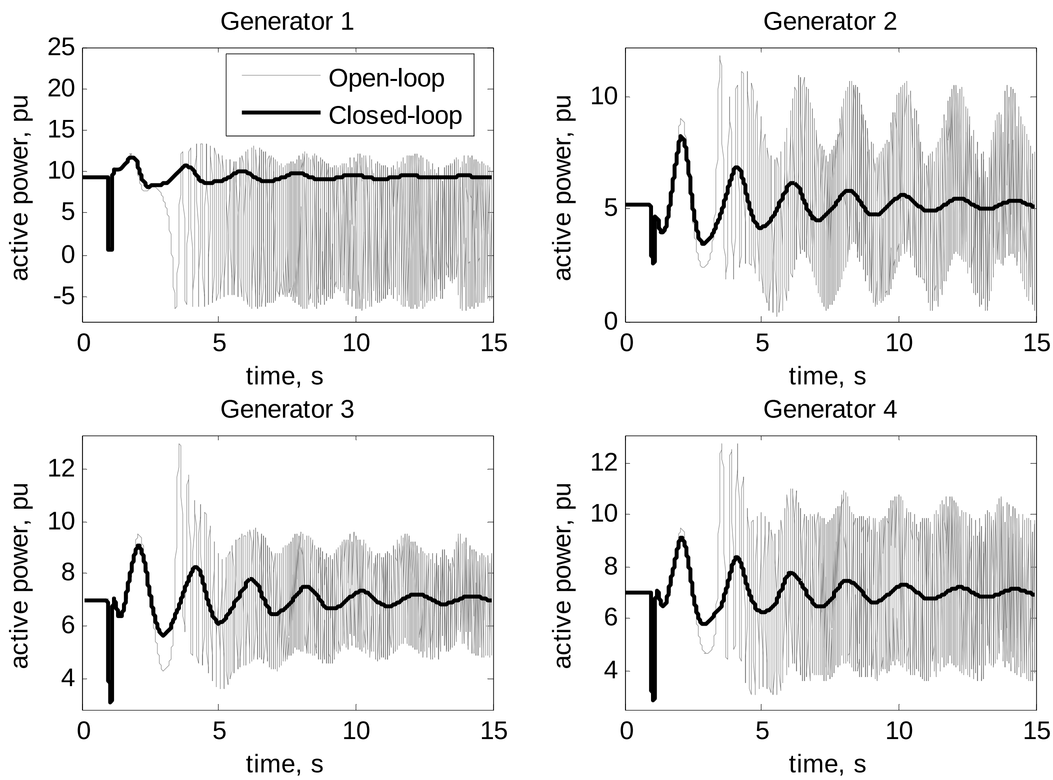

Figure 3-31: Active power responses (OC-B5)
(loss of synchronism in the open-loop system occurs at t≈4s)

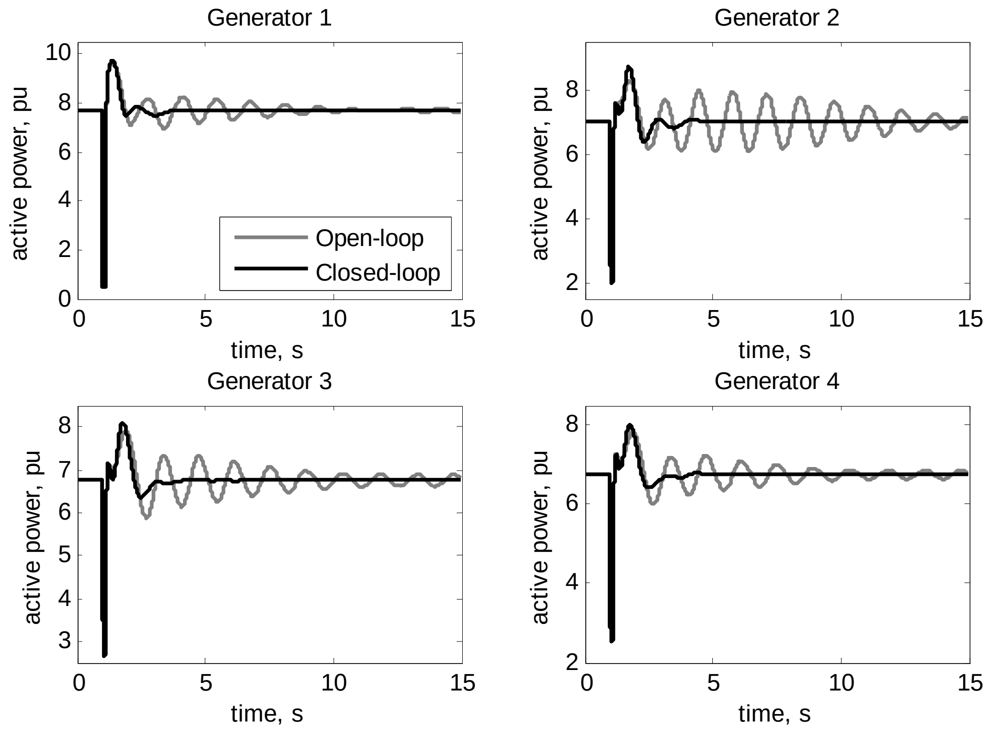

Figure 3-32: Active power responses (OC-C1)

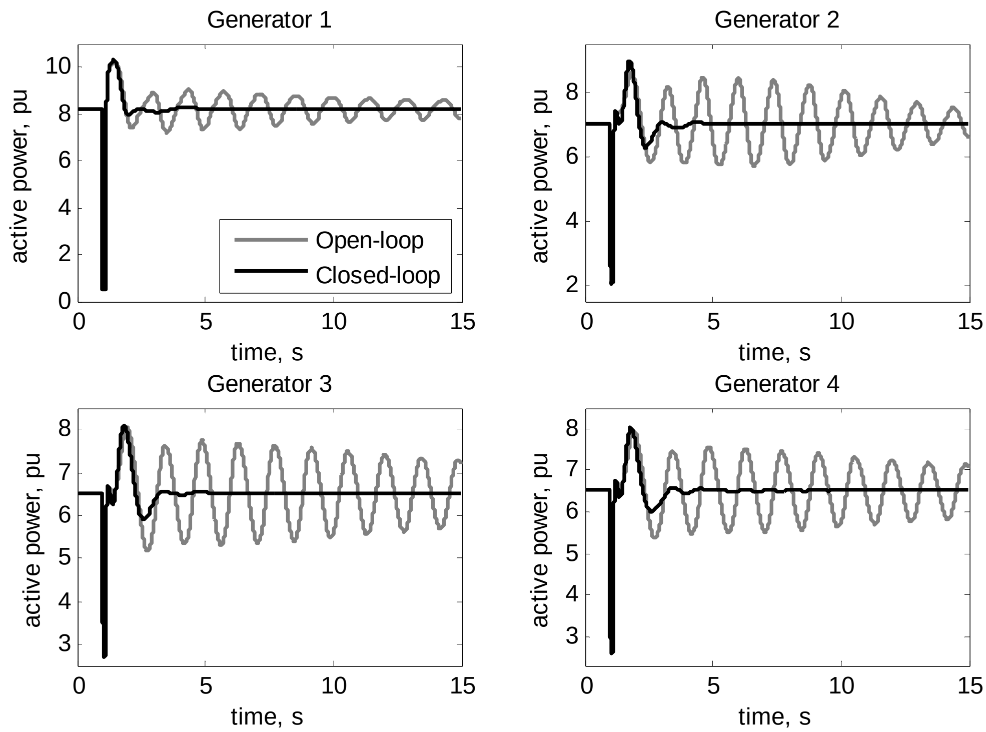

Figure 3-33: Active power responses (OC-C2)

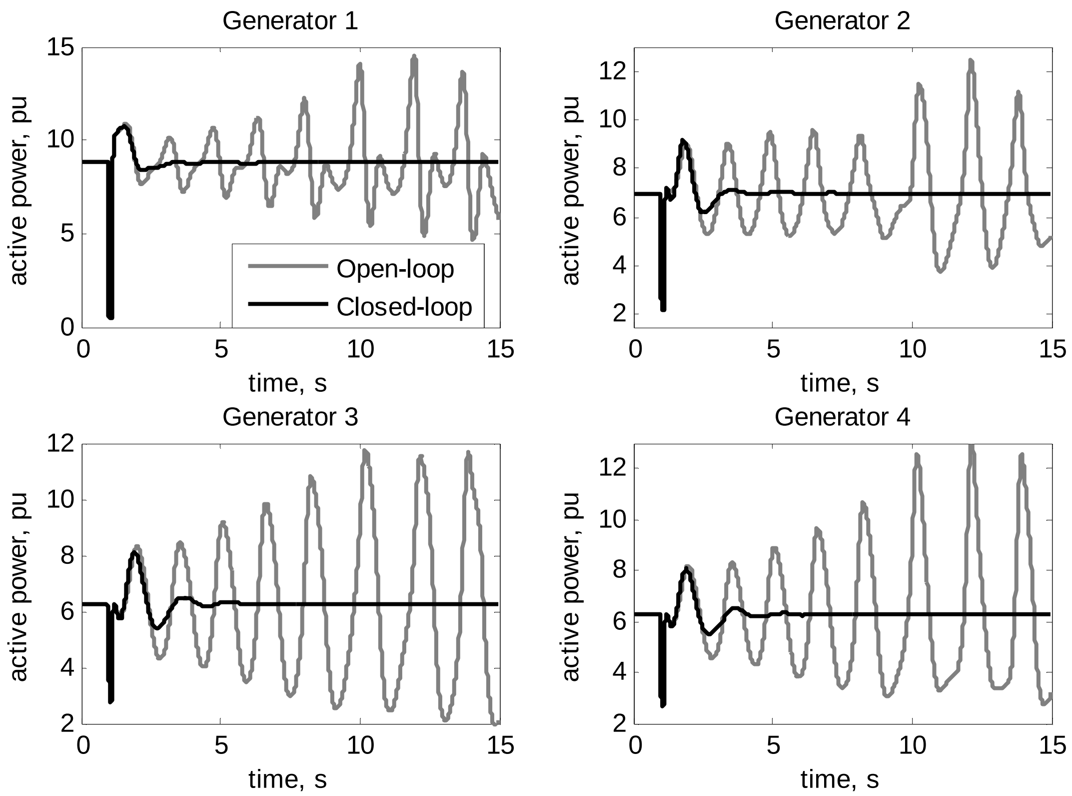

Figure 3-34: Active power responses (OC-C3)

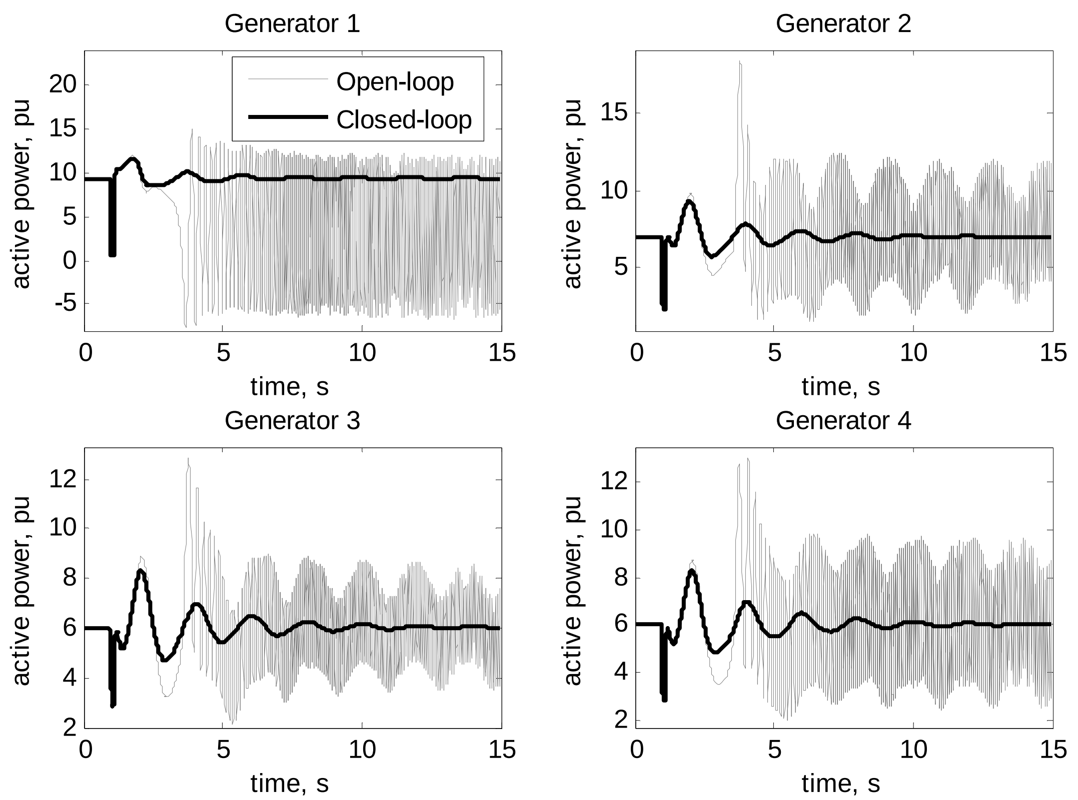

Figure 3-35: Active power responses (OC-C4)
(loss of synchronism in the open-loop system occurs at t≈4s)

3.4.4.3 Robustness to Variations of Time Delays

The SWAC is also assessed for variations in signal transmission time delay from the value considered at design stage, i.e. 100 ms for one way (200 ms for round trip communication from PMUs to the SWAC and then back to generators' exciters). Table 3-13 lists the closed-loop electromechanical modes for different time delays. It can be seen that the increase in time delay degrades the damping ratios of the two interarea modes. For up to 400 ms delays the damping ratios of the interarea modes are greater than their values in the open-loop case. In all cases, the local mode is not affected by these increased time delays.

Table 3-13: Closed-loop electromechanical modes for different time delays

Total delay	Mode 1 [1/s , rad/s]	ζ_1 [%]	Mode 2 [1/s , rad/s]	ζ_2 [%]	Mode 3 [1/s , rad/s]	ζ_3 [%]
200 ms	-1.37±j4.66	28.21	-1.58±j5.12	29.43	-0.39±j6.90	5.65
250 ms	-1.19±j5.17	22.50	-1.29±j5.72	22.06	-0.39±j6.90	5.65
300 ms	-0.80±j5.36	14.71	-0.83±j5.94	13.85	-0.39±j6.90	5.65
350 ms	-0.49±j5.38	9.09	-0.48±j5.95	7.97	-0.39±j6.90	5.64
400 ms	-0.26±j5.33	4.90	0.22±j5.89	3.66	-0.39±j6.90	5.64
450 ms	-0.09±j5.26	1.67	0.02±j5.80	0.40	-0.39±j6.90	5.64

Figure 3-36 and Figure 3-37 show, respectively, the active power and speed deviation responses, for the large disturbance, of the closed-loop system for some examples of increased time delays. Wide-area control signals for the same disturbance are shown in Figure 3-38. Note in the figure the increasing time lag of the action of the wide-area control signal. As can be seen from the two figures (Figure 3-36 and Figure 3-37) that although the damping is degraded by the increased delays, the SWAC is still effectively damping out the oscillations for longer delays up to 200% of the one considered at the design stage. The figures show that the modal LQG controller can tolerate longer time delays than the ones considered at the design stage for damping improvement above the open-loop system case.

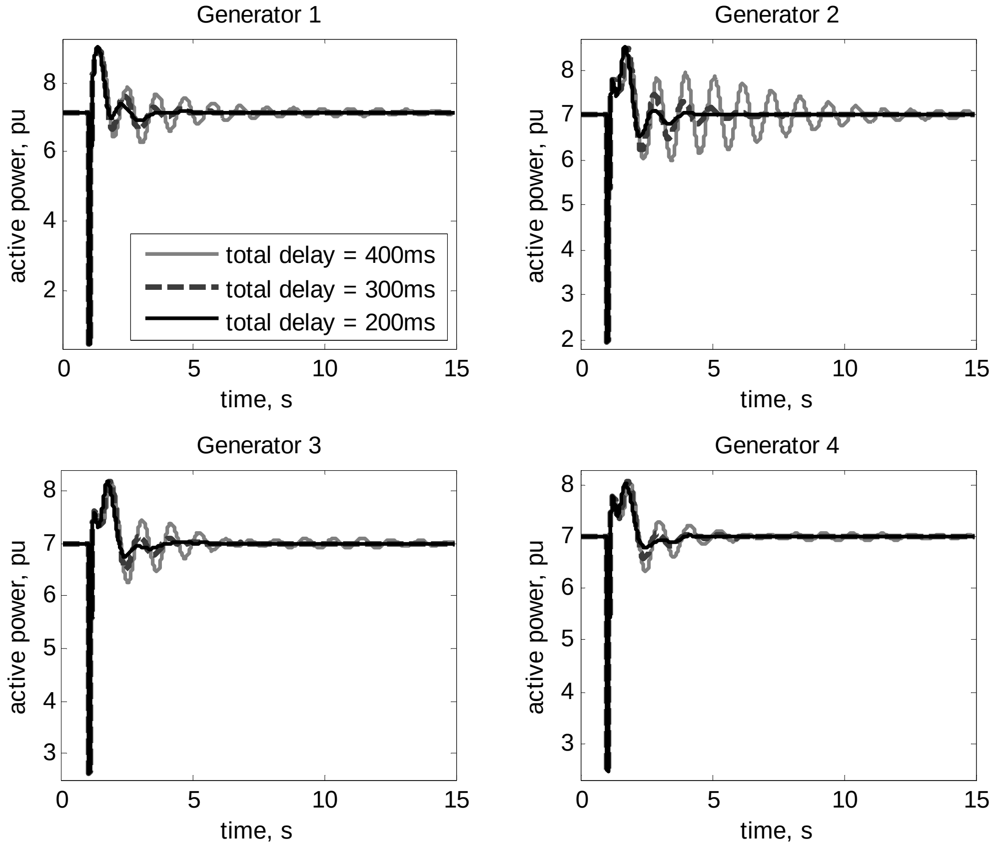

Figure 3-36: Active power responses for different time delays

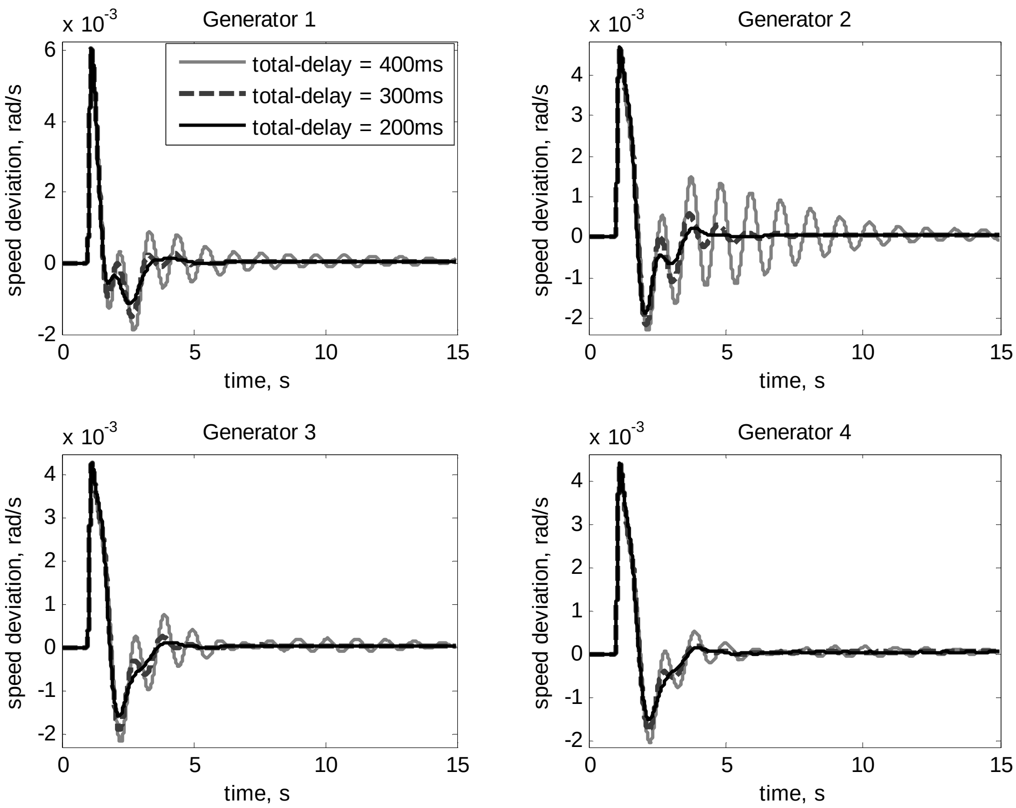

Figure 3-37: Speed deviation responses for different time delays

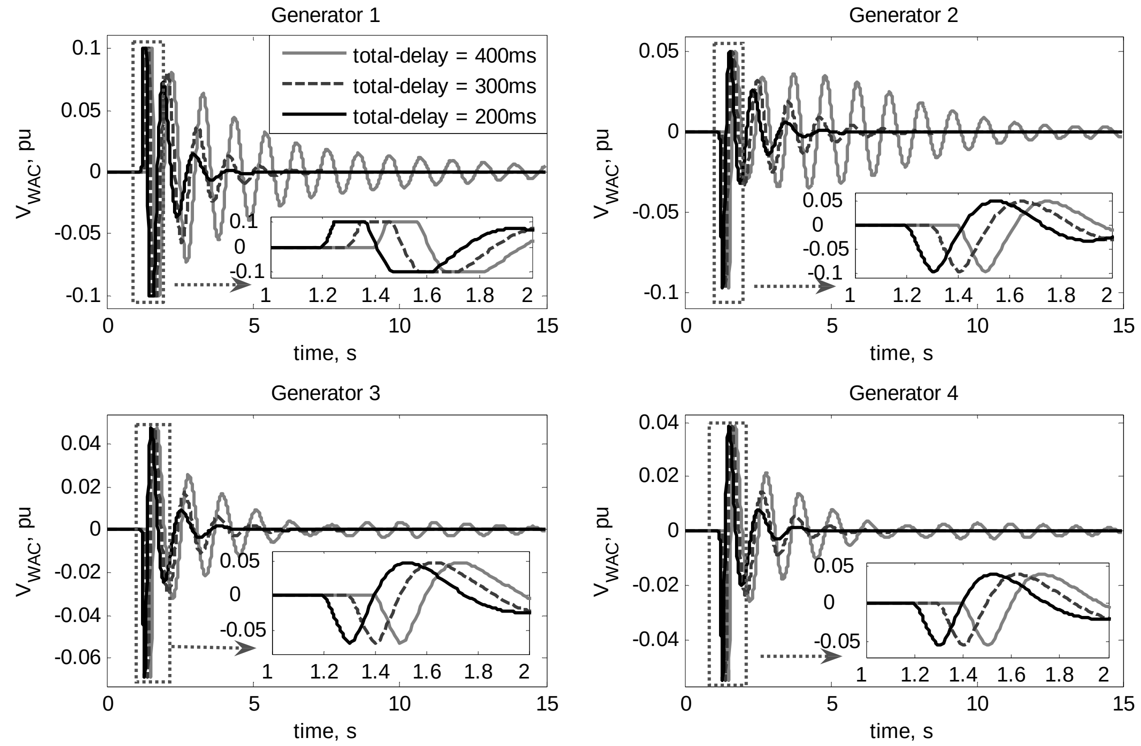

Figure 3-38: Wide-area control signal for different time delays

Assessment of the SWAC's robustness to variations in time delays is extended to cases when different values of delays are considered at the design stage. Two SWACs are designed using the modal LQG approach by considering 25 ms one-way delay (25 ms-based SWAC) and 250 ms one-way delay (250 ms-based SWAC). The purpose is to show the applicability of the modal LQG approach, using the 2^{nd} order Padé approximation, to wide range of time delays experienced in the WAMS. The new delay values are chosen based on real data from existing WAMS [42]. The 25 ms delay is selected assuming fibre optic communication link and the 250 ms delay is selected assuming satellite-based link. The target damping ratios for the two SWACs are the same as in the base case, i.e. 30.04 % for mode 1 and 32.71 % for mode 2. The target damping ratios were achieved by fine tuning of the LQR and the modal weights used are listed in Table 3-14. Kalman filter is synthesised using the LTR procedure with the same tuning parameters as in (3.45). Time delays were modelled using 2^{nd} order Padé approximation due to its accuracy in modelling both the 25 ms and 250 ms delays over the frequency range of electromechanical modes (see Figure 3-4).

Table 3-14: Fine tuning using the modal LQG approach for different time delays considered at the design stage

SWAC	Modal weights $\left[q_{m_1} \mid q_{m_2} \mid q_{m_3}\right]$	ζ_1 [%]	ζ_2 [%]	ζ_3 [%]
25 ms-based SWAC	$[0.04137 \mid 0.885 \mid 0]$	30.04	32.71	5.65
250 ms-based SWAC	$[2.465 \mid 1.842 \mid 0]$	30.04	32.71	5.65

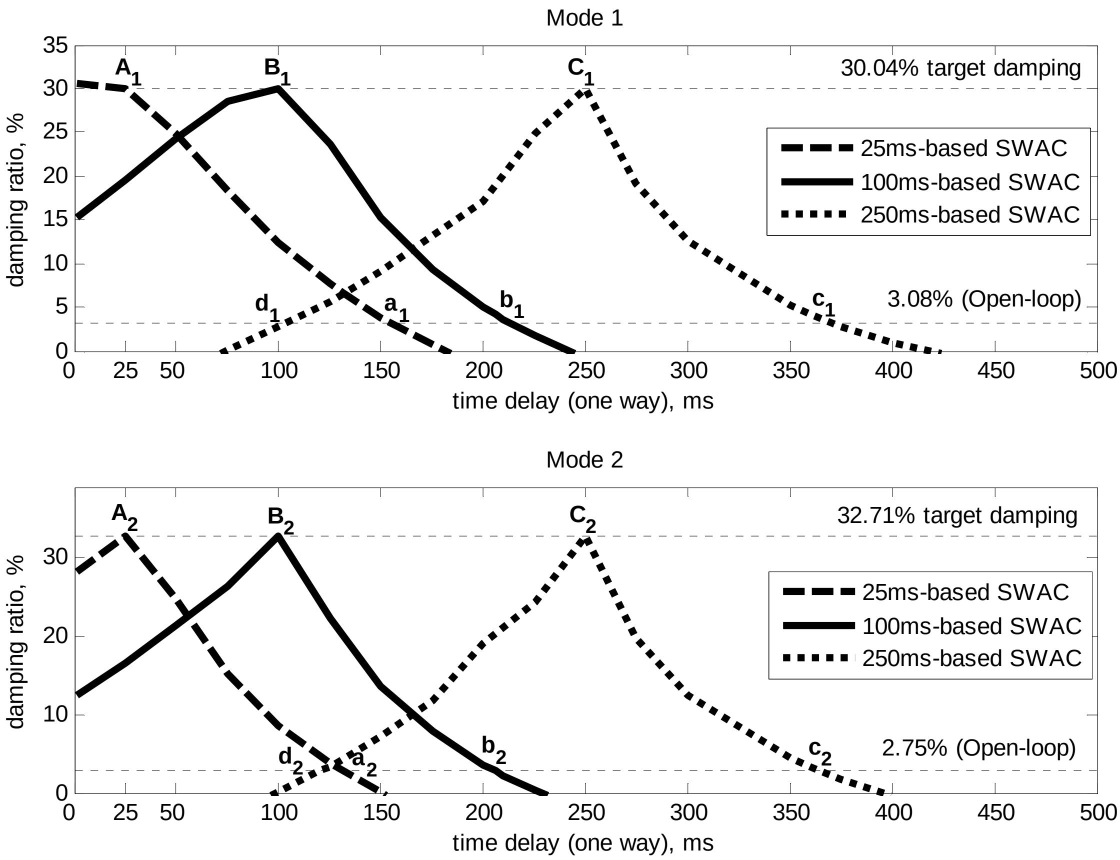

Figure 3-39: Curves of damping ratios of the interarea modes over increasing time delays (For different time delays considered at the design stage)

Small-signal stability analysis is conducted on the closed-loop system formed with each of the new SWACs (full 63rd order SWACs are used) and Figure 3-39 shows curves of damping ratios of the interarea modes over increasing time delays. The figure compares three SWACs designed by considering 25 ms, 100 ms, and 250 ms time delays. The damping ratio of the local mode (mode 3) stays fixed at 5.65 % with increased time delays for the three cases. The figure shows that the maximum damping is achieved at the time delay value considered at the design stage, labelled (**A_1,B_1,C_1**) for mode 1 and (**A_2,B_2,C_2**) for mode 2. The figure also shows that, for the three controllers, the damping degrades with increased time delay from the considered value at the design stage. The damping, however, stays better than the open-loop case for time delays up to the ones labelled in the figure as (**a_1,b_1,c_1**) for mode 1 and (**a_2,b_2,c_2**) for mode 2. It can be seen also from the figure that the damping ratios decrease as well with decreased time delay from the considered value at the design stage. The damping stays better (with shorter delays down to 1 ms) than the open-loop case for the 25 ms and 100 ms based SWACs. For the 250ms-based SWAC the damping improvement is achieved with shorter delays down to the points labelled (**d_1**=103 ms) for mode 1 and (**d_2**=120 ms) for mode 2.

Table 3-15 lists the maximum time delays that each controller can tolerate for improvement in the damping above the open-loop case (above 3.08 % for mode 1 and 2.75 % for mode 2). The table shows that mode 2 is more sensitive to longer time delays than mode 1 (as can be seen also from Figure 3-39). The maximum time delay that each controller can tolerate, for improvement in damping above the open-loop system case, therefore are the ones corresponding to mode 2, i.e. maximum delays (**a_2,b_2,c_2**).

Table 3-15: Maximum time delays for damping improvement

Mode	Damping ratio	Label	Maximum (one way) delay [ms]
mode 1	ζ_1=3.08 %	**a_1**	156
		b_1	213
		c_1	371
mode 2	ζ_2=2.75 %	**a_2**	131
		b_2	206
		c_2	364

Figure 3-40, Figure 3-41, and Figure 3-42 show active power responses of the open-loop and closed-loop systems formed with the 25 ms-based SWAC, 100 ms-based SWAC, and 250 ms-based SWAC, respectively, for the maximum time delays (**a_2,b_2,c_2**). The figures show that system transient performance is maintained by the modal LQG controller under these maximum time delays. It can be concluded that the modal LQG approach is suitable for different WAMS with different signal transmission time delays. In addition the designed SWAC enhances the stability of the system in cases of increased time delays without affecting the local mode. The SWAC is therefore robust to variations in time delays regardless of the considered value at the design stage.

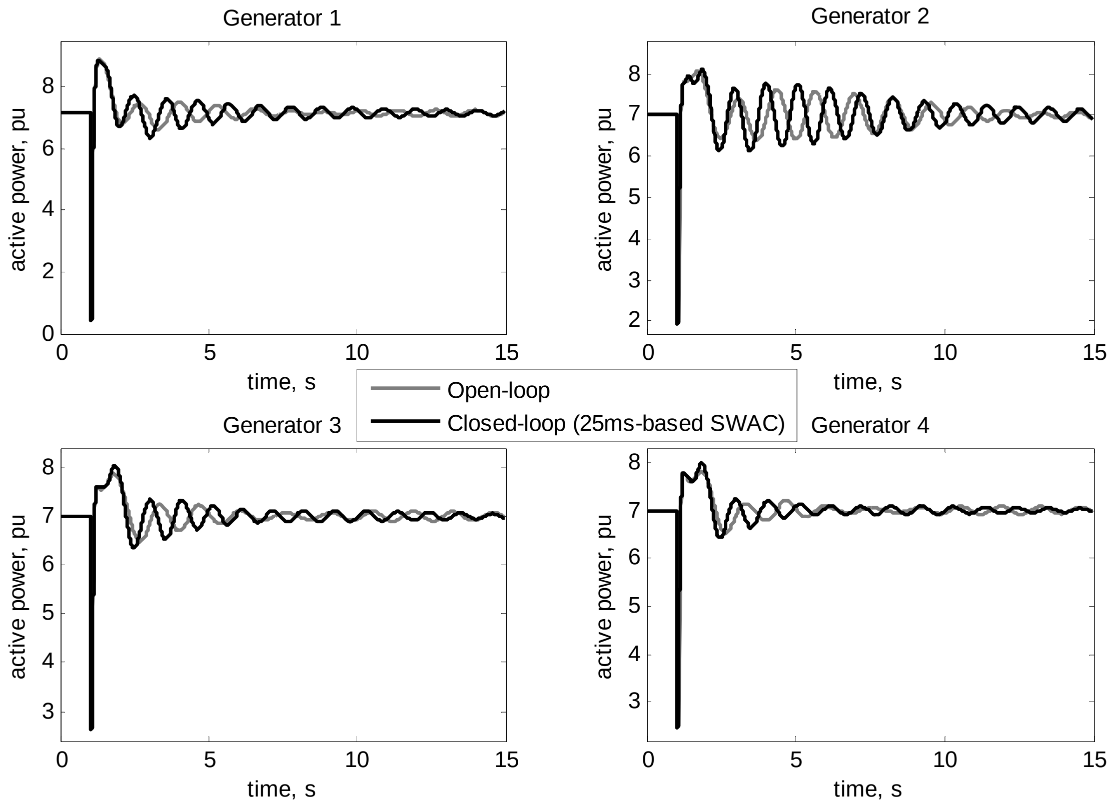

Figure 3-40: Active power responses with maximum time delay (a_2)

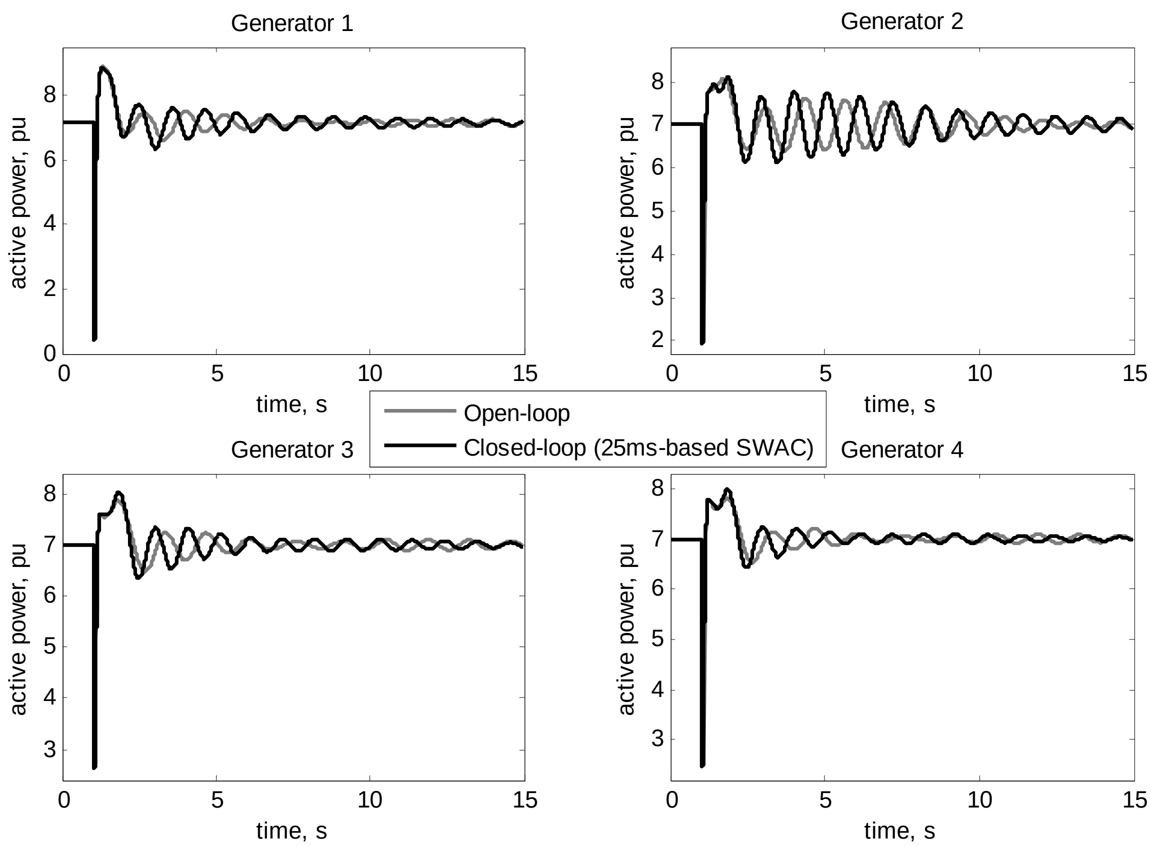

Figure 3-41: Active power responses with maximum time delay (b_2)

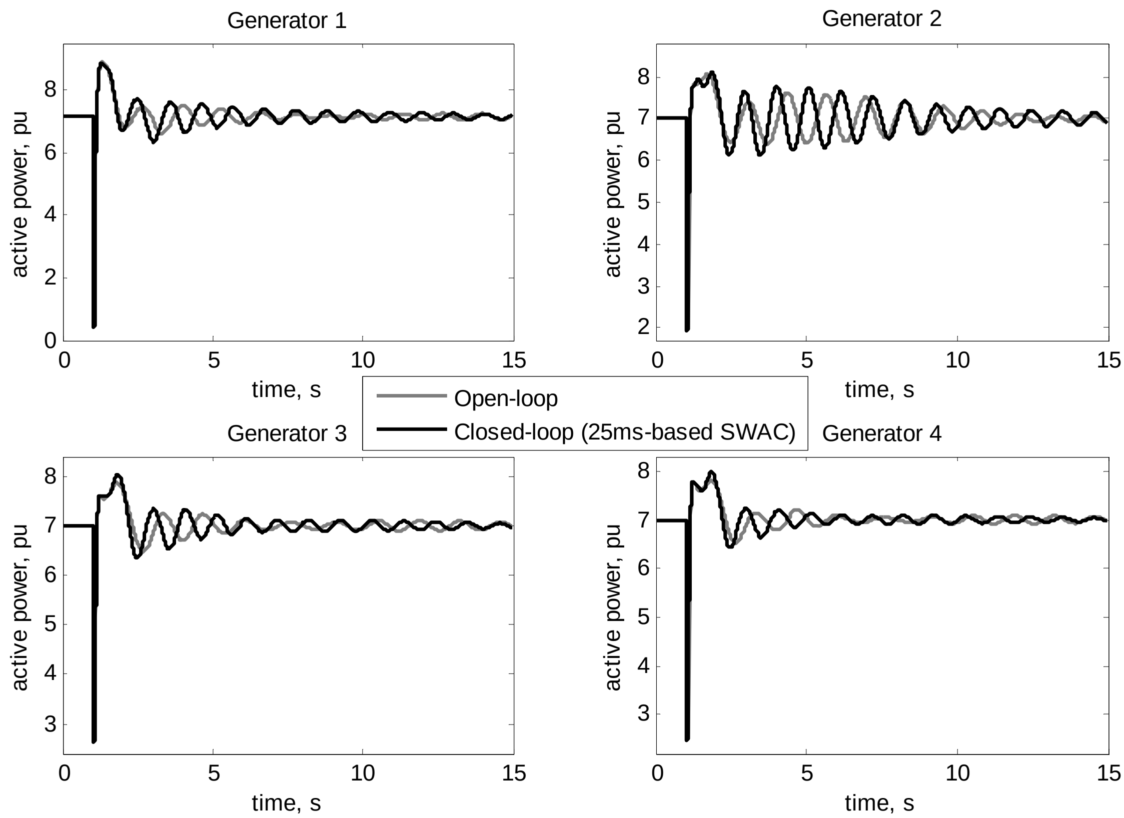

Figure 3-42: Active power responses with maximum time delay (c_2)

3.4.4.4 Robustness to Loss Failures of Communication Links

The SWAC is finally assessed for different failures of communication links used in the transmission of its input/output signals. Table 3-16 lists the closed-loop electromechanical modes for different communication link failures. It can be seen that losses of signals degrade damping ratios of the closed-loop interarea modes. The SWAC however still improves the stability of the system without affecting the local mode under these conditions. For the worst case scenario when all output and input communication links are failed to transmit signals from and to the SWAC (cases #13 and #14, respectively), the damping ratios of all the modes are the same as in the open-loop system case. The stability of the system is maintained by local PSSs in the lower level of the hierarchical control structure. Active power responses for the large disturbance under these communication failures are shown in (Figure 3-43 - Figure 3-48). The figures compare the open-loop and closed-loop system responses. It can be seen from the figures that although that damping is degraded by these failures, the SWAC satisfactorily stabilises the system in cases of large disturbances.

Table 3-16: Closed-loop electromechanical modes for different communication link failures

no.	Failed Link(s)	Mode 1 [1/s, rad/s]	ζ_1 [%]	Mode 2 [1/s, rad/s]	ζ_2 [%]	Mode 3 [1/s, rad/s]	ζ_3 [%]
1	(u_1)	-1.32±j4.63	27.38	-0.41±j4.89	8.40	-0.39±j6.90	5.65
2	(u_2)	-0.46±j4.76	9.58	-1.53±j5.06	28.99	-0.39±j6.90	5.65
3	(u_3)	-0.86±j4.54	18.50	-1.52±j5.05	28.77	-0.40±j6.90	5.76
4	(u_4)	-1.03±j4.54	22.05	-1.54±j5.06	29.09	-0.38±j6.90	5.54
5	(y_1)	-1.37±j4.66	28.20	-1.73±j5.25	31.27	-0.39±j6.90	5.65
6	(y_2)	-1.44±j4.85	28.52	-0.20±j4.96	4.00	-0.39±j6.90	5.66
7	(y_3)	-0.58±j4.62	12.54	-1.46±j4.92	28.41	-0.39±j6.90	5.71
8	(y_4)	-0.70±j4.48	15.45	-1.46±j4.89	28.70	-0.39±j6.90	5.58
9	(u_1,y_1)	-1.31±j4.64	27.22	-0.42±j4.88	8.55	-0.39±j6.90	5.65
10	(u_2,y_2)	-0.28±j4.87	5.72	-1.14±j4.93	22.55	-0.39±j6.90	5.65
11	(u_3,y_3)	-0.42±j4.56	9.10	-1.46±j4.98	28.10	-0.42±j6.95	6.07
12	(u_4,y_4)	-0.55±j4.48	12.17	-1.45±j4.91	28.30	-0.41±j6.94	5.89
13	$(u_1$-$u_4)$	-0.14±j4.49	3.08	-0.14±j4.99	2.75	-0.39±j6.90	5.65
14	$(y_1$-$y_4)$	-0.14±j4.49	3.08	-0.14±j4.99	2.75	-0.39±j6.90	5.65

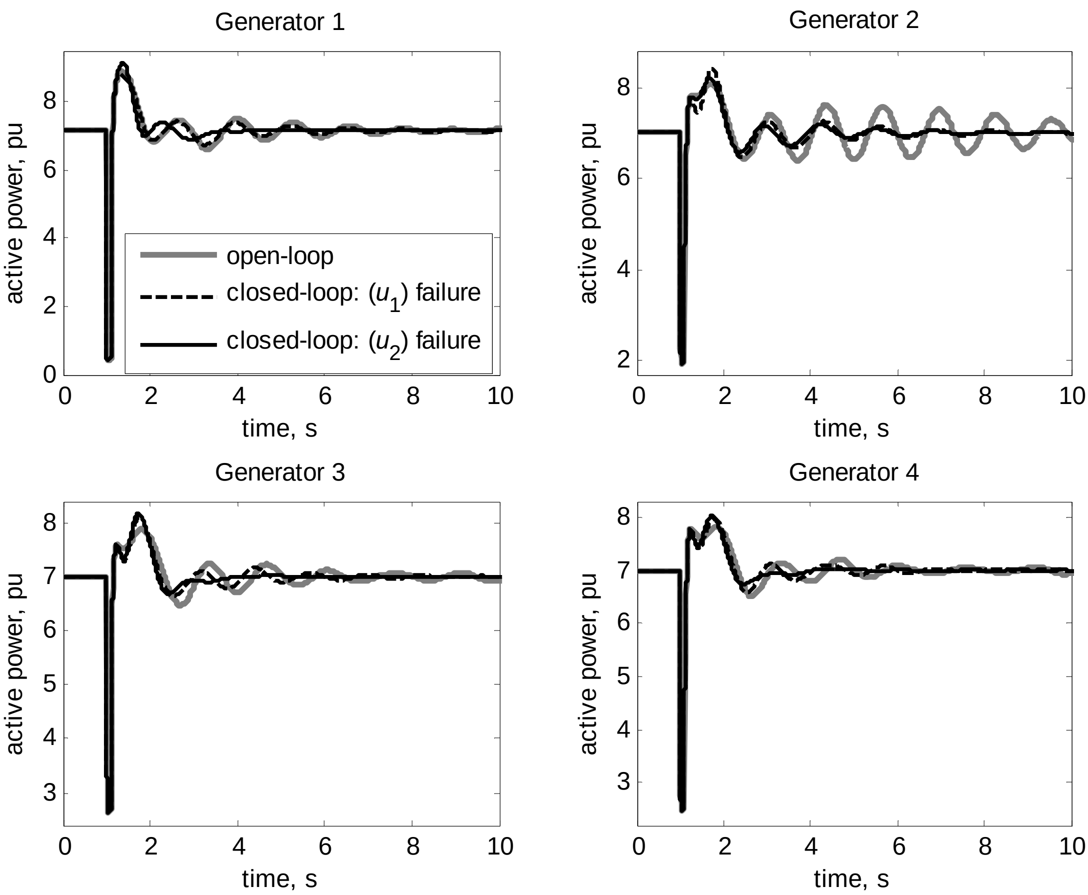

Figure 3-43: Active power responses for different losses of control signals (a)

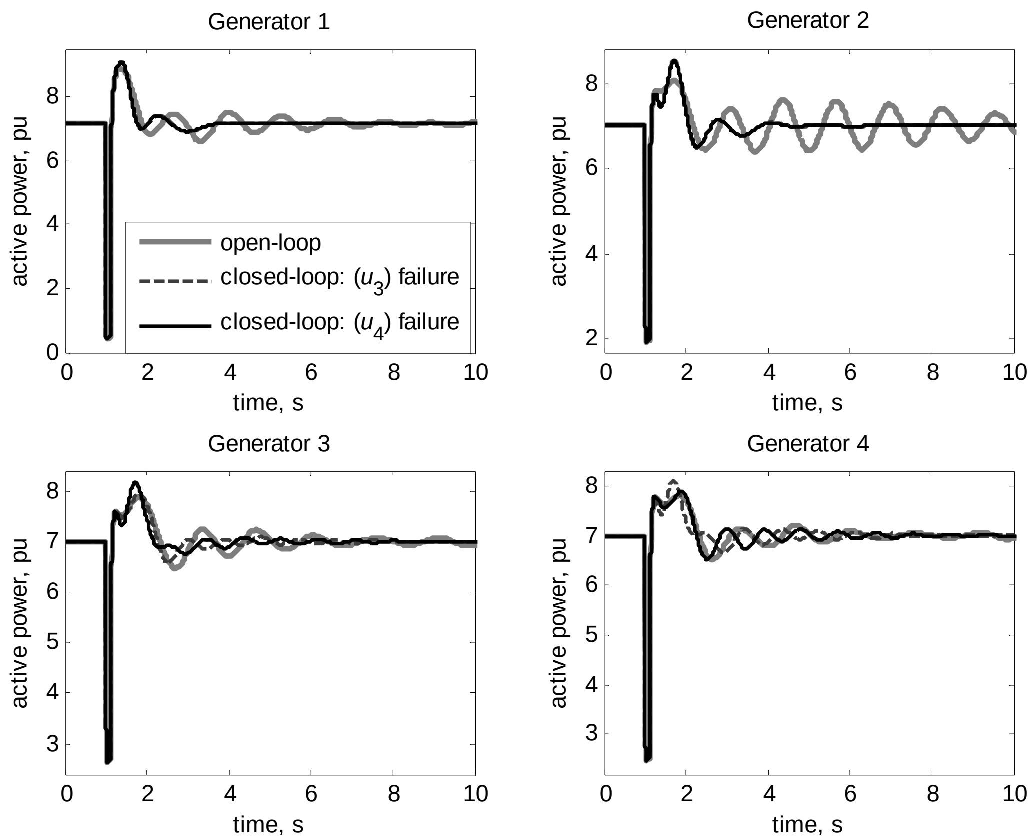

Figure 3-44: Active power responses for different losses of control signals (b)

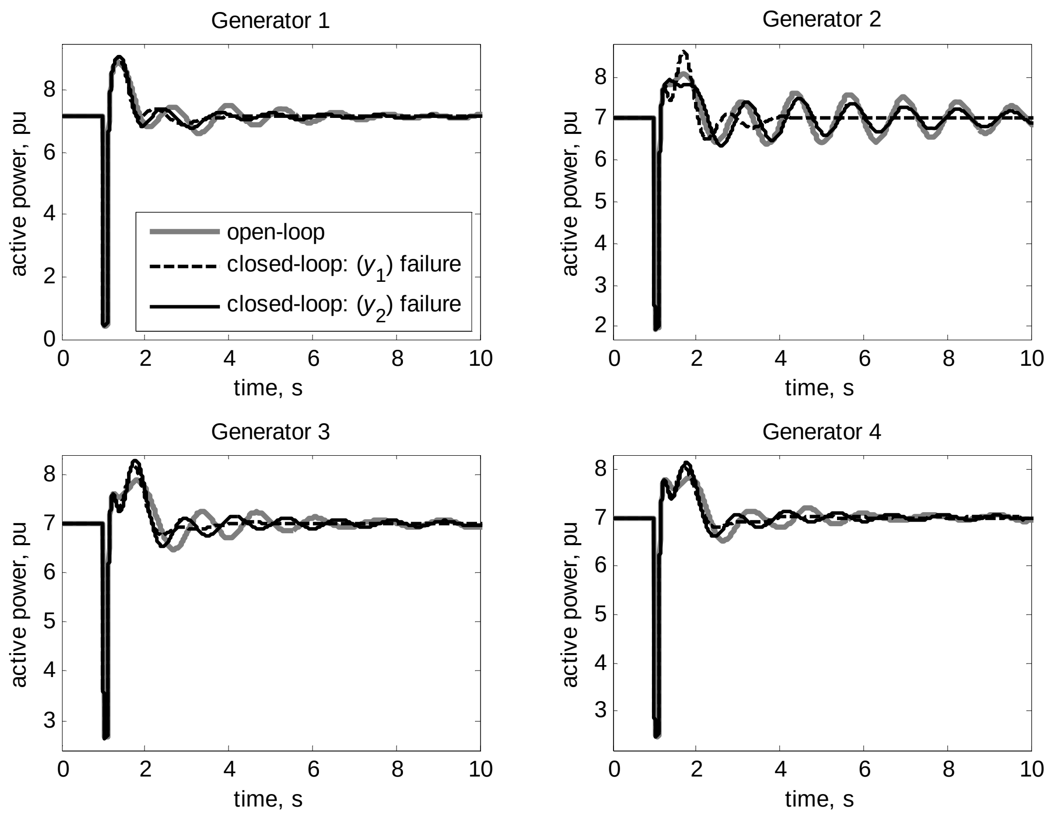

Figure 3-45: Active power responses for different losses of measurement signals (a)

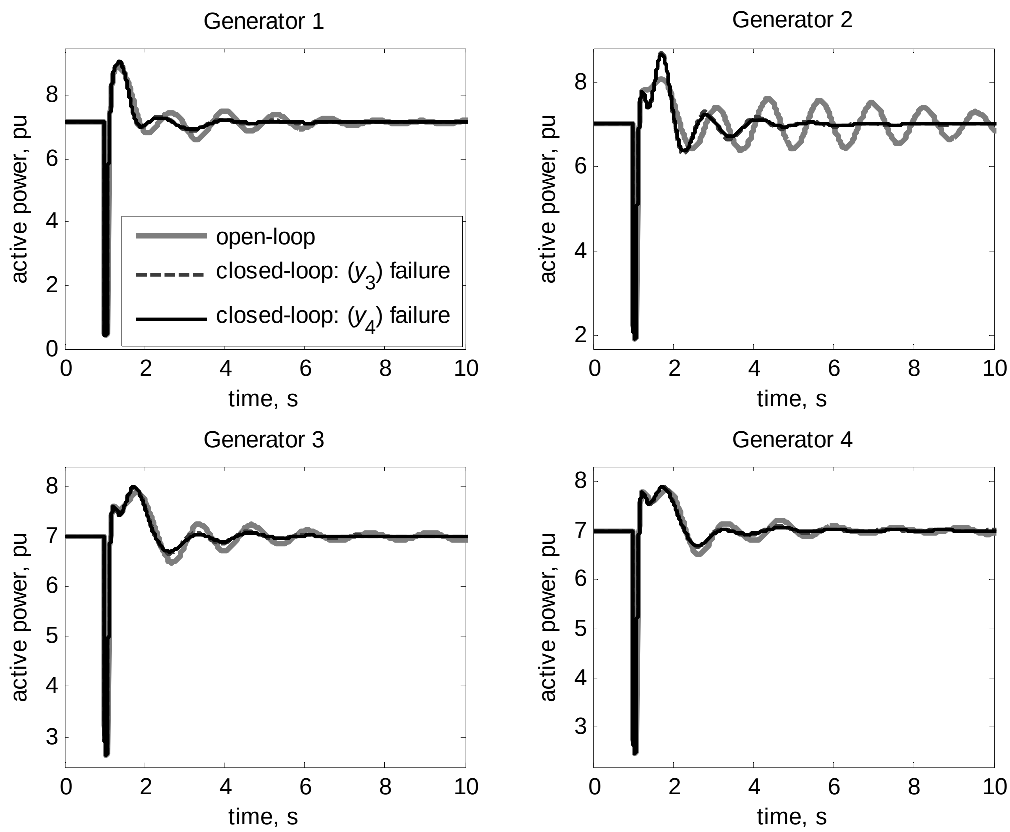

Figure 3-46: Active power responses for different losses of measurement signals (b)

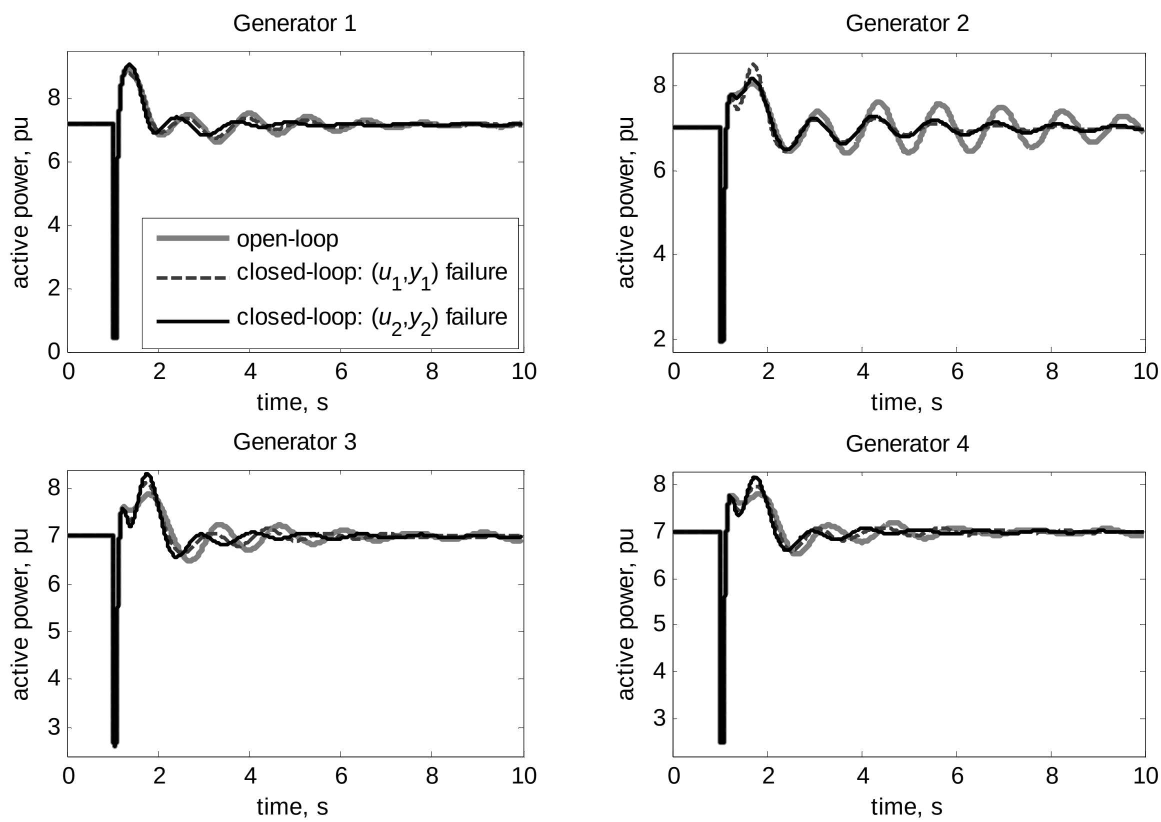

Figure 3-47: Active power responses for different losses of control and measurement signals (a)

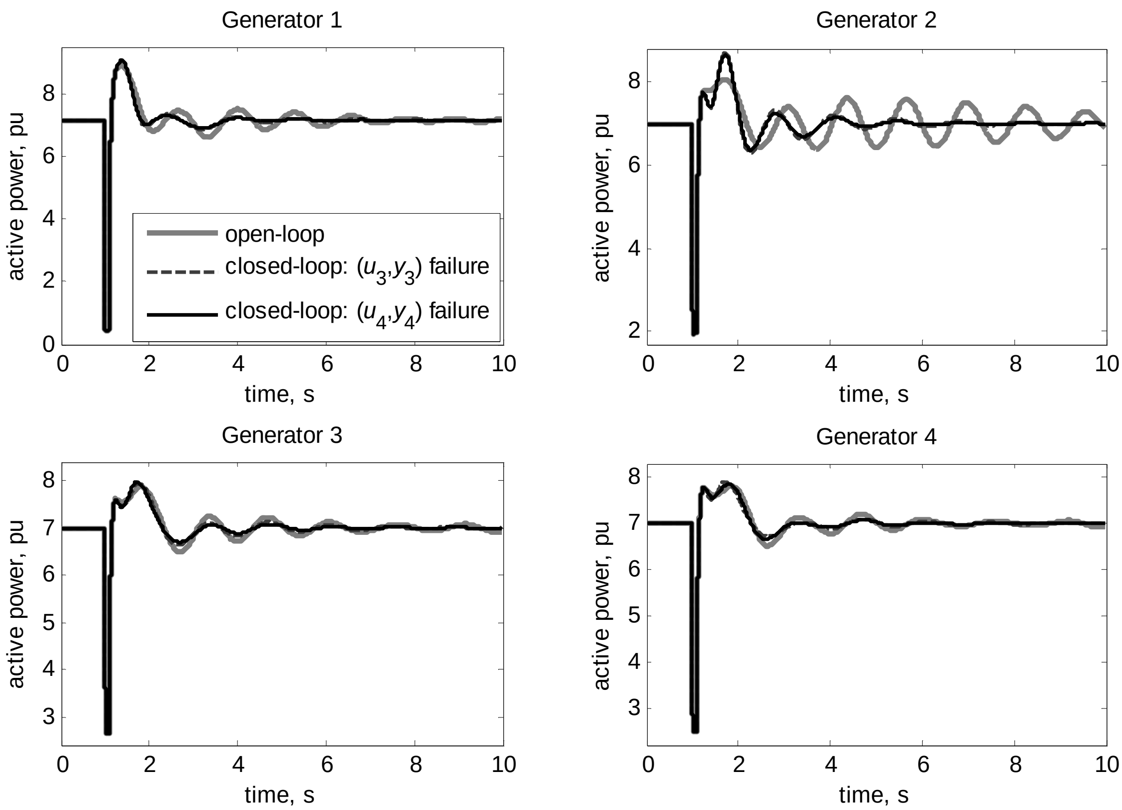

Figure 3-48: Active power responses for different losses of control and measurement signals (b)

In real WAMS, failure of transmission of measurement signals to the SWAC can be compensated by the use of signals from nearby buses [49]. For example, consider the case when communication link (y_2) is failed, the damping ratio of the closed-loop mode 2 is 4.00 % (see case #6 in Table 3-16). Lost signal θ_2 (voltage phase angle of bus 2) can be replaced by signal θ_7 (voltage phase angle of bus 7) in case communication link y_2 fails. Table 3-17 lists the resulting damping ratios of the closed-loop electromechanical modes when using the alternative signal. The same original reduced 5th order SWAC is used and is supplied with the new (alternative) signal. It can be seen that the use of the alternative signal improves the damping ratio of mode 2 considerably. Figure 3-49 shows the improvement achieved in active power responses of the closed-loop system, for the large disturbance, when using the alternative signal.

Table 3-17 also shows another example when all original measurement signals are lost (see last row in Table 3-16) and replaced by signals from adjacent buses (note that both lost signals at bus 3 and 4 are replaced by the same alternative signal at bus 9). It can be seen that the use of these alternative signals increases the damping ratios of the interarea modes. Figure 3-50 shows the improvement achieved in the transient performance of the system when using these alternative signals. It can be concluded that the high degree of effectiveness of the SWAC, designed using the modal LQG approach, can be recovered in case of multiple communication link failures by the use of alternative signals from adjacent locations.

Table 3-17: Closed-loop electromechanical modes using alternative signals

no.	Lost PMU measurement(s)	Alternative PMU measurement(s)	ζ_1 [%]	ζ_2 [%]	ζ_3 [%]
1	θ_2	-	28.52	4.00	5.54
2	θ_2	θ_7	27.10	20.57	5.65
3	(θ_1, θ_2, θ_3, θ_4)	-	3.08	2.75	5.65
4	(θ_1, θ_2, θ_3, θ_4)	(θ_8, θ_7, θ_9, θ_9)	17.83	19.56	5.71

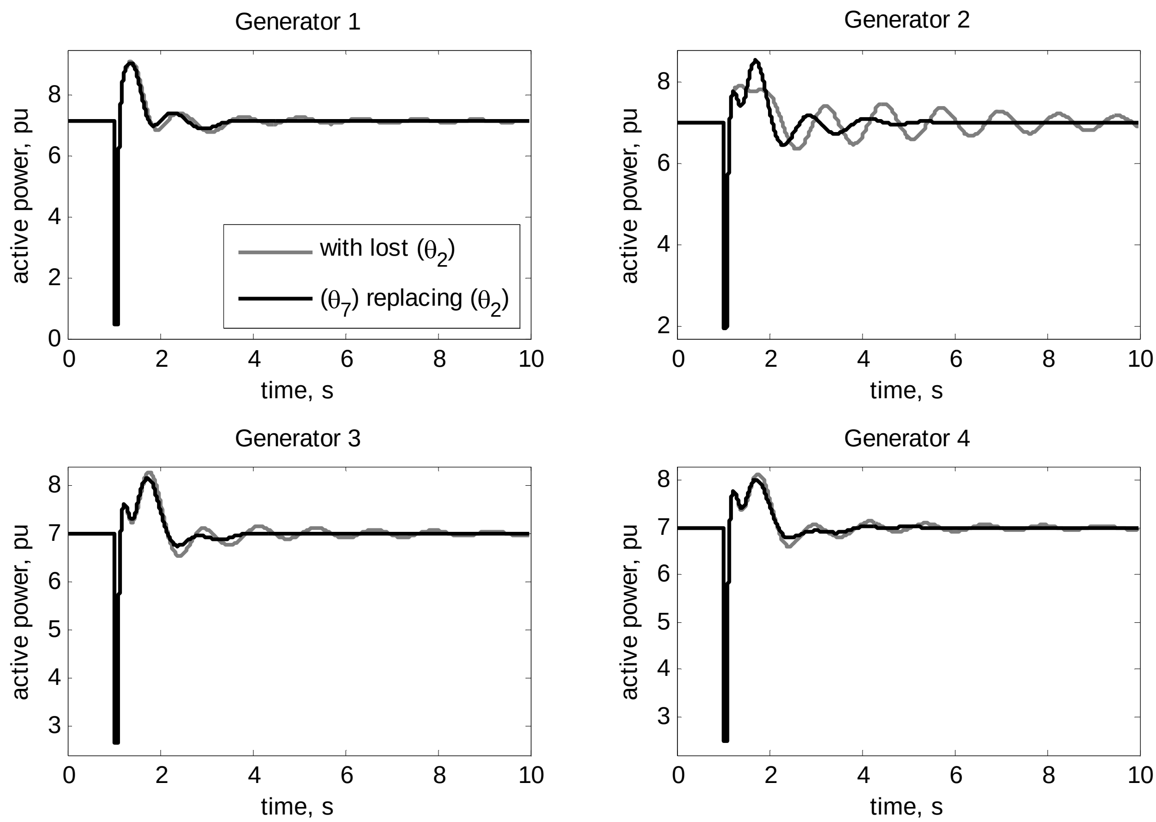

Figure 3-49: Active power responses with alternative measurement signal (a)

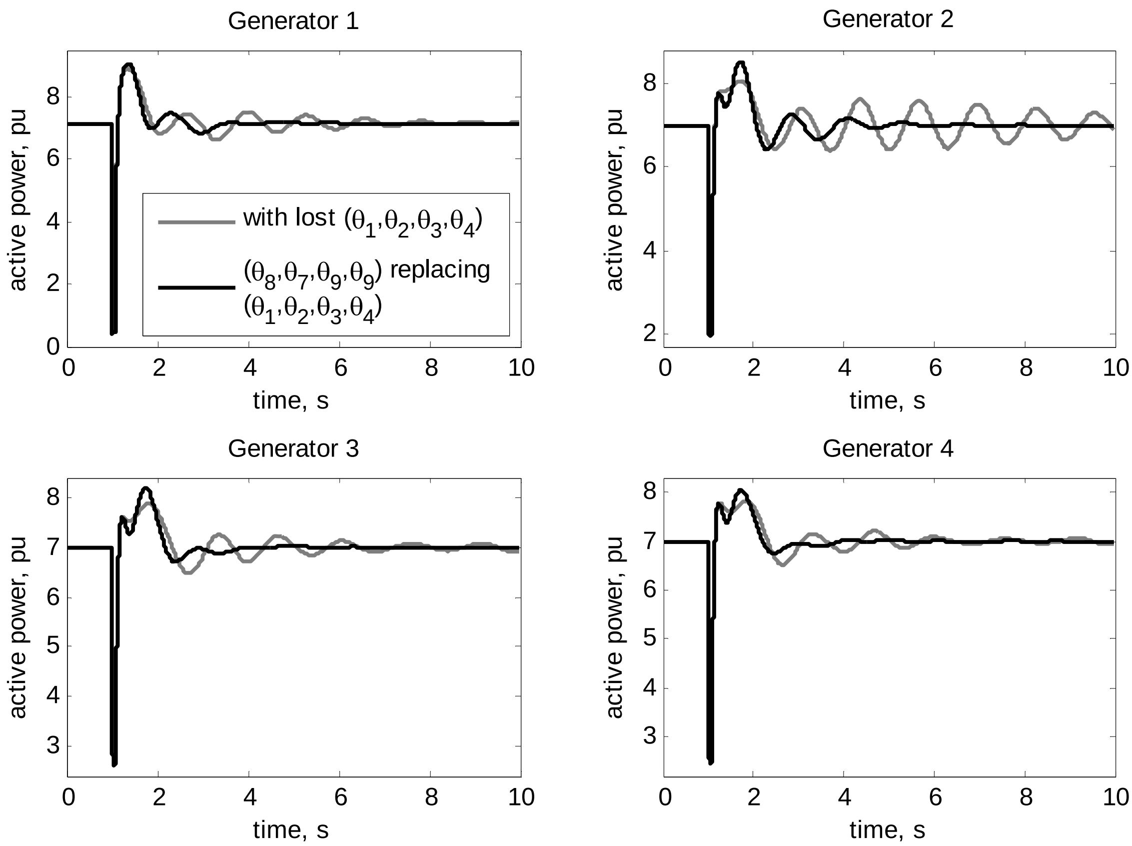

Figure 3-50: Active power responses with alternative measurement signals (b)

3.5 Summary

The modal LQG approach for design of supplementary wide-area controllers was presented. Comparisons with conventional LQG controllers showed clear advantages of using the proposed approach. It offers flexibility in adding damping to any set of modes of interest. The tuning process is simple when tackling multiple modes with minimised control efforts. The feature of leaving other modes unaltered while stabilising the lightly damped interarea modes, makes this controller highly suitable for wide-area damping control applications as many utilities hesitate to add remote signals to PSSs due to concerns regarding interference with the functionality of PSSs.

Different model order reduction scenarios were studied and it was found that the reduced order modal LQG controller is as effective as the full order controller in enhancing the system stability; thus making the proposed design approach applicable to large scale power system. Results showed good robustness properties of the modal LQG controller to changes in network topology. In addition, the modal LQG controller was effective in enhancing the system stability in cases of heavy power transfers.

Time delays encountered in the transmission of wide-area measurements and control signals were incorporated in the design approach. The 2^{nd} order Pade approximation was used due to its accuracy in modelling long time delays. Different values of time delays were considered at the design stage and the designed controller was effective in enhancing the system stability. The modal LQG approach therefore is suitable to different WAMS with different time delays. In cases of longer time delays (other than the ones considered at the design stage) improvement of system stability, though degraded, was achieved by the controller. The modal LQG controller can clearly tolerate longer time delays with adequate improvement in the system damping.

The controller's effectiveness under communication link failures was also assessed. Results showed that improvement in system stability is still maintained, though slightly degraded, by the controller. For the worst case scenario, when all signals from/to the controller are lost, the system is still controlled by local PSSs in the usual way. The use of alternative signals, from adjacent buses, instead of the lost signals however showed that the high effectiveness of the controller could be fully recovered.

4 SELECTION OF INPUT/OUTPUT SIGNALS

4.1 Introduction

This chapter presents different methods for the selection of Input/Output (I/O) signals for the supplementary wide-area controller (SWAC). The first method is based on modal observability/controllability factors analysis. The second method is based on the Sequential Orthgonalisation (SO) algorithm generalised in this thesis for the selection of both optimal input and output signals. The third method is based on combined clustering and modal factors analysis. The clustering of generators' measurements is done using a novel Principal Component Analysis (PCA) based cluster analysis technique. Each method is presented and applied to a multi-machine power system to select sets of reduced I/O signals. Results of the methods are assessed and compared using both small-signal and transient performance analysis.

4.2 Multivariable WAMS based Damping Controller

4.2.1 Input/Output Signals for Wide-area Controllers

In the hierarchical WAMS based control configuration, described in Chapter 1, the WAMS based damping controller (the SWAC) receives signals which are derived from synchronised measurements provided by PMUs installed at system buses. Due to the costs associated with the installations of PMUs, e.g. communication infrastructure costs, number of installed measurement devices should be minimised. Measurements supplied to the SWAC from all buses in the network should ideally provide full coverage of observability information in the system. With a reduced set of measurements, supplied by reduced set of PMUs important modal observability information should be highly covered by the reduced set in order to ensure effective operation of the SWAC. Redundant information between signals should also be minimised as well. Locations of system measurements (inputs to the SWAC) therefore should be optimally selected to ensure high modal observability coverage with minimal number of PMUs. The same principle of signal reduction applies similarly to the global control signals (outputs of the SWAC). Reduced control signals should be optimally selected to ensure high modal controllability coverage. Less measurement and control devices will lead to less cost for the required WAMS communication links. In addition, it leads to less control loops thus reducing the possible interactions between them and reducing complexity of the overall control system.

In WAMS based control schemes, less measurements are desirable to reduce costs of the communication links. Reduction of these measurements however is done with the aim of maximising the observability information carried by them about the interarea modes. The two problems, optimal placement of PMUs and reduction of signals, are therefore similar as they take into account the maximisation of observability information. Input signals to the wide-area controller are in fact supplied by the optimally placed PMUs.

The block diagram of a power system equipped with a multivariable SWAC is shown in Figure 4-1. Input reference signals and signal transmission time delays are not shown in the figure for simplicity. The SWAC receives reduced set of synchronised measurements $\begin{bmatrix} \boldsymbol{y}_1 & \cdots & \boldsymbol{y}_{p_r} \end{bmatrix}$ from PMUs installed at different locations in the network, processes these signals, and then sends its control signals $\begin{bmatrix} \boldsymbol{u}_1 & \cdots & \boldsymbol{u}_{m_r} \end{bmatrix}$ to different generators in the network (see Figure 1-5). The SWAC's control signals are added to the excitation system summation junction of those m_r generators. The multi-input multi-output (MIMO) SWAC therefore has p_r inputs and m_r outputs. Measurement signals are voltage phase angle at generator buses. The objective of the input and output signal selection methods is to reduce the number of measurement signals from p to p_r and the number of control signals from m to m_r, while maximising the observability and controllability, respectively, information about the modes of interest.

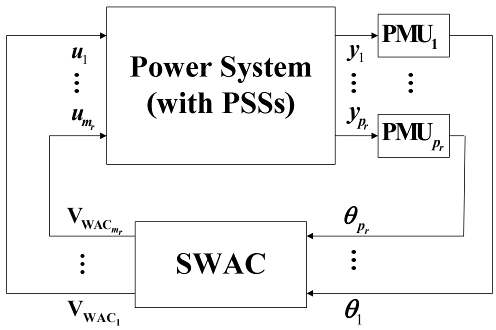

Figure 4-1: Input and output signals of the SWAC

4.2.2 Multi-machine Test System

The test system used in this study is the New England Test System (NETS) shown in Figure 4-2. The system is modified such that it has multiple interarea modes. Full system and model data are given in Appendix A. The system is modelled and linearised using Matlab/Simulink software.

The electromechanical modes of the linearised NETS and their frequencies, damping ratios, and mode shapes are listed in Table 4-1. Plots of mode shapes are shown in Appendix A. The order of the linearised system model (with time delays) is 164. Modes of interest are modes 1-3. Number of candidate measurement signals (inputs to the SWAC) p is 10. Number of candidate control signals (outputs of the SWAC) m is 10. Sets of candidate measurements and control signals are listed in Table 4-2.

4.3 Modal Factors Analysis

The methodology for selection of I/O signals using modal factors analysis is as follows: signal having the highest modal factors of observability/controllability for the modes of interest are selected as controller's inputs/outputs, respectively. For each individual mode of interest, only one signal is selected to cover that mode and minimise redundancy of information. The maximum number of selected I/O signals therefore equals the number of modes of interest. The number of signals however is reduced in cases when selected signals, with highest modal factors, are common between the considered modes of interest.

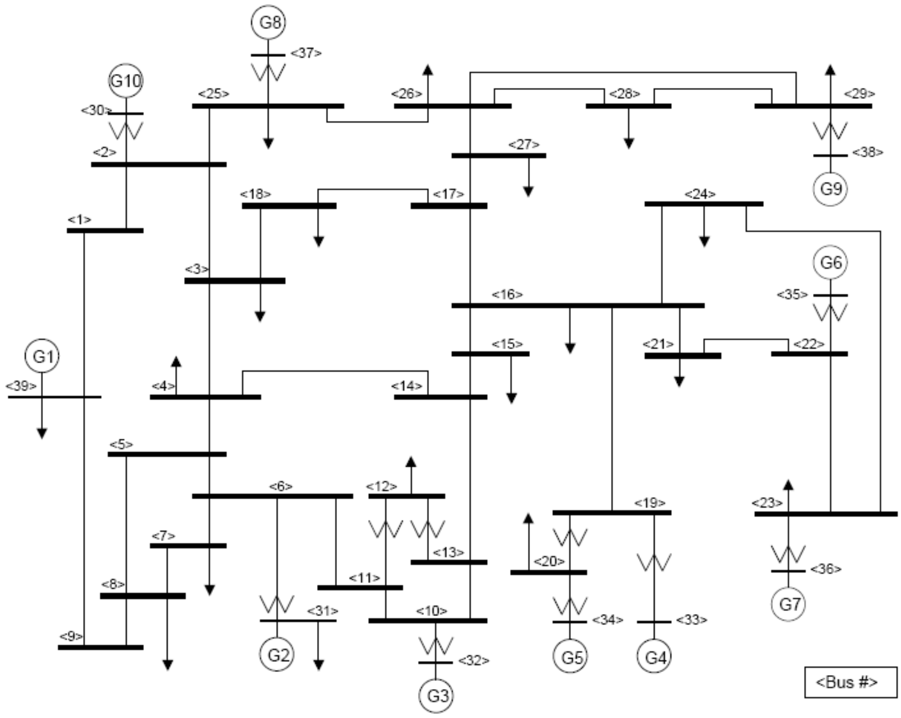

Figure 4-2: New England test system (NETS) [95]

Table 4-1: Electromechanical modes of modified NETS

Mode no.	**Mode [1/s, rad/s]**	**ζ [%]**	***f* [Hz]**	**Mode shape**
1	-0.13±j1.91	6.63	0.30	G1 vs. (G4,G5,G6,G7)
2	-0.25±j2.61	9.58	0.42	(G4,G5) vs. (G6,G7)
3	-0.37±j3.48	10.54	0.55	(G6,G7) vs. (G2,G3,G8,G9,G10)
4	-0.88±j4.30	19.96	0.68	G2 vs. (G3,G8,G9,G10)
5	-1.05±j4.98	20.66	0.79	G3 vs. (G2,G8,G9,G10)
6	-1.15±j6.10	18.52	0.97	G10 vs. (G8,G9)
7	-1.28±j6.75	18.70	1.07	G8 vs. G9
8	-1.45±j7.64	18.59	1.21	G6 vs. G47
9	-1.63±j8.42	19.03	1.34	G4 vs. G45

Table 4-2: Candidate measurement and control signals

Candidate measurements signals		Candidate control signals		Signal location
Link	**Signal**	**Link**	**Signal**	
y_1	θ_{39}	u_1	V_{WAC1}	G1
y_2	θ_{31}	u_2	V_{WAC2}	G2
y_3	θ_{32}	u_3	V_{WAC3}	G3
y_4	θ_{33}	u_4	V_{WAC4}	G4
y_5	θ_{34}	u_5	V_{WAC5}	G5
y_6	θ_{35}	u_6	V_{WAC6}	G6
y_7	θ_{36}	u_7	V_{WAC7}	G7
y_8	θ_{37}	u_8	V_{WAC8}	G8
y_9	θ_{38}	u_9	V_{WAC9}	G9
y_{10}	θ_{30}	u_{10}	V_{WAC10}	G10

Modal observability factors for the modes of interest are listed in Table 4-3. For each individual mode of interest, the signal with the largest modal observability factor (shown in bold face in Table 4-3) is selected as input signal to the SWAC. Note that measurement signal from location (G5) has the largest modal observability factor for both of modes 1 and 2. For mode 3 the largest modal observability factor is for the signal at location G6. The selected input signals to the SWAC therefore are two signals from locations G5 and G6 (measured by PMUs).

Table 4-3: Magnitudes of modal observability factors (normalised to the highest)

Generator	Mode 1	Mode 2	Mode 3
G1	0.16	0.35	0.82
G2	0.08	0.08	0.43
G3	0.09	0.07	0.46
G4	0.97	0.95	0.87
G5	**1.00**	**1.00**	0.88
G6	0.41	0.76	**1.00**
G7	0.41	0.76	0.99
G8	0.09	0.09	0.52
G9	0.12	0.08	0.48
G10	0.08	0.10	0.53

The same approach is applied for the selection of output signals of the SWAC using the modal controllability factors (listed in Table 4-4). Control signal at location G7 has the largest modal controllability factor for both of modes 1 and 2. For mode 3 the largest modal controllability factor is for the signal at location G6. The selected output signals from the SWAC therefore are two signals sent to locations G7 and G6. Sets of reduced input and output signals for the SWAC selected using the modal factors analysis are listed in Table 4-5.

Table 4-4: Magnitudes of modal controllability factors (normalised to the highest)

Generator	Mode 1	Mode 2	Mode 3
G1	0.47	0.15	0.23
G2	0.06	0.09	0.38
G3	0.10	0.12	0.32
G4	0.94	0.37	0.12
G5	0.92	0.32	0.44
G6	0.28	0.53	**1.00**
G7	**1.00**	**1.00**	0.23
G8	0.15	0.17	0.90
G9	0.17	0.24	0.57
G10	0.06	0.07	0.15

Table 4-5: Locations of selected I/O signals using modal factors analysis

Locations of measurement signals	Locations of control signals
(G5, G6)	(G6, G7)

4.4 The Sequential Orthogonalisation Algorithm

The Sequential Orthogonalisation (SO) algorithm, originally introduced in [70], was applied to the optimal placement of angle transducers in power systems. Research conducted at Hydro-Quebec allowed a minimum number of PMUs to be optimally placed on the system in order to collectively maximise the amount of dynamic information contained in the wide-area measurements [3]. The algorithm places GPS based monitoring devices so as to maximise their sensitivity to the lightly damped interarea modes while minimising their sensitivity to the more heavily damped local modes. The algorithm ensures that these devices are placed so as to give the greatest coverage of the various interarea modes as possible giving modal estimates with a high degree of precision.

4.4.1 The SO Algorithm

4.4.1.1 Selection of First Location

The SO algorithm [70] starts by constructing the *mode observability matrix* $\boldsymbol{H}$, whose entries are the modal observability factors of the linearised power system. From the matrix $\boldsymbol{H}$ the following two matrices are formed,

- $p\times n_I$ matrix $\boldsymbol{H_I}$ whose columns are equal to the columns of $\boldsymbol{H}$ corresponding to the interarea modes.
- $p\times n_L$ matrix $\boldsymbol{H_L}$ whose columns are equal to the columns of $\boldsymbol{H}$ corresponding to the local modes.

where $(n_I/2)$ is number of interarea modes, $(n_L/2)$ is number of local modes, and p is number of system outputs (measurements). System outputs are voltage angles measured at each bus (location) in the system. Then a weighting factor $\boldsymbol{w_i}$ is computed as follows

$$\boldsymbol{w_i} = \boldsymbol{\varepsilon} + \frac{\|\boldsymbol{h_{Li}}\|_2}{\|\boldsymbol{h_{Ii}}\|_2} \tag{4.1}$$

where $\boldsymbol{h_{Li}}$ is the ith row of $\boldsymbol{H_L}$ and $\boldsymbol{h_{Ii}}$ is the ith row of $\boldsymbol{H_I}$, $\boldsymbol{\varepsilon}$ is a constant determining the local mode sensitivity, and $\|\ \|_2$ is the Euclidean norm of a vector. The higher the value of $\boldsymbol{\varepsilon}$, the higher toleration of local modes effect.

The weighting factor $\boldsymbol{w_i}$ is computed for each of the p outputs. Then each row of $\boldsymbol{H_I}$ is divided by the corresponding weighting factor. This division will yield a weighted modal observability of interarea modes for each output. Let the modified rows of $\boldsymbol{H_I}$ be grouped to form a $p\times n_{\mathrm{I}}$ matrix $\boldsymbol{Q}$. Then the output having the largest weighted modal observability of the interarea modes is determined by ranking the Euclidean norms of rows of $\boldsymbol{Q}$, i.e. $\|\boldsymbol{q}_i\|_2$. Location of this output is the first selection and will be called the reference location.

The selection criterion for subsequent locations is such that the total set of selected optimal locations should give as much observability information as possible about interarea modes. The mode observation equation used with minimum p_r output selections will be

$$\boldsymbol{y}_{p_r} = \boldsymbol{J}\boldsymbol{z}_{ia} \tag{4.2}$$

where $\boldsymbol{y}_{p_r}$ is the vector of selected outputs, $\boldsymbol{z}_{ia}$ is a vector of modal states corresponding to the interarea modes, and $\boldsymbol{J}$ is a ($p_r \times m_I$) matrix formed from the elements of $\boldsymbol{H}$ whose row numbers correspond to the selected output locations and whose column numbers correspond to the interarea modes.

It is desirable that modal estimates obtained from the solution of (4.2) for $\boldsymbol{z}_{ia}$ be as precise as possible. In other words the condition number of $\boldsymbol{J}$ must be as low as possible so it will be invertible [88]. Mathematically, a low condition number means that the rows are linearly independent and the cross correlation between them is small. Each row of $\boldsymbol{Q}$ is a multi-dimensional vector. In other words, it contains observability information in multi-space n_I directions. To avoid redundancy of observability information between measurements, and having as much observability information as possible, it is logical for the second selected location to have its information in a far away and different direction than the reference location. The most far away direction in multi-space is the *orthogonal* direction. The degree of how far away two vectors are in terms of their directions could be computed using vector orthogonal projection.

4.4.1.2 Illustrative Example on Vector Orthogonal Projection

Consider the 2-dimensional row vectors $\boldsymbol{a}$ and $\boldsymbol{b}$ (where both are real) shown in Figure 4-3. The in-phase projection component of $\boldsymbol{a}$ onto vector $\boldsymbol{b}$ is

$$\boldsymbol{\beta} = \lambda \boldsymbol{b} \tag{4.3}$$

where λ is a scalar. The orthogonal projection component is computed as follows

$$\boldsymbol{\gamma} = \boldsymbol{a} - \boldsymbol{\beta} = \boldsymbol{a} - \lambda \boldsymbol{b} \tag{4.4}$$

The angle $\boldsymbol{\delta}(\boldsymbol{a},\boldsymbol{b})$ is computed as follows

$$\boldsymbol{\delta}(\boldsymbol{a},\boldsymbol{b}) = \mathbf{cos}^{-1}\left(\frac{\boldsymbol{a} \cdot \boldsymbol{b}^{\boldsymbol{T}}}{\|\boldsymbol{a}\|_2 \, \|\boldsymbol{b}\|_2} \right) \tag{4.5}$$

where $\| \ \|_2$ stands for the Euclidean norm of a vector. Since $\boldsymbol{\delta}(\boldsymbol{\gamma},\boldsymbol{b}) = 90^\circ$, then (4.5) leads to

$$\gamma \cdot \boldsymbol{b}^T = 0 \tag{4.6}$$

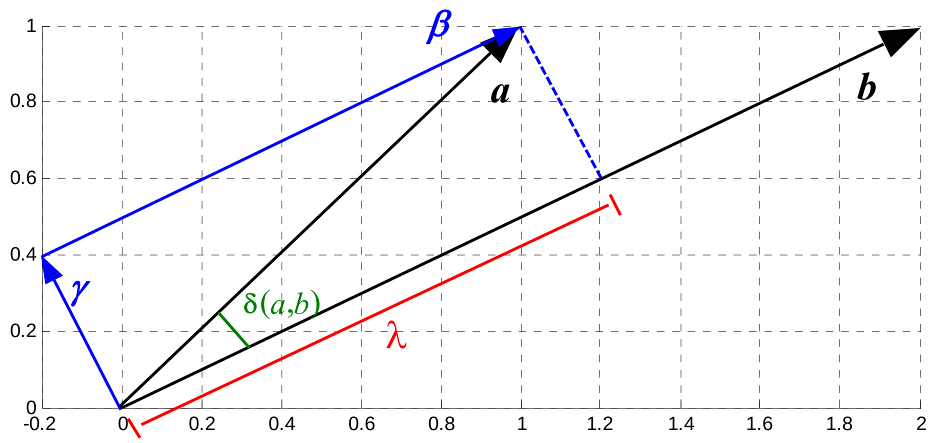

Figure 4-3: Projection of *a* onto *b* in 2-dimensional space

Substituting (4.4) into (4.6) yields

$$\boldsymbol{ab}^T - \lambda \boldsymbol{bb}^T = \boldsymbol{ab}^T - \lambda\left(\|\boldsymbol{b}\|_2\right)^2 = 0$$

$$\Rightarrow \lambda = \frac{\boldsymbol{ab}^T}{\left(\|\boldsymbol{b}\|_2\right)^2} \tag{4.7}$$

Then (4.3) becomes

$$\beta = \frac{\left(\boldsymbol{ab}^T\right)\boldsymbol{b}}{\left(\|\boldsymbol{b}\|_2\right)^2} \tag{4.8}$$

and (4.4) becomes

$$\gamma = \boldsymbol{a} - \frac{\left(\boldsymbol{ab}^T\right)\boldsymbol{b}}{\left(\|\boldsymbol{b}\|_2\right)^2} \tag{4.9}$$

For an orthogonal projection of vector $\boldsymbol{a}$ onto a hyper plane constituted by N vectors $\boldsymbol{b}_j$, (4.9) is generalised to

$$\gamma = \boldsymbol{a} - \sum_{j=1}^{N} \frac{\left(\boldsymbol{ab}_j^T\right)\boldsymbol{b}_j}{\left(\|\boldsymbol{b}_j\|_2\right)^2} \tag{4.10}$$

When $\boldsymbol{a}$ and $\boldsymbol{b}$ are complex, then (4.5), (4.7)-(4.10) become

$$\delta(\boldsymbol{a},\boldsymbol{b}) = \cos^{-1}\left(\frac{|\boldsymbol{a}\cdot\boldsymbol{b}^*|}{\|\boldsymbol{a}\|_2\,\|\boldsymbol{b}\|_2}\right) \tag{4.11}$$

$$\lambda = \frac{\boldsymbol{a}\boldsymbol{b}^*}{\left(\|\boldsymbol{b}\|_2\right)^2} \tag{4.12}$$

$$\boldsymbol{\beta} = \frac{\left(\boldsymbol{a}\boldsymbol{b}^*\right)\boldsymbol{b}}{\left(\|\boldsymbol{b}\|_2\right)^2} \tag{4.13}$$

$$\boldsymbol{\gamma} = \boldsymbol{a} - \frac{\left(\boldsymbol{a}\boldsymbol{b}^*\right)\boldsymbol{b}}{\left(\|\boldsymbol{b}\|_2\right)^2} \tag{4.14}$$

$$\boldsymbol{\gamma} = \boldsymbol{a} - \sum_{j=1}^{N}\frac{\left(\boldsymbol{a}\boldsymbol{b}_j^*\right)\boldsymbol{b}_j}{\left(\|\boldsymbol{b}_j\|_2\right)^2} \tag{4.15}$$

where $|\;|$ stands for the magnitude (modulus) of a complex scalar, and the superscript $*$ stands for the complex conjugate transpose of a vector.

Table 4-6 shows a numerical example on orthogonal projection for real vectors and is illustrated in Figure 4-3. Table 4-7 show a numerical example on orthogonal projection for complex vectors. Values of angles shown in the last two columns in both tables verify the accuracy of the projection process.

Table 4-6: Numerical example on orthogonal projection for real vectors

$\boldsymbol{a}$	$\boldsymbol{b}$	$\delta(\boldsymbol{a},\boldsymbol{b})$ using (4.5)	λ using (4.7)	$\boldsymbol{\beta}$ using (4.8)	$\boldsymbol{\gamma}$ using (4.9)	$\delta(\boldsymbol{\beta},\boldsymbol{b})$ using (4.5)	$\delta(\boldsymbol{\gamma},\boldsymbol{b})$ using (4.5)
$\begin{bmatrix}2\\1\end{bmatrix}^T$	$\begin{bmatrix}1\\1\end{bmatrix}^T$	18.43°	0.6	$\begin{bmatrix}1.2\\0.6\end{bmatrix}^T$	$\begin{bmatrix}-0.2\\0.4\end{bmatrix}^T$	0°	90°

Table 4-7: Numerical example on orthogonal projection for complex vectors

$\boldsymbol{a}$	$\boldsymbol{b}$	$\delta(\boldsymbol{a},\boldsymbol{b})$ using (4.11)	λ using (4.12)	$\boldsymbol{\beta}$ using (4.13)	$\boldsymbol{\gamma}$ using (4.14)	$\delta(\boldsymbol{\beta},\boldsymbol{b})$ using (4.11)	$\delta(\boldsymbol{\gamma},\boldsymbol{b})$ using (4.11)
$\begin{bmatrix}4+\mathrm{j}\\1-\mathrm{j}\end{bmatrix}^T$	$\begin{bmatrix}-5-\mathrm{j}3\\-5+\mathrm{j}3\end{bmatrix}^T$	26.10°	$-1.63-\mathrm{j}0.47$	$\begin{bmatrix}-6.05-\mathrm{j}3.53\\-2.11+\mathrm{j}1.16\end{bmatrix}^T$	$\begin{bmatrix}1.05+\mathrm{j}0.53\\-2.89+\mathrm{j}1.84\end{bmatrix}^T$	0°	90°

4.4.1.3 Selection of Subsequent Locations

Based on orthogonal projection theory, the row vectors chosen in $\boldsymbol{J}$ should be orthogonal as much as possible. This means that in choosing the subsequent *i*th location it should be the one whose weighted modal observability, i.e. $\|\boldsymbol{q}_i\|_2$, is the most orthogonal, among other un-selected locations, to the weighted modal observability of each of the *i*-1 locations previously selected. Orthogonalisation of vectors is done using the *Gram-Schmidt* orthogonalisation process [96]. The orthogonal projection component is computed as follows

$$\boldsymbol{\theta}_i = \boldsymbol{q}_i - \sum_{j \in S} \frac{\left(\boldsymbol{q}_i \boldsymbol{\theta}_j^*\right) \boldsymbol{\theta}_j}{\left(\|\boldsymbol{\theta}_j\|_2\right)^2} \tag{4.16}$$

where S is the set containing the previously selected locations, $\boldsymbol{q_i}$ is row vector of matrix $\boldsymbol{Q}$ corresponding to unselected location $i \notin S$, and $\boldsymbol{\theta}_j$ is the orthogonal projection component of row $\boldsymbol{q_j}$ corresponding to previously selected $j \in S$ locations. For the reference location $\boldsymbol{\theta}_1 = \boldsymbol{q}_1$. The in-phase projection component, denoted $\boldsymbol{\alpha}_{ij}$, of the *i*th unselected location onto the orthogonal projection $\boldsymbol{\theta}_j$ of previously selected locations is computed as follows

$$\boldsymbol{\alpha}_{ij} = \frac{\left(\boldsymbol{q}_i \boldsymbol{\theta}_j^*\right) \boldsymbol{\theta}_j}{\left(\|\boldsymbol{\theta}_j\|_2\right)^2} \tag{4.17}$$

The subsequent selected location is determined such that it has the highest orthogonal projection component $\boldsymbol{\theta}_i$ among other candidate locations. The orthogonal projection component, however, depend on the magnitude of $\boldsymbol{q_i}$, i.e. $\|\boldsymbol{q}_i\|_2$. Note that a high value of $\boldsymbol{\theta}_j$ corresponds to a low value of $\boldsymbol{\alpha}_{ij}$ and vice versa. The relative projection, denoted $\hat{\boldsymbol{\alpha}}_{ij}$, therefore is used to select the subsequent location and is computed as follows

$$\hat{\boldsymbol{\alpha}}_{ij} = \frac{\boldsymbol{\alpha}_{ij}}{\boldsymbol{\theta}_i} \tag{4.18}$$

The *i*th location to be selected is the one which minimises $\max\limits_{j \in S} \|\hat{\boldsymbol{\alpha}}_{ij}\|$. Thus, ensuring the algorithm will reduce the cross correlation of modal observability information between selected locations. The procedure continues in selecting locations *sequentially*. A location having a very low relative in-phase projection, i.e. $\hat{\alpha}_{ij}$, onto the set of previously selected locations has new, non-redundant, observability information. As a result, the condition number of $\boldsymbol{J}$ is improved and consequently maximises the precision of the estimates of the modal states. When the rest of unselected locations have high relative in-phase projections then they will add little, i.e. high redundancy, to the observability information carried by the previously selected set of locations. The condition number of $\boldsymbol{J}$ will increase in this case due to the high redundancy in observability information by the last selection. The information redundancy measure used to stop the selection process at this point is the rise in the condition number of the observation matrix $\boldsymbol{J}$.

4.4.1.4 Upper-bound of Condition Number

Recall the observation matrix $\boldsymbol{J}$ which consists of the selected rows of the inter-area modal response matrix, $\boldsymbol{H_I}$. Size of $\boldsymbol{J}$ is assumed as $N\times N$. The matrix $\boldsymbol{J}$ may be decomposed into the product of a lower triangular matrix $\boldsymbol{K}$ and a matrix $\boldsymbol{F}$ whose rows form an orthonormal basis set for the row space of $\boldsymbol{J}$, as

$$\boldsymbol{J} = \boldsymbol{K}\boldsymbol{F} \tag{4.19}$$

The diagonal element of the ith row of $\boldsymbol{K}$, i.e. θ_i, gives the component of row i of $\boldsymbol{J}$ which is orthogonal to the orthogonal directions of previous i-1 rows, and the off-diagonal elements give the components of row i of $\boldsymbol{J}$ which lie in the directions of the diagonal elements of the previous i-1 rows. Therefore $\boldsymbol{K}$ is composed as the following

$$\boldsymbol{K} = \begin{bmatrix} \theta_1 & & & & \\ \alpha_{2,1} & \theta_2 & & & \\ \alpha_{3,1} & \alpha_{3,2} & \theta_3 & & \\ \vdots & & & \ddots & \\ \alpha_{N,1} & \alpha_{N,2} & \cdots & \alpha_{N,N-1} & \theta_N \end{bmatrix} \tag{4.20}$$

If the rows of $\boldsymbol{J}$ were perfectly orthogonal then $\boldsymbol{K}$ would be purely diagonal. Since $\boldsymbol{F}$ is an orthonormal matrix then

$$\boldsymbol{c}(\boldsymbol{J}) = \boldsymbol{c}(\boldsymbol{K}) \tag{4.21}$$

where $\boldsymbol{c}$ stands for the condition number. Thus invertibility of $\boldsymbol{J}$ will be dependent on the condition number of $\boldsymbol{K}$. The lower triangular matrix $\boldsymbol{K}$ may be described as the product of diagonal matrix $\boldsymbol{D}$ and a unit lower triangular matrix $\boldsymbol{L}$ as follows

$$\boldsymbol{K} = \boldsymbol{D}\boldsymbol{L} \tag{4.22}$$

where

$$\boldsymbol{D} = \begin{bmatrix} \theta_1 & & & & \\ & \theta_2 & & & \\ & & \theta_3 & & \\ & & & \ddots & \\ & & & & \theta_N \end{bmatrix} \tag{4.23}$$

$$\boldsymbol{L} = \begin{bmatrix} 1 & & & & \\ \hat{\alpha}_{2,1} & 1 & & & \\ \hat{\alpha}_{3,1} & \hat{\alpha}_{3,2} & 1 & & \\ \vdots & & & \ddots & \\ \hat{\alpha}_{N,1} & \hat{\alpha}_{N,2} & \cdots & \hat{\alpha}_{N,N-1} & 1 \end{bmatrix} \tag{4.24}$$

$$\hat{\alpha}_{ij} = \frac{\alpha_{ij}}{\theta_j} \tag{4.25}$$

Now the condition number of $\boldsymbol{K}$, $\boldsymbol{c}(\boldsymbol{K})$ is defined as

$$\boldsymbol{c}(\boldsymbol{K}) = \|\boldsymbol{K}\| \; \|\boldsymbol{K}^{-1}\| \tag{4.26}$$

where $\|\boldsymbol{K}\|$ refers to any matrix norm (see [97], pp. 265). The infinity norm will be used here without loss of generality. The infinity norm of $\boldsymbol{K}$, $\|\boldsymbol{K}\|_\infty$, is equal to the maximum absolute row sum of $\boldsymbol{K}$, i.e.

$$\|\boldsymbol{K}\|_\infty = \max_i \sum_{j=1}^{N} |k_{ij}| \tag{4.27}$$

Now since

$$\|\boldsymbol{AB}\| \le \|\boldsymbol{A}\| \|\boldsymbol{B}\| \tag{4.28}$$

Then (4.22) becomes

$$\|\boldsymbol{K}\|_\infty \le \|\boldsymbol{D}\|_\infty \|\boldsymbol{L}\|_\infty \tag{4.29}$$

and

$$\left\|\boldsymbol{K}^{-1}\right\|_{\infty} \leq \left\|\boldsymbol{D}^{-1}\right\|_{\infty} \left\|\boldsymbol{L}^{-1}\right\|_{\infty} \tag{4.30}$$

where

$$\left\|\boldsymbol{D}\right\|_{\infty} = \left\|\boldsymbol{\theta}_{\mathbf{max}}\right\| \text{ and } \left\|\boldsymbol{D}^{-1}\right\|_{\infty} = \frac{1}{\left\|\boldsymbol{\theta}_{\mathbf{min}}\right\|} \tag{4.31}$$

The matrix $\boldsymbol{L}$ can be decomposed into the product of N elementary triangular matrices $\boldsymbol{L_j}$ (see [98], pp. 3-5) as follows

$$\boldsymbol{L} = \boldsymbol{L}_1\left(\boldsymbol{l}_1\right)\boldsymbol{L}_2\left(\boldsymbol{l}_2\right)\cdots\boldsymbol{L}_N\left(\boldsymbol{l}_N\right) \tag{4.32}$$

where the elementary triangular matrices are defined as

$$\boldsymbol{L}_j\left(\boldsymbol{l}_j\right) = \boldsymbol{I}_N - \boldsymbol{l}_j\boldsymbol{e}_j^{\boldsymbol{T}} \tag{4.33}$$

where $\boldsymbol{l_j}$ is a column vector whose first j elements are zero, and $\boldsymbol{e_j}$ is the jth column of the $N\times N$ identity matrix $\boldsymbol{I_N}$. The first elementary triangular matrix can be computed as follows

$$\boldsymbol{L}_1\left(\boldsymbol{l}_1\right) = \boldsymbol{I}_N - \boldsymbol{l}_1\boldsymbol{e}_1^{\boldsymbol{T}} = \begin{bmatrix} 1 & & & \\ & 1 & & \\ & & \ddots & \\ & & & 1 \end{bmatrix} - \begin{bmatrix} 0 \\ -\hat{\boldsymbol{\alpha}}_{2,1} \\ -\hat{\boldsymbol{\alpha}}_{3,1} \\ \vdots \\ -\hat{\boldsymbol{\alpha}}_{N,1} \end{bmatrix} \begin{bmatrix} 1 \\ 0 \\ \vdots \\ 0 \end{bmatrix}^{\boldsymbol{T}}$$

$$= \begin{bmatrix} 1 & & & \\ & 1 & & \\ & & \ddots & \\ & & & 1 \end{bmatrix} - \begin{bmatrix} 0 & & & & \\ -\hat{\boldsymbol{\alpha}}_{2,1} & 0 & & & \\ -\hat{\boldsymbol{\alpha}}_{3,1} & 0 & 0 & & \\ \vdots & \vdots & & \ddots & \\ -\hat{\boldsymbol{\alpha}}_{N,1} & 0 & \cdots & & 0 \end{bmatrix}$$

$$= \begin{bmatrix} 1 & & & & \\ \hat{\boldsymbol{\alpha}}_{2,1} & 1 & & & \\ \hat{\boldsymbol{\alpha}}_{3,1} & 0 & 1 & & \\ \vdots & \vdots & & \ddots & \\ \hat{\boldsymbol{\alpha}}_{N,1} & 0 & \cdots & 0 & 1 \end{bmatrix} \tag{4.34}$$

Then equation (4.32) can be rewritten as

$$
\boldsymbol{L}=\begin{bmatrix} 1 & & & & \\ \hat{\boldsymbol{\alpha}}_{2,1} & 1 & & & \\ \hat{\boldsymbol{\alpha}}_{3,1} & 0 & 1 & & \\ \vdots & \vdots & & \ddots & \\ \hat{\boldsymbol{\alpha}}_{N,1} & 0 & \cdots & 0 & 1 \end{bmatrix}\begin{bmatrix} 1 & & & & \\ 0 & 1 & & & \\ \vdots & \hat{\boldsymbol{\alpha}}_{3,2} & 1 & & \\ & \vdots & & \ddots & \\ 0 & \hat{\boldsymbol{\alpha}}_{N,2} & 0 & 0 & 1 \end{bmatrix}\cdots
$$

$$
\begin{bmatrix} 1 & & & & \\ 0 & 1 & & & \\ \vdots & & \ddots & & \\ & & & 1 & \\ 0 & \cdots & 0 & \hat{\boldsymbol{\alpha}}_{N,N-1} & 1 \end{bmatrix}\begin{bmatrix} 1 & & & & \\ & 1 & & & \\ & & \ddots & & \\ & & & 1 & \\ & & & & 1 \end{bmatrix}
$$

$$
=\begin{bmatrix} 1 & & & & \\ \hat{\boldsymbol{\alpha}}_{2,1} & 1 & & & \\ \hat{\boldsymbol{\alpha}}_{3,1} & \hat{\boldsymbol{\alpha}}_{3,2} & 1 & & \\ \vdots & & & \ddots & \\ \hat{\boldsymbol{\alpha}}_{N,1} & \hat{\boldsymbol{\alpha}}_{N,2} & \cdots & \hat{\boldsymbol{\alpha}}_{N,N-1} & 1 \end{bmatrix} \tag{4.35}
$$

It can be shown that

$$
\boldsymbol{L}_j^{-1}\left(\boldsymbol{l}_j\right)=\boldsymbol{L}_j\left(-\boldsymbol{l}_j\right) \tag{4.36}
$$

and hence

$$
\boldsymbol{L}_j^{-1}\left(\boldsymbol{l}_i\right)=\boldsymbol{L}_N\left(-\boldsymbol{l}_N\right)\boldsymbol{L}_{N-1}\left(-\boldsymbol{l}_{N-1}\right)\cdots\boldsymbol{L}_2\left(-\boldsymbol{l}_2\right)\boldsymbol{L}_1\left(-\boldsymbol{l}_1\right) \tag{4.37}
$$

Then (4.29) and (4.30) can be rewritten as follows

$$
\|\boldsymbol{K}\|_\infty \le \|\boldsymbol{D}\|_\infty \|\boldsymbol{L}\|_\infty \le \|\boldsymbol{D}\|_\infty \left\|\boldsymbol{L}_1\left(\boldsymbol{l}_1\right)\right\|_\infty \cdots \left\|\boldsymbol{L}_N\left(\boldsymbol{l}_N\right)\right\|_\infty \tag{4.38}
$$

$$
\left\|\boldsymbol{K}^{-1}\right\|_\infty \le \left\|\boldsymbol{D}^{-1}\right\|_\infty \left\|\boldsymbol{L}^{-1}\right\|_\infty \le \left\|\boldsymbol{D}^{-1}\right\|_\infty \left\|\boldsymbol{L}_1\left(-\boldsymbol{l}_1\right)\right\|_\infty \cdots \left\|\boldsymbol{L}_N\left(-\boldsymbol{l}_N\right)\right\|_\infty \tag{4.39}
$$

Therefore, the condition number of $\boldsymbol{K}$ expressed in terms of the infinity norm will have an upper bound computed as follows

$$
\boldsymbol{c}\left(\boldsymbol{K}\right) \le \|\boldsymbol{D}\|_\infty \left\|\boldsymbol{D}^{-1}\right\|_\infty \prod_{j=1}^{N} \left\|\boldsymbol{L}_j\left(\boldsymbol{l}_j\right)\right\|_\infty \left\|\boldsymbol{L}_j^{-1}\left(\boldsymbol{l}_j\right)\right\|_\infty \tag{4.40}
$$

where

$$
\left\|\boldsymbol{L}_j\left(\boldsymbol{l}_j\right)\right\|_\infty = \max_i \left\|\hat{\boldsymbol{\alpha}}_{ij}\right\| + 1 \tag{4.41}
$$

$$\left\| \boldsymbol{L}_j^{-1}\left(\boldsymbol{l}_j\right) \right\|_\infty = \max_i \left\| \hat{\boldsymbol{\alpha}}_{ij} \right\| + 1 \tag{4.42}$$

By substituting equations (4.31), (4.41), and (4.42) into (4.40), the upper bound for the condition number $\boldsymbol{c}\left(\boldsymbol{J}\right)$ will be

$$\boldsymbol{c}\left(\boldsymbol{J}\right) \leq \frac{\left\| \boldsymbol{\theta}_{\max} \right\|}{\left\| \boldsymbol{\theta}_{\min} \right\|} \prod_{j=1}^{N} \left(1 + \max_i \left\| \hat{\boldsymbol{\alpha}}_{ij} \right\| \right)^2 \tag{4.43}$$

4.4.1.5 Summary of the Algorithm

The SO algorithm [70] in summary proceeds as follows:

1) Determination of reference output location:
   a) Compute the system mode observability matrix $\boldsymbol{H}$ using modal observability factors.
   b) Form the matrices $\boldsymbol{H_L}$ and $\boldsymbol{H_I}$.
   c) Form the $\boldsymbol{Q}$ matrix from $\boldsymbol{H_I}$ by dividing each row of $\boldsymbol{H_I}$ by the corresponding weighting factor as per (4.1).
   d) Choose the reference output location with greatest weighted modal observability as determined by the Euclidean norms of the rows of $\boldsymbol{Q}$, i.e. $\max_i \left(\left\| \boldsymbol{q}_i \right\|_2 \right)$.
   e) Form the observation matrix $\boldsymbol{J}$ with the row corresponding to the reference location from the $\boldsymbol{H_I}$ matrix. Add this bus to the set of selected locations $j \in \boldsymbol{S}$.
2) For the remaining output locations $i \notin \boldsymbol{S}$ not yet selected:
   a) Compute $\boldsymbol{\theta}_i$, $\boldsymbol{\alpha}_{ij}$, and $\hat{\boldsymbol{\alpha}}_{ij}$ as per (4.16), (4.17), and (4.18), respectively.
   b) Choose the maximum $\hat{\boldsymbol{\alpha}}_{ij}$, i.e. $\max_{j \in \boldsymbol{S}} \left\| \hat{\boldsymbol{\alpha}}_{ij} \right\|$, for each location $i \notin \boldsymbol{S}$.
   c) Select the location which has the minimum $\hat{\boldsymbol{\alpha}}_{ij}$, i.e. $\min \left(\max_{j \in \boldsymbol{S}} \left\| \hat{\boldsymbol{\alpha}}_{ij} \right\| \right)$.
   d) Add this new location to the set of selected locations $j \in \boldsymbol{S}$ and update the matrix $\boldsymbol{J}$ by adding a new row corresponding to this location from the $\boldsymbol{H_I}$ matrix.
   e) Go back to step 2(a) until a big rise in the condition number of $\boldsymbol{J}$ occurs.

4.4.2 Application of the SO Algorithm to Input/Output Signal Selection

The SO algorithm was originally introduced in the literature for the optimal placement of angle transducers. The aim is to have high coverage of system observability information about the interarea modes using synchronised measurements (voltage phase angles) from the optimally placed devices. In the context of WAMS based control applications, these optimally placed devices supply synchronised measurements (through the WAMS) to the SWAC. The SO algorithm therefore can be applied to the selection of measurement signals (inputs to the SWAC) through optimal placement of PMUs. The dual process can be applied to the transpose of mode controllability matrix to select the optimal control signals (outputs of the SWAC). Candidate locations of these control signals are at the generators' exciters. The observability/controllability information of concern will be about the lightly damped interarea modes, i.e. modes of interest, with consideration to signals' sensitivity to other modes in the system.

The SO algorithm is applied to the mode observability matrix $\boldsymbol{H}$, constructed using the modal observability factors, to select the optimal set of input signals to the SWAC. The ($p \times n_I$) matrix $\boldsymbol{H_I}$ is formed from the columns of $\boldsymbol{H}$ corresponding to the modes of interest, i.e. modes 1-3, and is shown in Table 4-8. The ($p \times n_L$) matrix $\boldsymbol{H_L}$ is formed similarly from the columns of $\boldsymbol{H}$ corresponding to the other modes, i.e. modes 4-9 and is shown in Table 4-9. The weighting factor $\boldsymbol{w_i}$ is computed as per equation (4.1) using the Euclidean norms of rows of $\boldsymbol{H_I}$ and $\boldsymbol{H_L}$. Each row of $\boldsymbol{H_I}$ is then divided by the corresponding weighting factors to form the matrix $\boldsymbol{Q}$. Table 4-10 lists the parameters used in determining the first reference location. Measurement signal at G5 which has the largest weighted observability response $\|\boldsymbol{q}_5\|_2$ (shown in bold face in the table) therefore is chosen as the first selection.

Table 4-8: Magnitudes of formed matrix $\boldsymbol{H_I}$ ($\times 10^3$)

Signal location	Mode 1	Mode 2	Mode 3
G1	20.26	33.54	106.73
G2	9.70	7.63	55.87
G3	11.10	7.08	60.18
G4	120.10	92.28	113.45
G5	123.97	96.83	113.65
G6	51.10	73.71	129.67
G7	51.16	73.31	129.32
G8	11.60	8.32	67.08
G9	14.35	8.13	62.43
G10	10.35	9.39	68.75

Subsequent locations are selected sequentially by following the orthogonal projection procedure applied to the remaining rows of matrix $\boldsymbol{Q}$ and the weighted observability response of the reference location $\|\boldsymbol{q}_5\|_2$. The orthogonal projection components $\boldsymbol{\theta}_i$, in-phase projection components $\boldsymbol{\alpha}_{ij}$, and the relative in-phase projection components $\hat{\boldsymbol{\alpha}}_{ij}$ are computed and are listed in Table 4-11. It can be seen from the table that the measurement signal at location G6 (shown in bold face) has the minimum relative in-phase projection to the weighted observability response of the previous selected signal (G5: the reference location). This means that signal at G6 has a weighted observability response far different from the weighted observability response of the signal at G5. Note in the table that the weighted observability response of signal at G4 (shown underlined in the table) has the largest in-phase projection component to the weighted response of the reference signal at G5. This indicates the high degree of correlation between the two measurements. Signal at G6 therefore is selected as the second location. The third signal is selected similarly based on the minimum relative in-phase projection to the weighted responses of the previously selected two signals. The procedure continues until the condition number of the observation matrix $\boldsymbol{J}$, i.e. $\boldsymbol{c}(\boldsymbol{J})$, rises noticeably as shown in Table 4-12. The fourth selection leads to a large condition number thus indicating a high degree of correlation with the previous selected signals. The SO algorithms therefore stops and number of selected measurement signals (p_r) is limited to 3. The optimal set of selected measurement signals using the SO algorithm is listed in Table 4-13.

Table 4-9: Magnitudes of formed matrix H_L (×10^3)

Signal location	Mode 4	Mode 5	Mode 6	Mode 7	Mode 8	Mode 9
G1	50.46	27.76	1.20	1.13	0.40	0.10
G2	42.95	29.57	2.77	1.95	0.71	0.22
G3	55.22	58.12	1.35	0.84	0.62	0.19
G4	46.39	25.14	4.12	1.90	1.66	4.39
G5	46.63	25.49	3.02	1.37	1.25	8.00
G6	47.44	27.13	1.70	0.24	10.72	0.51
G7	47.45	27.25	1.36	1.14	15.78	0.64
G8	66.45	28.37	13.03	16.56	0.22	0.13
G9	71.31	31.61	18.20	22.85	1.73	0.25
G10	63.76	24.36	2.52	2.00	0.61	0.18

The dual process of selecting the control signals (outputs of the SWAC) is done similarly by applying the SO algorithm to the transpose of the ($n\times m$) mode controllability matrix constructed using the modal controllability factors. Locations of the optimally selected control signals using the SO algorithm are listed in Table 4-13. It can be seen from the table that the selected signals are from different regions in the network and generators geographically close to each other are not repeated in the optimal set.

Table 4-10: Parameters used in selecting the first location (ε=0.01)

Generator	***i***	$\left\lVert \boldsymbol{h}_{L_i} \right\rVert_2$	$\left\lVert \boldsymbol{h}_{I_i} \right\rVert_2$	w_i	$\left\lVert \boldsymbol{q}_i \right\rVert_2$
G1	1	0.082	0.161	0.517	0.311
G2	2	0.074	0.081	0.923	0.088
G3	3	0.113	0.087	1.312	0.066
G4	4	0.075	0.268	0.291	0.920
G5	5	0.076	0.274	0.288	**0.955**
G6	6	0.079	0.223	0.363	0.614
G7	7	0.081	0.222	0.372	0.597
G8	8	0.106	0.097	1.107	0.088
G9	9	0.118	0.091	1.300	0.070
G10	10	0.097	0.099	0.984	0.101

Table 4-11: Parameters used in selecting the second location (j=5)

Signal location	***i***	$\lVert \theta_i \rVert$	$\lVert \alpha_{ij} \rVert$	$\lVert \hat{\alpha}_{ij} \rVert$
G1	1	0.243	0.194	0.797
G2	2	0.060	0.064	1.055
G3	3	0.046	0.048	1.042
G4	4	0.031	0.919	<u>29.317</u>
G6	6	0.544	0.285	**0.523**
G7	7	0.529	0.277	0.525
G8	8	0.061	0.063	1.025
G9	9	0.049	0.051	1.034
G10	10	0.071	0.072	1.013

Table 4-12: Condition number of observation matrix *J*

Number of selected signals	**Condition number $c(\boldsymbol{J})$**
1	1
2	1.727
3	3.150
4	**61.306**

Table 4-13: Locations of selected I/O signals using the SO algorithm

Locations of measurement signals	Locations of control signals
(G5, G6, G1)	(G5, G2, G1, G6)

4.5 Combined Clustering and Modal Factors Analysis

In this approach generators are clustered using PCA-based clustering method. One representative measurement signal is selected from each cluster. The selection criterion of the representative signal is based on the modal factors analysis. The measurement signal having the largest cumulative sum of modal observability factors for the modes of interest is selected as the representative signal. In this way, number of selected signals is reduced and all clusters of generators are represented in the set of measurement signals. Furthermore, redundancy of information in the chosen set of signals is reduced as well. The reduced set of chosen measurement signals, covering all clusters of generators, maximises the observability information about the modes of interest. The control signals are selected similarly by selecting one representative signal from each cluster of generators. The representative control signal is chosen such that it has the largest cumulative sum of modal controllability factors among other signals in the same cluster for the set of modes of interest.

4.5.1 Principal Component Analysis

Principal component analysis is a technique that transforms a set of m correlated variables to a new set of uncorrelated variables called principal components [99]. The original set of variables then can be expressed as a linear combination of the new principal components. The principal components are derived in decreasing order according to their capturing of data in the original variables. For example, the first principal component accounts for as much as possible of the variation in the original data. The transformation is, in fact, an orthogonal rotation in m-space. Objective of the analysis is to see if the first few components account for most of the variation in the original data. The data matrix $\boldsymbol{X}$, consisting of m process variables, is obtained from online measurements of the considered system variables measured over time t for N ($m \ll N$) samples. A full PCA decomposition reconstructs the original $m \times N$ data matrix $\boldsymbol{X}$

as a sum over m orthonormal basis functions (principal components) $\boldsymbol{w}_1'$ to $\boldsymbol{w}_m'$, which are arranged as row vectors as follows

$$\boldsymbol{X} = \begin{pmatrix} t_{1,1} \\ \vdots \\ t_{m,1} \end{pmatrix} \boldsymbol{w}_1' + \begin{pmatrix} t_{1,2} \\ \vdots \\ t_{m,2} \end{pmatrix} \boldsymbol{w}_2' + \ldots + \begin{pmatrix} t_{1,m} \\ \vdots \\ t_{m,m} \end{pmatrix} \boldsymbol{w}_m' \tag{4.44}$$

where dimensions of each principal component $\boldsymbol{w}_i$ are N×1. The expression (4.44) may be written compactly as

$$\boldsymbol{X}=\boldsymbol{TW}' \tag{4.45}$$

where the ith column of $\boldsymbol{T}$ is $\left(\boldsymbol{t}_{1,i} \quad \cdots \quad \boldsymbol{t}_{m,i}\right)'$, and the rows of $\boldsymbol{W}$ are $\boldsymbol{w}_1'$ to $\boldsymbol{w}_m'$. Elements of $\boldsymbol{T}$ matrix are called the scores (or t-scores). Orthonormality of rows of $\boldsymbol{W}'$ means that $\boldsymbol{T} = \boldsymbol{XW}$. Singular value decomposition (SVD) provides a means for computation of PCA as follows,

$$\boldsymbol{X} = \boldsymbol{UDV}' \tag{4.46}$$

where

$$\boldsymbol{T} = \boldsymbol{UD} \tag{4.47}$$

$$\boldsymbol{W}' = \boldsymbol{V}' \tag{4.48}$$

Diagonal elements of $\boldsymbol{D}$ are the singular values of $\boldsymbol{X}$. The $\boldsymbol{w}_i'$-vectors are the normalised right eigenvectors of the N×N matrix $\boldsymbol{X'X}$. The ratio between each eigenvalue of $\boldsymbol{X'X}$ and the sum of all the eigenvalues gives a measure of the total variation captured by the corresponding eigenvector (or principal component) [99]. The weightings of each principal component in each data variable of $\boldsymbol{X}$ may be represented graphically. When three $\boldsymbol{w}_i'$-components are in use, their corresponding t-scores could be plotted in a three dimensional (3-D) space spanned by the three orthogonal principal components. The ith original variable then maps to a point having the coordinates $\left(t_{i,1}, t_{i,2}, t_{i,3}\right)$ in 3-D space. The plots of these coordinates are called the scores plot. Similar original variables have similar t-coordinates. Groups of similar original variables then form clusters in the 3-D scores plot. In the context of power systems, this formation of clusters can be used to identify coherent groups of generators

[73]. Generators' responses to large disturbances in the system, such as rotor speeds, could be used as the original variables and their *t*-scores are then used to identify clusters in the 3-D space.

4.5.1.1 Coherency identification using PCA

Modern power networks tend to be exposed to more stressed operating conditions in a liberalised electricity market due to market driven power transfers. These stressed conditions could easily lead to onset of stability problems. The major stability issue in large interconnected power systems is poorly damped interarea oscillations. The size of the system, however, restricts straightforward modelling of each generator and inclusion of those models in the overall power system model. Generators behaving dynamically in a similar way (rotors of generators oscillate almost in phase with each other) during an interarea event constitute a coherent area. Each coherent group of generators can be therefore aggregated and replaced by a dynamic equivalent. A major benefit of dynamic equivalencing is reduction in overall system model and computational time needed for stability studies. Further, the network decomposition into several areas and creation of coherency-based dynamic equivalent can be used for more efficient monitoring and control of power systems by using reduced number of monitors and controllers strategically placed in the network [100].

An early work in coherency identification is the linear time simulation method [101]. The method uses swing curves following a network disturbance and compares rotor angles to specified tolerance. Time domain methods for dynamic equivalencing do not need detailed modelling of the system as the modal coherency methods [102, 103]. They record the system response following a disturbance and process it to define the coherent groups of generators. In fact, this advantage is set to become even more pronounced with the increased growth of PMU installations in power networks.

Principal component analysis as a time domain method can be applied to the coherency identification of generators [73]. System responses, e.g. generator rotor angle variation, following a disturbance can be transformed using the PCA to uncorrelated variables. The required system response can be provided by PMUs through the WAMS. Coherent groups of generators are then identified by the visual inspection of a three dimensional, as will be seen later, plots representing the response of each generator in the system. The PCA method is fast and identifies coherent generators without any model information thus making it suitable for very large networks analysis. The method does not need linearisation and modal information, e.g. eigen-analysis results, of the system as it relies only on PMUs measurements. Therefore it can be regarded as an effective tool for the identification of coherent generators.

Large disturbances, i.e. a self-clearing three-phase fault lasting for 100 ms, at different buses (27 cases) in the network are simulated in the modified NETS. Figure 4-4 shows the rotor speed deviation responses of network generators for 27 large disturbances. For each generator, its speed deviation responses for all the 27 disturbances are combined (in cascade order) together into one row vector; representing the individual generator response to all disturbances. This is done to reduce the influence of fault location on the speed deviation responses, and hence the coherency identification results, and to take into account all possible scenarios of large disturbances. Each response vector is pre-processed by subtracting the mean value and scaling to unit standard deviation. Response vectors of all generators are then combined to form the $m \times N$ data matrix. The PCA decomposition is computed using SVD as in (4.46) and the resulting t-scores are listed in Table 4-14. The 3-D scores plot is obtained by plotting the t-scores corresponding to the first three principal components (the plotted t-scores are listed in Table 4-14 in bold face) and is shown in Figure 4-5. It can be seen from the figure that generators, indicated by numbers, with similar responses form clusters (indicated by circles) in the 3-D space.

Table 4-14: t-scores ($\times 10^4$)

Generator	t_1	t_2	t_3	t_4	t_5	t_6	t_7	t_8	t_9	t_{10}
G1	**-0.258**	**0.52**	**-0.41**	-0.18	-1.35	-1.83	0.14	-0.00	0.37	-0.03
G2	**3.31**	**2.68**	**0.19**	1.12	0.75	0.10	0.66	0.46	0.51	0.06
G3	**2.63**	**2.05**	**-0.11**	0.42	1.15	-0.95	-0.44	-0.58	-0.43	-0.20
G4	**0.11**	**-0.57**	**-3.60**	0.03	0.52	0.11	-0.50	-0.29	0.52	0.49
G5	**-0.88**	**0.40**	**-4.07**	0.56	-0.13	0.04	0.53	0.24	-0.43	-0.41
G6	**3.21**	**-4.39**	**-0.02**	0.68	-0.21	0.09	0.47	-0.60	0.14	-0.22
G7	**2.67**	**-2.83**	**-0.30**	-0.39	0.26	-0.55	-0.39	0.96	-0.29	0.18
G8	**1.92**	**1.19**	**-0.28**	-0.85	-0.82	0.14	0.49	-0.28	-0.51	0.74
G9	**2.36**	**1.04**	**-0.67**	-3.50	-0.30	0.43	-0.12	-0.01	0.20	-0.39
G10	**2.34**	**1.36**	**-0.27**	1.87	-1.61	0.69	-0.68	0.07	-0.02	-0.15

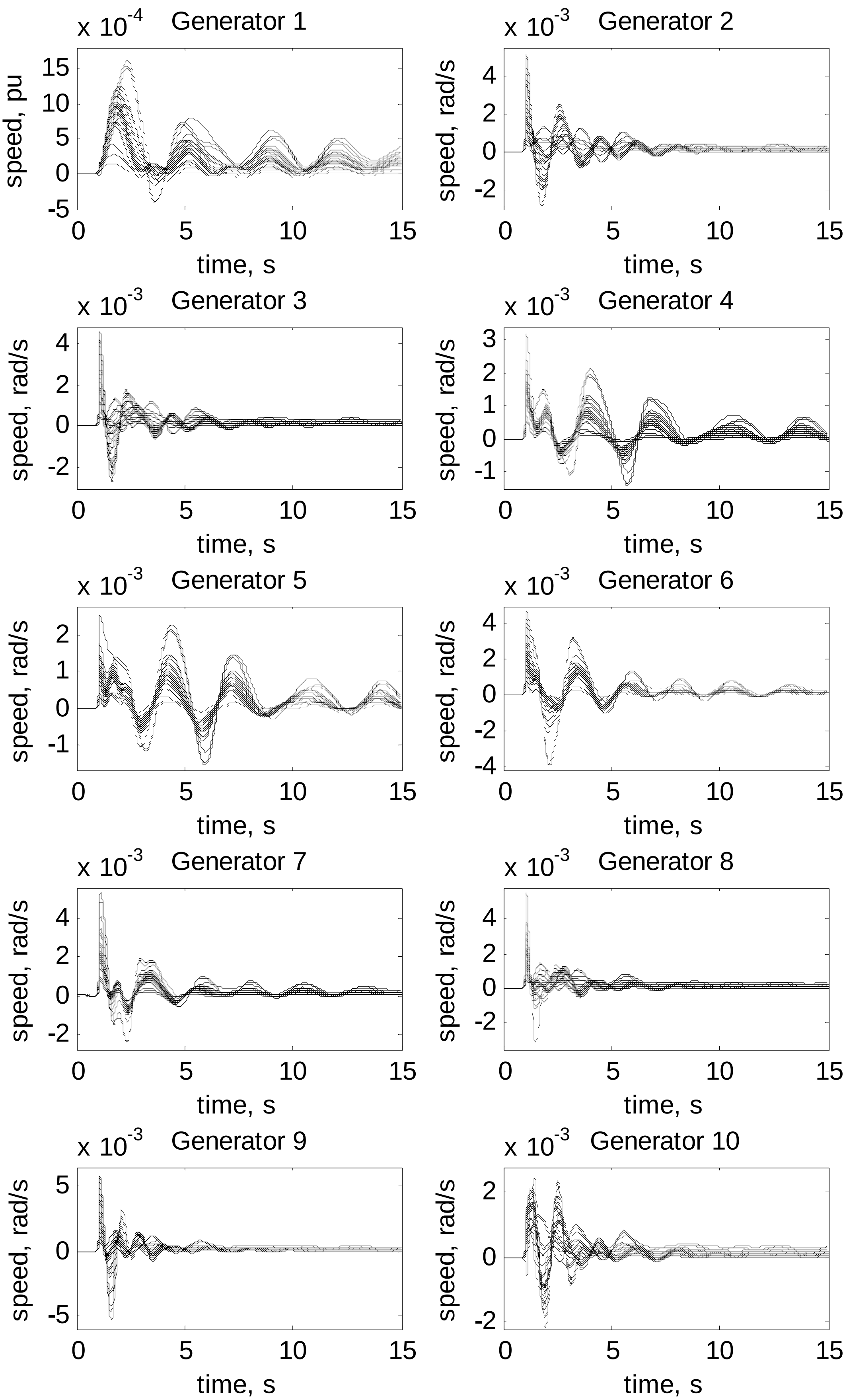

Figure 4-4: Speed deviation responses for 27 large disturbances

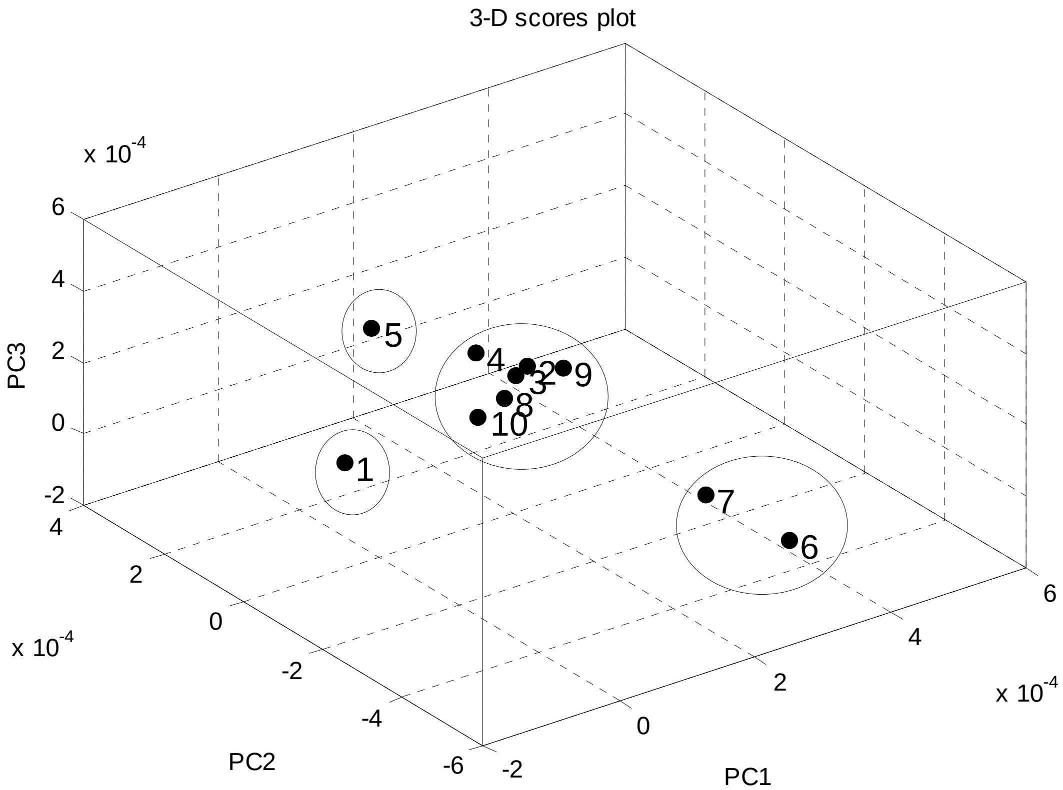

Figure 4-5: Three dimensional scores plot (viewing angle 1)

4.5.1.2 Limitations of PCA

As shown in the PCA example, identification of coherent groups of generators depends on the visual inspection of the scores plot. The viewing angle in the 3-D plot could lead to inaccurate clustering of generators, mainly due to human judgement. For example, Figure 4-6 and Figure 4-7 show two different viewing angles in the 3-D scores plot different from the one used in Figure 4-5. Table 4-15 lists groups of coherent generators identified using visual inspection of the 3-D scores plots with different viewing angles. Results in the table show clearly that the viewing angle, in a 3-D plot of the transformed PCA data, can influence/change the coherency analysis results. Furthermore, the coherency identification generally needs to be performed quickly and visual inspection obviously cannot meet this requirement.

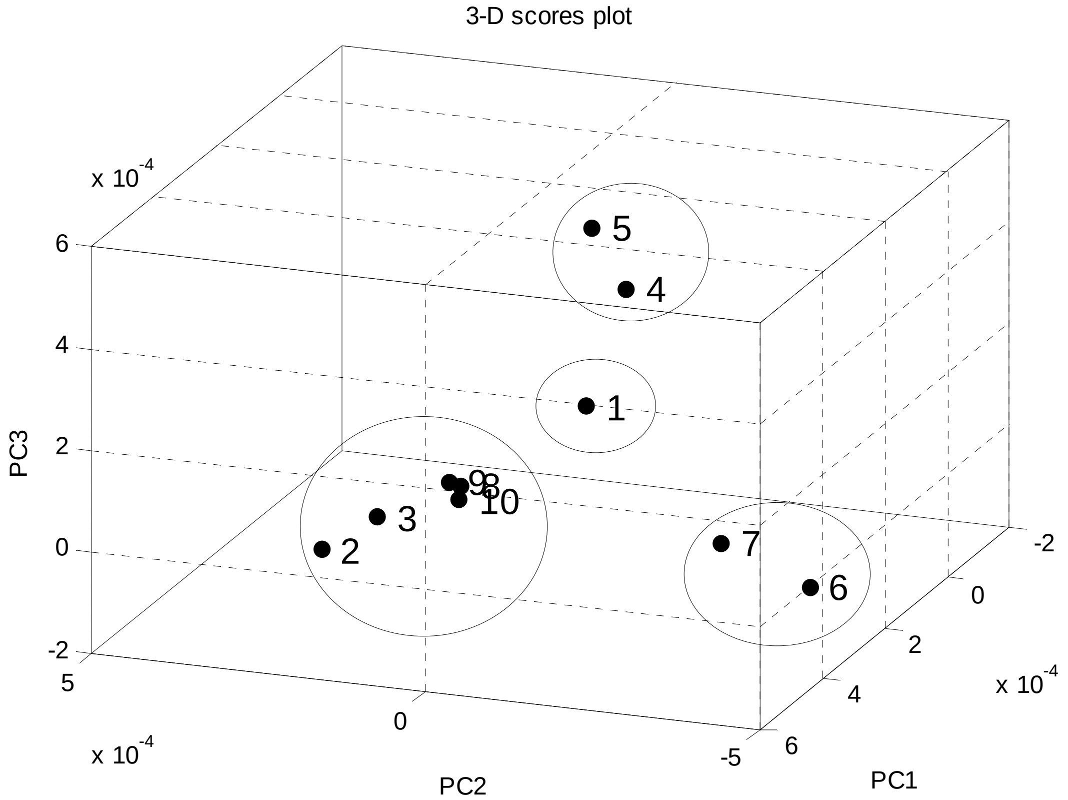

Figure 4-6: Three dimensional scores plot (viewing angle 2)

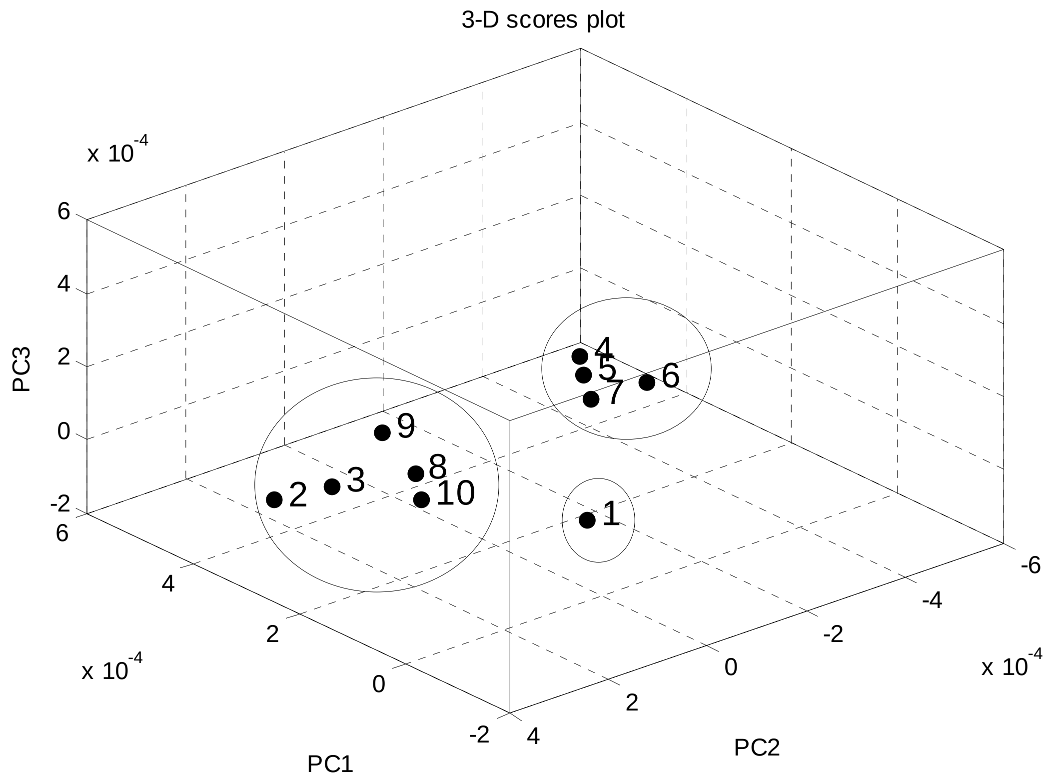

Figure 4-7: Three dimensional scores plot (viewing angle 3)

Table 4-15: Coherent groups of generators identified using different viewing angles

Coherent groups	Viewing angle 1	Viewing angle 2	Viewing angle 3
Group 1	(G1)	(G1)	(G1)
Group 2	(G5)	(G4,G5)	(G4,G5,G6,G7)
Group 3	(G6,G7)	(G6,G7)	(G2,G3,G8,G9,G10)
Group 4	(G2,G3,G4,G8,G9,G10)	(G2,G,G8,G9,G10)	-

The grouping of coherent generators by the PCA was done by using only three principal components. The use of three principal components however could lead to insufficient capturing of original data in the PCA transformation process. Number of principal components needed for sufficient capturing of variations in original data can be determined using the cumulative percent variance (***CPV***) [104] measure computed as follows

$$\boldsymbol{CPV(l)} = 100\left[\frac{\sum_{j=1}^{l}\lambda_j}{\sum_{j=1}^{m}\lambda_j}\right]\% \tag{4.49}$$

where λ_j is the jth eigenvalue of $\boldsymbol{X'X}$, l is number of first principal component, and m is the total number of eigenvalues. The desired value of ***CPV*** is selected in order to account for as much capturing of original data variations as possible while retaining as few principal components as possible. Specifying the ***CPV*** value, i.e. 90%, 95%, …etc, however is subjective [104] to different applications. Table 4-16 lists the captured variation of original data by principal components.

If the CPV measure is specified as 95% then the first 4 principal components are needed to capture 95% of variations in original data. The t-scores cannot be plotted in this case and therefore coherency identification results cannot be obtained using visual inspection. The visual inspection of PCA results therefore restricts the identification process to only three principal components and thus may lead to inaccurate results.

Table 4-16: Captured variations by principal components

Principal component	Captured variation [%]	Cumulative captured variation [%]
1st	56.82	56.82
2nd	24.86	81.68
3rd	12.06	93.74
4th	4.99	98.73
5th	0.75	99.48
6th	0.34	99.82
7th	0.07	99.89
8th	0.06	99.95
9th	0.03	99.98
10th	0.02	100.00

4.5.2 PCA-based Clustering

4.5.2.1 Cluster Analysis

Classification of PCA results can be done alternatively using a cluster analysis technique instead of the visual inspection. The PCA method is supplemented by cluster analysis to accurately identify coherent generators. Spatial distances in a multi-dimensional space between transformed data are used to construct a proximity measure describing the coherency relationship between all generators. The generators are then linked together to build a multi-level hierarchical tree representing the dynamic behaviour of network generators.

In Hierarchical clustering [105] used in this study the data are not partitioned into a particular number of clusters at a single step. The clustering consists of a series of partitions which may run from m clusters, each containing a single individual generator, to a single cluster containing all individuals. So, the clustering is obtained by the merger of clusters from the previous level by applying similarity and dissimilarity measure as the frame of reference for clustering. A dissimilarity (*distance*) matrix is formed using distances between objects. The distance matrix is an $m \times m$ off-diagonal matrix, with zeros on the main diagonal, where m is the total number of objects to be clustered. Each entry in the matrix represents the distance measure between the objects notated by the entry's indices. Therefore, the main diagonal in the matrix contains all zeros. A common measure of distance is the *Euclidean Norm* [105];

$$d_{ij} = \left(\sum_{k=1}^{p} \left(x_{ik} - x_{jk} \right)^2 \right)^{1/2} \tag{4.50}$$

where x_{ik} and x_{jk} are the kth variable value of the p-dimensional observation for individuals i and j, respectively. This distance measure has the appealing property that the d_{ij} can be interpreted as physical distances between two p-dimensional points $x_i=(x_{i1}, \dots, x_{ip})$ and $x_j=(x_{j1}, \dots, x_{jp})$ in Euclidean space. Formally this distance is also known as the l_2 norm [105].

The nearest-neighbour distance is the basis of the *single linkage* clustering method [105]. The defining feature of the method is that the distance between groups is defined as that of the closest pair of objects from considered groups, i.e. only pairs consisting of one object from each group are considered.

4.5.2.2 Illustrative Example on Cluster Analysis

In order to illustrate the above approach and facilitate understanding of it a simple numerical example is given below. Consider the case when the number of variables is five and only two principal components are needed to capture most of the data variations. The required T matrix will therefore have 5 rows and two columns. Let the T matrix be

$$T = \begin{bmatrix} 1 & 2 & 2 & 6 & 6 \\ 2 & 2 & 5 & 5 & 7 \end{bmatrix}^{\mathrm{T}}$$

The scores plot is shown in Figure 4-8 in two-dimensional (2-D) coordinate space where the five objects are shown as numbered dots and the formed clusters (to be explained later) as the big circles. Dissimilarity (distance) 5×5 matrix is constructed using the Euclidean distances between objects as

$$D_1 = \begin{array}{c} \\ 1 \\ 2 \\ 3 \\ 4 \\ 5 \end{array} \begin{array}{c} \begin{array}{ccccc} 1 & 2 & 3 & 4 & 5 \end{array} \\ \begin{bmatrix} 0 & 1 & 3.16 & 5.83 & 7.07 \\ 1 & 0 & 3 & 5 & 6.4 \\ 3.16 & 3 & 0 & 4 & 4.47 \\ 5.83 & 5 & 4 & 0 & 2 \\ 7.07 & 6.4 & 4.47 & 2 & 0 \end{bmatrix} \end{array}$$

The smallest non-zero entry in the matrix is that for objects 1 and 2, so they are joined to form a two-member cluster. This new formed cluster will be called object 6, shown in Figure 4-8 as a big circle containing objects 1 and 2. When applying the single linkage clustering method, minimum distances between this cluster and the other three objects are obtained as

$$d_{6,3} = min\ [d_{1,3},\ d_{2,3}] = d_{2,3} = 3$$

$$d_{6,4} = min\ [d_{1,4},\ d_{2,4}] = d_{2,4} = 5$$

$$d_{6,5} = min\ [d_{1,5},\ d_{2,5}] = d_{2,5} = 6.4$$

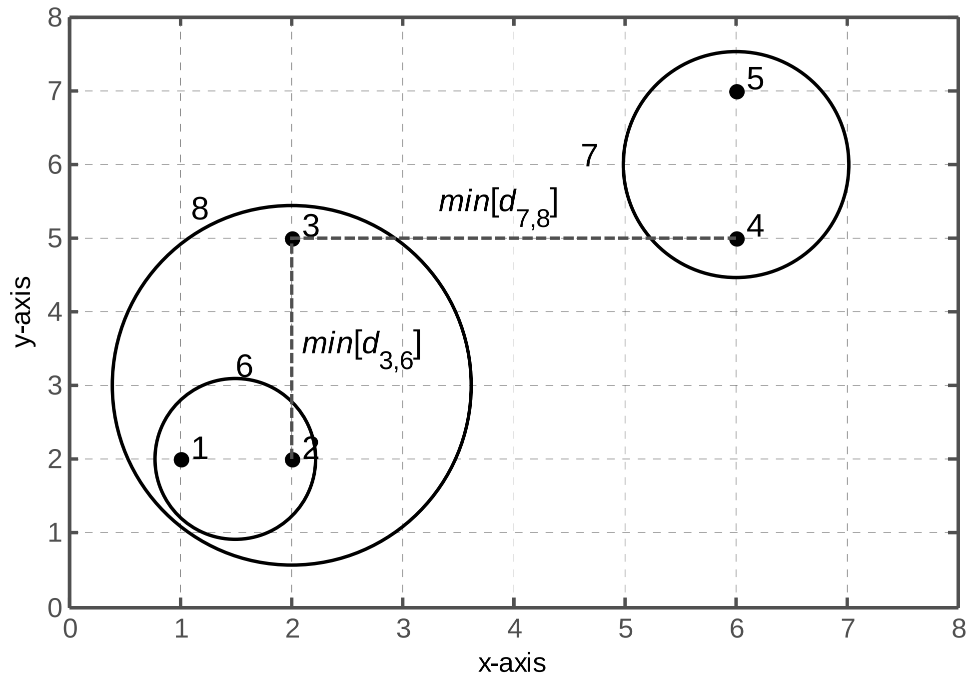

Figure 4-8: Two dimensional scores plot

A new 4×4 matrix may now be constructed whose entries are inter-objects and cluster-objects distance values:

$$\boldsymbol{D}_2 = \begin{array}{c} \\ 6 \\ 3 \\ 4 \\ 5 \end{array} \begin{array}{c} \begin{array}{cccc} 6 & 3 & 4 & 5 \end{array} \\ \begin{bmatrix} 0 & 3 & 5 & 6.4 \\ 3 & 0 & 4 & 4.47 \\ 5 & 4 & 0 & 2 \\ 6.4 & 4.47 & 2 & 0 \end{bmatrix} \end{array}$$

The smallest entry in $\boldsymbol{D}_2$ is that for objects 4 and 5, so these now form a second two-member cluster, to be called object 7, and a new set of distances is found:

$d_{6,3} = 3$ (as before)

$d_{6,7} = min\ [d_{1,4}, d_{1,5}, d_{2,4}, d_{2,5}] = d_{2,4} = 5$

$d_{7,3} = min\ [d_{3,4}, d_{3,5}] = d_{3,4} = 4$

These may be arranged in a 3×3 matrix $\boldsymbol{D}_3$

$$\boldsymbol{D}_3 = \begin{array}{c} \\ 6 \\ 3 \\ 7 \end{array} \begin{array}{c} \begin{matrix} 6 & 3 & 7 \end{matrix} \\ \begin{bmatrix} 0 & 3 & 5 \\ 3 & 0 & 4 \\ 5 & 4 & 0 \end{bmatrix} \end{array}$$

The smallest entry in $\boldsymbol{D}_3$ is that for objects 6 and 3, shown as dashed line $min(d_{3,6})$ in Figure 4-8, so these now form a third cluster, to be called object 8. This new cluster is formed by joining the remaining object, object 3, and a previously formed cluster, object 6.

Finally, the remaining clustering is obtained by joining object 7 and object 8 into a single cluster. The minimum distance between the two clusters, shown as dashed line $min(d_{7,8})$ in Figure 4-8, is calculated as

$$d_{7,8} = min\ [d_{1,4}, d_{1,5}, d_{2,4}, d_{2,5}, d_{3,4}, d_{3,5}] = d_{3,4} = 4$$

The hierarchical clustering produced is represented by a two-dimensional diagram known as a *dendrogram* [105], which illustrates the fusions made at each stage of the analysis. The dendrogram, or hierarchical tree, illustrating the process and the partitions produced at each stage is shown in Figure 4-9 (top view); the *height* in this diagram represents the distance at which each fusion is made. The partitions (levels) range from each object forming individual cluster to one cluster containing all the objects.

4.5.2.3 Coherency Identification using PCA-based Clustering

Identification of coherent generators using the PCA-based clustering method starts by applying the PCA decomposition to the data matrix as demonstrated previously. The cluster analysis then follows using the matrix of *t*-scores (listed in Table 4-14). The spatial distances between the 10 objects, corresponding to responses of 10 generators, in 10-D space are computed using the Euclidian norm and are listed in Table 4-17. Note that the coefficients, i.e. the *t*-scores, of the 10 principal components are used in the computations. The single linkage method is then applied to link generators and the hierarchical clustering tree is built as in Figure 4-10.

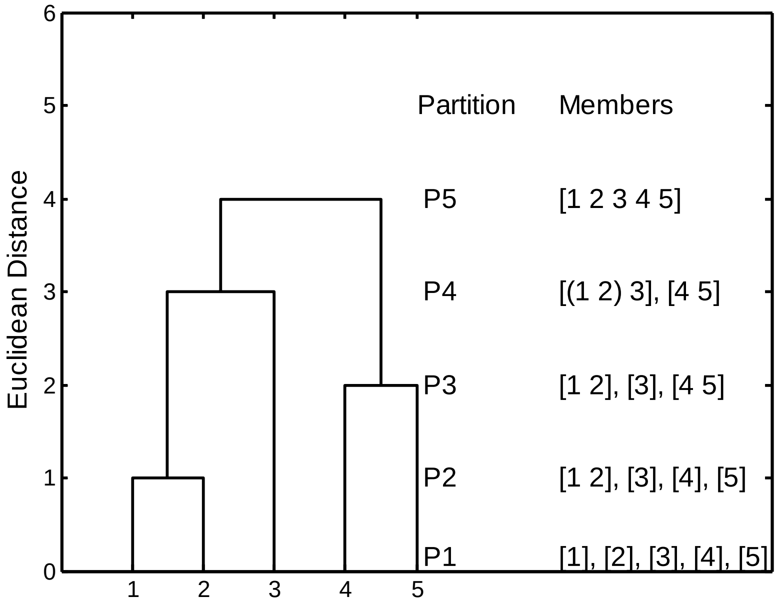

Figure 4-9: Dendrogram illustrating the clustering process

Table 4-17: Distance matrix (×10⁴)

Generator	G1	G2	G3	G4	G5	G6	G7	G8	G9	G10
G1	0.00	5.64	4.83	4.53	4.52	6.74	5.39	3.77	5.45	4.36
G2	5.64	0.00	2.42	6.28	6.68	7.33	6.14	3.73	5.46	3.66
G3	4.83	2.42	0.00	5.44	6.05	6.86	5.45	3.30	4.85	3.90
G4	4.53	6.28	5.44	0.00	2.43	6.30	5.09	4.74	5.67	5.37
G5	4.52	6.68	6.05	2.43	0.00	7.58	6.40	5.26	6.51	5.60
G6	6.74	7.33	6.86	6.30	7.58	0.00	2.82	6.14	7.09	6.39
G7	5.39	6.14	5.45	5.09	6.40	2.82	0.00	4.74	5.45	5.53
G8	3.77	3.73	3.30	4.74	5.26	6.14	4.74	0.00	3.25	3.52
G9	5.45	5.46	4.85	5.67	6.51	7.09	5.45	3.25	0.00	5.85
G10	4.36	3.66	3.90	5.37	5.60	6.39	5.53	3.52	5.85	0.00

Table 4-18 lists the clustering process where grouping of generators starts from 10 separate generators to one area containing all generators. Height of each link represents the degree of similarity between rotor speed deviation responses of generators grouped in the link. As an example, generators 4 and 5 are grouped in a short link (Link 2); thus indicating similarity of their responses as can be seen from Figure

4-11. Figure 4-12 shows an example of non-coherent generators (G5 and 6) grouped in high link (Link 9). The height of the link therefore gives an indication of the coherency degree between generators grouped in that link.

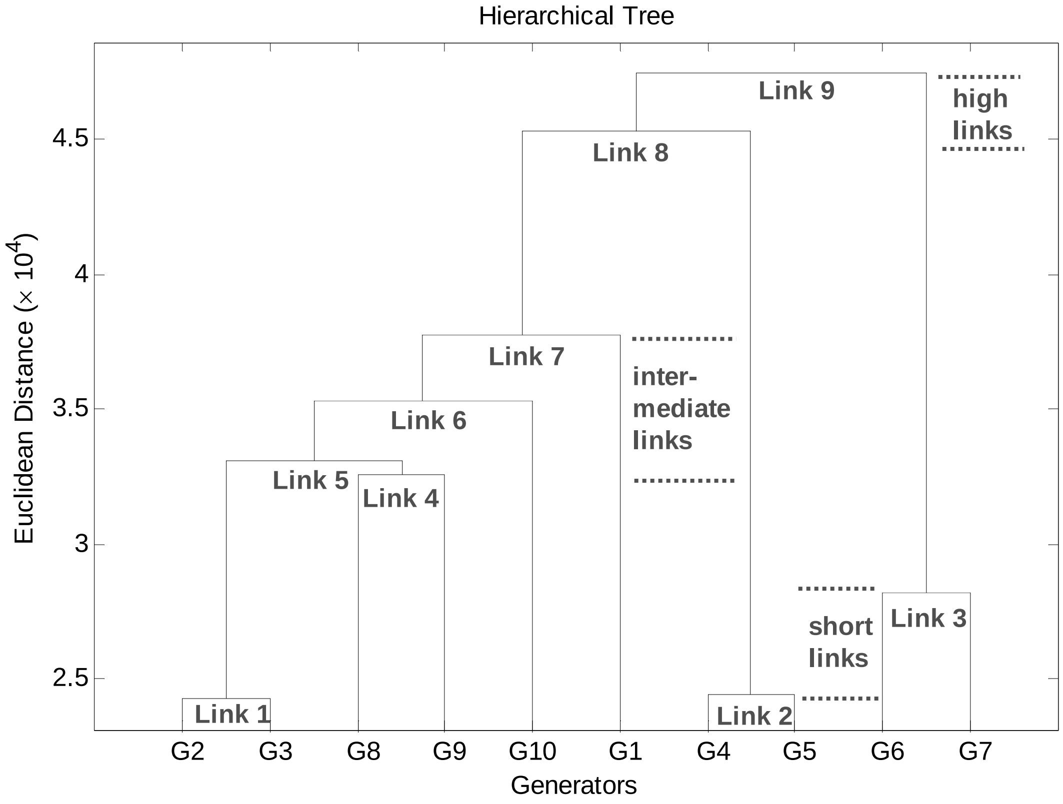

Figure 4-10: Hierarchical clustering using PCA-based cluster analysis

Table 4-18: Variable degree of clustering

Number of areas	**Link**	**Areas**
10 areas	**-**	(G2), (G3), (G8), (G9), (G10), (G1), (G4), (G5), (G6), (G7)
9 areas	**Link 1**	(G2,G3), (G8), (G9), (G10), (G1), (G4), (G5), (G6), (G7)
8 areas	**Link 2**	(G2,G3), (G8), (G9), (G10), (G1), (G4,G5), (G6), (G7)
7 areas	**Link 3**	(G2,G3),(G8), (G9), (G10), (G1), (G4,G5), (G6,G7)
6 areas	**Link 4**	(G2,G3),(G8,G9), (G10), (G1), (G4,G5), (G6,G7)
5 areas	**Link 5**	(G2,G3,G8,G9), (G10), (G1), (G4,G5), (G6,G7)
4 areas	**Link 6**	(G2,G3,G8,G9,G10), (G1), (G4,G5), (G6,G7)
3 areas	**Link 7**	(G2,G3,G8,G9,G10,G1), (G4,G5), (G6,G7)
2 areas	**Link 8**	(G2,G3,G8,G9,G10,G1,G4,G5), (G6,G7)
1 area	**Link 9**	(G2,G3,G8,G9,G10,G1,G4,G5,G6,G7)

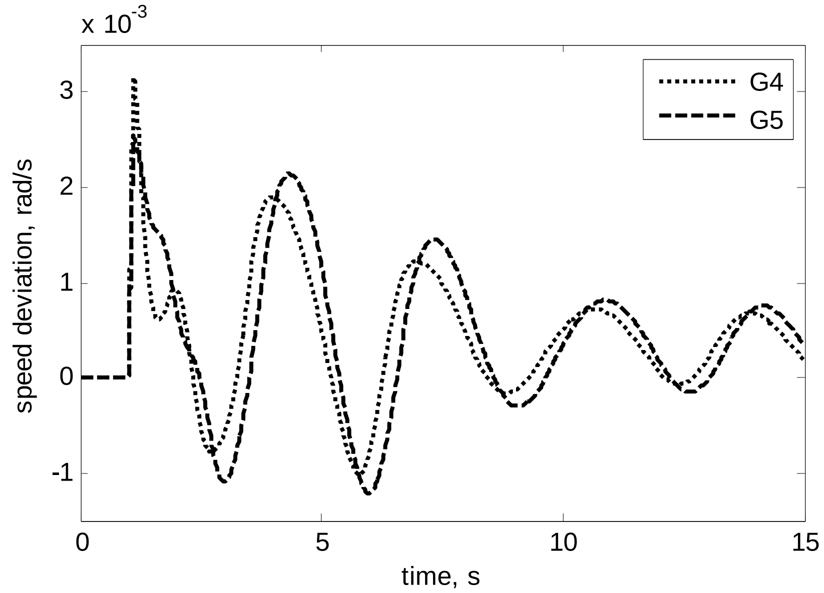

Figure 4-11: Example of coherent generators
(speed deviation response for large disturbance at bus 16)

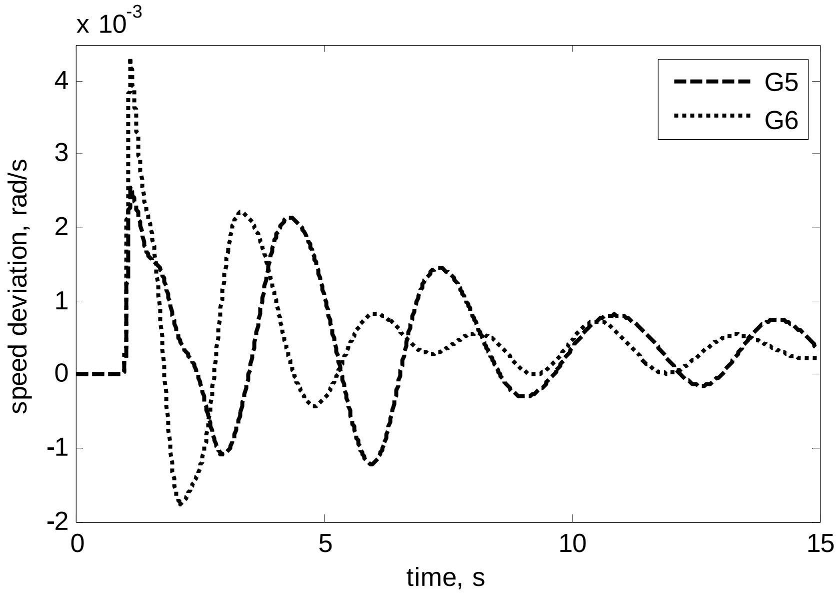

Figure 4-12: Example of non-coherent generators
(speed deviation response for a large disturbance at bus 16)

4.5.3 Selection of Input/Output Signals

The presented PCA-based cluster analysis method can be used to reduce number of I/O signals for WAMS based damping controllers. Candidate measurement signals, i.e. voltage phase angles, can be clustered using the method to identify similarities/differences between them. Signals from generators clustered in the same group have similar observability/controllability information. Amount of redundant information in the final reduced set of signals can be reduced by selecting only one signal from each group. These representative signals are chosen such that they carry the highest modal information among other signals from the same group. A representative signal is selected in this approach such that it has the largest cumulative sum of modal observability/controllability factors for the set of modes of interest among other signals in the same group. Each group therefore is represented by one measurement signal (one input signal to the SWAC) and one control signal (one output signal from the SWAC). Number of I/O signals hence is the same as the number of clusters.

The voltage phase angle responses of each generator bus for large disturbance, consisting of a self-clearing three-phase fault lasting for 100 ms, are used to form the data matrix. In order to reduce effect of disturbance location on the clustering result, 27 fault locations are considered. Figure 4-13 shows the voltage phase angle responses of generator buses for 27 disturbances. The 27 responses of each generator bus are combined (in cascade order) to form one row vector. The data matrix $\boldsymbol{X}$ is then formed using the 10 column vectors and the PCA decomposition is applied. The resulting *t*-scores are listed in Table 4-19 for each principal component. Spatial distances between the objects (each corresponding to a generator) in the 10-D space are computed using the Euclidean norm and are listed in Table 4-20.

The single linkage method is then applied to the distance matrix and the multi-level clustering tree is shown in Figure 4-14. An initial interpretation of the clustering tree indicates that the pair (G4,G5) has a very short height of the link combining them; thus indicating a very small spatial distance between them in the 10-D space. The height of the links combining the pairs (G6,G7) and (G2,G3) also indicate the similarity between the responses of generators in each pair. Figure 4-15 shows the voltage angle responses for a large disturbance of pairs (G2,G3), (G4,G5), and (G6,G7) where the similarity can be seen between responses of generators at each cluster.

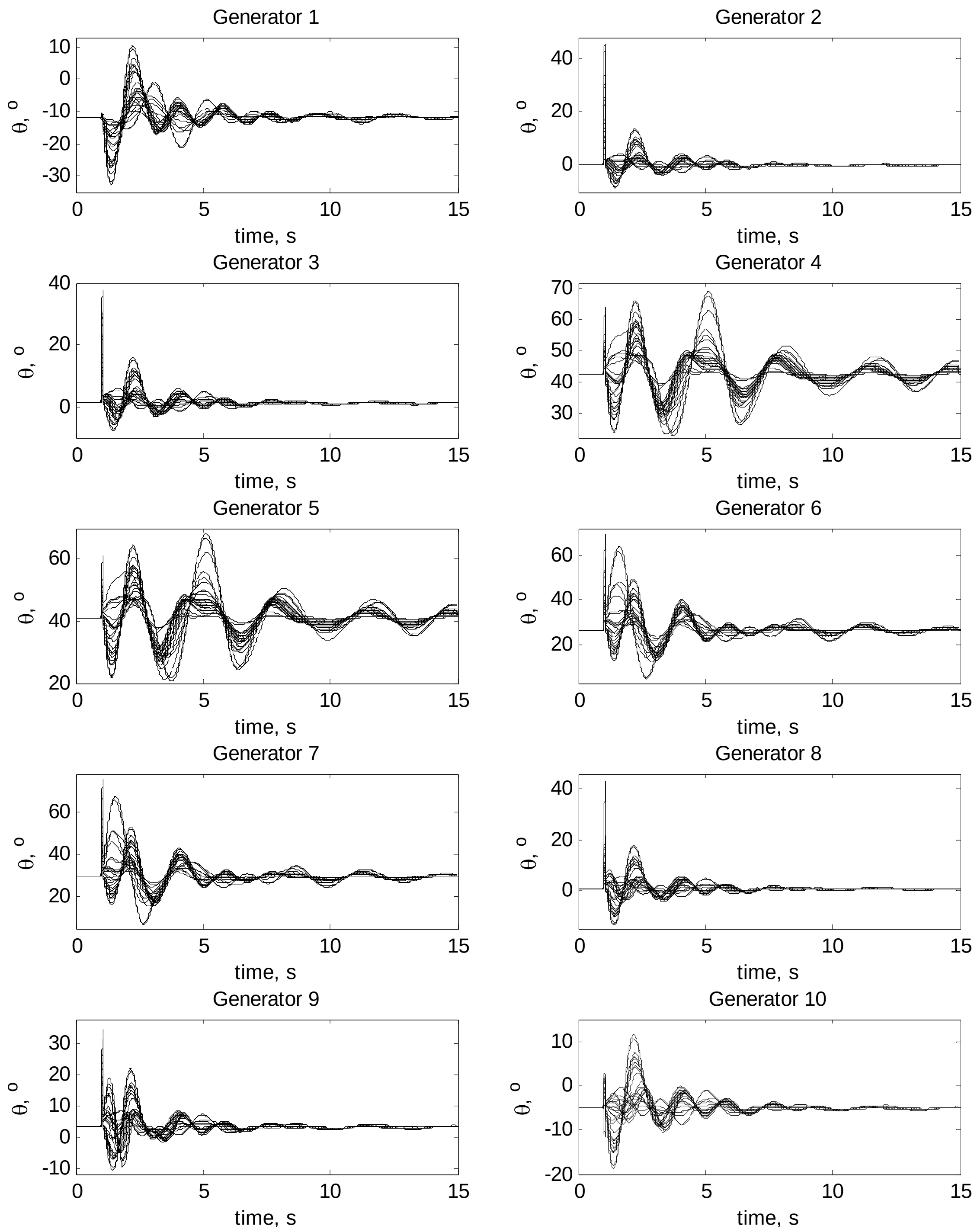

Figure 4-13: Voltage phase angle responses of generator buses for 27 large disturbances

Based on heights of the links in the multi-level hierarchical tree four clusters are formed and are shown with circles in Figure 4-14. The final clustering result is listed in Table 4-21. Each cluster then is represented by one I/O signal according to the cumulative sum of modal factors (listed in Table 4-22). Each measurement signal having the largest cumulative sum of modal observability factors among other signals in the same group is selected as the representative signal. Representative control signals are selected similarly and are listed in Table 4-23 in addition to the representative measurement signals. The final chosen set of I/O signals using the combined clustering and modal factors analysis method is listed in Table 4-24.

Table 4-19: *t*-scores (×10^4)

Generator	t_1	t_2	t_3	t_4	t_5	t_6	t_7	t_8	t_9	t_{10}
G1	-348.54	-97.12	414.74	-120.56	26.58	-20.50	0.12	-0.91	0.81	-0.48
G2	-246.04	10.70	126.34	7.43	-38.53	-4.29	-4.95	-2.98	-11.00	7.05
G3	-264.34	17.92	127.44	20.80	-70.42	-21.24	3.19	0.45	5.81	-4.39
G4	-862.00	-341.08	-148.52	-0.72	1.54	-4.74	5.08	0.53	7.05	7.51
G5	-872.19	-371.46	-149.96	-7.94	3.06	2.90	-4.86	-0.53	-6.66	-7.31
G6	-652.45	472.69	-89.75	-30.11	2.86	5.67	-14.76	-12.19	3.37	-0.11
G7	-652.58	473.94	-87.96	-22.35	6.69	-10.60	14.66	11.98	-3.39	-0.25
G8	-316.91	24.31	177.03	60.13	3.19	23.82	-17.63	15.29	2.42	0.53
G9	-329.73	47.04	170.55	169.02	29.98	-22.58	4.83	-6.45	-0.66	-0.64
G10	-302.96	11.82	175.28	5.56	-7.57	61.01	14.02	-5.43	0.29	-0.74

Table 4-20: Distance matrix (×10^2)

Generator	G1	G2	G3	G4	G5	G6	G7	G8	G9	G10
G1	0.00	3.55	3.64	8.10	8.26	8.25	8.26	3.29	4.06	3.09
G2	3.55	0.00	0.49	7.62	7.85	6.55	6.55	1.18	2.04	1.07
G3	3.64	0.49	0.00	7.54	7.78	6.43	6.43	1.22	1.98	1.22
G4	8.10	7.62	7.54	0.00	0.41	8.43	8.44	7.36	7.52	7.39
G5	8.26	7.85	7.78	0.41	0.00	8.75	8.76	7.60	7.78	7.62
G6	8.25	6.55	6.43	8.43	8.75	0.00	0.43	6.28	6.28	6.40
G7	8.26	6.55	6.43	8.44	8.76	0.43	0.00	6.28	6.25	6.41
G8	3.29	1.18	1.22	7.36	7.60	6.28	6.28	0.00	1.28	0.79
G9	4.06	2.04	1.98	7.52	7.78	6.28	6.25	1.28	0.00	1.93
G10	3.09	1.07	1.22	7.39	7.62	6.40	6.41	0.79	1.93	0.00

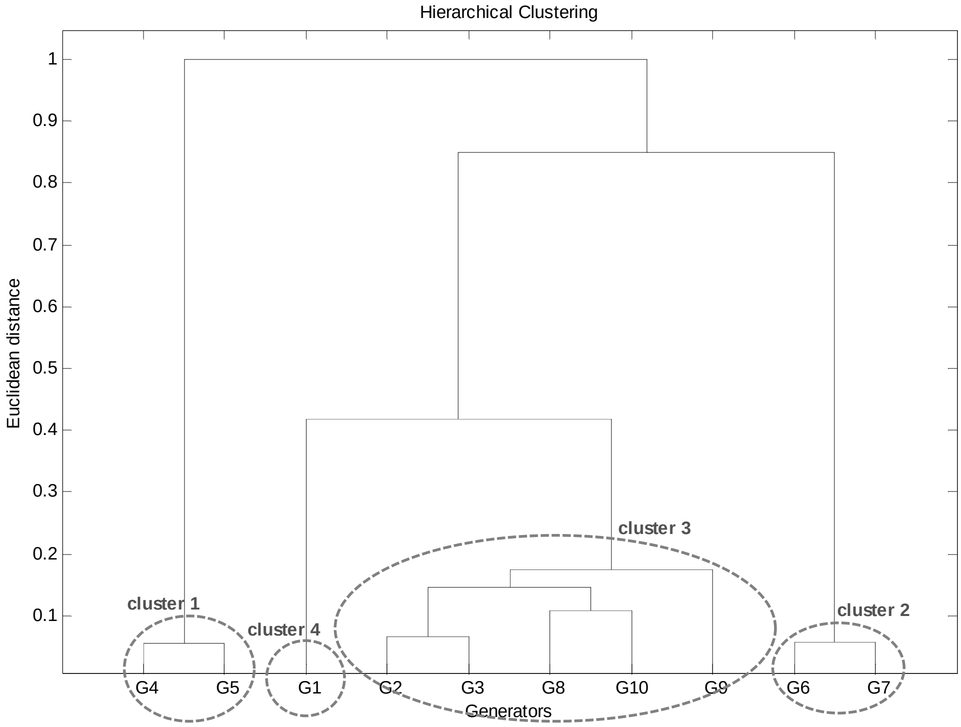

Figure 4-14: Hierarchical clustering of generators

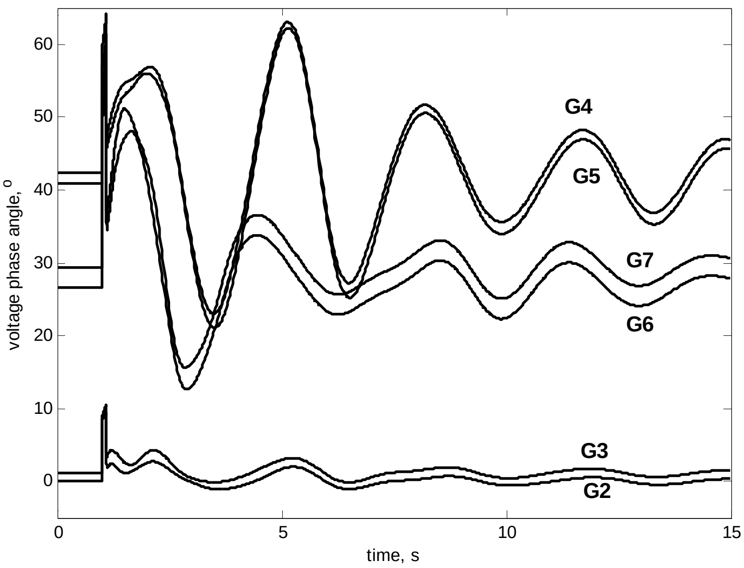

Figure 4-15: Voltage angle responses of generators in clusters (G2,G3), (G4,G5) and (G6,G7) for a large disturbance at bus 16

Table 4-21: Multi-level clustering

Clusters	Members
cluster 1	(G4,G5)
cluster 2	(G6,G7)
cluster 3	(G2,G3,G8,G10,G9)
cluster 4	G1

Table 4-22: Magnitudes of cumulative sums of modal factors

Generator	Cumulative sum of modal observability factors	Cumulative sum of modal controllability factors
G1	0.160529	26.06540
G2	0.073205	19.41411
G3	0.078349	19.22860
G4	0.325825	41.80652
G5	0.334454	52.13027
G6	0.254482	65.42227
G7	0.253798	70.19259
G8	0.087002	45.08417
G9	0.084905	35.50353
G10	0.088499	10.18689

Table 4-23: Representative I/O signals

Cluster	Members	Location of the representative measurement signal	Location of the representative control signal
cluster 1	(G4,G5)	G5	G5
cluster 2	(G6,G7)	G6	G7
cluster 3	(G2,G3,G8,G9,G10)	G10	G8
cluster 4	G1	G1	G1

Table 4-24: Locations of selected I/O signals using combined clustering and modal factors analysis

Locations of measurement signals	Locations of control signals
(G5, G6, G10, G1)	(G5, G7, G8, G1)

4.6 Comparison of Input/Output Selection Methods

As shown previously, different sets of I/O signals are selected using different selection methods. The aim of each method is to reduce number of signals while maximising the observability/controllability information carried by them. The final target is to maximise the effectiveness of the SWAC which uses the set of reduced signals. The best set of reduced signals therefore is the one that maximises the degree of effectiveness of the SWAC. Hence, the comparison of these different methods is done by comparing the degree of effectiveness of the SWAC in enhancing system stability.

4.6.1 Fixed Design of the SWAC

The SWAC is designed based on the linearised model of the New England Test System (NETS). The system is equipped with PSSs (details are included in Appendix A). Time delays are incorporated in the design and modelled using 2nd order Padé approximation. The one way delay (from the PMUs to the SWAC) is assumed to be fixed and identical for all communication channels and equals 100 ms (200 ms in total for the round-trip to generators' exciters). The modal LQG control approach is implemented to design the SWAC with (30 %) target damping ratios for the modes of interest (modes 1-3). Inputs to the SWAC are the 10 candidate measurement signals (voltage phase angles at generator buses) and its outputs are the 10 candidate wide-area control signals sent to 10 the generators' exciters (see Table 4-2).

Table 4-25 lists the open-loop and closed-loop electromechanical modes. The table lists the modal weights used to achieve the (30 %) damping ratios by fine tuning of the LQR. The Kalman filter is synthesised by following the loop transfer recovery (LTR) procedure and the tuning parameters used are as follows

$$\boldsymbol{V_o} = 10^{-3} \times \boldsymbol{I}_{\boldsymbol{p}\times\boldsymbol{p}},\ \Gamma = \boldsymbol{I}_{\boldsymbol{n}\times\boldsymbol{n}},\ \boldsymbol{W_o} = 10^{-3} \times \boldsymbol{I}_{\boldsymbol{n}\times\boldsymbol{n}}, \Theta = 10^{-3} \times \boldsymbol{I}_{\boldsymbol{m}\times\boldsymbol{m}},\ \boldsymbol{q} = 1 \tag{4.51}$$

Table 4-25: Electromechanical modes of NETS

Mode no.	Open-loop (with PSSs only)		Closed-loop (with PSSs and SWAC)		
	Mode [1/s, rad/s]	ζ [%]	Mode [1/s, rad/s]	ζ [%]	Modal weight $\left(q_{m_i}\right)$
1	-0.13±j1.91	6.63	-0.61±j1.95	30.00	0.002255
2	-0.25±j2.61	9.58	-0.81±j2.58	30.00	0.005421
3	-0.37±j3.48	10.54	-1.09±j3.47	30.00	0.003810
4	-0.88±j4.30	19.96	-0.88±j4.30	19.96	0
5	-1.05±j4.98	20.66	-1.05±j4.98	20.66	0
6	-1.15±j6.10	18.52	-1.15±j6.10	18.52	0
7	-1.28±j6.75	18.70	-1.28±j6.75	18.70	0
8	-1.45±j7.64	18.59	-1.45±j7.64	18.59	0
9	-1.63±j8.42	19.03	-1.63±j8.42	19.03	0

4.6.2 Comparisons of the Methods

Sets of I/O signals chosen by the three selection methods (listed in Table 4-26) are compared by assessing the effectiveness of the fixed SWAC. In this way fair comparison can be done between the selection methods. Table 4-27 lists the damping ratios of the closed-loop modes of interest resulting with different sets of I/O signals for the fixed SWAC. The table shows that the I/O signals selected by Method 3 (the SO algorithm) lead to the best small-signal stability improvement.

Table 4-26: Selected locations of I/O signals using different methods

No.	Method	Locations of measurement signals (inputs to the WAC)	Locations of control signals (outputs of the SWAC)
1	Modal factors analysis	(G5,G6)	(G6,G7)
2	Combined clustering and modal factors analysis	(G5, G6, G10, G1)	(G5, G7, G8, G1)
3	The SO algorithm	(G5, G6, G1)	(G5, G2, G1, G6)

Table 4-27: Damping ratios of closed-loop modes of interest using different I/O signals (fixed SWAC)

Method	ζ_1 [%]	ζ_2 [%]	ζ_3 [%]
1	7.11	13.91	11.29
2	11.90	13.01	13.53
3	12.18	14.54	16.40

The three methods are compared by assessing the effectiveness of the SWAC using transient performance analysis. Figure 4-16 and Figure 4-17 show active power and speed deviation responses, respectively, of the closed-loop system for a self-clearing three-phase fault lasting for 100 ms at bus 14 (in the middle of the network). The figures compare the closed-loop system responses when using I/O signals selected by the three methods for the SWAC. The two figures are re-printed in Figure 4-18 and Figure 4-19 zoomed in for the last 10 seconds of simulation (for a better analysis of the responses). It can be seen from the figures that the set of I/O signals selected by Method 3 leads to the best performance of the SWAC during large disturbances. It can be concluded from the shown small-signal and transient performance analysis results that the best set of reduced I/O signals is the one selected by Method 3 (the SO algorithm).

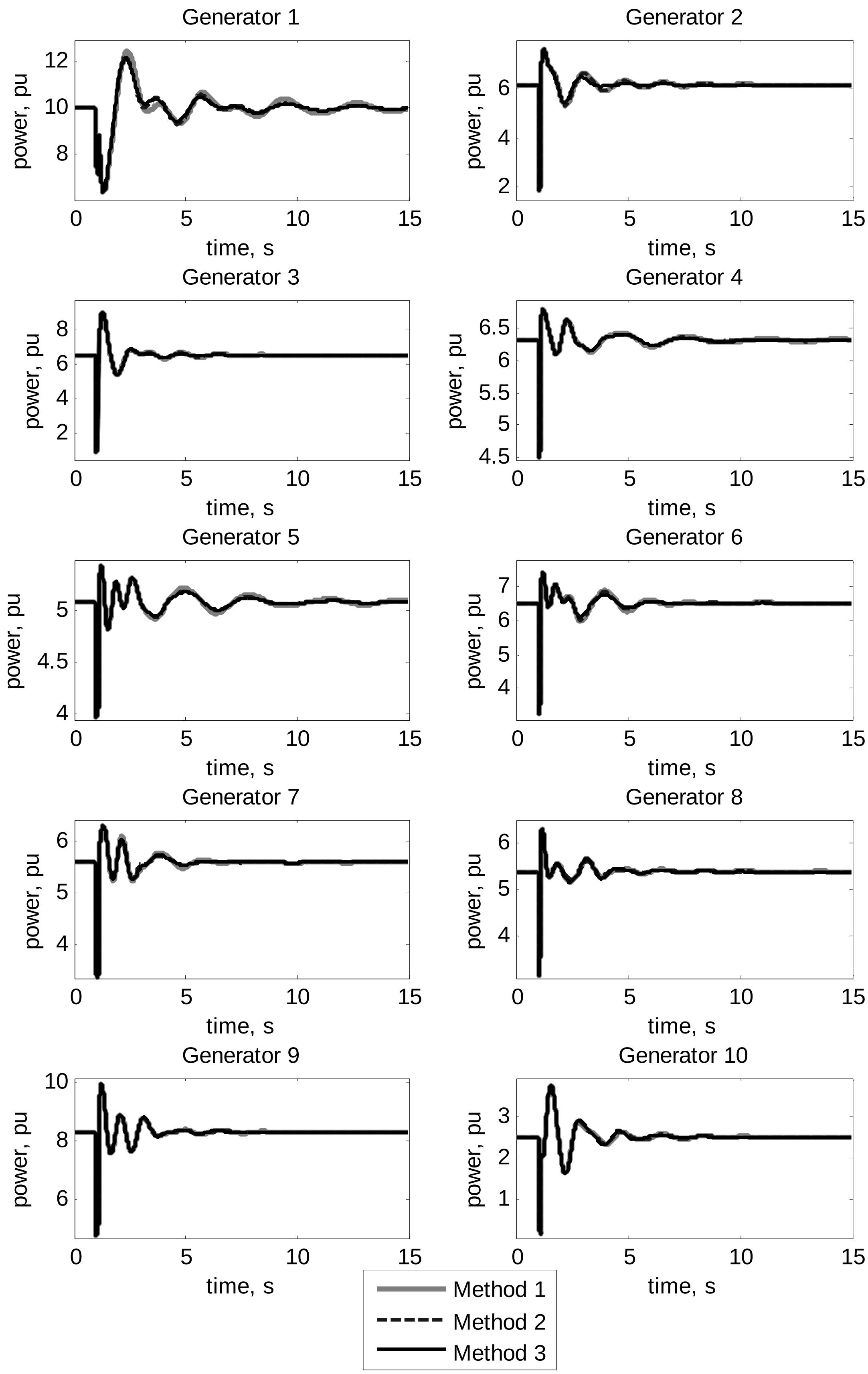

Figure 4-16: Active power responses for a large disturbance at bus 14 using different I/O signals

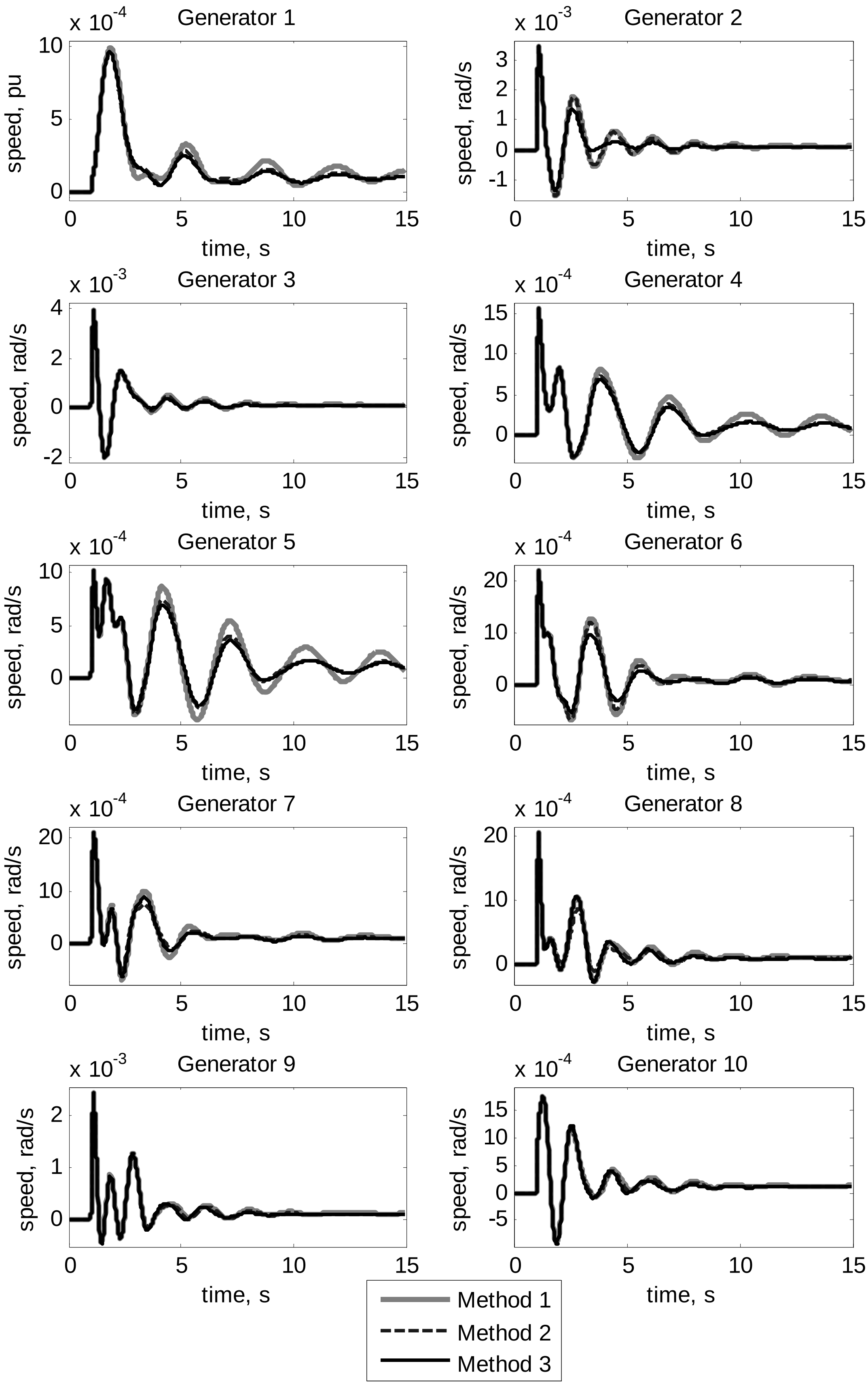

Figure 4-17: Speed deviation responses for a large disturbance at bus 14 using different I/O signals

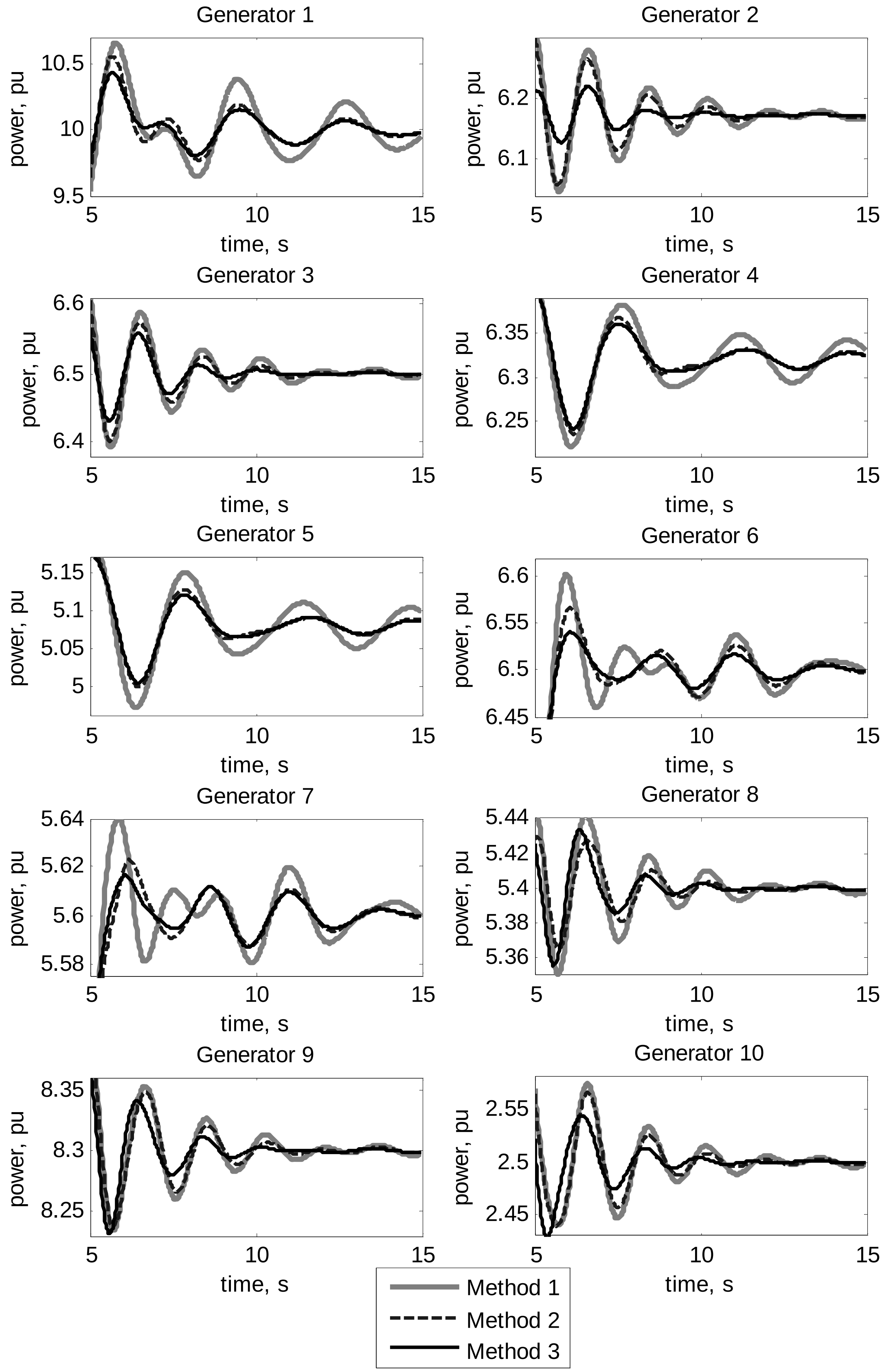

Figure 4-18: Active power responses for a large disturbance at bus 14 using different I/O signals (last 10 seconds of simulation)

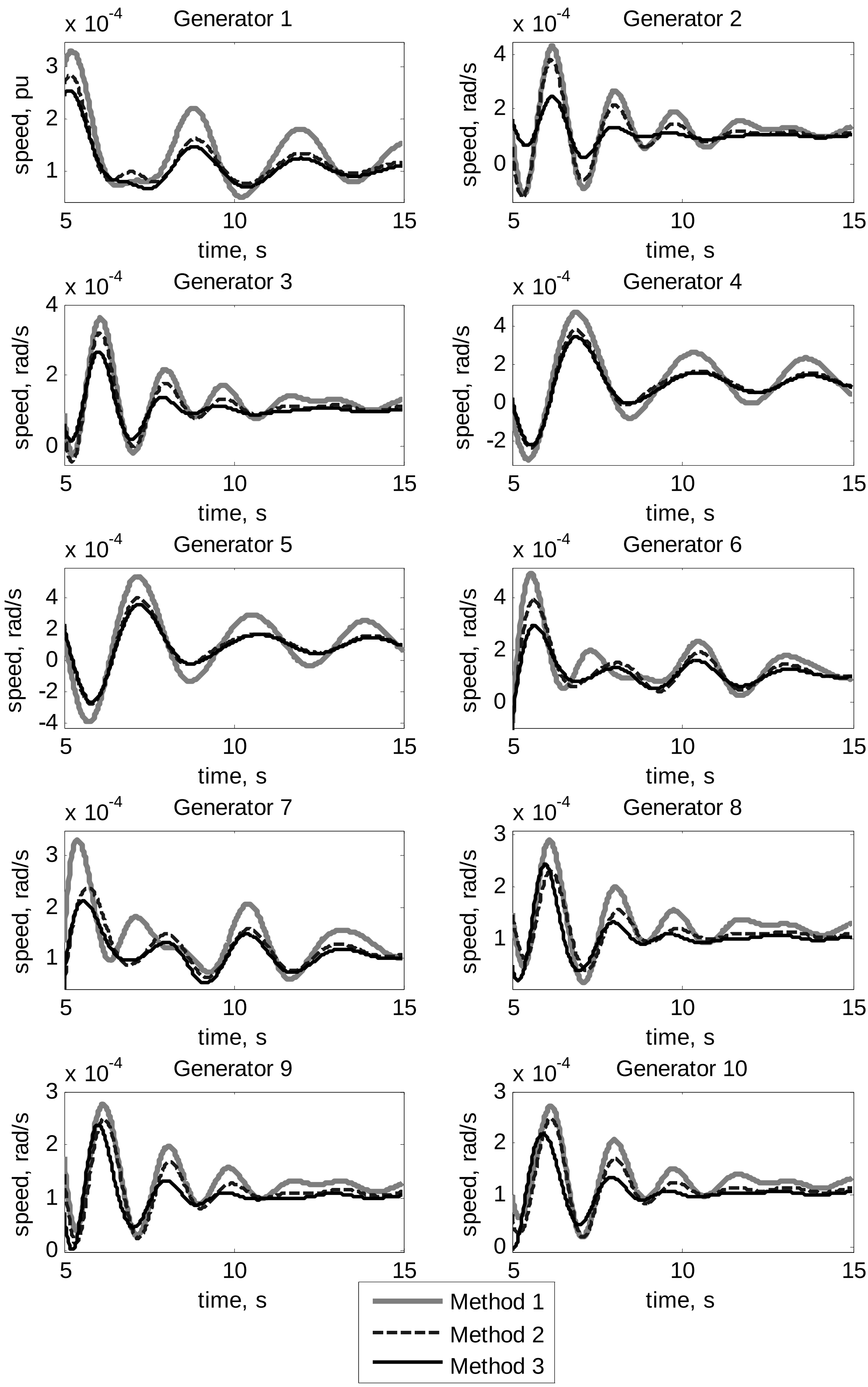

Figure 4-19: Speed deviation responses for a large disturbance at bus 14 using different I/O signals (last 10 seconds of simulation)

4.7 Summary

Three approaches for selection of I/O signals for WAMS based damping controllers were presented. The methods were applied to the modified NETS and results of each method were presented and discussed. The methods emphasis is on increasing the effectiveness of the SWAC in enhancing the stability of the system while reducing the number of used signals.

The presented methods include approach based on modal factors analysis where signals with the largest modal observability/controllability factors for each individual mode of interest are selected. The second selection method is based on the SO algorithm, a tool for the optimal placement of measurement devices, where its application is extended to handle the problem of I/O signal selection for WAMS based damping controllers. The algorithm maximises the coverage of dynamic (observability) information about the modes of interest while considering sensitivity of selected sites to other modes in the system. Detailed mathematical description of the selection procedure was presented with illustrative example on vector orthogonal projection used in the algorithm.

The PCA time domain coherency identification method was presented and reviewed in this chapter. Features of the method include fast identification of coherent generators without any model information, it does not need linearisation and modal information of the system and it relies only on PMUs measurements. The method therefore can be regarded as an effective tool for the identification of coherent generators. Classification made by the method however depends entirely on visual inspection that may lead to inaccurate results and the method alone is limited to those cases that require only three principal components. A novel approach was presented in this chapter to overcome these limitations and draw backs. The method is supplemented by a cluster analysis technique to accurately classify coherent groups of generators. The PCA-based clustering method is used to select optimal I/O signal by combining it with modal factors analysis. Locations of candidate signals are firstly clustered into different groups using the PCA-based clustering technique. The cumulative sums of modal factors for the set of modes of interest are then used to select representative signals from each individual group. I/O signals for the SWAC are therefore selected and reduced using the combined method.

Reduced sets of I/O signals determined using the three selection methods were compared using small-signal and transient performance analysis. The degree of effectiveness of a fixed SWAC, designed using all sets of candidate signals, in enhancing system stability is used for the comparisons. Results showed that the best set of reduced I/O signals that enhances the effectiveness of the SWAC is the one determined using the SO algorithm.

5 ENHANCEMENT OF MULTI-MACHINE SYSTEM STABILITY

5.1 Introduction

This chapter presents a Wide-Area Measurement System (WAMS) based control scheme for damping of multiple interarea oscillations in a multi-machine power system. Optimal set of input/output (I/O) signals is used for the WAMS based damping controller. The multi-input multi-output (MIMO) damping controller is designed using the modal Linear Quadratic Gaussian (LQG) control approach. Effectiveness of the controller in enhancing the system stability is demonstrated using small-signal and transient performance analysis on different case studies.

5.2 Design of the Controller

The multi-machine test system used in this study is the New England Test System (NETS) described in Chapter 4. The electromechanical modes of linearised model of the NETS and their frequencies, damping ratios, and mode shapes are listed in Table 5-1. The system is equipped with PSSs (full details are included in Appendix A). The targeted modes by the WAMS based damping controller, i.e. modes of interest, are modes 1-3. The best set of reduced I/O signals, according to the comparisons made in Chapter 4, is used by the Supplementary Wide-Area Controller (SWAC) and is listed in Table 5-2. Figure 5-1 shows the network diagram of the NETS, locations of PMUs, and

I/O signals of the used SWAC. Fibre optics communication links are assumed for the transmission of PMU measurements to the SWAC and for transmission of the wide-area control signals to the chosen generators' exciters. The one way time delays (from PMUs to the SWAC) are assumed to be fixed and identical for all communication channels and equal to 100 ms (200 ms in total for the round-trip to generators' exciters).

Table 5-1: Electromechanical modes of modified NETS

Mode no.	Mode [1/s, rad/s]	ζ [%]	f [Hz]	Mode shape
1	-0.13±j1.91	6.63	0.30	G1 vs. (G4,G5,G6,G7)
2	-0.25±j2.61	9.58	0.42	(G4,G5) vs. (G6,G7)
3	-0.37±j3.48	10.54	0.55	(G6,G7) vs. (G2,G3,G8,G9,G10)
4	-0.88±j4.30	19.96	0.68	G2 vs. (G3,G8,G9,G10)
5	-1.05±j4.98	20.66	0.79	G3 vs. (G2,G8,G9,G10)
6	-1.15±j6.10	18.52	0.97	G10 vs. (G8,G9)
7	-1.28±j6.75	18.70	1.07	G8 vs. G9
8	-1.45±j7.64	18.59	1.21	G6 vs. G47
9	-1.63±j8.42	19.03	1.34	G4 vs. G45

Table 5-2: Reduced I/O signals of the SWAC

Measurements signals			Control signals		
Link	**Signal**	**Location**	**Link**	**Signal**	**Location**
y_1	θ_{39}	G1	u_1	V_{WAC1}	G1
y_5	θ_{34}	G5	u_2	V_{WAC2}	G2
y_6	θ_{35}	G6	u_3	V_{WAC3}	G5
-	-	-	u_4	V_{WAC4}	G6

The SWAC is designed using the modal Linear Quadratic Gaussian (LQG) control approach described in Chapter 3. The approach enables the controller to be designed based on either full or reduced order power system model. In real power systems controllers are designed usually based on reduced models; due to the size of the system, difficulties in getting full model data …etc. The second approach therefore is implemented here to demonstrate the methodology in compliance with real power systems.

The Hankel singular values of the 124th order linearised power system model, without time delays, are shown in Figure 5-2. Reduction to 13th order was found to give good approximation of the 124th order linearised power system model in the frequency range of the modes of interest as can be seen from the singular value plot shown in Figure 5-3 (only the largest singular value is shown). Modes of interest are retained with good accuracy in the reduced system model and are listed in Table 5-3.

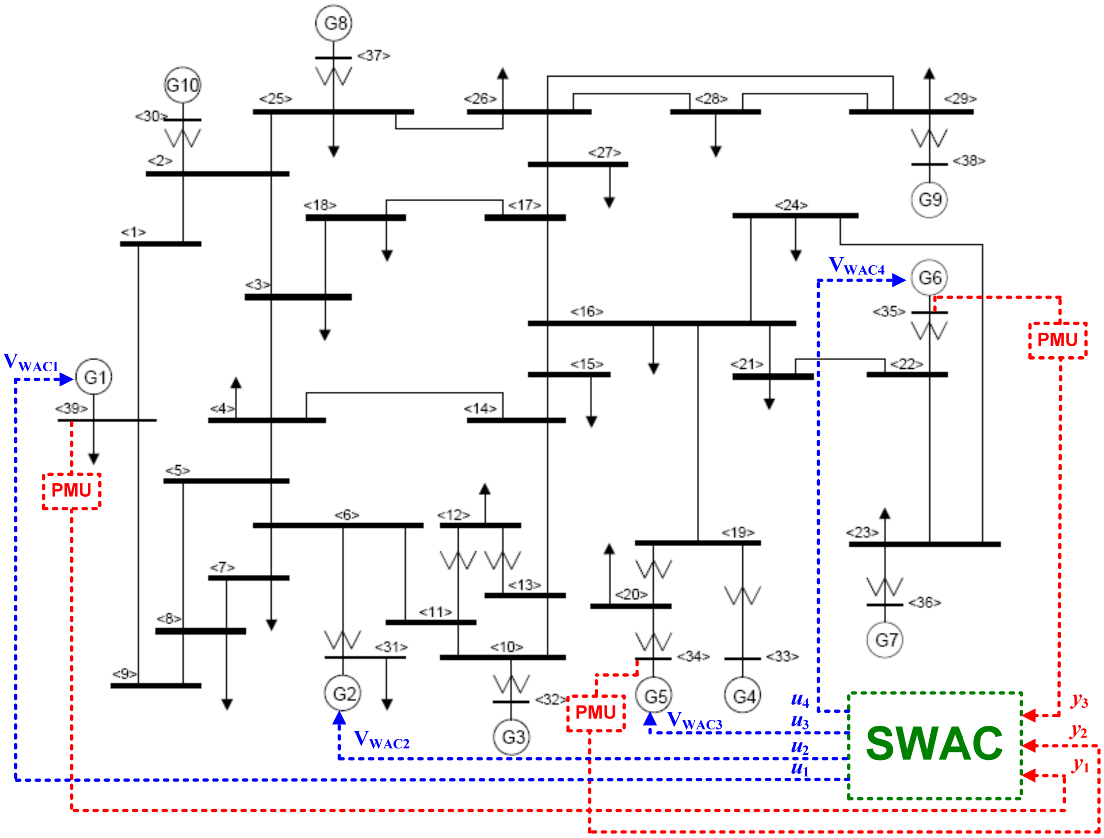

Figure 5-1: New England test system with SWAC

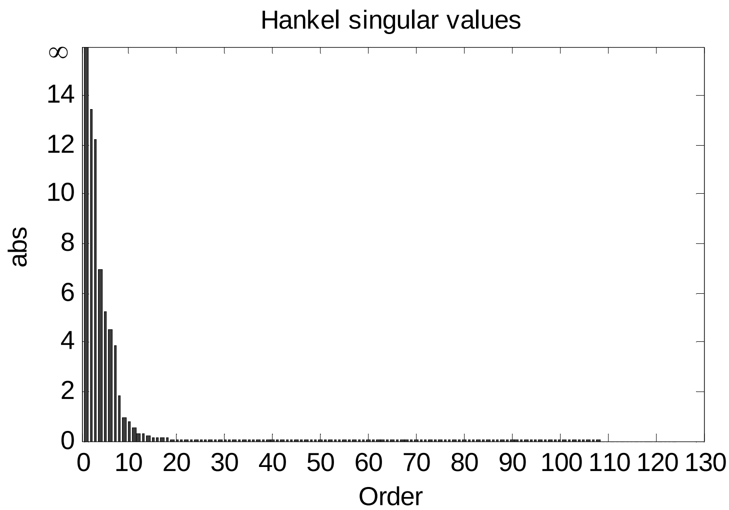

Figure 5-2: Hankel singular value plot of the 124th open-loop model (without time delays) (the first singular value in infinity)

Models of time delays, using 2nd order Padé approximation, of the SWAC's p=3 inputs and m=4 outputs are then added to the 13th order reduced model. The open-loop system model with time delays therefore is (13+14=27th) order. The LQR is designed using the modal LQG approach based on the 27th order model, incorporating time delays, with target damping ratios of 30 % for modes 1-3. Table 5-4 lists the resulting modes of interest of the LQR system where it can be seen that exact target damping ratios are obtained by fine tuning of modal weights.

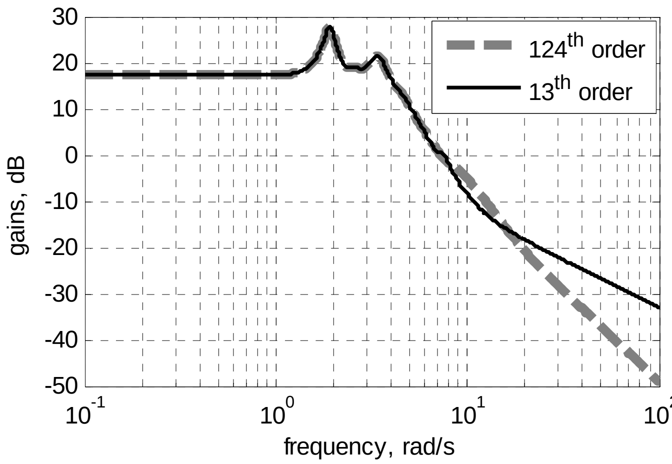

Figure 5-3: Open-loop system order reduction

Table 5-3: Modes of interest of the full and reduced order open-loop models

Order	Mode 1 [1/s , rad/s]	ζ_1 [%]	Mode 2 [1/s , rad/s]	ζ_2 [%]	Mode 3 [1/s , rad/s]	ζ_3 [%]
124	-0.13±j1.91	6.63	-0.25±j2.61	9.58	-0.37±j3.48	10.54
13	-0.13±j1.91	6.63	-0.25±j2.61	9.53	-0.36±j3.46	10.34

Table 5-4: Modes of interest of the LQR system
(designed based on reduced order open-loop model)

Modal Weights $\left[q_{m_1} \mid q_{m_2} \mid q_{m_3}\right]$	Mode 1 [1/s , rad/s]	ζ_1 [%]	Mode 2 [1/s , rad/s]	ζ_2 [%]	Mode 3 [1/s , rad/s]	ζ_3 [%]
$\left[0.1161 \mid 0.2442 \mid 0.2726\right]$	-0.61±j1.94	30.00	-0.81±j2.59	30.00	-1.09±j3.46	30.00

The Kalman filter is synthesised by following the Loop Transfer Recovery (LTR) procedure and the tuning parameters used are as follows

$$\boldsymbol{V_o} = 10^{-3} \times \boldsymbol{I}_{p\times p},\ \Gamma = \boldsymbol{I}_{n\times n},\ \boldsymbol{W_o} = 10^{-3} \times \boldsymbol{I}_{n\times n}, \Theta = 10^{-3} \times \boldsymbol{I}_{m\times m},\ \boldsymbol{q} = 10 \tag{5.1}$$

Figure 5-4 shows the LTR procedure with various values of $\boldsymbol{q}$ (only the largest singular value is shown). The tuning parameter $\boldsymbol{q}$ was selected such that the best partial recovery, in the frequency range of modes of interest, is achieved without having excessive Kalman filter gains.

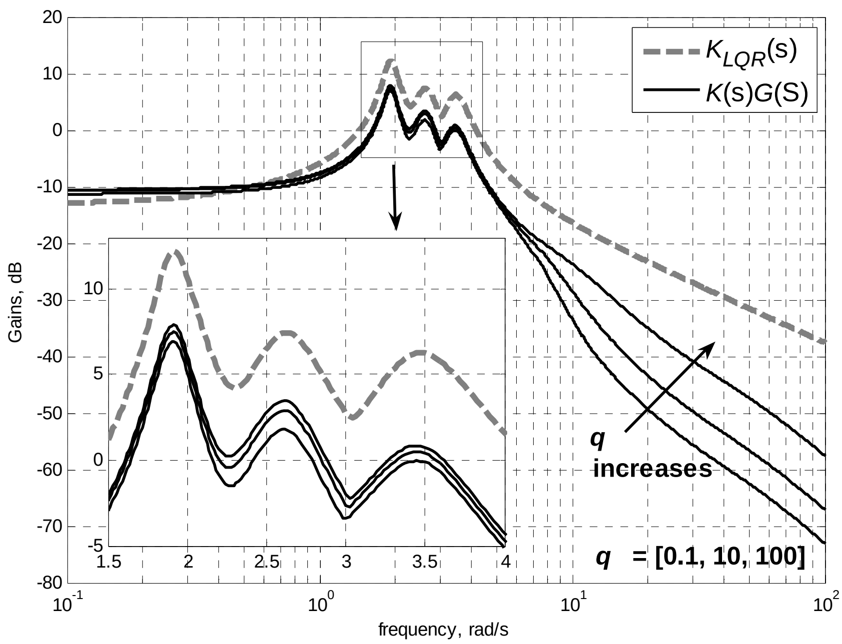

Figure 5-4: LTR procedure with various values of *q*

The closed-loop system is formed with the SWAC designed using the modal LQG approach and the resulting electromechanical modes are listed in Table 5-5. It can be seen that the damping ratios of mode 1-3 are very close to the target ratio, i.e. 30 %. The small differences are resulting from designing the SWAC based on an approximation of the open-loop system. Other modes in the closed-loop system are almost the same as in the open-loop system case.

Figure 5-5 shows the SWAC's Hankel singular values where it can be seen that a further reduction can be made to the controller. Reduction to order 16 was found to give a good approximation of the 27th order SWAC as can be seen from the singular value plot shown in Figure 5-6. The closed-loop electromechanical modes resulting when using the 16th order SWAC are listed in Table 5-5 and compared with the case when using the 27th order SWAC. The damping ratios of the modes of interest are similar when using either of the two SWACs and therefore confirm the good approximation achieved using a 16th order reduced SWAC.

Table 5-5: Closed-loop electromechanical modes

Mode no.	with 27th order SWAC		with 16th order SWAC	
	Mode [1/s, rad/s]	ζ [%]	Mode [1/s, rad/s]	ζ [%]
1	-0.60±j1.93	29.50	-0.59±j1.91	29.57
2	-0.78±j2.53	29.54	-0.76±j2.53	28.78
3	-1.11±j3.19	32.82	-1.08±j3.26	31.47
4	-0.86±j4.38	19.30	-0.88±j4.40	19.53
5	-1.06±j4.95	20.94	-1.07±j4.95	21.03
6	-1.14±j6.09	18.39	-1.14±j6.09	18.40
7	-1.28±j6.75	18.69	-1.28±j6.75	18.69
8	-1.50±j7.73	19.10	-1.51±j7.73	19.22
9	-1.63±j8.31	19.24	-1.63±j8.32	19.24

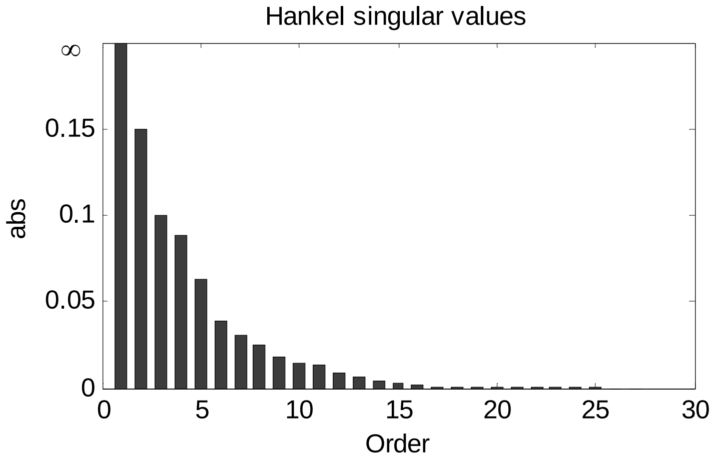

Figure 5-5: Hankel singular value plot of the 27th order SWAC (the first singular value in infinity)

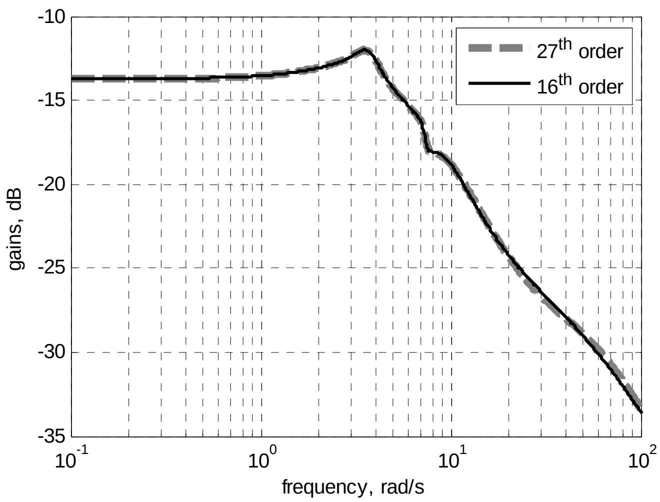

Figure 5-6: Further controller reduction

5.3 Assessment of System Stability

The stability of the power system, with the proposed control scheme, is comprehensively assessed for different case studies using both small-signal and transient performance analysis. The assessment starts with system performance following small and large disturbances. The stability of the power system then is analysed over wide range of operating conditions (410 in total) involving different network topologies and power transfers. The performance of the system is also assessed for variations in time delays associated with the transmission of the SWAC's I/O signals. Finally, the stability of the system is assessed for possible communication link failures.

5.3.1 Small Disturbances

The system performance following small disturbances consisting of 5 % step increase in the reference voltage for each of network generators is assessed. Figure 5-7 shows the active power responses of network generators for a small disturbance at generator 1. System responses to small disturbances at the rest of network generators are shown in Appendix D. The figures clearly show that the WAMS based damping controller, i.e. the 16th order SWAC, effectively enhances system stability in case of small disturbances.

5.3.2 Large Disturbances

The system is assessed for a large disturbance consisting of a 100 ms, self-clearing, three-phase fault (the same type of fault will be used in all subsequent large disturbance simulations). System responses for a large disturbance at bus 14, in the middle of the network, are shown in Figure 5-8 and Figure 5-9. The figures show that system transient performance is enhanced using the WAMS based damping controller. Figure 5-10 shows the control actions of PSSs and the SWAC for the disturbance. The control signals of PSSs in the closed-loop system (with PSSs and the SWAC) are settling down faster than in the case of open-loop system (with PSSs only). The figure shows also that the magnitude of the SWAC's control signals, at the selected generators, are much smaller than the control signals of PSSs. This indicates the supplementary action of the SWAC without affecting the functionality of PSSs.

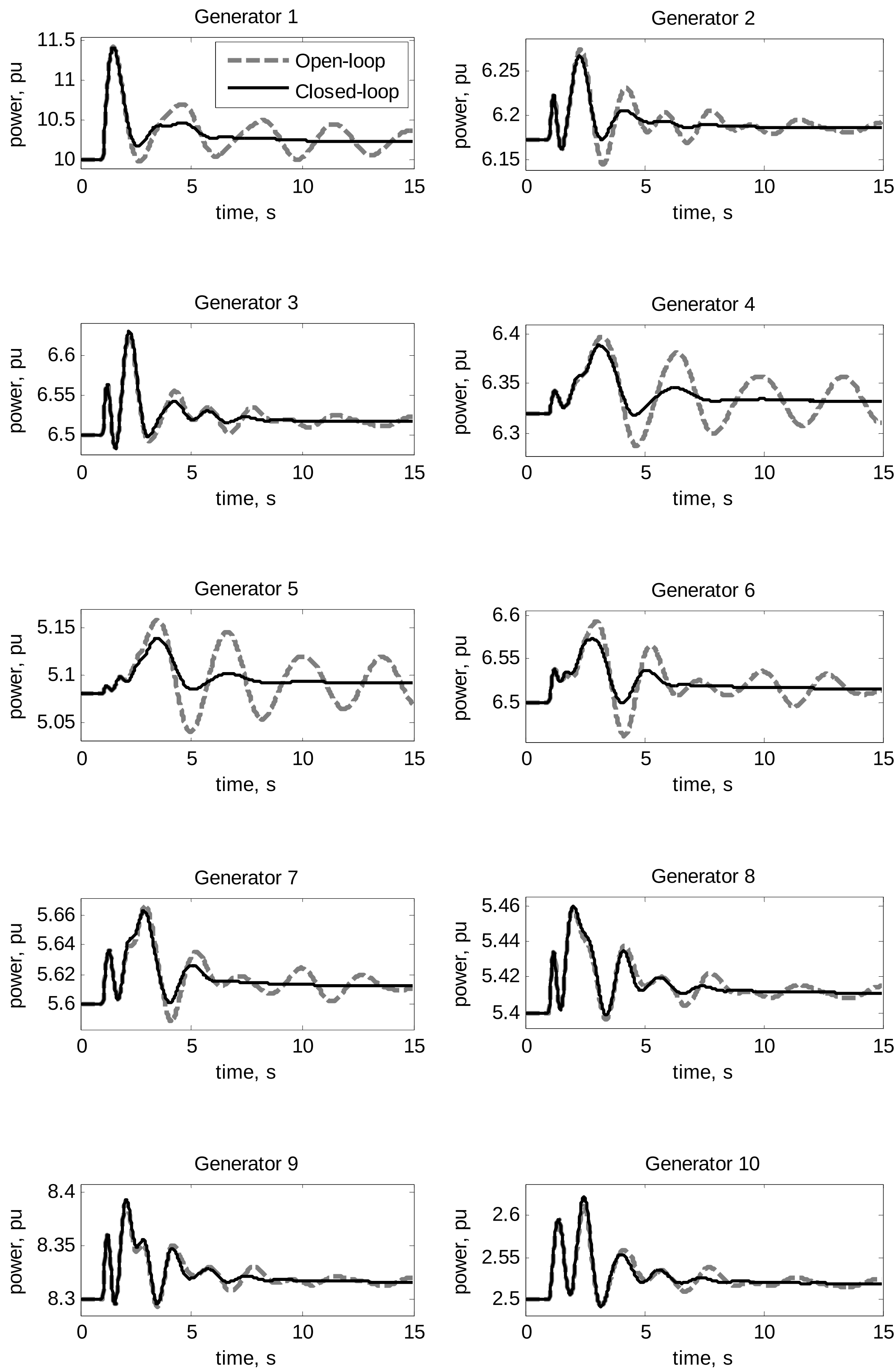

Figure 5-7: Active power responses for a small disturbance at generator 1

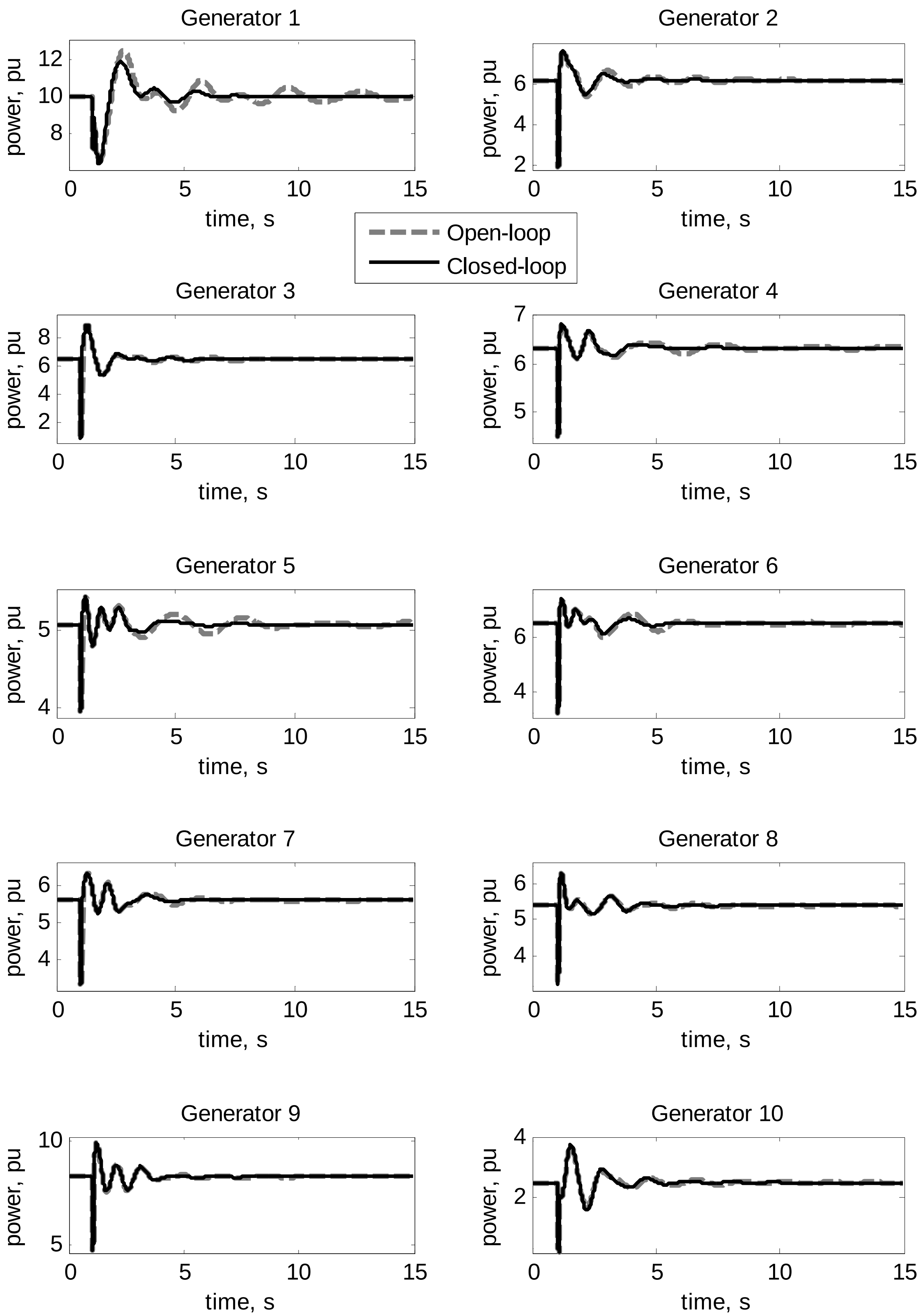

Figure 5-8: Active power responses for a large disturbance at bus 14

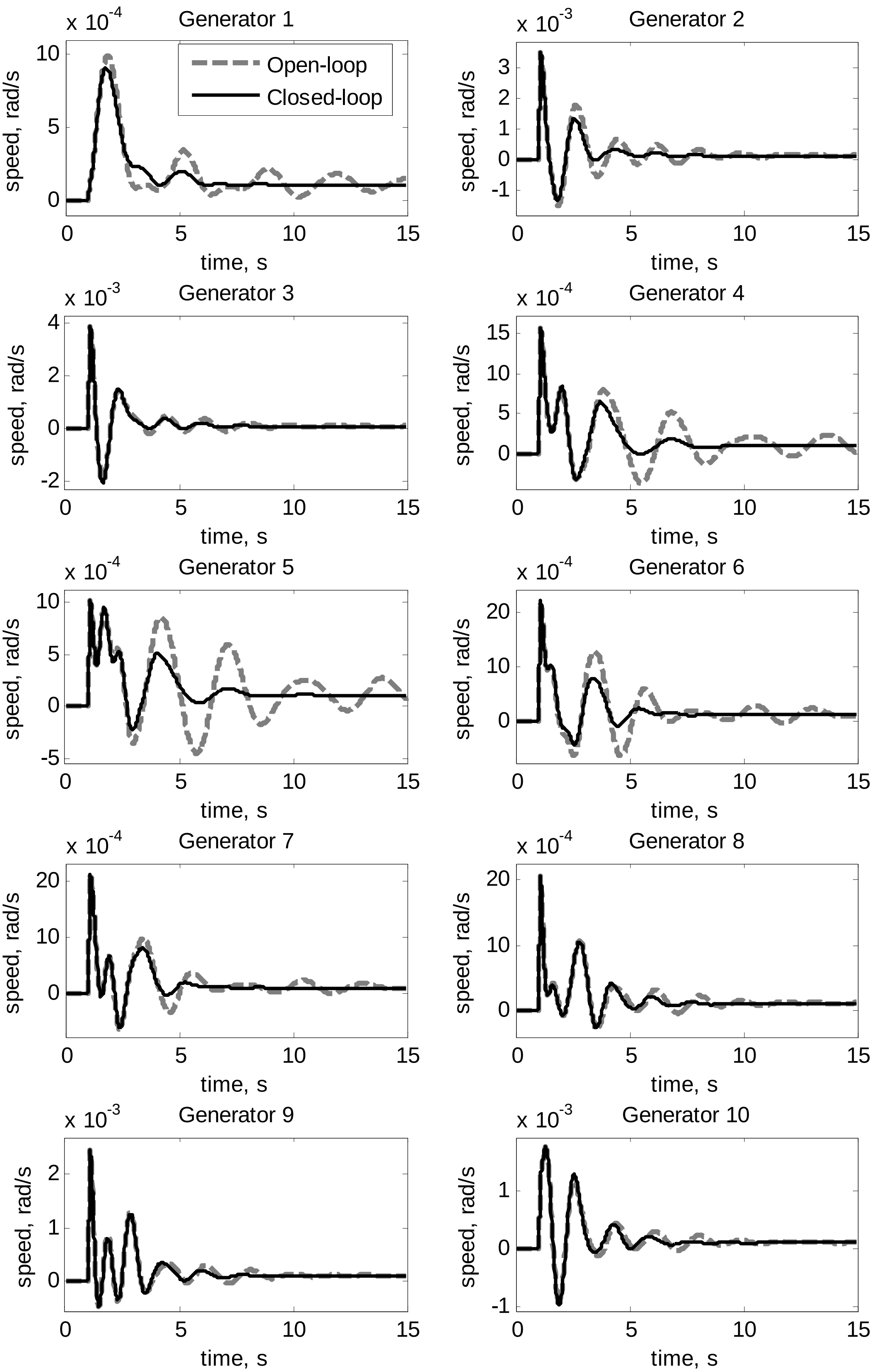

Figure 5-9: Speed deviation responses for a large disturbance at bus 14

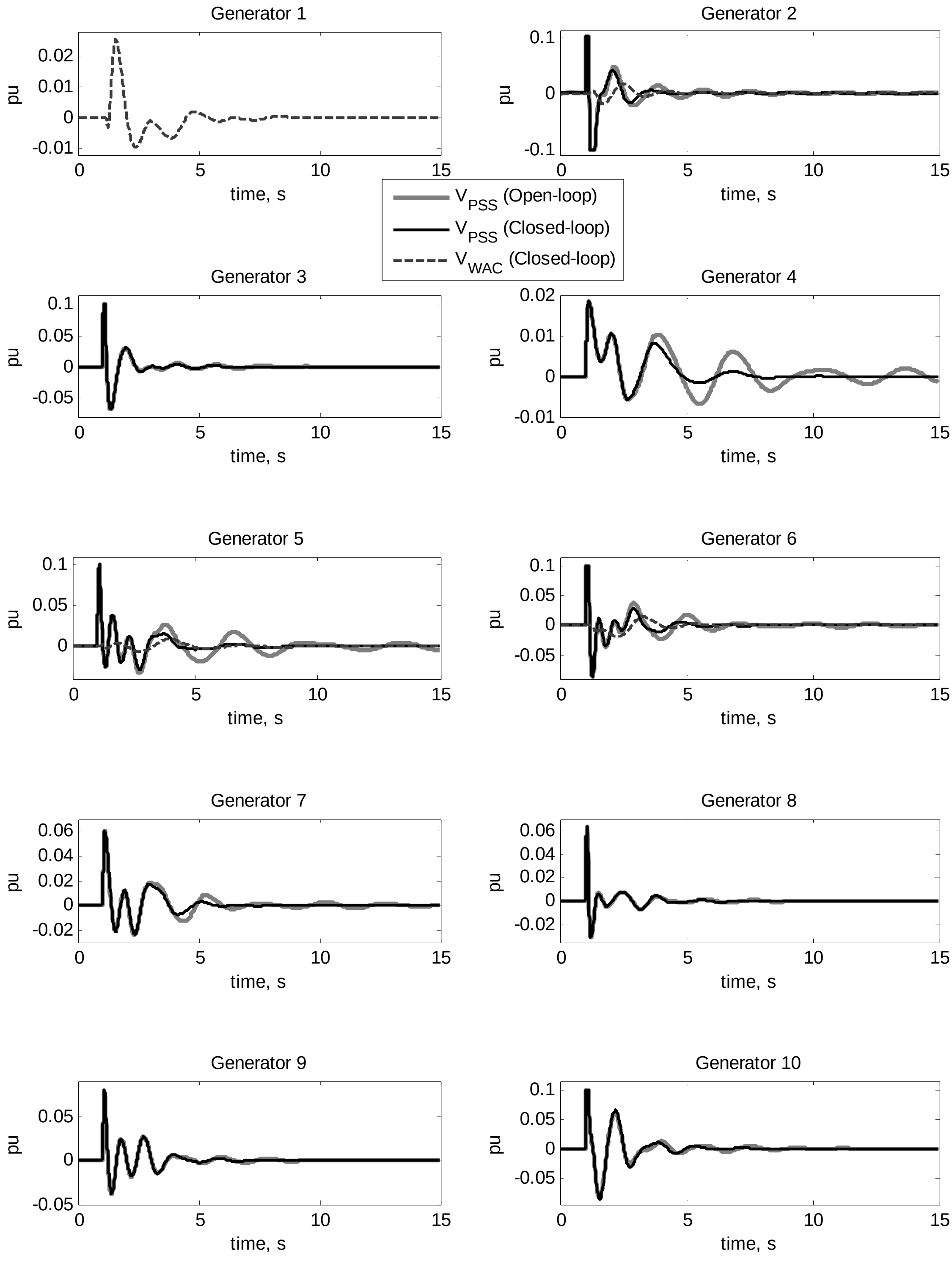

Figure 5-10: Control actions for a large disturbance at bus 14

5.3.3 Topological Changes

Stability of the system is comprehensively assessed for cases when network topology changes. The assessment includes those cases when one or two of network 34 lines are out of service. Fixed parameters were used for the voltage support devices, i.e.

capacitors, for all operating conditions used in the assessment. Table 5-6 lists the load flow statistics for these changes in network topology. The load flow condition was examined for each of these cases to ensure that network voltages are within acceptable ranges, i.e. 0.90-1.10 p.u.

Table 5-6: Load flow statistics for changes in network topology

Out of service lines	Number of cases	Load flow status			
		Not converging	Converging		
			Acceptable voltages $0.9p.u. \geq \lvert V_i \rvert \geq 1.1p.u.$	Over-voltages $\lvert V_i \rvert \geq 1.1p.u.$	Under-voltages $0.9p.u. \geq \lvert V_i \rvert$
one line	34	4	29	1	0
two lines	561	151	371	29	10
total	595	155	400	30	10

Modal analysis statistics are listed in Table 5-7. The SWAC, together with PSSs, stabilises the system for 30 contingencies where PSSs alone couldn't. The damping ratios of modes 1-3 are listed in Table 5-8 for those cases when the system with PSSs only becomes unstable. The listed unstable open-loop system cases involve one or two modes of interest (modes 1-3). Other electromechanical modes were stable for all studied cases and had not been affected by the disconnected lines. The table shows that the SWAC stabilises modes 1-3 and was able to keep their damping ratios close to 30 % in most of the cases.

Table 5-7: Modal analysis statistics for changes in network topology

Out of service lines	Number of cases	Open-loop (with PSSs only)		Closed-loop (with PSSs and SWAC)	
		Stable	Unstable	Stable	Unstable
one line	29	28	1	29	0
two lines	371	342	29	371	0
total	400	370	30	400	0

Figure 5-11 shows the active power responses for a large disturbance at bus 14 at operating condition (OC-A1). Active power responses for the listed operating conditions are shown in Appendix D. Transient simulations confirm the small-signal stability results listed in Table 5-8 that the SWAC stabilises the system for different possible contingencies while PSSs alone couldn't.

Table 5-8: Damping ratios of modes 1-3 for different operating conditions (A)

Operating condition	Out of service lines(s)		Open-loop (with PSSs only)			Closed-loop (with PSSs and SWAC)		
			ζ_1 [%]	ζ_2 [%]	ζ_3 [%]	ζ_1 [%]	ζ_2 [%]	ζ_3 [%]
OC-A1	16-17	-	-0.88	11.22	8.97	35.08	32.57	29.50
OC-A2	16-17	1-2	-0.72	10.70	7.11	21.87	32.15	32.67
OC-A3	16-17	1-39	-0.71	10.67	7.09	22.59	32.14	32.79
OC-A4	16-17	2-3	-1.26	11.11	9.13	21.96	32.89	28.77
OC-A5	16-17	2-25	-0.96	11.23	8.10	35.59	32.55	32.81
OC-A6	17-18	2-25	-4.06	11.63	8.65	10.93	32.49	29.82
OC-A7	16-17	3-4	-0.12	11.24	5.67	6.38	33.08	26.17
OC-A8	16-17	3-18	-0.88	11.20	9.98	34.35	32.59	30.60
OC-A9	13-14	4-5	6.47	12.20	-5.66	38.78	31.76	2.36
OC-A10	16-17	4-5	-0.95	11.22	9.26	33.34	32.60	29.87
OC-A11	16-17	4-14	-1.17	11.40	9.22	24.08	32.72	28.41
OC-A12	16-17	5-6	-1.15	11.12	8.04	31.62	32.62	27.13
OC-A13	16-17	5-8	-0.95	11.21	8.32	32.91	32.62	28.86
OC-A14	16-17	6-7	-1.00	11.19	8.24	32.61	32.62	28.65
OC-A15	16-17	6-11	-1.38	11.16	8.63	25.37	32.65	30.73
OC-A16	16-17	7-8	-0.91	11.22	8.60	33.71	32.61	28.73
OC-A17	16-17	8-9	-0.28	11.82	7.21	10.09	32.55	27.18
OC-A18	16-17	9-39	-0.25	11.84	7.17	11.27	32.51	27.30
OC-A19	16-17	10-11	-1.23	11.18	8.68	28.54	32.62	30.34
OC-A20	16-17	10-13	-1.26	11.31	8.21	28.82	32.63	29.30
OC-A21	16-17	13-14	-1.20	11.46	8.01	29.93	32.59	29.28
OC-A22	17-18	16-17	-0.94	11.18	9.49	33.17	32.61	30.64
OC-A23	17-27	16-17	-0.93	11.18	9.50	33.37	32.61	30.67
OC-A24	22-23	16-17	-0.35	6.36	8.99	32.25	31.67	23.69
OC-A25	25-26	16-17	-0.90	11.22	10.41	34.27	32.62	30.03
OC-A26	26-27	16-17	-1.21	11.06	8.57	28.46	32.70	30.08
OC-A27	26-28	16-17	-0.91	11.21	9.07	34.65	32.58	30.50
OC-A28	26-29	16-17	-0.93	11.20	8.92	34.44	32.58	30.55
OC-A29	28-29	16-17	-0.95	11.19	8.44	34.01	32.58	30.68
OC-A30	17-27	17-18	-0.37	11.67	9.52	45.24	32.38	30.91

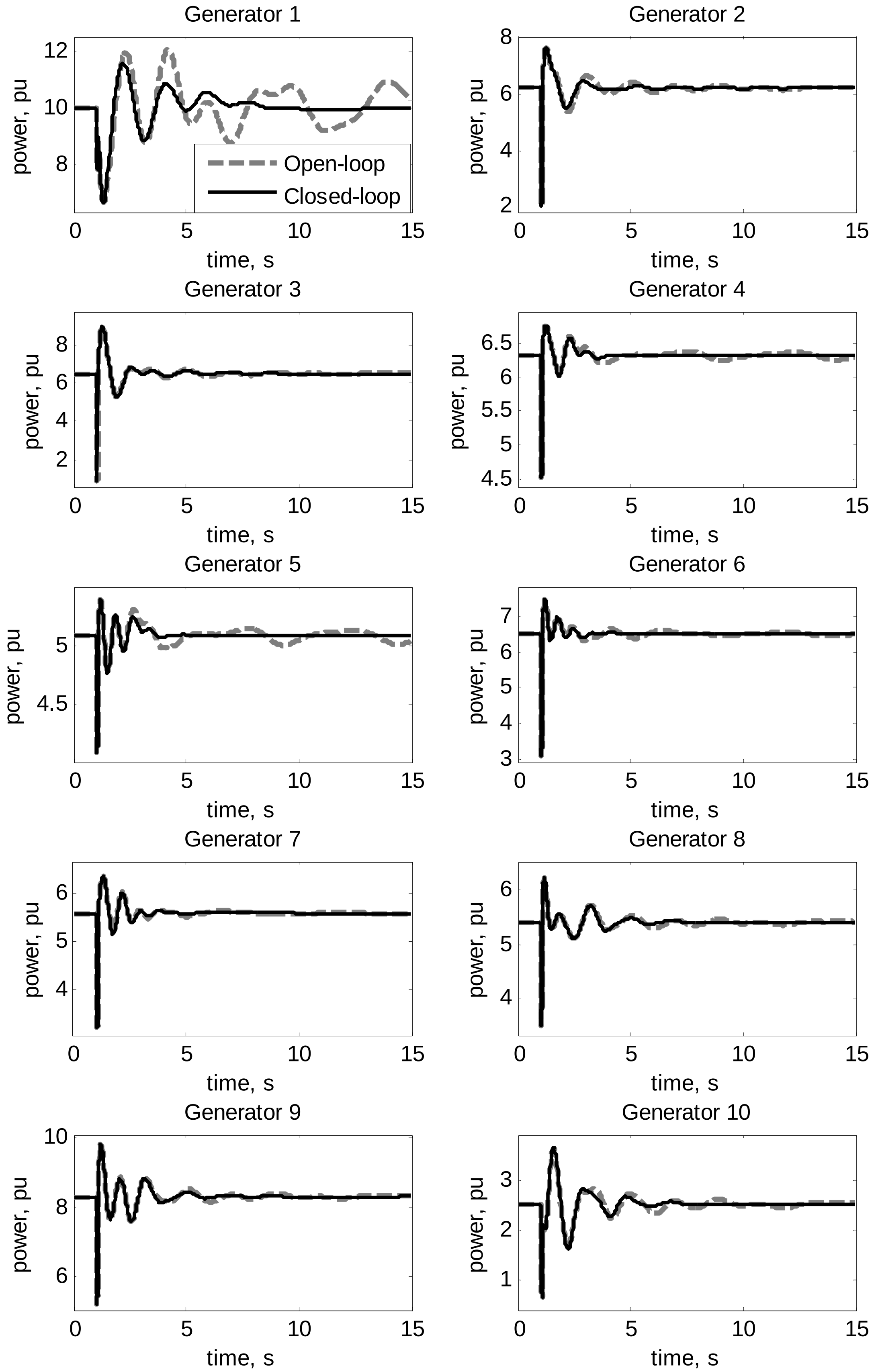

Figure 5-11: Active power responses for a large disturbance at bus 14 (OC-A1)

5.3.4 Power Transfer Changes

System stability is assessed for different scenarios of changes in power transfers across transmission lines in the network (power transfers at the nominal operating condition are shown in Appendix A). The first studied case includes increased power transfer across line 16-19, resulting from increase in generated active power by generators (G4,G5) and decrease in generated power by (G6,G7). Table 5-9 lists the resulting frequency and damping ratios of modes 1-3 for power transfer changes across line 16-19. Active power responses for a large disturbance at bus 14 for operating condition (OC-B4) are shown in Figure 5-12. Both results show that the SWAC stabilises the system while PSSs alone couldn't.

Table 5-9: Modes 1-3 for different operating conditions (B)

Operating condition	Power transfer increase across line 16-19	Open-loop (with PSSs only)						Closed-loop (with PSSs and SWAC)					
		f_1 [Hz]	ζ_1 [%]	f_2 [Hz]	ζ_2 [%]	f_3 [Hz]	ζ_3 [%]	f_1 [Hz]	ζ_1 [%]	f_2 [Hz]	ζ_2 [%]	f_3 [Hz	ζ_3 [%]
OC-B1	30 MW	0.29	5.15	0.42	9.42	0.55	10.70	0.29	29.94	0.41	28.78	0.52	31.47
OC-B2	60 MW	0.28	3.01	0.42	9.31	0.55	10.86	0.27	31.09	0.41	28.78	0.52	31.44
OC-B3	90 MW	0.26	-0.45	0.41	9.26	0.55	10.98	0.22	34.71	0.40	28.73	0.52	31.33
OC-B4	120 MW	0.20	-9.95	0.40	9.19	0.55	11.01	0.10	21.60	0.40	28.53	0.52	30.97

Table 5-10 lists the resulting frequencies and damping ratios of modes 1-3 for increases in power transfer across line 21-16. The system with PSSs only becomes unstable at operating condition (OC-C3). The transient simulation showed in Figure 5-13 shows that the SWAC effectively enhances system stability under a stressed operating condition.

Table 5-10: Modes 1-3 for different operating conditions (C)

Operating condition	Power transfer increase across line 21-16	Open-loop (with PSSs only)						Closed-loop (with PSSs and SWAC)					
		f_1 [Hz]	ζ_1 [%]	f_2 [Hz]	ζ_2 [%]	f_3 [Hz]	ζ_3 [%]	f_1 [Hz]	ζ_1 [%]	f_2 [Hz]	ζ_2 [%]	f_3 [Hz	ζ_3 [%]
OC-C1	50 MW	0.32	8.91	0.40	10.15	0.55	10.12	0.33	29.49	0.39	29.15	0.52	31.34
OC-C2	100 MW	0.36	14.99	0.35	5.46	0.55	9.71	0.35	35.92	0.35	23.63	0.51	31.04
OC-C3	150 MW	0.35	24.25	0.34	-4.24	0.55	9.39	0.34	41.74	0.33	19.08	0.51	30.55

The system is further assessed for a stressed operating condition with increased power transfers across line 9-39 while line 3-4 is out of service. Table 5-11 lists the resulting damping ratios of modes 1-3 and Figure 5-14 shows active power responses at operating condition (OC-D3). Both results show that the SWAC stabilises mode 3 while PSSs couldn't.

Table 5-11: Modes 1-3 for different operating conditions (D)

Operating condition	Power transfer across line 9-39	Open-loop (with PSSs only)						Closed-loop (with PSSs and SWAC)					
		f_1 [Hz]	ζ_1 [%]	f_2 [Hz]	ζ_2 [%]	f_3 [Hz]	ζ_3 [%]	f_1 [Hz]	ζ_1 [%]	f_2 [Hz]	ζ_2 [%]	f_3 [Hz	ζ_3 [%]
OC-D1	50 MW	0.30	6.49	0.42	10.07	0.54	3.42	0.30	28.93	0.40	28.98	0.59	9.75
OC-D1	100 MW	0.30	6.47	0.42	10.02	0.54	1.65	0.30	28.64	0.40	28.90	0.58	9.03
OC-D3	150 MW	0.30	6.44	0.42	9.97	0.54	-0.18	0.30	28.36	0.40	28.84	0.57	8.31

5.3.5 Time Delay Variations

The SWAC is assessed for variation in signal transmission time delays from the value considered at design stage, i.e. 100 ms for one way (200 ms for round trip communication from PMUs to the SWAC and then back to generators' exciters). Table 5-12 lists the closed-loop modes of interest for different time delays. It can be seen that an increase in time delay degrades the damping ratios of the modes of interest. In all cases, local modes are not affected by these increased time delays. Figure 5-15 shows the active power responses for a large disturbance at bus 14 with increased delays from the value considered at the design stage. It can be seen that the effectiveness of the SWAC in damping out the oscillations is reduced with increased time delays.

Table 5-12: Closed-loop modes of interest for different time delays

Total delay [ms]	Mode 1 [1/s , rad/s]	ζ_1 [%]	Mode 2 [1/s , rad/s]	ζ_2 [%]	Mode 3 [1/s , rad/s]	ζ_3 [%]
200	-0.59±j1.91	29.57	-0.76±j2.53	28.78	-1.08±j3.26	31.47
400	-0.49±j2.18	21.99	-0.67±j3.01	21.70	-0.53±j3.79	13.84
600	-0.29±j2.26	12.83	-0.32±j3.06	10.35	-0.31±j3.87	8.05
800	-0.14±j2.24	6.43	-0.12±j2.97	4.14	-0.11±j3.75	2.82
1000	-0.04±j2.19	2.02	-0.02±j2.85	0.65	-0.02±j3.58	0.52
1200	0.02±j2.13	-1.01	0.03±j2.74	-1.19	-0.00±j3.42	0.01

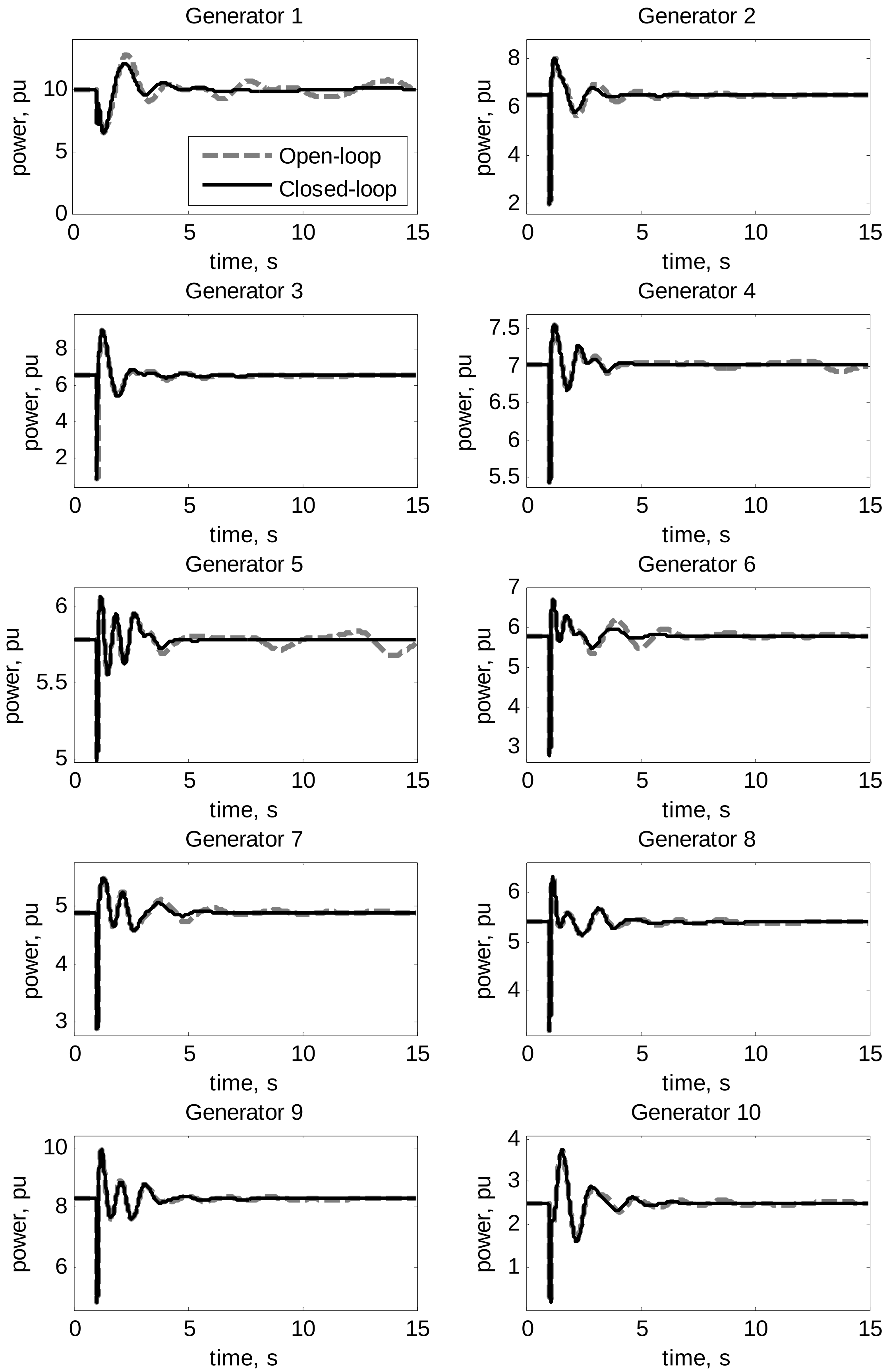

Figure 5-12: Active power responses for a large disturbance at bus 14 (OC-B4)

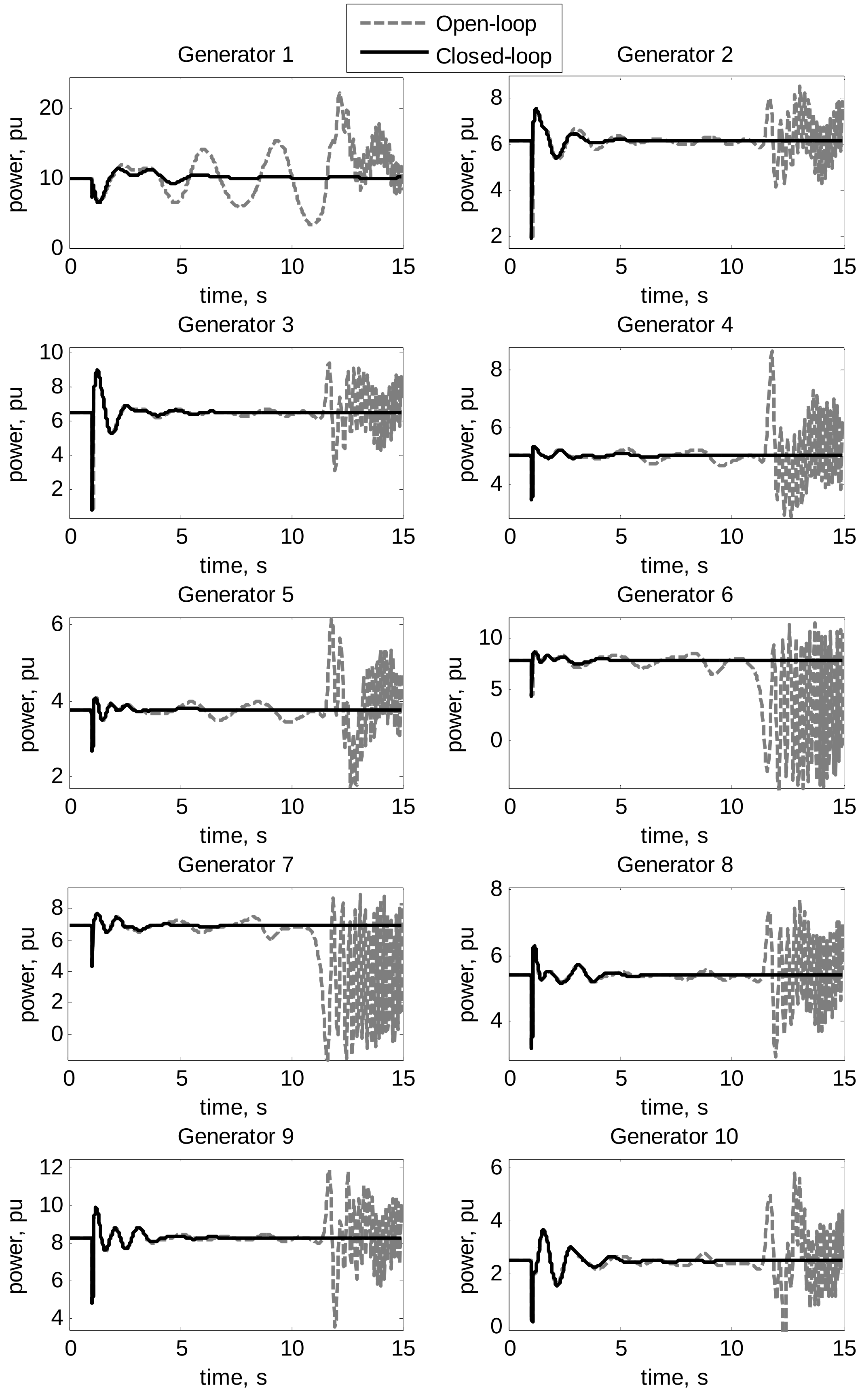

Figure 5-13: Active power responses for a large disturbance at bus 14 (OC-C3) (loss of synchronism in the open-loop system occurs at t≈12s)

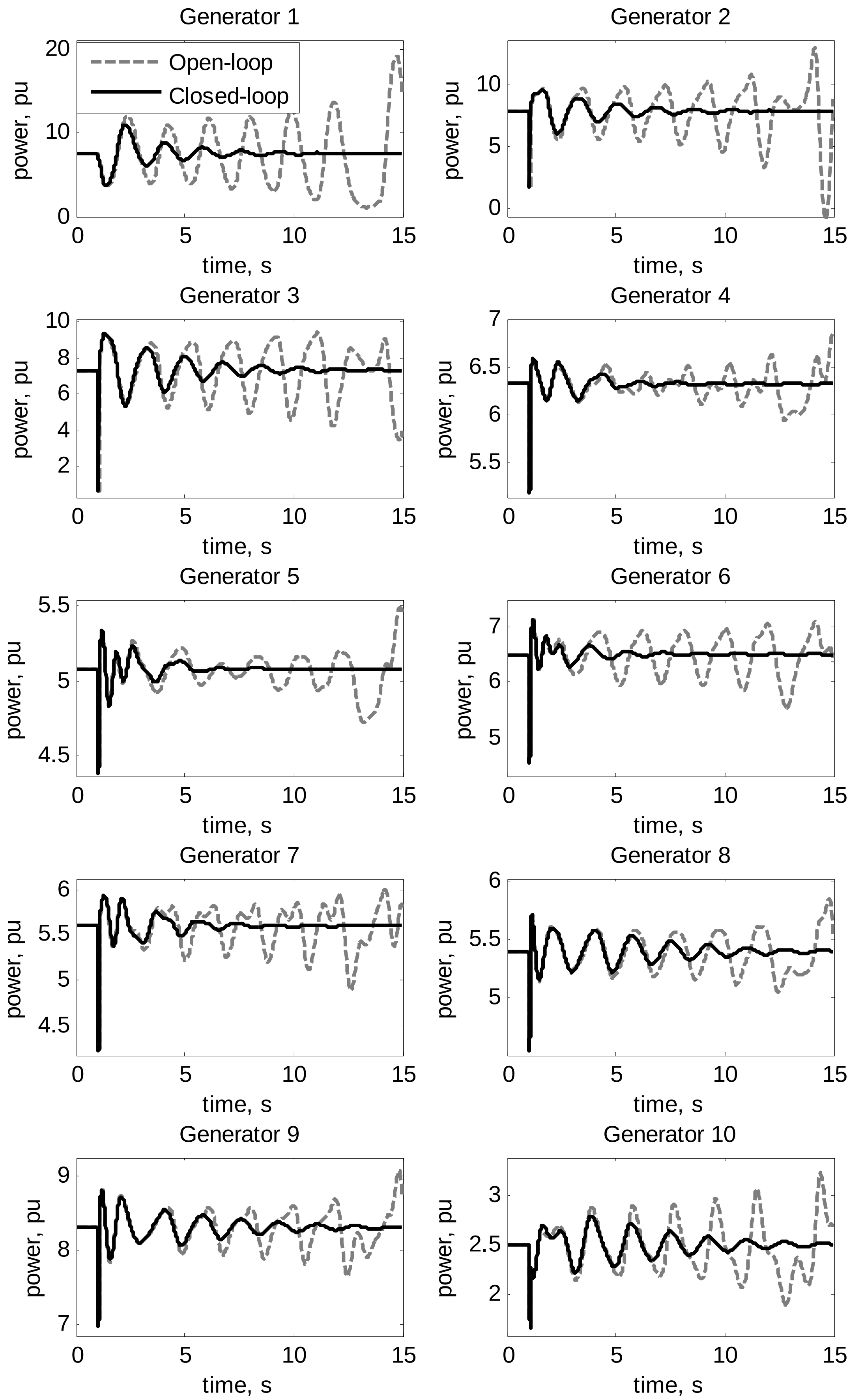

Figure 5-14: Active power responses for a large disturbance at bus 14 (OC-D3)

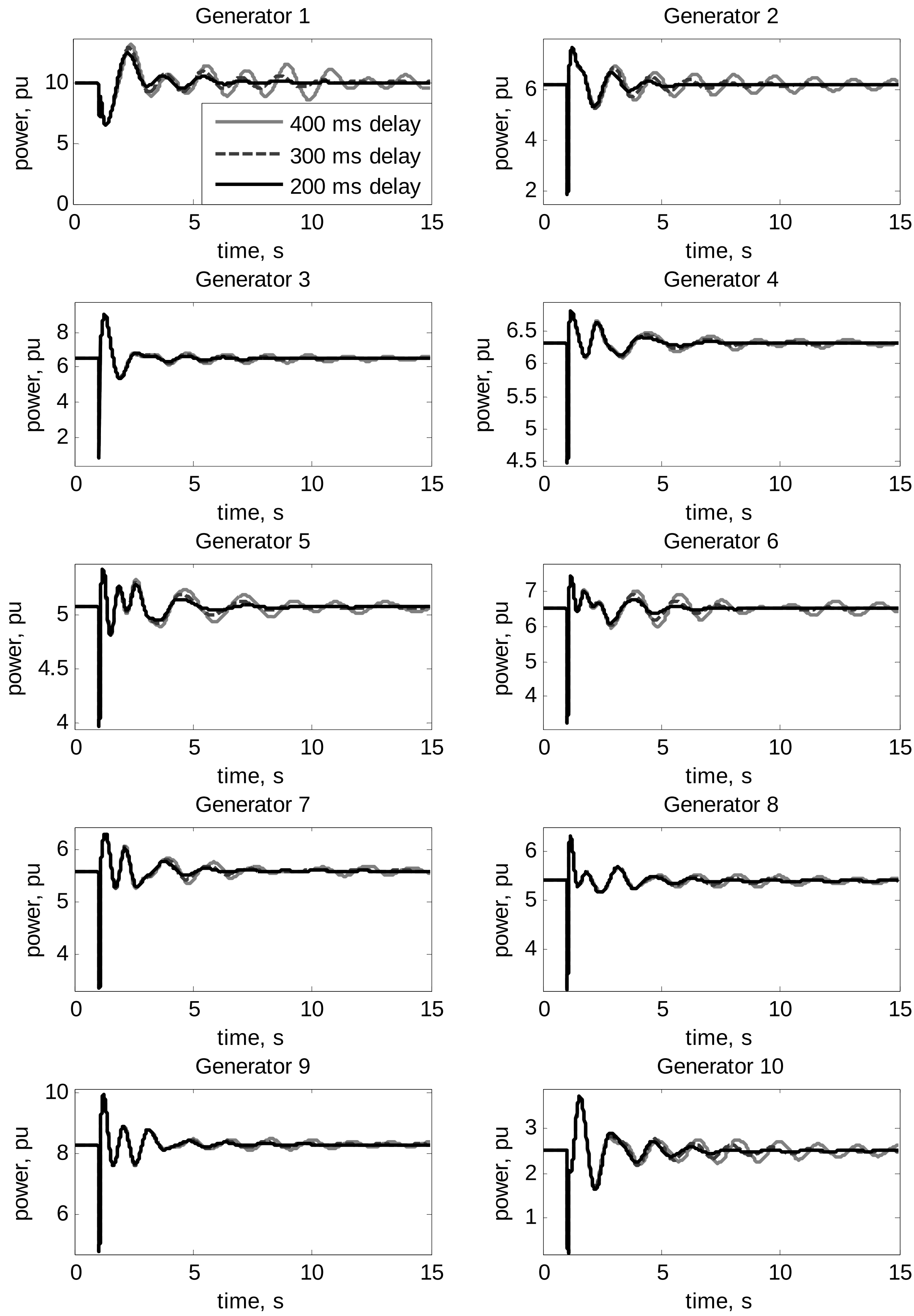

Figure 5-15: Active power responses for a large disturbance at bus 14 with different (total) time delays

Figure 5-16 shows the damping ratios of the modes of interest versus the one-way time delays. In the figure the maximum time delays that the SWAC can keep the damping ratios of each mode of interest above its value in the open-loop case are labelled (**a**, **b**, **c**) for mode 1-3, respectively. These are the maximum time delays the SWAC can tolerate for damping improvement and are listed in Table 5-13. From the figure and the table it can seen that mode 3 is the most affected by the increased time delays. Figure 5-17 shows the active power responses for a large disturbance at bus 14 with the longest time delay the SWAC can tolerate, i.e. maximum delay (**c**), for stability improvement above the open-loop system case. The figure shows that system stability is enhanced with the SWAC even with a longer time delay than the one considered at the design stage.

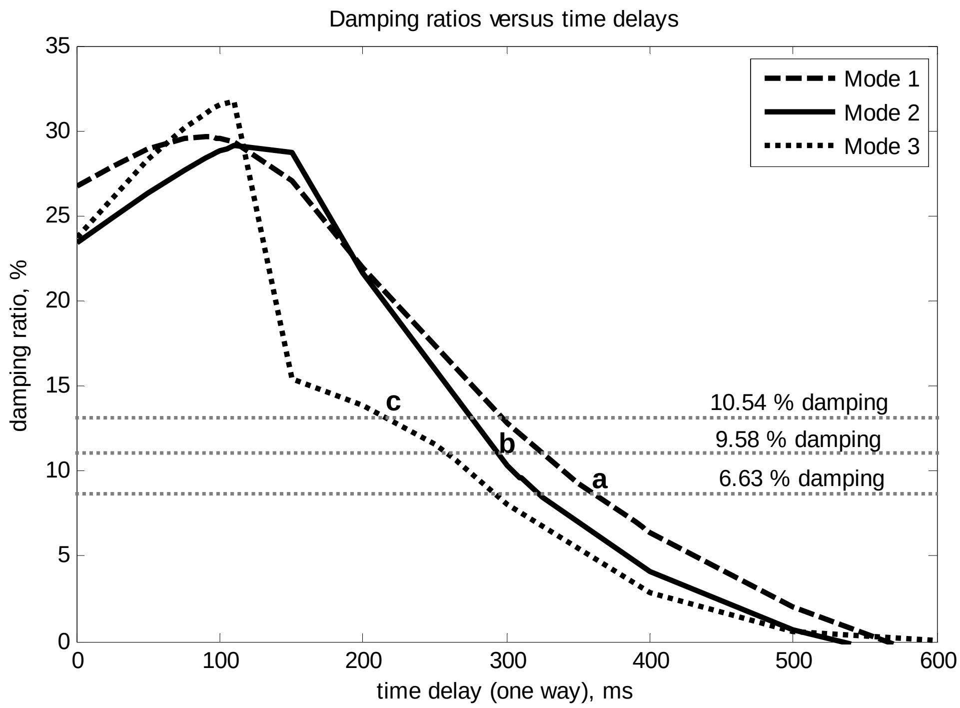

Figure 5-16: Damping ratios versus time delays

Table 5-13: Maximum time delays for damping improvement

Label	Maximum time delay (one-way) [ms]	ζ_1 [%]	ζ_2 [%]	ζ_3 [%]
a	396	**6.63**	4.33	2.96
b	310	12.08	**9.58**	7.35
c	266	15.61	13.43	**10.54**

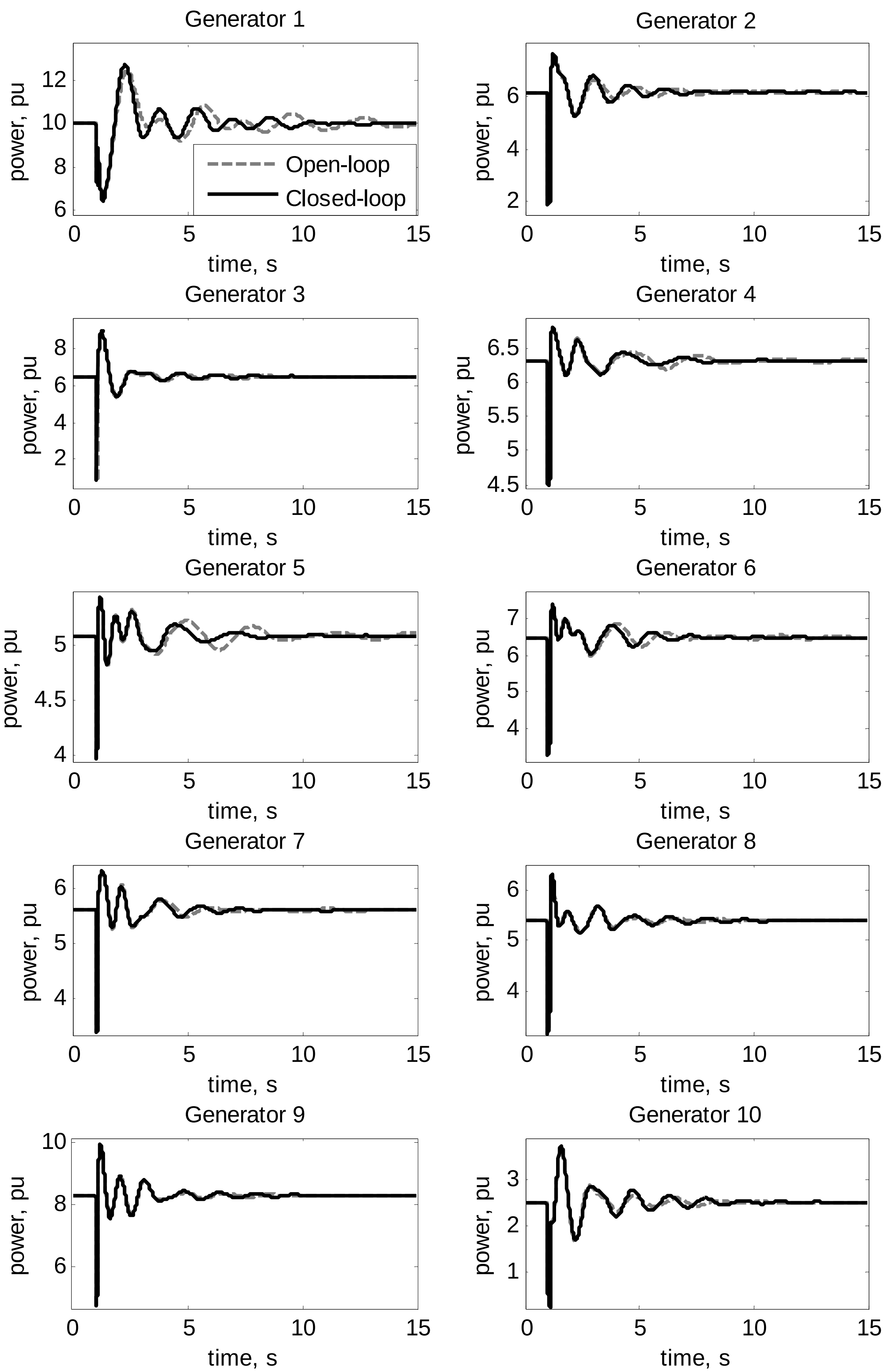

Figure 5-17: Active power responses for a large disturbance at bus 14 with maximum time delay (c)

5.3.6 Communication Link Failures

The SWAC is assessed for different failures of communication links used in the transmission of its I/O signals. Table 5-14 lists the closed-loop modes of interest for different communication link failures. It can be seen that loss of signals degrades damping ratios of the closed-loop interarea modes. The SWAC however still improves the stability of the system, and the damping ratios of modes 1-3 are better than in the open-loop case with PSSs only. For the worst case scenario when all I/O communication links are failed the damping ratios of all the modes are the same as in the open-loop system case. The stability of the system in such a case is maintained by local PSSs operating at the lower level of the hierarchical control structure.

Table 5-14: Closed-loop modes of interest for different communication link failures

no.	Failed control link	Failed measurement Link	Mode 1 [1/s, rad/s]	ζ_1 [%]	Mode 2 [1/s, rad/s]	ζ_2 [%]	Mode 3 [1/s, rad/s]	ζ_3 [%]
1	u_1	-	-0.45±j1.93	22.48	-0.72±j2.54	27.09	-1.10±j3.32	31.53
2	u_2	-	-0.59±j1.91	29.57	-0.75±j2.55	28.27	-0.65±j3.41	18.78
3	u_3	-	-0.26±j1.91	13.39	-0.65±j2.60	24.17	-1.08±j3.28	31.30
4	u_4	-	-0.56±j1.95	27.60	-0.40±j2.55	15.61	-1.02±j3.25	29.97
5	-	y_1	-0.60±j2.00	28.72	-0.66±j2.47	25.69	-0.34±j3.25	10.32
6	-	y_2	-0.23±j1.85	12.31	-0.58±j2.68	21.23	-1.07±j3.19	31.88
7	-	y_3	-0.58±j2.04	27.25	-0.43±j2.47	17.08	-1.11±j3.01	34.65
8	u_1	y_1	-0.41±j2.01	19.86	-0.68±j2.49	26.42	-0.37±j3.39	10.91
9	u_1	y_2	-0.18±j1.86	9.54	-0.50±j2.70	18.13	-1.08±j3.19	32.07
10	u_1	y_3	-0.47±j2.02	22.49	-0.42±j2.48	16.63	-1.07±j3.10	32.50
11	u_2	y_1	-0.56±j1.99	27.07	-0.63±j2.47	24.58	-0.40±j3.41	11.52
12	u_2	y_2	-0.23±j1.84	12.47	-0.58±j2.74	20.64	-0.68±j3.32	20.21
13	u_2	y_3	-0.60±j2.06	27.95	-0.41±j2.40	16.87	-0.71±j3.37	20.66
14	u_3	y_1	-0.24±j1.93	12.50	-0.55±j2.61	20.54	-0.34±j3.23	10.58
15	u_3	y_2	-0.24±j1.83	13.13	-0.55±j2.70	20.11	-1.12±j3.17	33.46
16	u_3	y_3	-0.18±j1.96	9.19	-0.37±j2.58	14.32	-1.08±j3.07	33.22
17	u_4	y_1	-0.56±j2.01	26.93	-0.39±j2.52	15.45	-0.30±j3.20	9.22
18	u_4	y_2	-0.17±j1.90	8.69	-0.32±j2.61	12.09	-0.92±j3.23	27.36
19	u_4	y_3	-0.56±j1.95	27.71	-0.35±j2.54	13.76	-1.20±j3.09	36.15
20	(u_1-u_4)	(y_1-y_3)	-0.13±j1.91	6.63	-0.25±j2.61	9.58	-0.37±j3.48	10.54

(Figure 5-18 - Figure 5-21) show the active power responses for a large disturbance at bus 14 with different communication link failures. The figures show transient responses for those cases when any of the damping ratios of the modes of interest decreases bellow 10 % (cases 9, 16-18 in Table 5-14). It can be seen from the figures that the SWAC still improves the transient performance of the system even though with failed communication links.

Under communication link failures the SWAC's full effectiveness can be recovered using alternative signals from nearby PMUs. Table 5-15 lists the closed-loop modes of interest when using alternative signals. The same SWAC's parameters are used with these alternative PMU measurements. It can be seen from the table that the use of alternative signals improves the damping ratios close to the original case when no communication link failure is encountered in the WAMS. Figure 5-22 shows the active power responses for a large disturbance at bus 14 using alternative PMU measurements (case 20 in Table 5-15). The figure shows that the effectiveness of the SWAC in enhancing the system transient performance under communication link failures can be recovered using alternative signals.

Table 5-15: Closed-loop modes of interest with alternative PMU measurements

no.	Failed control link	Lost PMU measurements	Alternative PMU measurements	Mode 1 [1/s, rad/s]	ζ_1 [%]	Mode 2 [1/s, rad/s]	ζ_2 [%]	Mode 3 [1/s, rad/s]	ζ_3 [%]
1	u_1	(θ_{39}, θ_{34}, θ_{35})	(θ_9, θ_{20}, θ_{22})	-0.41±j1.94	20.86	-0.66±j2.52	25.22	-1.13±j3.39	31.60
2	u_2	(θ_{39}, θ_{34}, θ_{35})	(θ_9, θ_{20}, θ_{22})	-0.54±j1.92	26.87	-0.67±j2.52	25.83	-0.62±j3.46	17.57
3	u_3	(θ_{39}, θ_{34}, θ_{35})	(θ_9, θ_{20}, θ_{22})	-0.24±j1.91	12.37	-0.57±j2.58	21.60	-1.10±j3.34	31.34
4	u_4	(θ_{39}, θ_{34}, θ_{35})	(θ_9, θ_{20}, θ_{22})	-0.51±j1.95	25.50	-0.39±j2.55	15.12	-1.05±j3.30	30.42
5	-	θ_{39}	θ_9	-0.55±j1.94	27.12	-0.74±j2.51	28.31	-1.11±j3.35	31.44
6	-	θ_{34}	θ_{20}	-0.58±j1.89	29.21	-0.74±j2.55	28.02	-1.08±j3.26	31.47
7	-	θ_{35}	θ_{22}	-0.54±j1.93	27.07	-0.72±j2.52	27.53	-1.08±j3.25	31.64
8	u_1	θ_{39}	θ_9	-0.42±j1.95	20.92	-0.71±j2.52	27.07	-1.13±j3.40	31.64
9	u_1	θ_{34}	θ_{20}	-0.44±j1.92	22.28	-0.70±j2.55	26.32	-1.10±j3.32	31.54
10	u_1	θ_{35}	θ_{22}	-0.45±j1.94	22.56	-0.68±j2.53	26.05	-1.10±j3.31	31.45
11	u_2	θ_{39}	θ_9	-0.55±j1.94	27.10	-0.73±j2.52	27.82	-0.61±j3.46	17.39
12	u_2	θ_{34}	θ_{20}	-0.58±j1.89	29.21	-0.73±j2.56	27.53	-0.65±j3.41	18.82
13	u_2	θ_{35}	θ_{22}	-0.59±j1.91	29.62	-0.71±j2.54	27.04	-0.66±j3.41	18.89
14	u_3	θ_{39}	θ_9	-0.24±j1.91	12.40	-0.61±j2.59	22.83	-1.10±j3.36	31.22
15	u_3	θ_{34}	θ_{20}	-0.58±j1.91	13.44	-0.64±j2.60	23.87	-1.08±j3.28	31.32
16	u_3	θ_{35}	θ_{22}	-0.26±j1.91	13.34	-0.62±j2.59	23.16	-1.08±j3.26	31.37
17	u_4	θ_{39}	θ_9	-0.53±j1.97	25.99	-0.40±j2.54	15.69	-1.05±j3.31	30.31
18	u_4	θ_{34}	θ_{20}	-0.54±j1.93	27.07	-0.40±j2.56	15.27	-1.02±j3.25	29.88
19	u_4	θ_{35}	θ_{22}	-0.56±j1.95	27.61	-0.40±j2.55	15.39	-1.03±j3.24	30.21
20	-	(θ_{39}, θ_{34}, θ_{35})	(θ_9, θ_{20}, θ_{22})	-0.54±j1.93	26.90	-0.68±j2.51	26.27	-1.11±j3.33	31.65

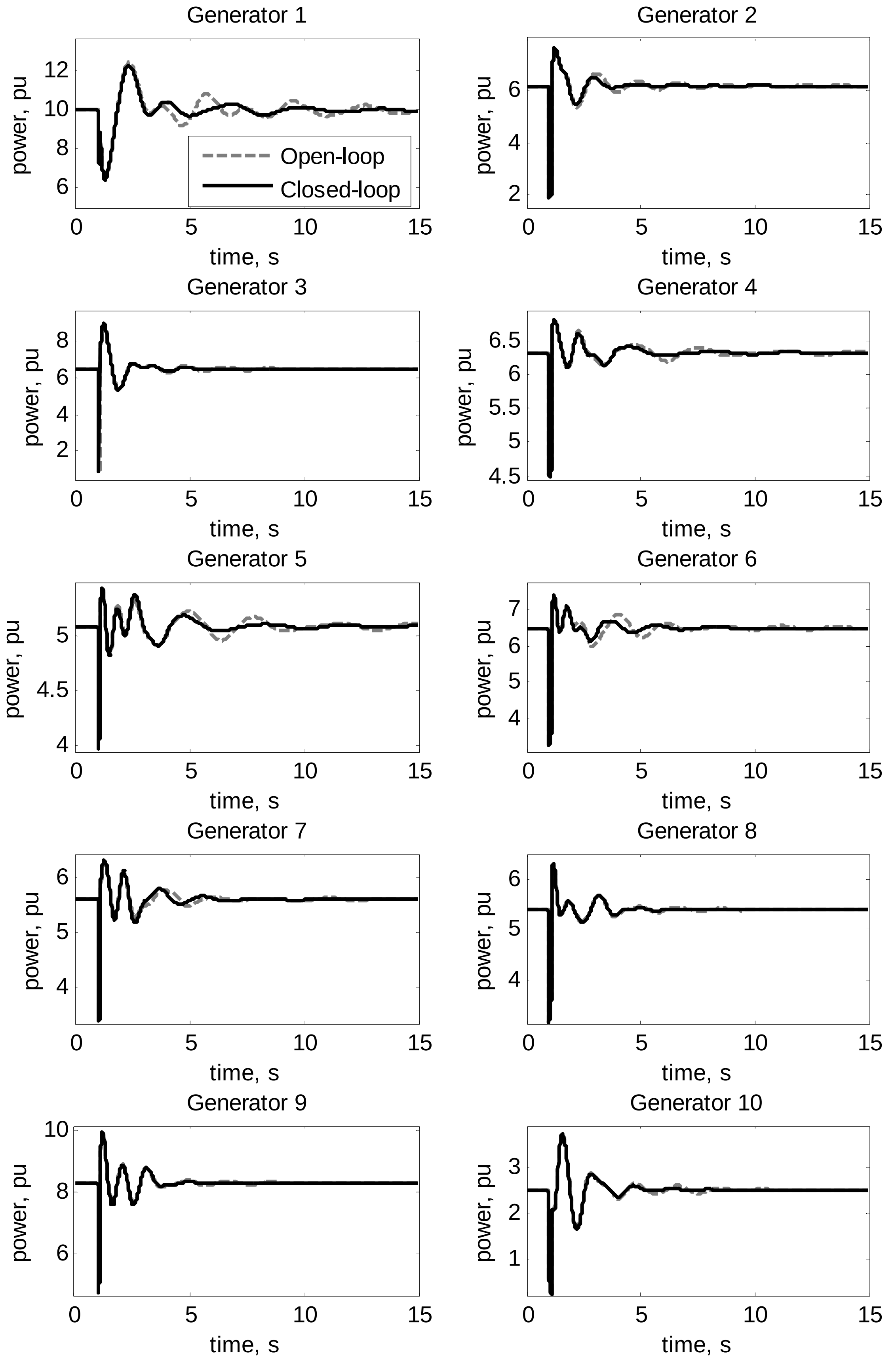

Figure 5-18: Active power responses for large disturbance at bus 14 with communication link failure (case 9)

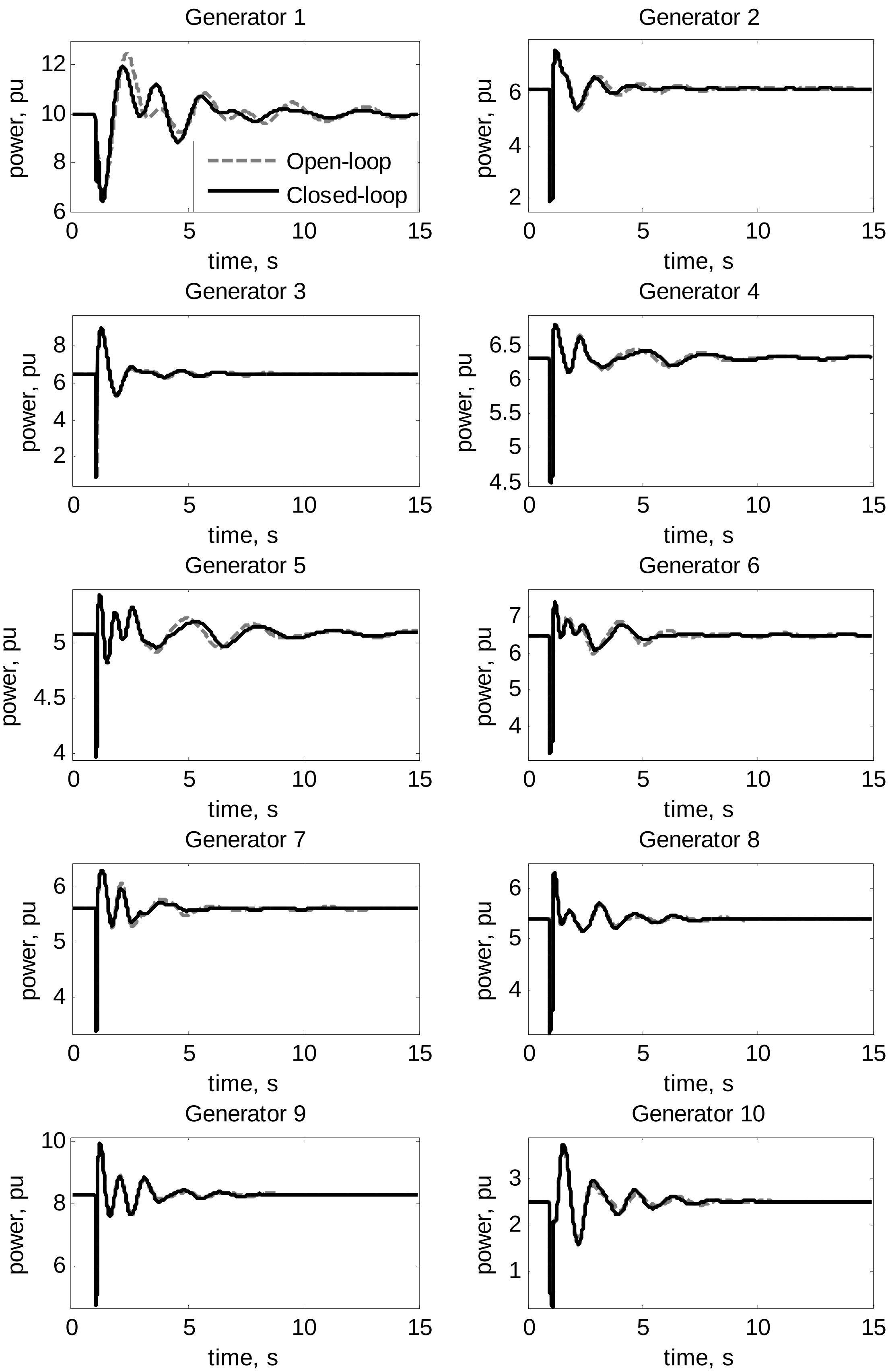

Figure 5-19: Active power responses for large disturbance at bus 14 with communication link failure (case 16)

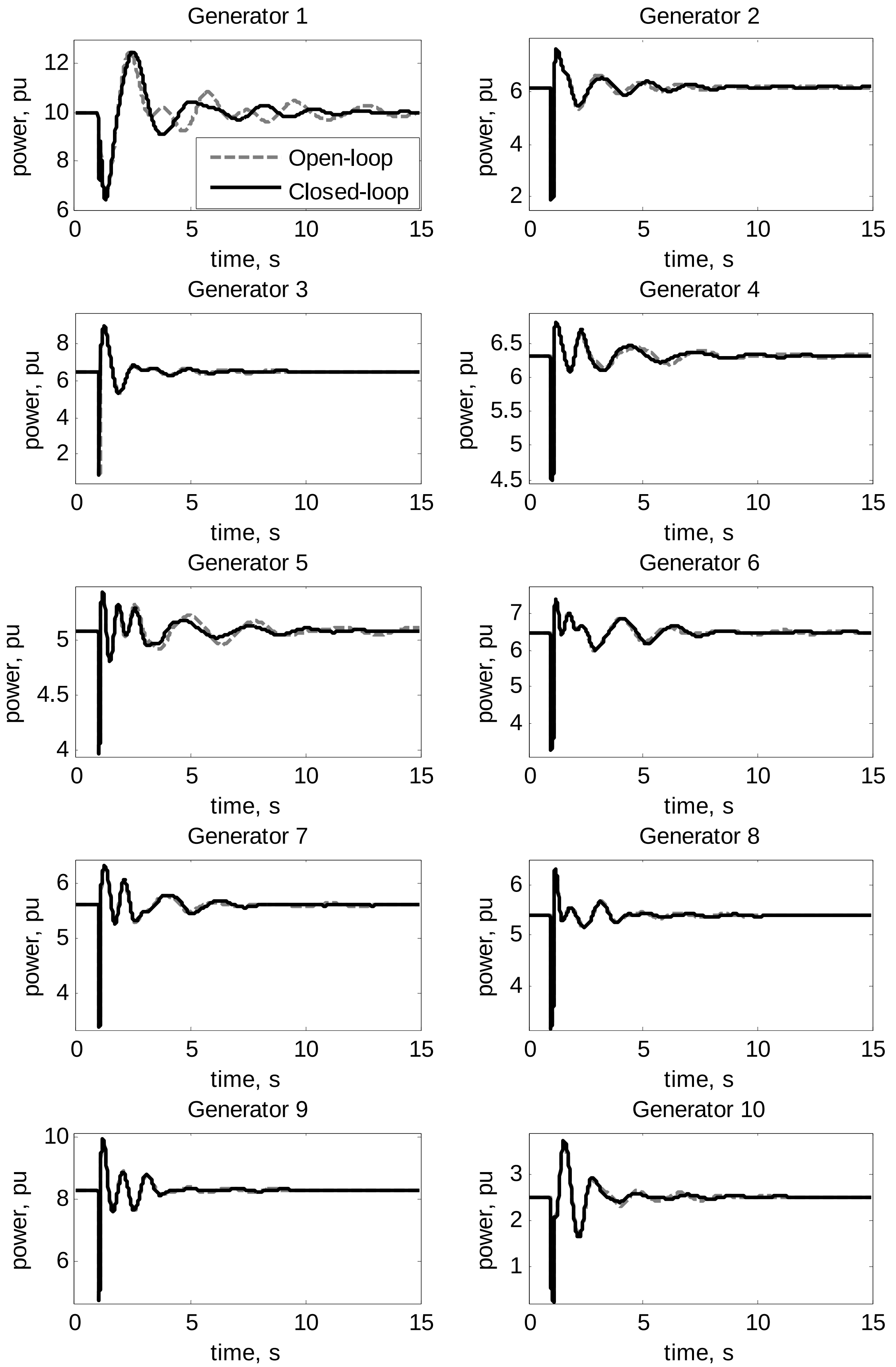

Figure 5-20: Active power responses for large disturbance at bus 14 with communication link failure (case 17)

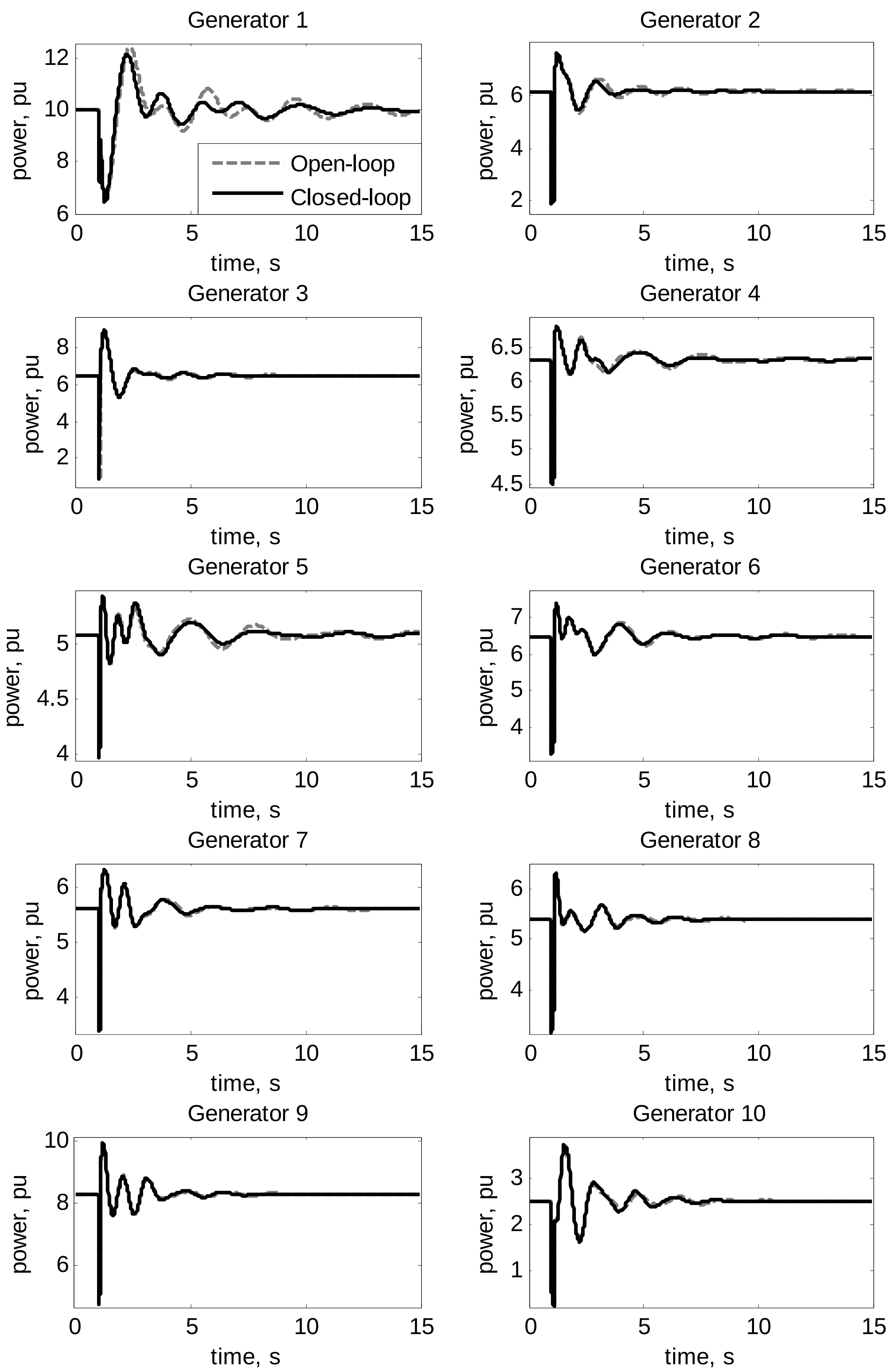

Figure 5-21: Active power responses for large disturbance at bus 14 with communication link failure (case 18)

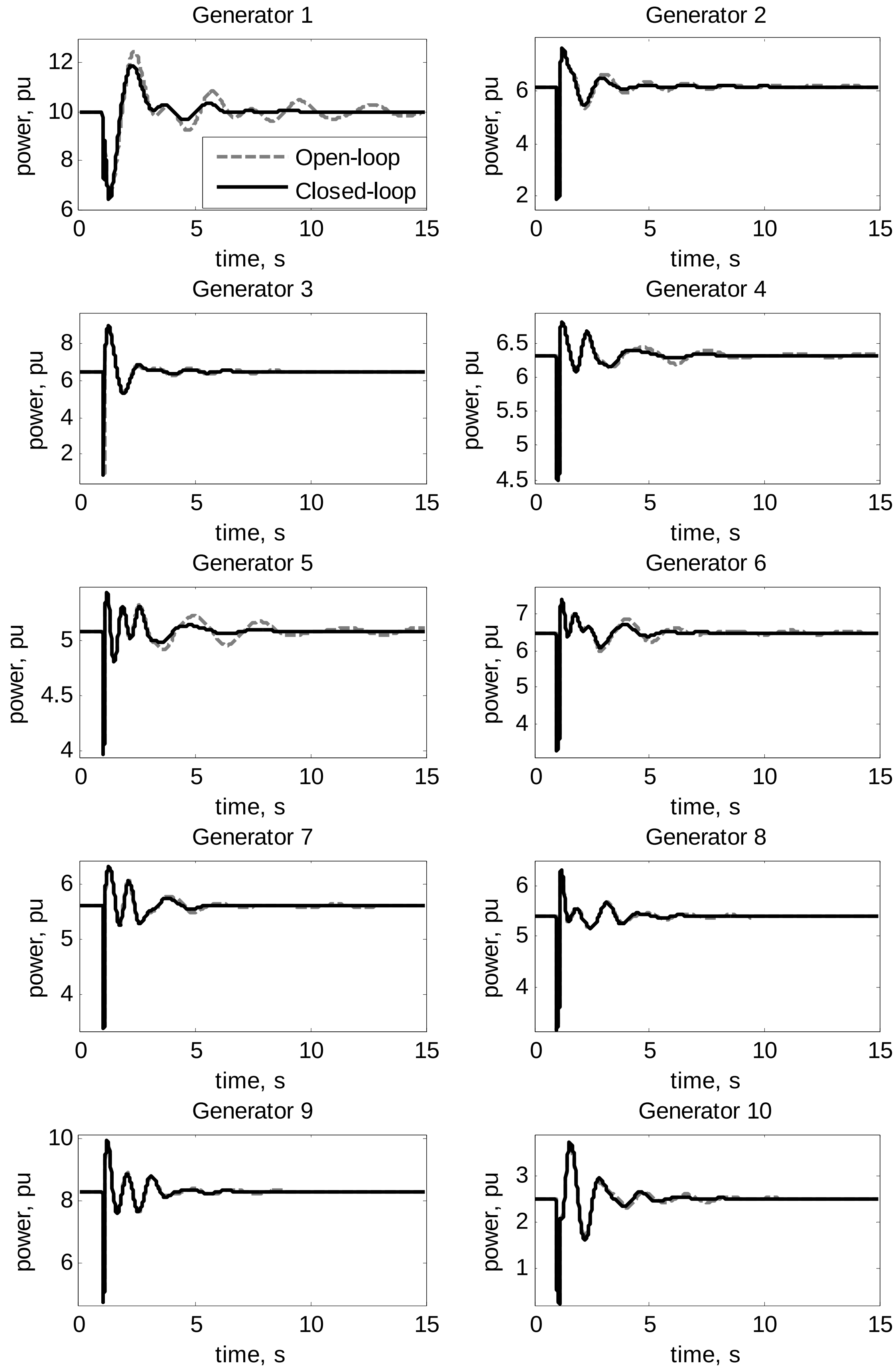

Figure 5-22: Active power responses for a large disturbance at bus 14 with alternative measurement signals (case 20)

5.4 Summary

Application of hierarchical WAMS based control scheme on the NETS has been presented in this chapter. Results showed that considerable enhancement to system stability can be achieved without affecting the functionality of existing PSSs. The WAMS based damping controller was designed using the modal LQG approach with few I/O signals. The focus of the designed SWAC was towards adding damping to the critical interarea modes only. The results showed that local modes in the system were not been affected by the added WAMS based control loop.

System stability was comprehensively assessed using small-signal and transient performance analysis over wide range of operating conditions (410 in total) involving changes to network topology and power transfers. Results showed that the WAMS based control scheme, with PSSs and the SWAC, effectively stabilises the system where in many cases PSSs alone couldn't.

Effectiveness of the WAMS based damping controller was verified for variations in time delays and results showed that it can tolerate longer delays than the ones considered at the design stage. Different scenarios of possible communication link failures and their effect on system stability were also studied. Results showed that the proposed control scheme can still maintain system stability under these failures. When alternative measurements from nearby PMUs are used instead of the original signals, the full effectiveness of the WAMS based damping controller can be recovered.

6 CONCLUSIONS AND FUTURE WORK

6.1 Conclusions

This thesis presented a Wide Area Measurement System (WAMS) based control scheme to enhance power system stability. The control scheme has a hierarchical (two-level) structure comprising a Supplementary Wide-Area Controller (SWAC) built on top of existing Power System Stabilisers (PSSs). The SWAC's focuses on stabilising the critical interarea oscillations in the system while leaving local modes to be controlled entirely by local PSSs. The SWAC uses a set of reduced input/output (I/O) signals in order to reduce the associated communication costs and also to reduce complexity of the overall control system. Both control systems work together to maintain system stability. The scheme relies on synchronised measurements supplied by the Phasor Measurement Units (PMUs) through the WAMS and the only cost is associated with the communication infrastructure which is already in place, or will be in the near future.

Several configuration options of the WAMS based control scheme were discussed in this thesis in terms of their compliance with the existing real power systems. The main issue in current power systems is that the utilities are reluctant to install control loops on top of the existing local controllers. This is due to concern about possible interference with functionality of existing local controllers, PSSs in particular. The hierarchical (two-level) control structure proposed in this research has the advantage, compared to other structures, of not interfering with, and keeping local controllers in place. It also provides greater reliability and functional flexibility. If the SWAC is not functioning, for example, due to loss of communication signals, the system stability is maintained by local controllers, as before.

Performance of the WAMS based damping controller, the SWAC, is highly influenced by the used control design method. It plays a major role in directing the SWAC's control effort towards damping of the critical interarea oscillations and hence the enhancement of the overall power system stability. In addition, it governs the effect of the SWAC on other modes and local controllers. Several control design methods were reviewed in the context of the WAMS based damping controller's effect on other modes and local controllers in the system. The Linear Quadratic Gaussian (LQG) control has the advantage, compared to other control methods, of flexibility and usability when specifying the underlying trade-off between state regulation and control action. The critical interarea modes can be addressed in the controller's cost function simply by putting more weights on the states with higher participating factors. In this way, damping of interarea oscillations is enhanced by the resulting LQG controller. Results however showed that such a conventional tuning procedure cannot be implemented in a straight forward manner and becomes complex especially when handling multiple interarea modes. Other modes with common participating states are also affected by the conventionally designed LQG controller in addition to the addressed interarea modes.

The LQG design is therefore enhanced in this thesis to simplify the controller's design process and also to reduce the associated complexities when handling multiple interarea modes. Instead of tackling the highly participating states, interarea modes are addressed directly in the controller's cost function using a simple transformation. The new cost function is expressed in terms of modal variables which are directly associated with system modes. The interarea modes are addressed by assigning higher modal weights to them and zero weights to other modes in the controller's cost function. In this way, damping of interarea modes is enhanced without affecting other modes.

Comparisons with the conventional tuning procedure showed the advantages of using the modal LQG approach. Results showed design simplicity even when handling multiple interarea modes. The method offers flexibility in adding damping to any set of modes of interest in the system without affecting the other modes. Degree of damping, i.e. modes' damping ratios, can be increased to any level by fine tuning of the modal weights. The resulting control effort by the modal LQG controller is minimised as it is focusing only on a subset of modes in the system. The feature of leaving other modes unaltered while stabilising the lightly damped interarea modes, in addition to other features of the method, makes the modal LQG controller highly suitable for WAMS based damping control applications.

Different model order reduction scenarios were also studied and it was found that the reduced order modal LQG controller is as effective as the full order controller in enhancing the system stability; thus making the proposed design approach applicable to large scale power system. The results showed very good robustness of the modal LQG controller to changes in network topology and operating conditions. The modal LQG controller was also effective in enhancing the system stability in cases of heavy power transfers.

The inevitable time delays associated with the transmission of wide-area measurements and control signals in realistic applications were incorporated in the modal LQG design approach. Different values of time delays were considered at the design stage and the designed controller was always effective in enhancing the system stability. The modal LQG approach therefore is suitable to different WAMS with different types of communication links. In cases of longer time delays, than the ones considered at the design stage, the improvement of system stability, though slightly degraded, was still achieved by the modal LQG controller. Results showed that the modal LQG controller could tolerate longer delays than those originally considered with adequate improvement in system damping.

The modal LQG controller's effectiveness under different scenarios of possible communication link failures was assessed using small-signal and transient performance analysis. The results showed that the improvement in system stability still can be achieved under these circumstances with the modal LQG controller. For the worst case scenario, when all signals from and/or to the SWAC are lost, the system continues to be controlled by local PSSs as before. The use of the alternative input signals, from the adjacent buses, instead of the lost signals, resulted in almost full recovery of the effectiveness of the controller and such additionally emphasised the robustness of the SWAC.

At present PMUs are installed only at few locations in the network, mainly due to the associated costs of infrastructure. The proposed WAMS based damping controller, therefore, uses only few measurement and control signals in order to reduce these costs and to reduce complexity of the overall control system. The reduced set of I/O signals, however, should be carefully selected so that it maximises the effectiveness of the WAMS based damping controller. Three methods for selection of I/O signals for WAMS based damping controllers were presented and compared in this research. Their comparative advantages and disadvantages are illustrated on the New England Test System (NETS).

The first selection method is based on modal factors analysis. The signals with the largest modal observability/controllability factors, for each individual mode of interest, are selected. Number of input or output signals using this method is less than or equal to the number of modes of interest in the system.

The second method is based on the Sequential Orthogonalisation (SO) algorithm, a tool for the optimal placement of measurement devices. The SO algorithm application is extended and generalised to handle the problem of I/O signal selection for WAMS based damping controllers. Detailed mathematical description of the selection procedure was presented and suitable illustrative example given. The algorithm maximises the observability/controllability information about the modes of interest while at the same time considering sensitivity of selected sites to other modes in the system. The algorithm selects the sites sequentially such that redundancy of information is minimised.

The third selection method combines clustering and modal factors analysis. Time responses of generators are clustered into groups and then a representative I/O signal is selected from each group. Representative signals are selected such that each one of them has the largest cumulative sum of observability/controllability factors for the set of modes of interest. In this way the method minimises redundancy of information about the modes of interest while using reduced number of signals.

The clustering method used for selection of I/O signals is an enhanced version of the Principal Component Analysis (PCA) method, i.e. time domain coherency identification method. The PCA method identifies coherent generators without any model information, it does not require linearisation of the model and it relies only on PMUs measurements. The method therefore can be regarded as an effective tool for the identification of coherent generators in power systems. Results showed that the classification made by the method using visual inspection, of 3-D plots in most cases, may lead to inaccurate results. Results also showed that the PCA method alone is limited to those cases that require only three principal components.

Supplementing the PCA method with cluster analysis showed that its limitations and drawbacks can be overcame. The hierarchical tree produced by the PCA-based clustering method depicts the coherency picture of the system. The results showed that the PCA-based clustering method can identify coherent groups of generators with a high degree of accuracy.

Reduced sets of I/O signals determined using the three selection methods were compared using small-signal and transient performance analysis. The degree of effectiveness of a fixed SWAC (designed using all sets of candidate I/O signals) in enhancing system stability was used for the comparisons as a benchmark. The results showed that the best set of reduced I/O signals that enhances the effectiveness of the SWAC is the one determined using the SO algorithm.

Application of hierarchical WAMS based control scheme on the NETS showed that considerable enhancement to system stability can be achieved without affecting the functionality of existing PSSs. The multi-input multi-output (MIMO) WAMS based damping controller was designed using the modal LQG approach with few I/O signals. The focus of the designed SWAC was towards adding damping to the critical interarea modes only. The results showed that this had been achieved as local modes remained unaffected by the added WAMS based control loop. System stability was comprehensively assessed using small-signal and transient performance analysis over wide range of operating conditions (410 in total) involving different network topologies and power transfers. Results showed that the WAMS based control scheme, with PSSs and the SWAC, effectively stabilises the system even in many cases when PSSs alone couldn't.

The effectiveness of the WAMS based damping controller was also verified for variations in time delays and results showed that it can tolerate time delays longer than the ones considered at the design stage. Different scenarios of possible communication link failures and their effect on system stability were also studied. It is shown that system stability had not been deteriorated under these scenarios and that the recovery of the effectiveness of the WAMS based damping controller could be achieved by using alternative signals from nearby PMUs.

6.2 Directions for Future Research

This thesis demonstrated the advantages of applying hierarchical WAMS based control scheme to damp out interarea oscillations in power systems. Comprehensive studies were carried out in this research to show the benefits of applying the scheme to enhance system stability. The demonstration of the economic benefits gained using this scheme would undoubtedly emphasise its importance. This can be done using the evolving topic of power system stability pricing. The monetary value of the control scheme could be assessed using pricing of stability to aid with making the decision regarding future developments of power system. Using pricing of system stability the WAMS based control scheme proposed in this thesis could be compared with other schemes, especially those involving the costly Flexible AC Transmission System (FACTS) devices, in the context of the economic value it brings to overall system performance.

The WAMS based control scheme presented in this thesis was applied to the relatively large New England Test System (NETS). The presented modal LQG design approach was illustrated under different scenarios of model order reduction to show its applicability to large power systems. A route for future research is to apply the proposed control scheme to a real large-scale power system. In this case the selection of I/O signals for the WAMS based damping controller would be more challenging due to the size of the real power system. For large power systems with hundreds of candidate I/O signals the process of signal selection is time consuming. A search method, like Artificial Immune System (AIS), can be used to reduce the decision time for selecting the best optimal set among hundreds or maybe thousands of mutations of candidate signals. Fixed design of the WAMS based damping controller can be used to assess the effectiveness of each set of candidate I/O signals in enhancing the controller's performance.

Many applications of LQG control for power system damping were proposed in the literature. The modal LQG approach presented in this thesis in fact replaces the conventional LQG design method and eliminates the need for participation factor analysis. Results showed the advantages of using the modal LQG approach and its suitability to WAMS based damping control applications. A broad future direction of research therefore is to apply the modal LQG approach to those previous LQG applications for power system damping. One of the LQG applications in power systems is Power Oscillation Damping (POD) controllers for FACTS devices [8] and High Voltage Direct Current (HVDC) links. Installations of these devices are increasing all over the world and the effectiveness of their POD controllers can be increased using WAMS based signals. The modal LQG approach can be used to design these POD controllers with the aim of damping out the lightly damped interarea oscillations while keeping other modes and local controllers unaffected by the added control loop. Care however should be taken when selecting the controller's input and output signals. The measurement signals used as inputs to the LQG controller highly affect the estimation accuracy of Kalman filter. Locations of the LQG controller's signals (outputs of the controller) affect its controllability in stabilising the targeted interarea modes. Both of the input and output signals affect the effectiveness of the overall LQG control system.

Another application of LQG is to control the Sub-Synchronous Resonance (SSR) oscillations in power systems [64]. The modal LQG approach could be applied instead of the conventional method to design the controller. There are some issues however that need to be considered for such an application. The modulus of SSR modes is higher than those of electromechanical modes. Higher modal weight might be needed at the design stage to increase the damping of the SSR modes. The resulting control action by the modal LQG controller therefore could be excessive.

A robust WAMS based damping controller should account for the uncertain nature of the post-disturbance dynamics of the power system. The results presented in this thesis showed good robustness properties of the WAMS based damping controller designed using the modal LQG approach. Nevertheless its robustness depends primarily on how the Loop Transfer Recovery (LTR) procedure is performed. Robust control methods like H_2/H_∞ have the property of optimising the control system for a compromise between performance and robustness [55]. The control problem is formulated in Linear Fraction Transformation (LFT) configuration to model uncertainties of disturbances and plant model. H_2 control in fact was firstly introduced in the literature by defining LQG control in the LFT configuration [106]. A direction of future research is to generalise the modal LQG approach in the LFT configuration. The goal would be to design H_2/H_∞ controllers to target only certain modes in the power system while at the same time having desired robustness properties.

Another way of increasing the robustness of the WAMS based damping controller is to change the controller's parameters for each of the changing operating conditions. Fuzzy logic switch can be used to select the appropriate controller model from a bank of designed control loops for the corresponding operating condition [46]. A probabilistic approach can be used to determine the corresponding operating condition from a bank of linearised plant models [107, 108]. In such adaptive scheme the probability of each plant model in the bank representing the actual power system response is computed and the resultant control action is derived as probability-weighted average of the individual control moves of the controller. The robustness of the resulting WAMS based damping controller, which uses plant and controller banks, would be increased in this way without any prior knowledge about the specific post-disturbance contingencies.

Finally, the PCA-based clustering method presented in this thesis has the feature of producing a hierarchical tree representing the similarity/dissimilarity of considered time responses. The general application of the method, as a classification tool, is the grouping of time responses. A possible power system application of the proposed PCA-based clustering method is the aggregation of wind turbines. Due to the small size of wind turbines, compared to conventional generators, aggregation of them gains its importance as it simplifies power system analysis studies. Responses to variable wind speed and direction over wide range of time periods can be clustered using the PCA-based method to build aggregated models of wind turbines.

7 REFERENCES

[1] CIGRE TF 38.01.07, "Analysis and control of power system oscillations," CIGRE Brochure 111, Dec., 1996.

[2] M. E. Aboul-Ela, A. A. Sallam, J. D. McCalley, and A. A. Fouad, "Damping controller design for power system oscillations using global signals," *IEEE Trans. Power Syst.*, vol. 11, no. 2, pp. 767-773, May 1996.

[3] I. Kamwa, R. Grondin, and Y. Hebert, "Wide-area measurement based stabilizing control of large power systems-a decentralized/hierarchical approach," *IEEE Trans. Power Syst.*, vol. 16, no. 1, pp. 136-153, Feb. 2001.

[4] A. F. Snyder*, et al.*, "Inter-area oscillation damping with power system stabilizers and synchronized phasor measurements," in *Proc. Inter. Conf. on Power System Technology (POWERCON '98)*, Beijing, 1998, pp. 790-794.

[5] J. J. Sanchez-Gasca, N. W. Miller, A. Kurita, and S. Horiuchi, "Multivariable control for damping interarea oscillation in power systems," *IEEE Control Syst. Magazine*, pp. 28-32, Jan. 1989.

[6] B. Chaudhuri, B. C. Pal, A. C. Zolotas, I. M. Jaimoukha, and T. C. Green, "Mixed-sensitivity approach to H_∞ control of power system oscillations employing multiple FACTS devices," *IEEE Trans. Power Syst.*, vol. 18, no. 3, pp. 1149-1156, Aug. 2003.

[7] B. Chaudhuri and B. C. Pal, "Robust damping of multiple swing modes employing global stabilizing signals with a TCSC," *IEEE Trans. Power Syst.*, vol. 19, no. 1, pp. 499-506, Feb. 2004.

[8] A. C. Zolotas, B. Chaudhuri, I. M. Jaimoukha, and P. Korba, "A study on LQG/LTR control for damping inter-area oscillations in power systems," *IEEE Trans. Control Syst. Tech.*, vol. 15, no. 1, pp. 151-160, Jan. 2007.

[9] A. Ferreira, J. Barreiros, W. Barra, and J. Brito-de-Souza, "A robust adaptive LQG/LTR TCSC controller applied to damp power system oscillations," *Elect. Power Syst. Res.*, vol. 77, no. 8, pp. 956-964, June 2007.

[10] K. M. Son and J. K. Park, "On the robust LQG control of TCSC for damping power system oscillations," *IEEE Trans. Power Syst.*, vol. 15, no. 4, pp. 1306-1312, Nov. 2000.

[11] B. Pal and B. Chaudhuri, *Robust Control in Power Systems*, New York: Springer, 2005.

[12] I. Kamwa, R. Grondin, D. Asber, J. P. Gingras, and G. Trudel, "Large-scale active-load modulation for angle stability improvement," *IEEE Trans. Power Syst.*, vol. 14, no. 2, pp. 582-590, May 1999.

[13] J. H. Chow, J. J. Sanchez-Gasca, H. Ren, and S. Wang, "Power system damping controller design using multiple input signals," *IEEE Control Syst. Magazine*, pp. 82-90, Aug. 2000.

[14] A. G. Phadke, "Synchronized phasor measurements - A historical overview," in *Proc. Transmission and Distribution Conference and Exhibition 2002: Asia Pacific. IEEE/PES*, 2002, pp. 476-479.

[15] V. Centeno*, et al.*, "Adaptive out-of-step relaying using phasor measurement techniques," *Computer Applications in Power, IEEE*, vol. 6, no. 4, pp. 12-17, Oct. 1993.

[16] K. E. Holbert, G. I. Heydt, and H. Ni, "Use of satellite technologies for power system measurements, command, and control," *Proc. of the IEEE*, vol. 93, no. 5, pp. 947-955, May 2005.

[17] A. G. Phadke and J. S. Thorp, *Synchronized Phasor Measurements and Their Applications*, New

York: Springer, 2008.

[18] *IEEE Standard for Synchrophasors for Power Systems*, IEEE Std. 1344, 1995.

[19] *IEEE Standard for Synchrophasors for Power Systems*, IEEE Std. 1344 (R2001), 2001.

[20] *IEEE Standard for Synchrophasors for Power Systems*, IEEE Std. C37.118, 2005.

[21] C. W. Taylor, D. C. Erickson, K. E. Martin, R. E. Wilson, and V. Venkatasubramanian, "WACS - Wide-area stability and voltage control system: R & D and online demonstration," *Proc. of the IEEE*, vol. 93, no. 5, pp. 892-906, May 2005.

[22] R. O. Burnett, Jr., *et al.*, "Synchronized phasor measurements of a power system event," *IEEE Trans. Power Syst.*, vol. 9, no. 3, pp. 1643-1650, Aug. 1994.

[23] G. Andersson, *et al.*, "Causes of the 2003 major grid blackouts in North America and Europe, and recommended means to improve system dynamic performance," *IEEE Trans. Power Syst.*, vol. 20, no. 4, pp. 1922-1928, Nov. 2005.

[24] J. F. Hauer, N. B. Bhatt, K. Shah, and S. Kollurt, "Performance of WAMS East in providing dynamic information for the North East blackout of August 14, 2003," in *Proc. IEEE PES General Meeting*, 2004.

[25] D. Karlsson, M. Hemmingsson, and S. Lindahl, "Wide area system monitoring and control," *IEEE Power & Energy Mag.*, pp. 68-76, Sep./Oct. 2004.

[26] J. Bertsch, C. Carnal, D. Karlsson, J. McDaniel, and K. Vu, "Wide-area protection and power system utilization," *Proc. of the IEEE*, vol. 93, no. 5, pp. 997-1003, May 2005.

[27] M. A. Street, I. P. Thurein, and K. E. Martin, "Global positioning system applications at the Bonneville Power Administration," in *Proc. IEEE Technical Applications Conference and Workshops (Northcon95)*, 1995, pp. 244-251.

[28] A. R. Khatib, R. F. Nuqui, M. R. Ingram, and A. G. Phadke, "Real-time estimation of security from voltage collapse using synchronized phasor measurements," in *Proc. IEEE Power Engineering Society General Meeting*, 2004, pp. 582-588.

[29] L. Mili, T. Baldwin, and R. Adapa, "Phasor measurement placement for voltage stability analysis of power systems," in *Proc. the 29th IEEE Conf. Decision and Control*, 1990, pp. 3033-3038.

[30] M. L. Scala, *et al.*, "Development of applications in WAMS and WACS: an international cooperation experience," in *Proc. IEEE PES General Meeting*, 2006.

[31] I. Kamwa, *et al.*, "Wide-area monitoring and control at Hydro-Quebec: past, present and future," in *Proc. IEEE Power Eng. Soc. General Meeting*, 2006.

[32] K. E. Martin, "Phasor measurement systems in the WECC," in *Proc. IEEE PES General Meeting*, 2006.

[33] J. Y. Cai, Z. Huang, J. Hauer, and K. Martin, "Current status and experience of WAMS implementation in North America," in *Proc. IEEE/PES Transmission and Distribution Conference & Exposition: Asia and Pacific*, 2005.

[34] A. B. Leirbukt, *et al.*, "Wide area monitoring experience in Norway," in *Proc. Power System Conference and Exposition (PSCE2006)*, 2006.

[35] J. Rasmussen and P. Jorgensen, "Synchronized phasor measurements of a power system even in Eastern Denmark," in *Proc. IEEE PowerTech Conference*, 2003.

[36] I. C. Decker, D. Dotta, M. N. Agostini, S. L. Zimath, and A. S. Silva, "Performance of a synchronized phasor measurements system in the Brazilian power system," in *Proc. IEEE PES General Meeting*, 2006.

[37] Y. Ota, *et al.*, "PMU based power oscillation detection system and its application to Japanese longitudinal power system," in *Proc. 15th PSCC*, 2005.

[38] X. Xie, Y. Xin, J. Xiao, J. Wu, and Y. Han, "WAMS application in Chinese power systems," *IEEE Power & Energy Mag.*, pp. 54-63, Jan./Feb. 2006.

[39] H. Wu, K. S. Tsakalis, and G. T. Heydt, "Evaluation of time delay effects to wide-area power system stabilizer design," *IEEE Trans. Power Syst.*, vol. 19, no. 4, pp. 1935-1941, Nov. 2004.

[40] D. Ivanescu, *et al.*, "Control of an interconnected power system: a time delay approach," *IMA Journal of Mathematical Control and Information*, vol. 19, no. 1 and 2, pp. 115-131, 2002.

[41] H. Nguyen-Duc, L.-A. Dessaint, and A. F. Okou, "Power system robust stability analysis using structured singular value theory and model order reduction," in *Proc. Power & Energy Society General Meeting*, 2009.

[42] J. W. Stahlhut, T. J. Browne, G. T. Heydt, and V. Vittal, "Latency viewed as a stochastic process and its impact on wide area power system control signals," *IEEE Trans. Power Syst.*, vol. 23, no. 1, pp. 84-91, Feb. 2008.

[43] F. Okou, L.-A. Dessaint, and O. Akhrif, "Power systems stability enhancements using a wide-area signals based hierarchical controller," *IEEE Trans. Power Syst.*, vol. 20, no. 3, pp. 1465-1477, Aug. 2005.

[44] C.-x. Dou, X.-z. Zhang, S.-l. Guo, and C.-C. Mao, "Delay-independent excitation control for uncertain large power systems using wide-area measurement signals," *International Journal of Electrical Power & Energy Systems*, vol. 32, no. 3, pp. 210-217, March 2010.

[45] Z. Hu and J. V. Milanovic, "Damping of inter-area oscillations by WAM based supplementary controller," in *Proc. IEEE Power Engineering Society General Meeting, Tampa, FL*, 2007.

[46] H. Ni, G. T. Heydt, and L. Mili, "Power system stability agents using robust wide area control," *IEEE Trans. Power Syst.*, vol. 17, no. 4, pp. 1123-1131, Nov. 2002.

[47] Z. Hu and J. V. Milanovic, "The effectiveness of WAM based adaptive supervisory controller for global stabilization of power systems," in *Proc. IEEE Power Tech*, Lausanne, 2007, pp. 1652-1659.

[48] Y. Zhang and A. Bose, "Design of wide-area damping controllers for interarea oscillations," *IEEE Trans. Power Syst.*, vol. 23, no. 3, pp. 1136-1143, Aug. 2008.

[49] D. Dotta, A. S. e. Silva, and I. C. Decker, "Wide-area measurements-based two-level control design considering signal transmission delay," *IEEE Trans. Power Syst.*, vol. 24, no. 1, pp. 208-216, Feb. 2009.

[50] H. Jia, X. Yu, Y. Yu, and C. Wang, "Power system small signal stability region with time delays," *International Journal of Electrical Power & Energy Systems*, vol. 30, no. 1, pp. 16-22, Jan. 2008.

[51] M. Chenine, K. Zhu, and L. Nordstrom, "Survey on priotities and communication requirements for PMU-based applications in the Nordic region," in *Proc. IEEE PowerTech*, Bucharest, 2009.

[52] B. Chaudhuri, R. Majumder, and B. C. Pal, "Wide-area measurement-based stabilizing control of power considering signal transmission delay," *IEEE Trans. Power Syst.*, vol. 19, no. 4, pp. 1971-1979, Nov. 2004.

[53] T. Zabaiou, F. A. Okou, L.-A. Dessaint, and O. Akhrif, "Time-delay compensation of a wide-area measurements-based hierarchical voltage and speed regulator," *Canadian Jour. Elect. & Computer Eng.*, vol. 33, no. 2, pp. 77-85, Spring 2008.

[54] M. Klein, L. X. Le, G. J. Rogers, S. Farrokhpay, and N. J. Balu, "H_∞ damping controller design in large power systems," *IEEE Trans. Power Syst.*, vol. 10, no. 1, pp. 158-166, Feb. 1995.

[55] S. Skogestad and I. Postlethwaite, *Multivariable Feedback Control: Analysis and Design*, UK: John Wiley and Sons, 1996.

[56] C. Scherer, P. Gahinet, and M. Chilali, "Multiobjective output-feedback control via LMI optimization," *IEEE Trans. Automatic Control*, vol. 42, no. 7, pp. 896-911, July 1997.

[57] B. Dalela and G. Radman, "A study of multivariable supplementary power system stabilizers," in *Proc. 37th Annual North American Power Symposium*, 2005, pp. 134-140.

[58] Y.-N. Yu, K. Vongsuriya, and L. N. Wedman, "Application of an optimal control theory to a power system," *IEEE Trans. Power Apparatus and Syst.*, vol. 89, no. 1, pp. 55-62, Jan. 1970.

[59] E. J. Davison and N. S. Rau, "The optimal output feedback control of a synchronous machine," *IEEE Trans. Power Apparatus and Syst.*, vol. 90, no. 5, pp. 2123-2134, Sep. 1971.

[60] H. A. M. Moussa and Y.-n. Yu, "Optimal power system stabilization through excitation and/or governor control," *IEEE Trans. Power Apparatus and Syst.*, vol. 91, no. 3, pp. 1166-1174, May

1972.

[61] Y.-n. Yu and H. A. M. Moussa, "Optimal stabilization of a multi-machine system," *IEEE Trans. Power Apparatus and Syst.*, vol. 91, no. 3, pp. 1174-1182, May 1972.

[62] M. C. Menelaou and D. C. Macdonald, "Supplementary signals to improve transient stability, on-line application to a micro-generator," *IEEE Trans. Power Apparatus and Syst.*, vol. 101, no. 9, pp. 3543-3550, Sep. 1982.

[63] G. Radman, "Design of power system stabilizer based on LQG/LTR formulations," in *Proc. Industry Applications Society Annual Meeting*, 1992, pp. 1787-1792.

[64] J.-C. Seo, T.-H. Kim, H.-K. Park, and S.-I. Moon, "An LQG based PSS design for controlling SSR in power systems with series-compensated lines," *IEEE Trans. Energy Conversion*, vol. 11, no. 2, pp. 423-428, June 1996.

[65] F. Fatehi, J. R. Smith, and D. A. Pierre, "Robust power system controller design based on measured models," *IEEE Trans. Power Syst.*, vol. 11, no. 2, pp. 774-780, May 1996.

[66] T. Michigami, M. Terasaki, N. Sasazima, K. Hayashi, and T. Okamoto, "Development of a new adaptive LQG system generator for high-speed damping control techniques of power system oscillation," *Elect. Engr. in Japan (Wiley Periodicals, Inc.)*, vol. 142, no. 3, pp. 30-40, Feb. 2003.

[67] A. Elices, L. Rouco, H. Bourles, and T. Margotin, "Design of robust controllers for damping interarea oscillations: Application to the European power system," *IEEE Trans. Power Syst.*, vol. 19, no. 2, pp. 1058-1067, May 2004.

[68] G. C. Verghese, I. J. Perez-Arriaga, and F. C. Schweppe, "Selective modal analysis with applications to electric power systems, Part 1: Heuristic introduction," *IEEE Trans. Power Apparatus and Syst.*, vol. PAS-101, no. 9, pp. 3117-3125, Sep. 1982.

[69] G. C. Verghese, I. J. Perez-Arriaga, and F. C. Schweppe, "Selective modal analysis with applications to electric power systems, Part II: The dynamic stability problem," *IEEE Trans. Power Apparatus and Syst.*, vol. PAS-101, no. 9, pp. 3126-3134, Sep. 1982.

[70] E. W. Palmer and G. Ledwich, "Optimal placement of angle transducers in power systems," *IEEE Trans. Power Syst.*, vol. 11, no. 2, pp. 788-793, May 1996.

[71] I. Kamwa, L. Gerin-Lajoie, and G. Trudel, "Multi-loop power system stabilizers using wide-area synchronous phasor measurements," in *Proc. American Control Conf.*, 1998, pp. 2963-2967 vol.5.

[72] J. H. Chow, *Time-Scale Modeling of Dynamic Networks with Applications to Power Systems*: Springer-Verlag, 1982.

[73] K. K. Anaparthi, B. Chaudhuri, N. F. Thornhill, and B. C. Pal, "Coherency identification in power systems through principal component analysis," *IEEE Trans. Power Syst.*, vol. 20, no. 3, pp. 1658-1660, Aug. 2005.

[74] P. Kundur, *Power System Stability and Control*: McGraw Hill, 1993.

[75] M. A. Pai, *Energy Function Analysis for Power System Stability*, Boston: Kluwer Academic Publishers, 1989.

[76] T. J. Hammons and D. J. Winning, "Comparisons of synchronous-machine models in the study of the transient behaviour of electrical power systems," *Proc. of the IEE*, vol. 118, no. 10, pp. 1442-1458, Oct. 1971.

[77] *IEEE Recommended Practice for Excitation System Models for Power System Stability Studies*, IEEE Std 421.5-2005, 2005.

[78] E. V. Larsen and D. A. Swann, "Applying power system stabilizers - Part I, II and III," *IEEE Trans. Power Apparatus and Syst.*, vol. 100, no. 6, pp. 3017-3046, June 1981.

[79] IEEE Task Force on Load Representation for Dynamic Performance, "Load representation for dynamic performance analysis," *IEEE Trans. Power Syst.*, vol. 8, no. 2, pp. 472-482, May 1993.

[80] C. Concordia and S. Ihara, "Load representation in power system stability studies," *IEEE Trans. Power Apparatus and Syst.*, vol. PAS-101, no. 4, pp. 969-977, April 1982.

[81] J. Machowski, J. W. Bialek, and J. R. Bumby, *Power System Dynamics - Stability and Control*,

2nd. ed, Chichester: Wiley, 2008.

[82] P. M. Anderson and A. A. Fouad, *Power System Control and Stability*: IEEE Press, 1994.

[83] L. Philipp, A. Mahmood, and B. Philipp, "An improved refinable rational approximation to the ideal time delay," *IEEE Trans. Circuit Syst.*, vol. 46, no. 5, pp. 637-640, May 1999.

[84] N. Martins and L. T. G. Lima, "Determination of suitable locations for power system stabilizers and static VAR compensators for damping electromechanical oscillations in large scale power systems," *IEEE Trans. Power Syst.*, vol. 5, no. 4, pp. 1455-1469, Nov. 1990.

[85] J. M. Maciejowski, *Multivariable Feedback Design*, UK: Addison-Wesley, 1989.

[86] L. Meirovitch, *Dynamics and Control of Structures*, New York: John Wiley, 1992.

[87] Y.-H. Lin and C.-L. Chu, "A new design for independent modal space control of general dynamic systems," *Journal of Sound and Vibration*, vol. 180, no. 2, pp. 351-361 1995.

[88] G. H. Golub and C. F. V. Loan, *Matrix Computations*, Baltimore: The John Hopkins University Press, 1989.

[89] T. Kailath, *Linear Systems*, London: Englewood Cliffs, 1980.

[90] J. Doyle, "Guaranteed margins for LQG regulators," *IEEE Trans. Automatic Control*, vol. 23, no. 4, pp. 756-757, Aug. 1978.

[91] J. Doyle and G. Stein, "Robustness with observers," *IEEE Trans. Automatic Control*, vol. 24, no. 4, pp. 607-611, Aug. 1979.

[92] J. Doyle and G. Stein, "Multivariable feedback design: Concepts for a classical/modern synthesis," *IEEE Trans. Automatic Control*, vol. 26, no. 1, pp. 4-16, Feb. 1981.

[93] B. Moore, "Principal component analysis in linear systems: Controllability, observability, and model reduction," *IEEE Trans. Aut. Control*, vol. 26, no. 1, pp. 17-32, Feb. 1981.

[94] M. G. Safonov and R. Y. Chiang, "A Schur method for balanced model reduction," *IEEE Trans. Aut. Control*, vol. 34, no. 7, pp. 729-733, July 1989.

[95] *IEEE benchmark systems*, [online], Available: http://psdyn.ece.wisc.edu/IEEE_benchmarks/index.htm.

[96] I. Lloyd N. Trefethen and David Bau, *Numerical Linear Algebra*, Philadelphia: Society for Industrial and Applied Mathematics, 1997.

[97] B. Noble and J. W. Daniel, *Applied Linear Algebra*, Englewood Cliffs: Prentice-Hall Inc., 1988.

[98] A. S. Householder, *The Theory of Matrices in Numerical Analysis*, New York: Blaisdell Publishing Co., 1964.

[99] N. F. Thornhill, "Spectral principal component analysis of dynamic process data," *Control Eng. Practice*, vol. 10, no. 8, pp. 833-846, Aug. 2002.

[100] S. K. Yee, "Coordinated tuning of power system damping controllers for robust stabilization of the system," Ph.D. thesis, The University of Manchester, Manchester, UK, 2005.

[101] R. Podmore, "Identification of coherent generators for dynamic equivalents," *IEEE Trans. Power Apparatus and Syst.*, vol. PAS-97, no. 4, pp. 1344-1354, July 1978.

[102] J. R. Winkelman, J. H. Chow, B. C. Bowler, B. Avramovic, and P. V. Kokotovic, "An analysis of interarea dynamics of multi-machine systems," *IEEE Trans. Power Apparatus and Syst.*, vol. PAS-100, no. 2, pp. 754-763, Feb. 1981.

[103] S. B. Yusof, G. J. Rogers, and R. T. H. Alden, "Slow coherency based network partitioning including load buses," *IEEE Trans. Power Syst.*, vol. 8, no. 3, pp. 1375-1382, Aug. 1993.

[104] S. Valle, W. Li, and S. J. Qin, "Selection of the number of principal components: The variance of the reconstruction error criterion with a comparison to other methods," *Industrial and Engineering Chemistry Research*, vol. 38, no. 11, pp. 4389–4401, Sep. 1999.

[105] B. S. Everitt, *Cluster Analysis*, 3rd ed, London: Edward Arnold, 1993.

[106] J. C. Doyle, K. Glover, P. P. Khargonekar, and B. A. Francis, "State-space solutions to standard H_2

and H_∞ control problems," *IEEE Trans. Aut. Control*, vol. 34, no. 8, pp. 831-847, Aug. 1989.

[107] B. Chaudhuri, R. Majumder, and B. C. Pal, "Application of multiple-model apaptive control strategy for robust damping of interarea oscillations in power system," *IEEE Trans. Control Syst. Tech.*, vol. 12, no. 5, pp. 727-736, Sep. 2004.

[108] R. Majumder, B. Chaudhuri, and B. C. Pal, "A probabilistic approach to model-based adaptive control for damping of interarea oscillations," *IEEE Trans. Power Syst.*, vol. 20, no. 1, pp. 367-374, Feb. 2005.

[109] R. D. Zimmerman, C. E. Murillo-Sánchez, and D. Gan, *MATPOWER*, [online], Available: http://www.pserc.cornell.edu/matpower/.

8 APPENDICES

8.1 Appendix A

8.1.1 Four-Machine Test System Data

Original data are taken from [74]. Modifications to network parameters are listed in parenthesis. The system base is 100 MVA. Bus 1 is the slack bus.

Table 8-1: Line data

No.	From bus	To bus	***R*** [pu]	***X*** [pu]	***B*** [pu]
1	1	5	0.0000	0.15/9	0.00000
2	2	6	0.0000	0.15/9	0.00000
3	3	11	0.0000	0.15/9	0.00000
4	4	10	0.0000	0.15/9	0.00000
5	9	10	0.0001×10	0.001×10	0.00175×10
6	10	11	0.0001×25	0.001×25	0.00175×25
7	6	7	0.0001×10×(5)	0.001×10×(5)	0.00175×10×(5)
8	6	7	(0.0001×10×5)	(0.001×10×5)	(0.00175×10×5)
9	5	8	(0.0001×110)	(0.001×110)	(0.00175×110)
10	5	8	(0.0001×110)	(0.001×110)	(0.00175×110)
11	7	8	0.0001×110	0.001×110	0.00175×110
12	7	8	0.0001×110	0.001×110	0.00175×110
13	8	9	0.0001×110	0.001×110	0.00175×110
14	8	9	0.0001×110	0.001×110	0.00175×110

Table 8-2: Shunt capacitors

Bus	Q_c [MVAr]
7	200
8	(200)
9	350

Table 8-3: Load flow data

Bus	V_m [pu]	V_a [º]	P_G [MW]	Q_G [MVAr]	P_L [MW]	Q_L [MVAr]
1	1.03	0	715	137	0	0
2	1.01	-24.21	700	109	0	0
3	1.03	-10.88	700	124	0	0
4	1.01	-20.48	700	87	0	0
5	1.01	-6.55	0	0	0	0
6	1.00	-30.85	0	0	0	0
7	0.99	-41.02	0	0	967+(100)	1
8	1.01	-28.85	0	0	(100)	(10)
9	1.00	-35.06	0	0	1767-(200)	1
10	1.00	-27.10	0	0	0	0
11	1.02	-17.27	0	0	0	0

Table 8-4: Generator dynamic data

G_i	R_a [pu]	X_d [pu]	X'_d [pu]	T'_{d_o} [s]	X''_d [pu]	T''_{d_o} [s]	X_q [pu]	X'_q [pu]	T'_{q_o} [s]	X''_q [pu]	T''_{q_o} [s]	H [MW.s/MVA]
G1	0.0025/9	1.8/9	0.3/9	8.0	0.25/9	0.03	1.7/9	0.55/9	0.4	0.25/9	0.05	6.500×9
G2	0.0025/9	1.8/9	0.3/9	8.0	0.25/9	0.03	1.7/9	0.55/9	0.4	0.25/9	0.05	6.500×9
G3	0.0025/9	1.8/9	0.3/9	8.0	0.25/9	0.03	1.7/9	0.55/9	0.4	0.25/9	0.05	6.175×9
G4	0.0025/9	1.8/9	0.3/9	8.0	0.25/9	0.03	1.7/9	0.55/9	0.4	0.25/9	0.05	6.175×9

Table 8-5: PSS data

G_i	K_{PSS}	T_1	T_2	T_3	T_4	T_W	$V_{PSS\text{-}max}$	$V_{PSS\text{-}min}$
G1	20	0.05	0.02	3	5.4	10	+0.1	–0.1
G2	20	0.05	0.02	3	5.4	10	+0.1	–0.1
G3	20	0.05	0.02	3	5.4	10	+0.1	–0.1
G4	20	0.05	0.02	3	5.4	10	+0.1	–0.1

Table 8-6: AVR data

G_i	K_A	T_A	T_B	T_C	$E_{fd\text{-}max}$	$E_{fd\text{-}min}$
G1	200	0.01	10	1	+5.5	–5.5
G2	200	0.01	10	1	+5.5	–5.5
G3	200	0.01	10	1	+5.5	–5.5
G4	200	0.01	10	1	+5.5	–5.5

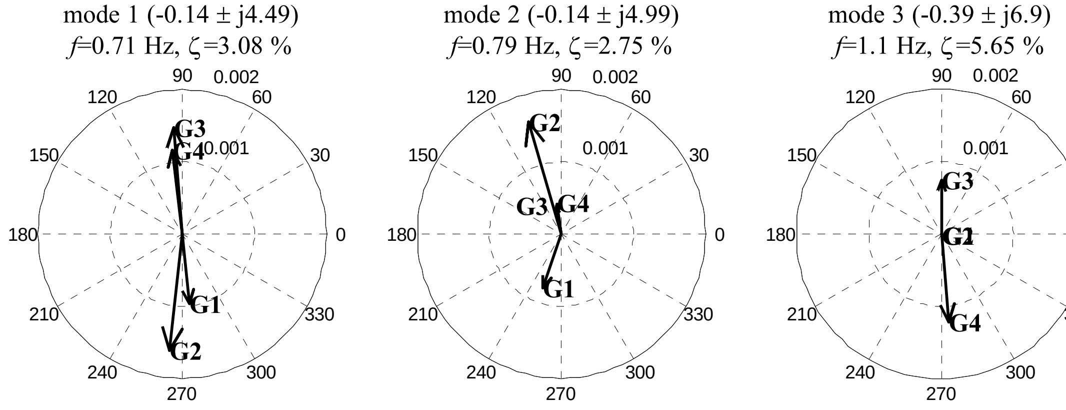

Figure 8-1: Mode shape plots (4-machine test system)

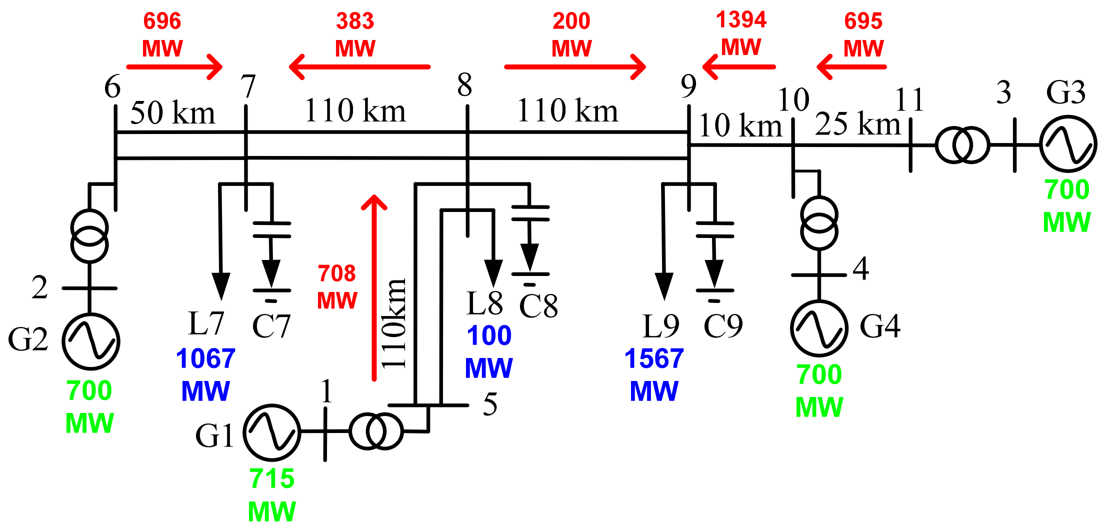

Figure 8-2: Power transfers across the 4-machine test system

8.1.2 New England Test System Data

Original data are taken from [75, 95, 109]. Modifications to network parameters are listed in parenthesis. The system base is 100 MVA. Bus 31 is the slack bus. All data are in per unit with system base 100 MVA.

Table 8-7: Line data

No.	**From bus**	**To bus**	***R* [pu]**	***X* [pu]**	***B* [pu]**
1	1	2	0.0035	0.0411	0.6987
2	1	39	0.0010	0.025	0.75
3	2	3	0.0013	0.0151	0.2572
4	2	25	0.0070	0.0086	0.146
5	3	4	0.0013/(2)	0.0213/(2)	0.2214/(2)
6	3	18	0.0011	0.0133	0.2138
7	4	5	0.0008/(2)	0.0128/(2)	0.1342/(2)
8	4	14	0.0008	0.0129	0.1382
9	5	6	0.0002/(2)	0.0026/(2)	0.0434/(2)
10	5	8	0.0008	0.0112	0.1476
11	6	7	0.0006	0.0092	0.113
12	6	11	0.0007	0.0082	0.1389
13	7	8	0.0004	0.0046	0.078
14	8	9	0.0023	0.0363	0.3804
15	9	39	0.0010	0.025	1.2
16	10	11	0.0004	0.0043	0.0729
17	10	13	0.0004	0.0043	0.0729
18	13	14	0.0009/(2)	0.0101/(2)	0.1723/(2)
19	14	15	0.0018×(3)	0.0217×(3)	0.366×(3)
20	15	16	0.0009×(3)	0.0094×(3)	0.171×(3)
21	16	17	0.0007×(3)	0.0089×(3)	0.1342×(3)
22	16	19	0.0016×(8)	0.0195×(8)	0.304×(8)
23	16	21	0.0008×(4)	0.0135×(4)	0.2548×(4)
24	16	24	0.0003×(4)	0.0059×(4)	0.068×(4)
25	17	18	0.0007	0.0082	0.1319
26	17	27	0.0013	0.0173	0.3216
27	21	22	0.0008×(4)	0.014×(4)	0.2565×(4)
28	22	23	0.0006	0.0096	0.1846
29	23	24	0.0022×(4)	0.035×(4)	0.361×(4)
30	25	26	0.0032/(2)	0.0323/(2)	0.513/(2)
31	26	27	0.0014/(2)	0.0147/(2)	0.2396/(2)
32	26	28	0.0043/(2)	0.0474/(2)	0.7802/(2)
33	26	29	0.0057/(2)	0.0625/(2)	1.029/(2)
34	28	29	0.0014/(2)	0.0151/(2)	0.249/(2)
35	12	11	0.0016	0.0435	0
36	12	13	0.0016	0.0435	0
37	6	31	0.0000	0.025	0
38	10	32	0.0000	0.02	0
39	19	33	0.0007	0.0142	0
40	20	34	0.0009	0.018	0
41	22	35	0.0000	0.0143	0
42	23	36	0.0005	0.0272	0
43	25	37	0.0006	0.0232	0
44	2	30	0.0000	0.0181	0
45	29	38	0.0008	0.0156	0
46	19	20	0.0007	0.0138	0

Table 8-8: Shunt capacitors

Bus	Q_c [MVAr]
15	(200)
21	(100)

Table 8-9: Load flow data

Bus	V_m [pu]	V_a [º]	P_G [MW]	Q_G [MVAr]	P_L [MW]	Q_L [MVAr]
1	1.0361	-10.25	0	0	0	0
2	1.0192	-7.55	0	0	0	0
3	0.9933	-10.19	0	0	322	2.4
4	0.9700	-10.43	0	0	500	184
5	0.9660	-9.65	0	0	0	0
6	0.9660	-9.22	0	0	0	0
7	0.9579	-11.50	0	0	233.8	84
8	0.9585	-11.99	0	0	522	176.6
9	1.0127	-11.94	0	0	0	0
10	0.9733	-6.68	0	0	0	0
11	0.9696	-7.55	0	0	0	0
12	0.9517	-7.60	0	0	8.5	88
13	0.9740	-7.50	0	0	0	0
14	0.9775	-8.46	0	0	0	0
15	1.0271	-10.56	0	0	320	153
16	1.0207	-6.30	0	0	329.4	32.3
17	1.0080	-8.89	0	0	0	0
18	1.0010	-9.83	0	0	158	30
19	0.9874	37.20	0	0	0	0
20	0.9854	35.79	0	0	680	103
21	1.0177	3.23	0	0	274	115
22	1.0390	21.69	0	0	0	0
23	1.0377	21.46	0	0	247.5	84.6
24	1.0385	-5.86	0	0	308.6	-92.2
25	1.0235	-6.24	0	0	224	47.2
26	1.0140	-7.28	0	0	139	17
27	1.0079	-8.56	0	0	281	75.5
28	1.0132	-5.39	0	0	206	27.6
29	1.0150	-3.92	0	0	283.5	26.9
30	1.0475	-5.12	250	169	0	0
31	0.9820	0.00	617	116	9.2	4.6
32	0.9831	1.13	650	93	0	0
33	0.9972	42.41	632	66	0	0
34	1.0123	40.97	508	149	0	0
35	1.0493	26.59	650	104	0	0
36	1.0635	29.36	560	129	0	0
37	1.0278	0.58	540	37	0	0
38	1.0265	3.18	830	85	0	0
39	1.0300	-11.80	1000	198	1104	250

Table 8-10: Generator dynamic data

G_i	R_a [pu]	X_d [pu]	X'_d [pu]	T'_{d_o} [s]	X''_d [pu]	T''_{d_o} [s]	X_q [pu]	X'_q [pu]	T'_{q_o} [s]	X''_q [pu]	T''_{q_o} [s]	H [MW.s/MVA]
G1	0	0.0200	0.0060	7.00	0.00590	0.09	0.019	0.008	0.7	0.0080	0.70	1000
G2	0	0.2950	0.0697	6.56	0.06969	0.09	0.282	0.170	1.5	0.1700	1.50	60.6
G3	0	0.2495	0.0531	5.70	0.05309	0.09	0.237	0.0876	1.5	0.0876	1.50	71.6
G4	0	0.2620	0.0436	5.69	0.04359	0.09	0.258	0.166	1.5	0.1660	1.50	57.2
G5	0	0.6700	0.1320	5.40	0.13190	0.09	0.620	0.166	0.44	0.1660	0.44	52.0
G6	0	0.2540	0.0500	7.30	0.04900	0.09	0.241	0.0814	0.4	0.0814	0.40	69.6
G7	0	0.2950	0.0490	5.66	0.04890	0.09	0.292	0.186	1.5	0.1860	1.50	52.8
G8	0	0.2900	0.0570	6.70	0.05690	0.09	0.280	0.0911	0.41	0.0911	0.41	48.6
G9	0	0.2106	0.0570	4.79	0.05690	0.09	0.205	0.0587	1.96	0.0587	1.96	69.0
G10	0	0.1000	0.0310	10.20	0.03090	0.09	0.069	0.008	0.0	0.0689	0.0	84.0

Table 8-11: PSS data
(PSSs are tuned using the Sequential Tuning method [100] based on the residues [84])

G_i	K_{PSS}	T_1	T_2	N_B	T_W	T_{L1}	T_{L2}	$V_{PSS\text{-}max}$	$V_{PSS\text{-}min}$
G2	4	0.44076	0.097012	3	10	0.0563	0.1125	+0.1	–0.1
G3	4	0.44789	0.081542	2	10	0.0563	0.1125	+0.1	–0.1
G4	14	0.43786	0.37256	1	10	0.0563	0.1125	+0.1	–0.1
G5	15	0.54302	0.13261	2	10	0.0563	0.1125	+0.1	–0.1
G6	5	0.7544	0.087956	2	10	0.0563	0.1125	+0.1	–0.1
G7	10	0.95532	0.18515	1	10	0.0563	0.1125	+0.1	–0.1
G8	3	0.4346	0.097012	2	10	0.0563	0.1125	+0.1	–0.1
G9	9	0.37999	0.13187	2	10	0.0563	0.1125	+0.1	–0.1
G10	7	0.60132	0.065542	2	10	0.0563	0.1125	+0.1	–0.1

Table 8-12: AVR data

G_i	K_A	T_A	T_B	T_C	$E_{fd\text{-}max}$	$E_{fd\text{-}min}$
G1	200	0.055	10	2	+5.5	–5.5
G2	200	0.055	10	2	+5.5	–5.5
G3	200	0.055	10	2	+5.5	–5.5
G4	200	0.055	10	2	+5.5	–5.5
G5	200	0.055	10	2	+5.5	–5.5
G6	200	0.055	10	2	+5.5	–5.5
G7	200	0.055	10	2	+5.5	–5.5
G8	200	0.055	10	2	+5.5	–5.5
G9	200	0.055	10	2	+5.5	–5.5
G10	200	0.055	10	2	+5.5	–5.5

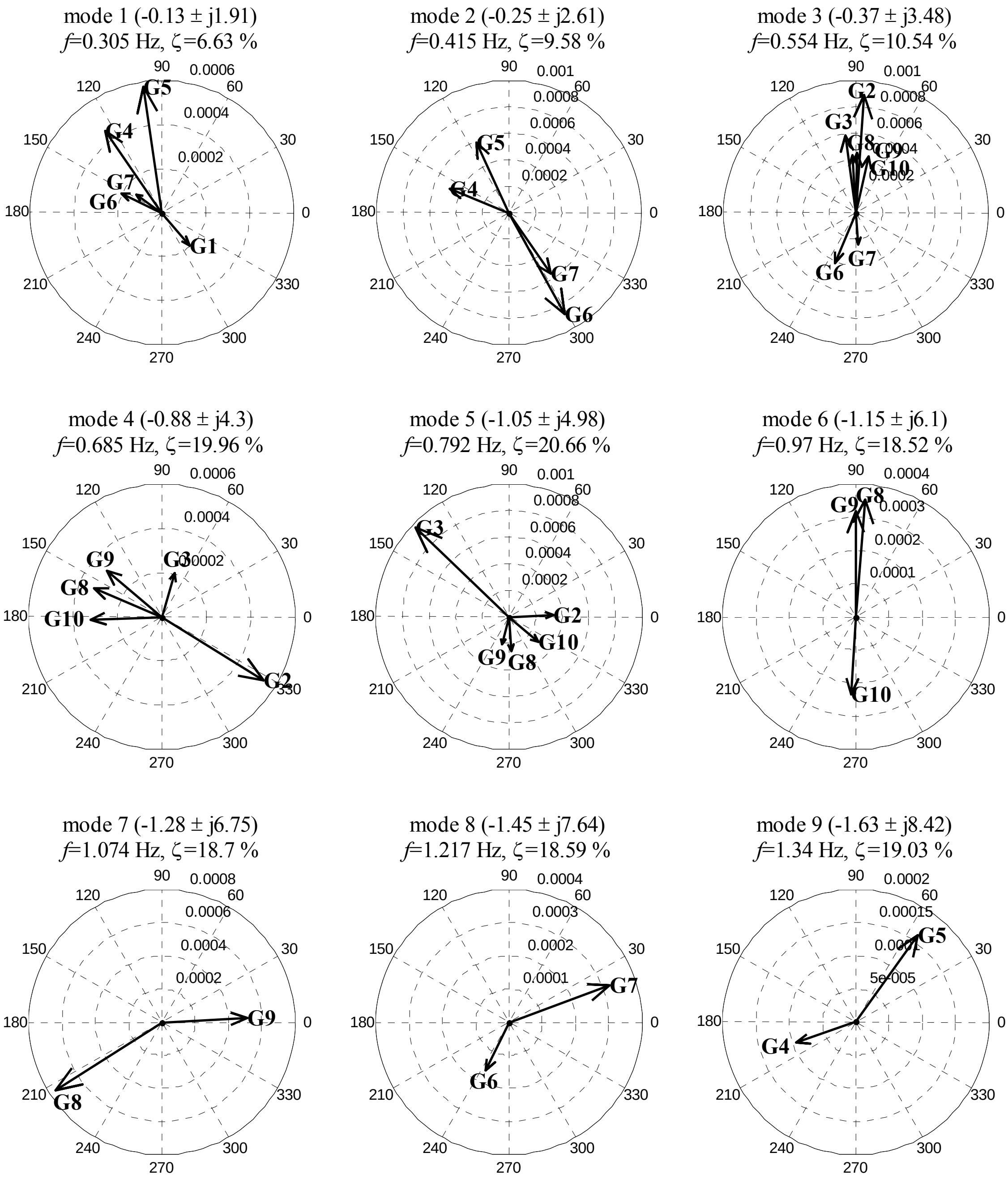

Figure 8-3: Mode shape plots (NETS)

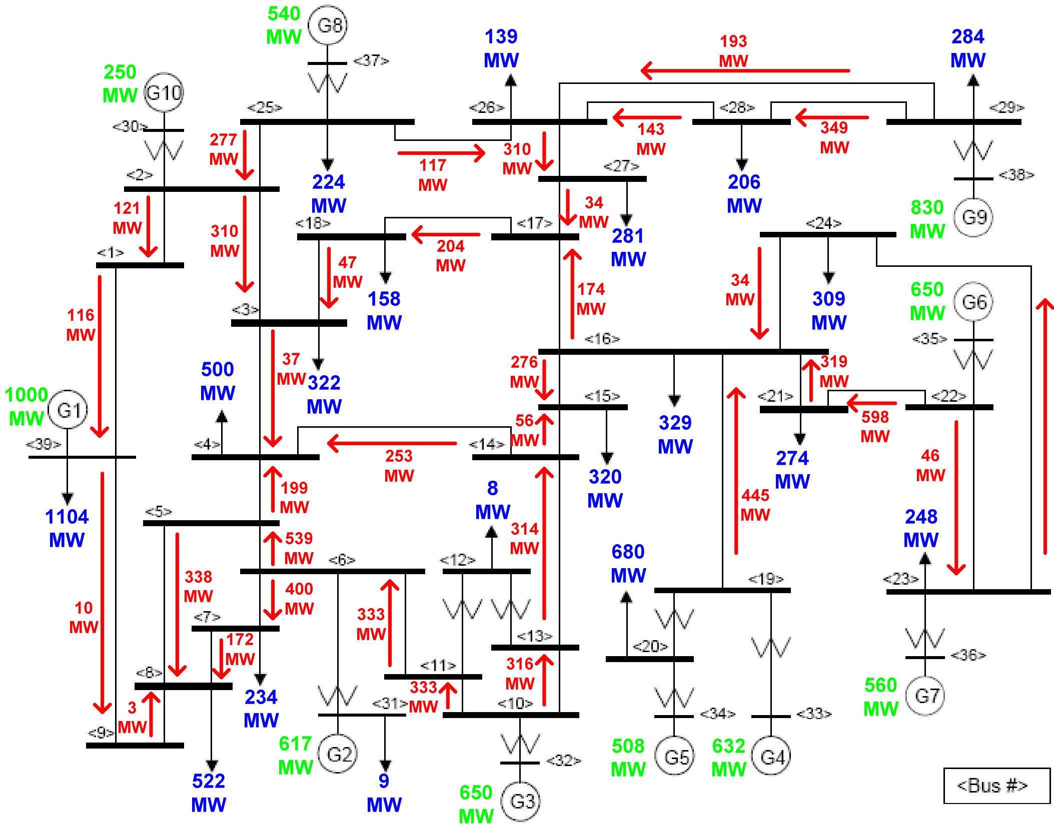

Figure 8-4: Power transfers across the New England test system

8.2 Appendix B

8.2.1 Illustrative Example on Real Modal Transformation

Consider the linear system, given in page 51, described in state-space representation

$$\dot{\boldsymbol{x}} = \boldsymbol{A}\boldsymbol{x} + \boldsymbol{B}\boldsymbol{u} \Rightarrow \begin{bmatrix} \dot{x}_1 \\ \dot{x}_2 \\ \dot{x}_3 \end{bmatrix} = \begin{bmatrix} 0 & 0 & -195 \\ 1 & 0 & -71 \\ 0 & 1 & -5 \end{bmatrix} \begin{bmatrix} x_1 \\ x_2 \\ x_3 \end{bmatrix} + \begin{bmatrix} 1 & 1.5 \\ 0 & 0.6 \\ 0 & 0 \end{bmatrix} \begin{bmatrix} u_1 \\ u_2 \end{bmatrix}$$

$$\boldsymbol{y} = \boldsymbol{C}\boldsymbol{x} + \boldsymbol{D}\boldsymbol{u} \Rightarrow \begin{bmatrix} y_1 \\ y_2 \\ y_3 \end{bmatrix} = \begin{bmatrix} 1 & -1 & 9 \\ 0 & 0 & 2 \\ -1 & 4 & 0 \end{bmatrix} \begin{bmatrix} x_1 \\ x_2 \\ x_3 \end{bmatrix} + \begin{bmatrix} 0 & 0 \\ 0 & 0 \\ 0 & 0 \end{bmatrix} \begin{bmatrix} u_1 \\ u_2 \end{bmatrix}$$

The real transformation matrices which map modal variables to state variables, obtained using the real Schur decomposition and computed using the Matlab function *canon.m*, are

$$\boldsymbol{U} = \begin{bmatrix} 1.7521 & -0.5445 & 1.5339 \\ 0.0539 & -0.0011 & 0.6019 \\ 0.0270 & 0.0601 & 0.0302 \end{bmatrix}, \quad \boldsymbol{M} = \begin{bmatrix} 0.5456 & -1.6367 & 4.91 \\ -0.2198 & -0.1743 & 14.635 \\ -0.0493 & 1.8076 & -0.4131 \end{bmatrix}$$

The system in modal-space representation, as in (3.25)-(3.26) and assuming zero input and output noises, is as follows

$$\dot{\boldsymbol{z}} = \boldsymbol{A}_m \boldsymbol{z} + \boldsymbol{B}_m \boldsymbol{u} \Rightarrow \begin{bmatrix} \dot{z}_1 \\ \dot{z}_2 \\ \dot{z}_3 \end{bmatrix} = \begin{bmatrix} -3 & 0 & 0 \\ 0 & -1 & 8 \\ 0 & 8 & -1 \end{bmatrix} \begin{bmatrix} z_1 \\ z_2 \\ z_3 \end{bmatrix} + \begin{bmatrix} 0.5456 & -0.1637 \\ -0.2198 & -0.4343 \\ -0.04926 & 1.011 \end{bmatrix} \begin{bmatrix} u_1 \\ u_2 \end{bmatrix}$$

$$\boldsymbol{y} = \boldsymbol{C}_m \boldsymbol{z} + \boldsymbol{D}_m \boldsymbol{u} \Rightarrow \begin{bmatrix} y_1 \\ y_2 \\ y_3 \end{bmatrix} = \begin{bmatrix} 1.941 & -0.002191 & 1.204 \\ 0.05391 & 0.1203 & 0.06041 \\ -1.536 & 0.5401 & 0.8738 \end{bmatrix} \begin{bmatrix} z_1 \\ z_2 \\ z_3 \end{bmatrix} + \begin{bmatrix} 0 & 0 \\ 0 & 0 \\ 0 & 0 \end{bmatrix} \begin{bmatrix} u_1 \\ u_2 \end{bmatrix}$$

where $\boldsymbol{A}_m$, $\boldsymbol{B}_m$, and $\boldsymbol{C}_m$ are computed using (3.21), (2.28), and (2.29), respectively, and $\boldsymbol{D}_m = \boldsymbol{D}$.

8.3 Appendix C

8.3.1 Numerical Values of Matrices in Chapter 3

The weighting matrix $\boldsymbol{Q_m}$ used for case 5 in Table 3-4 is

$$\begin{array}{cc} & \begin{array}{cccc} \text{mode 1} & \text{mode 2} & \text{mode 3} & \text{other modes} \end{array} \\ \boldsymbol{Q_m} = & \left[\begin{array}{cc:cc:cc:ccc} 0.2236 & & & & & & & & \\ & 0.2236 & & & & & & & \\ \hdashline & & 0.3725 & & & & & & \\ & & & 0.3725 & & & & & \\ \hdashline & & & & 0 & & & & \\ & & & & & 0 & & & \\ \hdashline & & & & & & 0 & & \\ & & & & & & & \ddots & \\ & & & & & & & & 0 \end{array}\right] \begin{array}{l} \\ \text{mode 1} \\ \\ \text{mode 2} \\ \\ \text{mode 3} \\ \\ \text{other modes} \\ \\ \end{array} \end{array}$$

The state-space representation of the 5th order SWAC, as in (3.16), used for robustness analysis in section (3.4.4) is as follows

$$\left[\begin{array}{c|c} \boldsymbol{A_c} & \boldsymbol{B_c} \\ \hline \boldsymbol{C_c} & \boldsymbol{D_c} \end{array}\right] = \left[\begin{array}{rrrrr|rrrr} 0 & -0.0004 & 0.0002 & 0.0005 & 0 & -0.0005 & 0.0001 & 0.0001 & 0.0001 \\ 0.0007 & -8.8041 & -5.8862 & -1.4678 & 2.8175 & 0.3278 & -2.4709 & 0.4976 & 0.3809 \\ -0.0002 & 13.0334 & -2.0949 & -3.8871 & -0.6564 & 0.1801 & 1.1936 & 0.1090 & 0.2411 \\ -0.0005 & -0.4302 & -0.1635 & -11.4605 & 9.0146 & -0.1002 & 0.3592 & 1.664 & 1.5692 \\ 0.0001 & 0.4518 & -0.9147 & -9.0090 & -0.4638 & 0.2358 & 0.3494 & -0.1058 & 0.1255 \\ \hline -0.0004 & -1.0551 & 0.9628 & 1.6188 & 0.1972 & 0 & 0 & 0 & 0 \\ -0.0002 & 2.1880 & -0.7579 & 0.4679 & -0.3680 & 0 & 0 & 0 & 0 \\ -0.0001 & -0.6402 & -0.1379 & -1.2270 & 0.1518 & 0 & 0 & 0 & 0 \\ -0.0003 & -0.5433 & -0.0808 & -1.0126 & 0.0849 & 0 & 0 & 0 & 0 \end{array}\right]$$

Table 8-13: Resulting LQR gain matrices when using conventional and modal LQG methods

no.	State	K^T (Conventional LQG, case 7 in Table 3-2)				K^T (Modal LQG, case 5 in Table 3-4)			
		u_1	u_2	u_3	u_4	u_1	u_2	u_3	u_4
1	x_{i1d}	0	0	0	0	0	0	0	0
2	x_{i1q}	0	0	0	0	0	0	0	0
3	E''_{1q}	0.142	-0.068	-0.035	-0.045	-0.052	0.012	0.022	0.019
4	E'_{1q}	2.472	-1.068	-0.732	-0.783	0.799	-0.371	-0.278	-0.203
5	E''_{1d}	-0.102	0.044	0.031	0.030	-0.0219	0.008	0.008	0.006
6	ω_1	-101.268	42.907	29.765	33.751	11.846	-1.015	-5.495	-5.21
7	x_{i2d}	0	0	0	0	0	0	0	0
8	x_{i2q}	0	0	0	0	0	0	0	0
9	E''_{2q}	-0.065	0.081	-0.008	-0.008	0.035	-0.048	0.005	0.007
10	E'_{2q}	-1.059	1.908	-0.451	-0.442	-0.264	0.705	-0.265	-0.208
11	E''_{2d}	0.050	-0.064	0.008	0.006	0.0072	-0.023	0.009	0.007
12	δ_2	-0.378	0.531	-0.072	-0.087	-0.251	0.451	-0.115	-0.095
13	ω_2	41.737	-64.096	12.605	10.849	-11.369	8.341	2.708	1.057
14	x_{i3d}	0	0	0	0	0	0	0	0
15	x_{i3q}	0	0	0	0	0	0	0	0
16	E''_{3q}	-0.041	-0.006	0.013	0.0389	0.013	0.023	-0.019	-0.017
17	E'_{3q}	-0.743	-0.441	1.261	-0.017	-0.320	-0.183	0.316	0.238
18	E''_{3d}	0.032	0.013	-0.035	-0.012	0.010	0.007	-0.011	-0.008
19	δ_3	-0.209	-0.125	0.465	-0.123	-0.208	-0.105	0.193	0.149
20	ω_3	33.387	11.853	-24.607	-24.334	-0.967	-5.235	2.582	3.222
21	x_{i4d}	0	0	0	0	0	0	0	0
22	x_{i4q}	0	0	0	0	0	0	0	0
23	E''_{4q}	-0.036	-0.005	0.032	0.013	0.008	0.016	-0.012	-0.012
24	E'_{4q}	-0.757	-0.430	-0.028	1.332	-0.255	-0.166	0.263	0.199
25	E''_{4d}	0.022	0.006	-0.002	-0.028	0.008	0.008	-0.009	-0.007
26	δ_4	-0.179	-0.069	-0.150	0.433	-0.133	-0.068	0.123	0.096
27	ω_4	25.346	8.862	-17.509	-19.573	0.301	-2.252	0.403	1.101
28	$x_{\tau y1}$	0	0	0	0	0	0	0	0
29	$x_{\tau y1}$	0	0	0	0	0	0	0	0
30	$x_{\tau y2}$	0	0	0	0	0	0	0	0
31	$x_{\tau y2}$	0	0	0	0	0	0	0	0
32	$x_{\tau y3}$	0	0	0	0	0	0	0	0
33	$x_{\tau y3}$	0	0	0	0	0	0	0	0
34	$x_{\tau y4}$	0	0	0	0	0	0	0	0
35	$x_{\tau y4}$	0	0	0	0	0	0	0	0
36	x_{PSS1}	-1.669	0.638	0.460	0.493	-0.226	0.039	0.104	0.089
37	x_{PSS1}	-121.951	52.046	36.196	38.632	-36.641	15.938	13.188	9.842
38	x_{PSS1}	2.057	-0.807	-0.595	-0.637	0.261	-0.024	-0.128	-0.114
39	x_{PSS2}	0.6438	-1.426	0.332	0.346	0.146	-0.201	0.019	0.031
40	x_{PSS2}	51.706	-95.947	23.126	22.892	13.127	-32.393	11.402	9.208
41	x_{PSS2}	-0.815	1.776	-0.447	-0.468	-0.187	0.233	-0.009	-0.029
42	x_{PSS3}	0.479	0.351	-1.161	0.205	0.062	0.103	-0.087	-0.081
43	x_{PSS3}	36.781	22.897	-66.018	3.340	14.306	9.258	-14.563	-11.217
44	x_{PSS3}	-0.6189	-0.474	1.472	-0.303	-0.064	-0.136	0.102	0.100
45	x_{PSS4}	0.507	0.355	0.235	-1.246	0.037	0.074	-0.056	-0.055
46	x_{PSS4}	37.731	22.515	4.008	-69.801	11.199	8.081	-11.846	-9.194
47	x_{PSS4}	-0.657	-0.483	-0.335	1.572	-0.033	-0.095	0.062	0.065
48	$x_{\tau u1}$	-1.8723	0.874	0.501	0.594	0.127	0.046	-0.082	-0.083
49	$x_{\tau u1}$	792.379	-336.277	-237.320	-251.087	267.817	-113.892	-97.285	-73.188
50	$x_{\tau u2}$	0.847	-1.220	0.199	0.198	-0.1806	0.131	0.051	0.014
51	$x_{\tau u2}$	-334.769	630.997	-155.319	-153.439	-99.932	237.423	-80.782	-65.981
52	$x_{\tau u3}$	0.544	0.177	-0.527	-0.247	0.008	-0.123	0.044	0.061
53	$x_{\tau u3}$	-239.695	-154.164	443.261	-30.458	-102.838	-70.116	106.149	82.495
54	$x_{\tau u4}$	0.523	0.167	-0.199	-0.563	0.0267	-0.077	0.009	0.028
55	$x_{\tau u4}$	-247.001	-151.665	-33.161	468.369	-79.937	-60.378	85.630	67.040
56	x_{AVR1}	1.044	-0.417	-0.314	-0.331	0.202	-0.037	-0.093	-0.079
57	E_{fd1}	0.003	-0.001	-0.001	-0.001	0.001	0	0	0
58	x_{AVR2}	-0.420	0.896	-0.236	-0.242	-0.1162	0.182	-0.029	-0.035
59	E_{fd2}	-0.001	0.002	-0.001	-0.001	0	0.001	0	0
60	x_{AVR3}	-0.321	-0.246	0.717	-0.127	-0.062	-0.091	0.083	0.075
61	E_{fd3}	-0.001	-0.001	0.001	0	0	0	0	0
62	x_{AVR4}	-0.339	-0.248	-0.136	0.760	-0.04	-0.067	0.057	0.053
63	E_{fd4}	-0.001	-0.001	0	0.002	0	0	0	0

8.4 Appendix D

8.4.1 System Responses to Small Disturbances

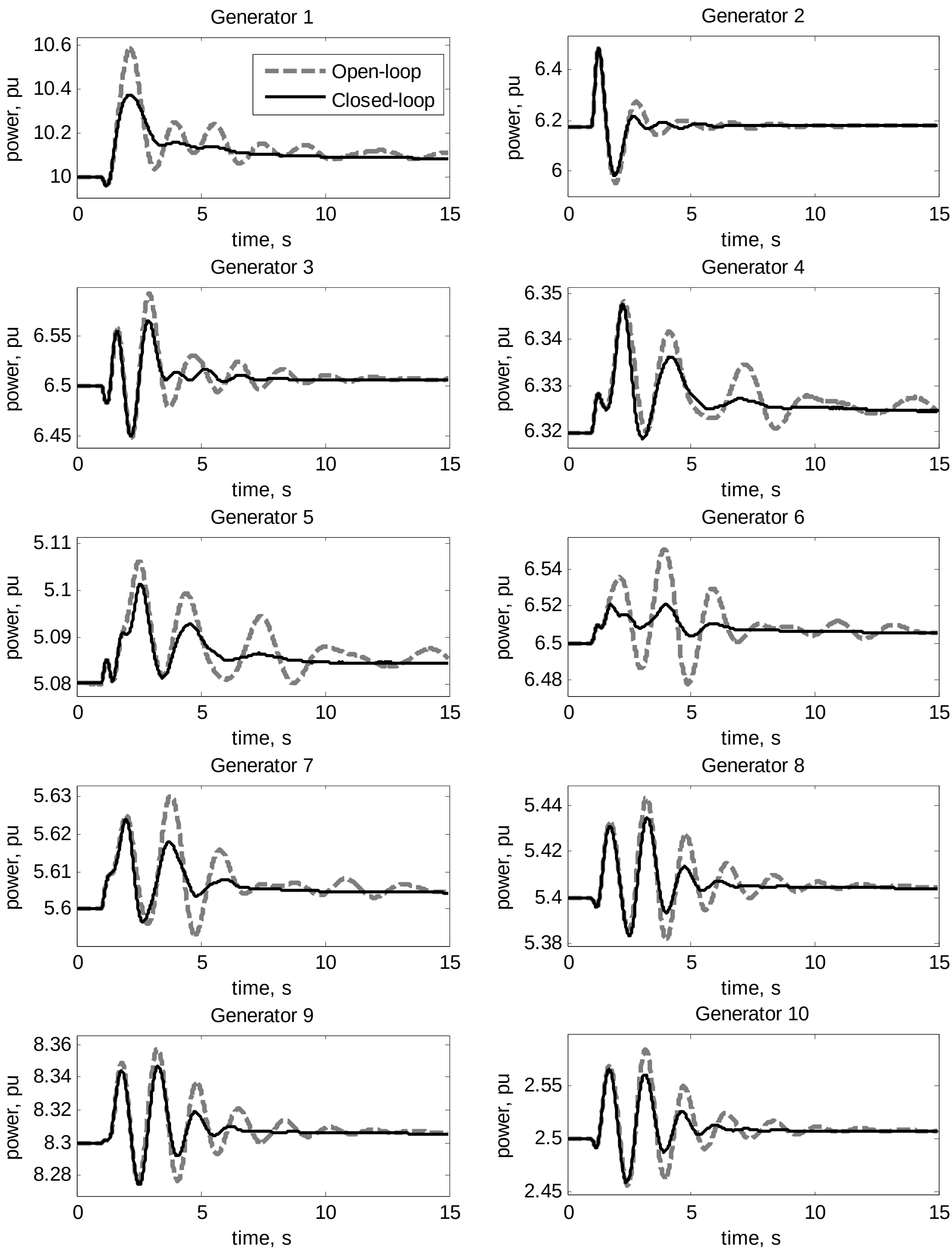

Figure 8-5: Active power responses for a small disturbance at generator 2

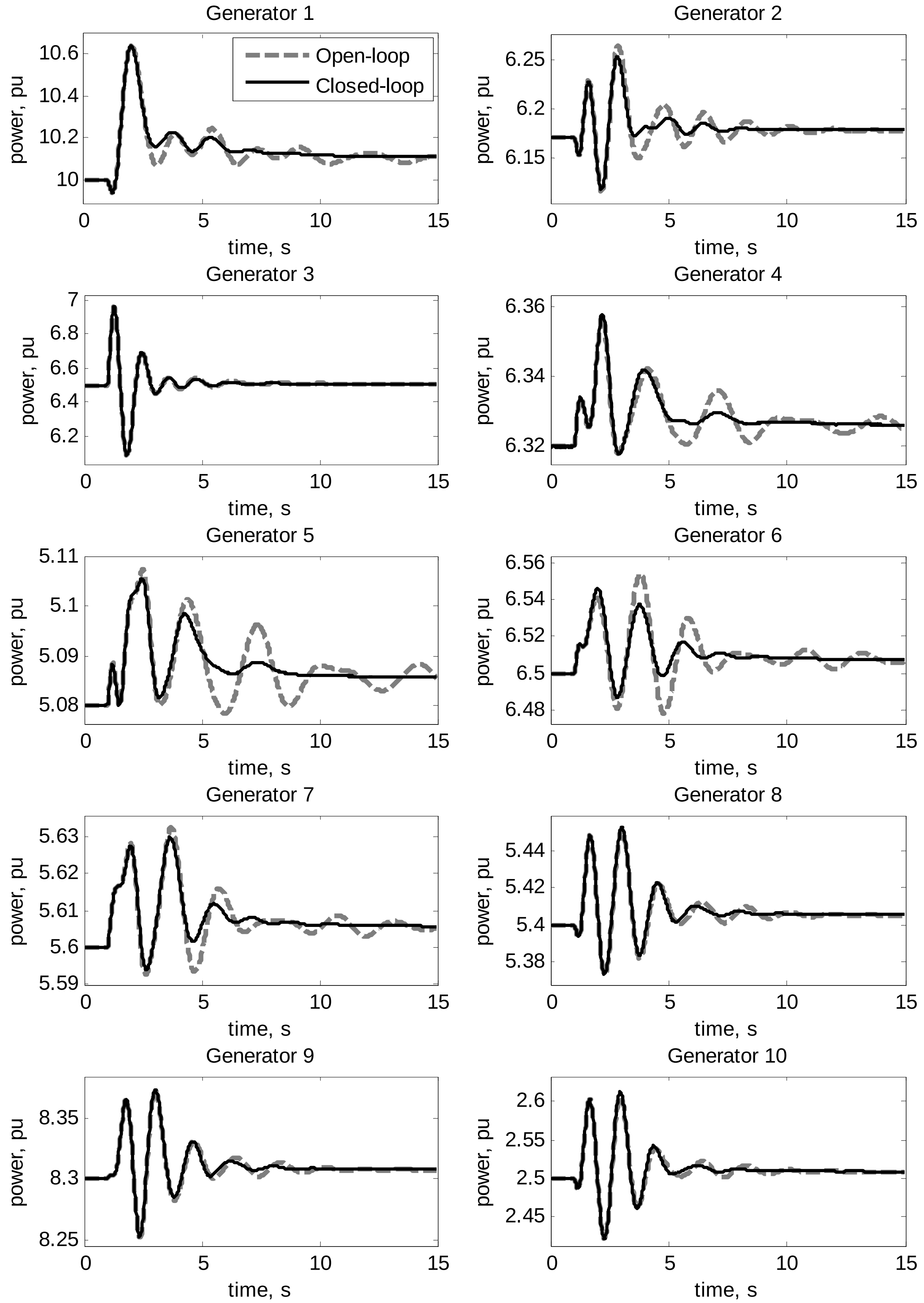

Figure 8-6: Active power responses for a small disturbance at generator 3

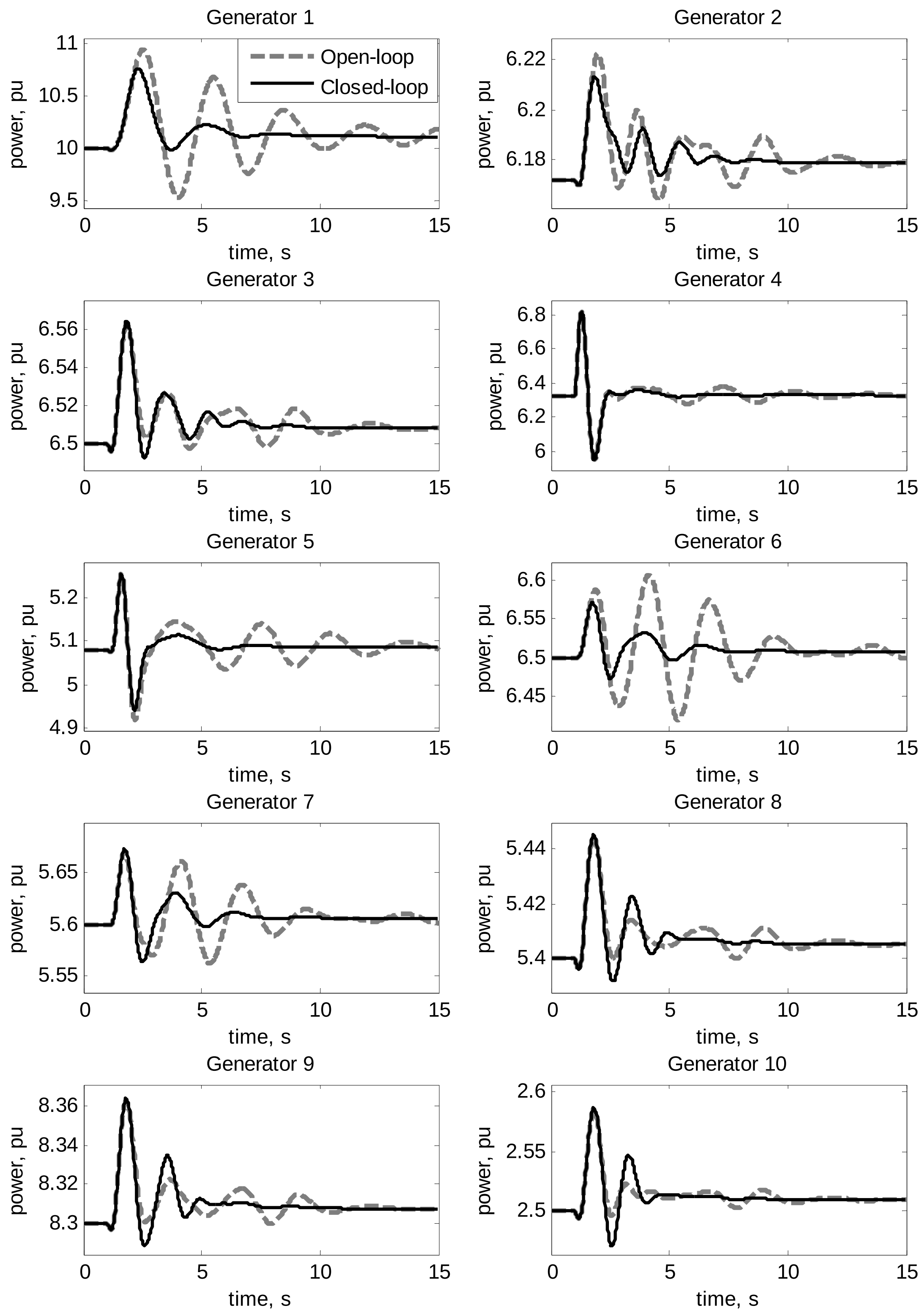

Figure 8-7: Active power responses for a small disturbance at generator 4

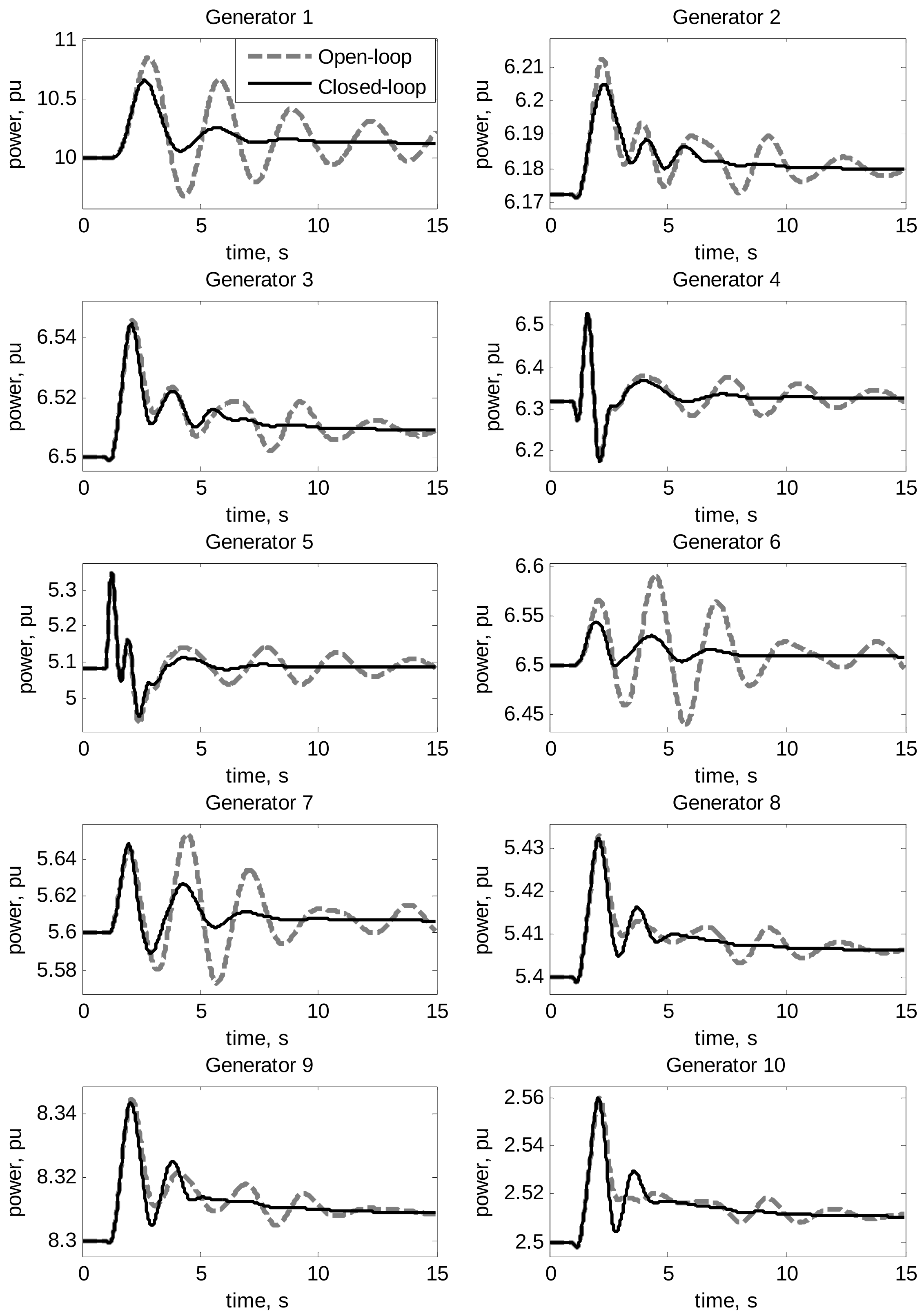

Figure 8-8: Active power responses for a small disturbance at generator 5

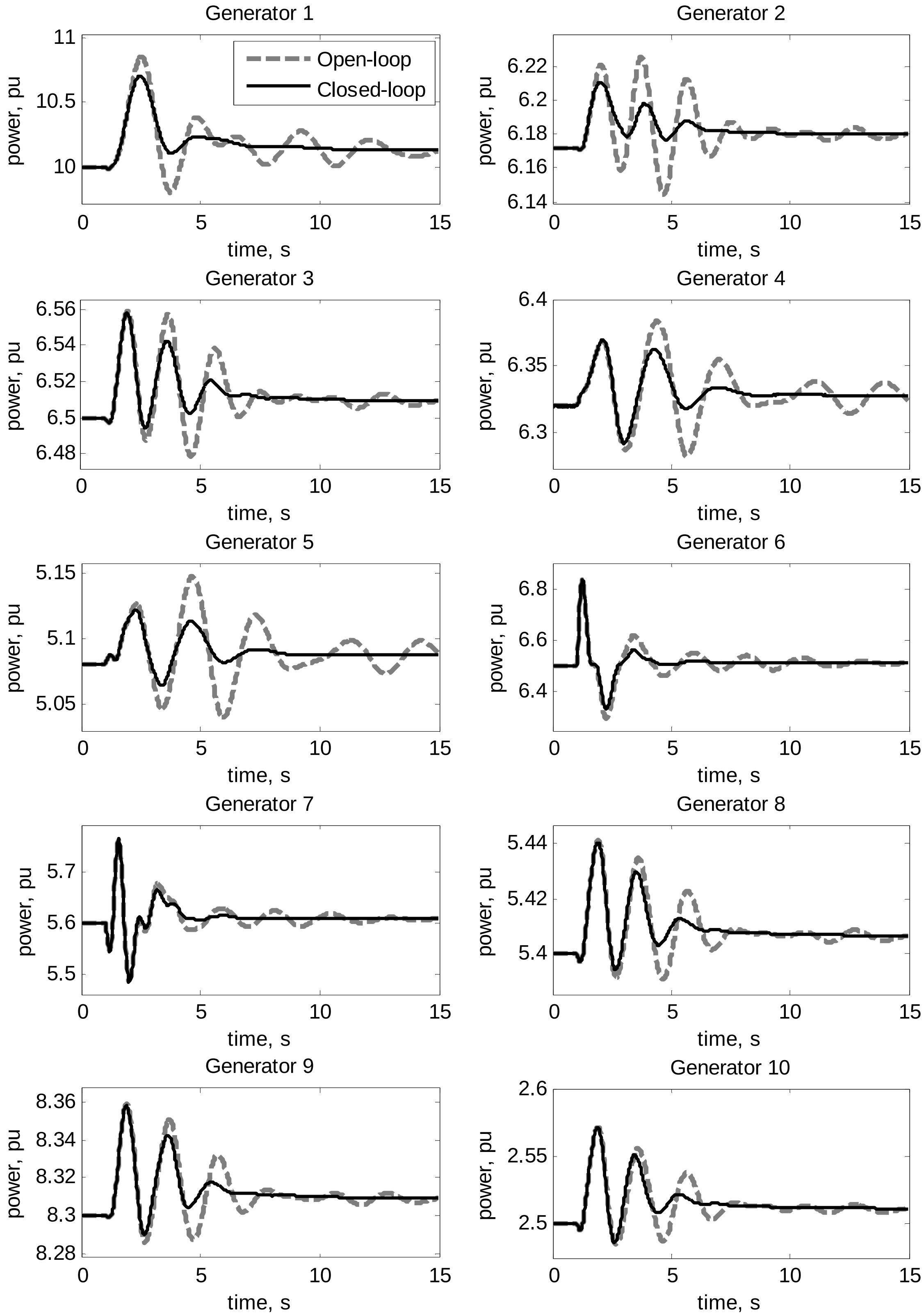

Figure 8-9: Active power responses for a small disturbance at generator 6

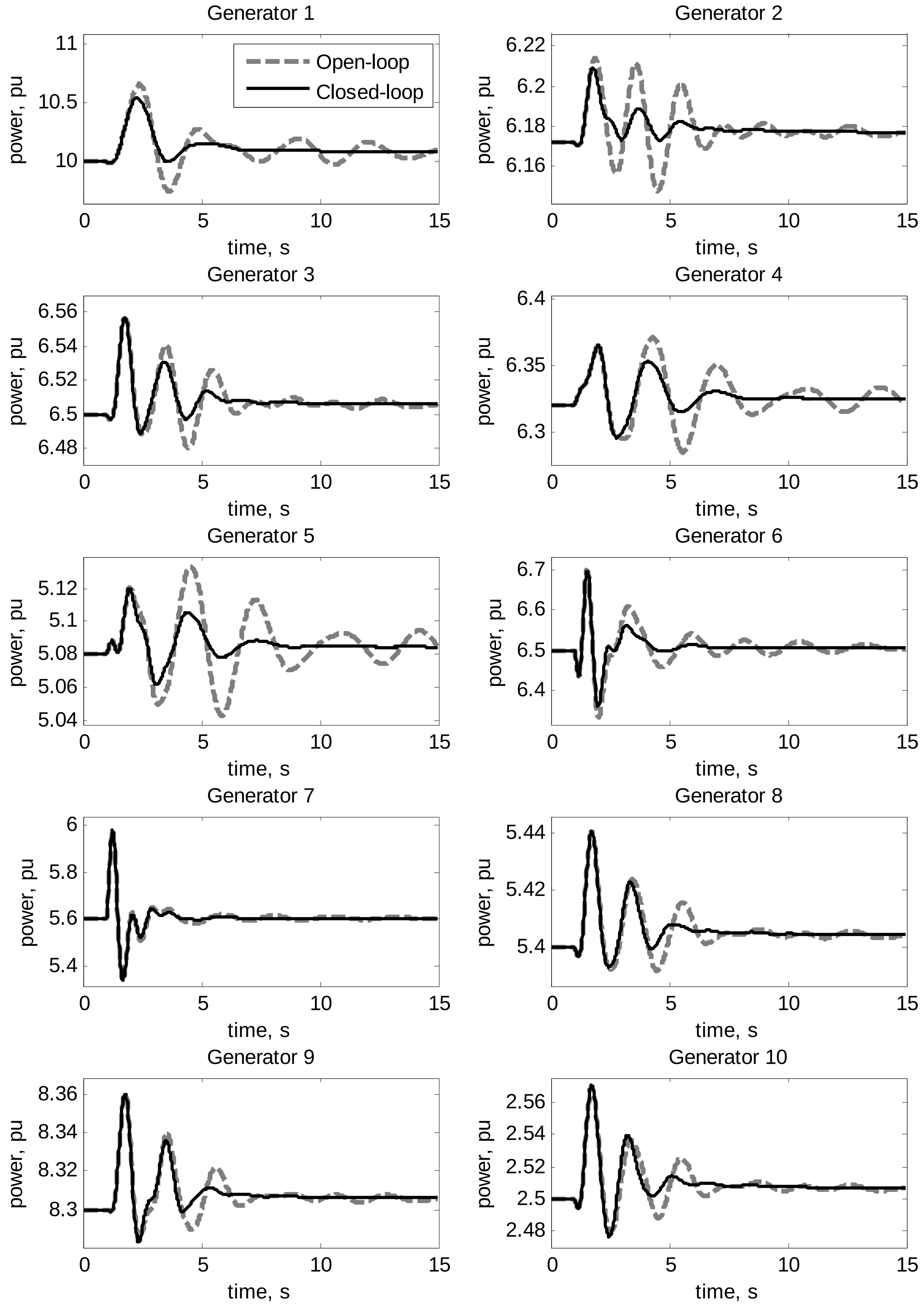

Figure 8-10: Active power responses for a small disturbance at generator 7

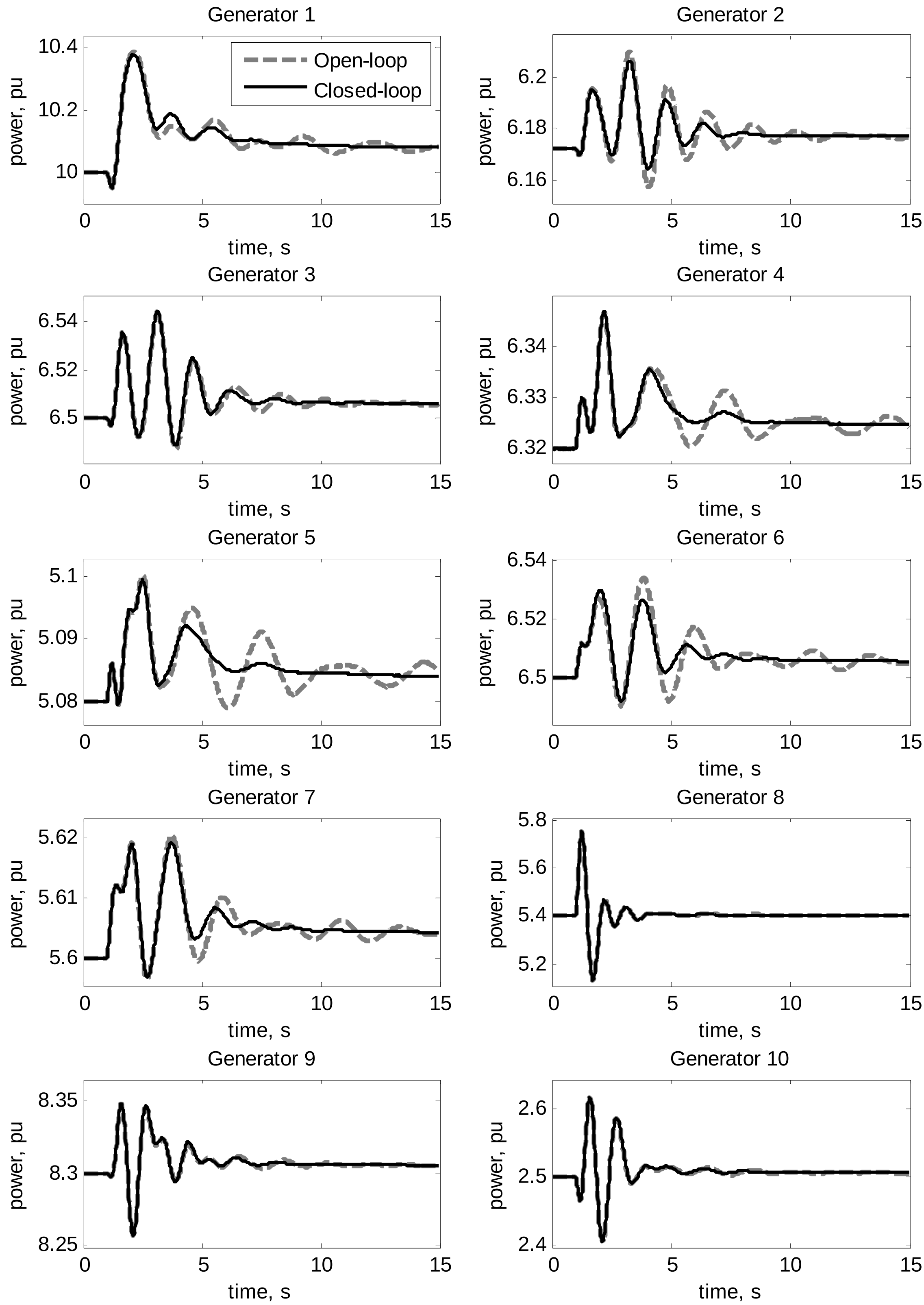

Figure 8-11: Active power responses for a small disturbance at generator 8

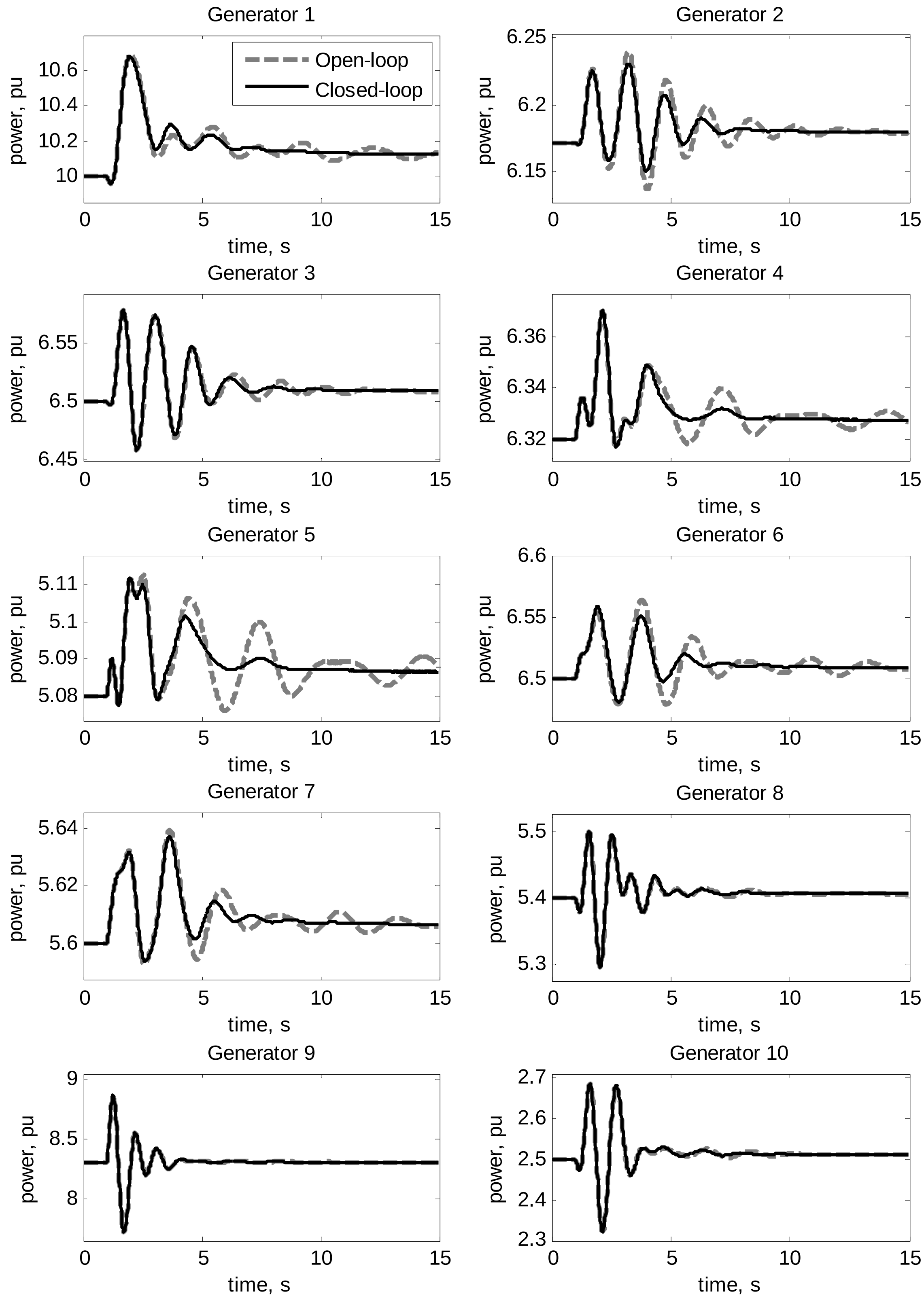

Figure 8-12: Active power responses for a small disturbance at generator 9

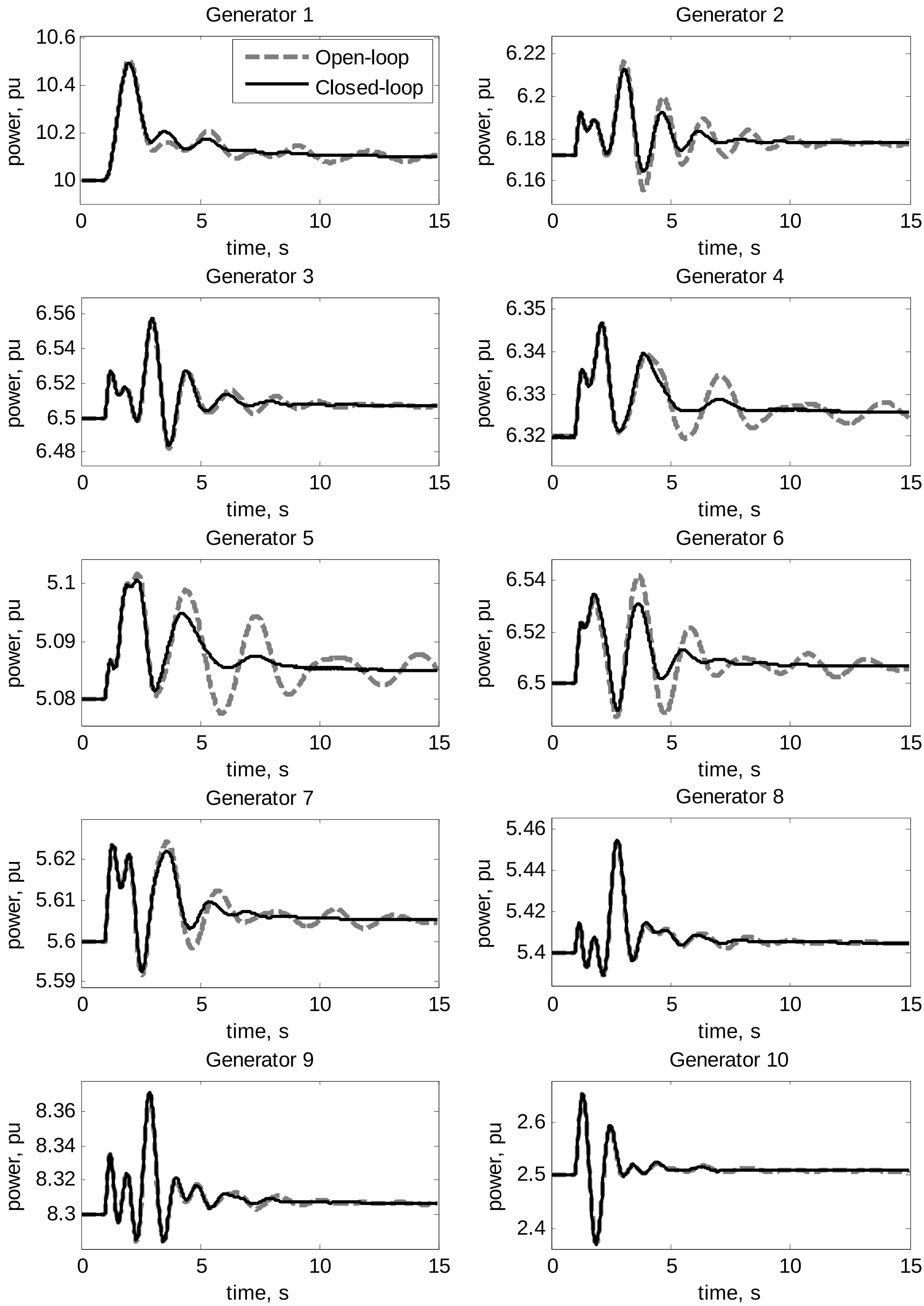

Figure 8-13: Active power responses for a small disturbance at generator 10

8.4.2 System Responses to Large Disturbances (OC-A*i*)

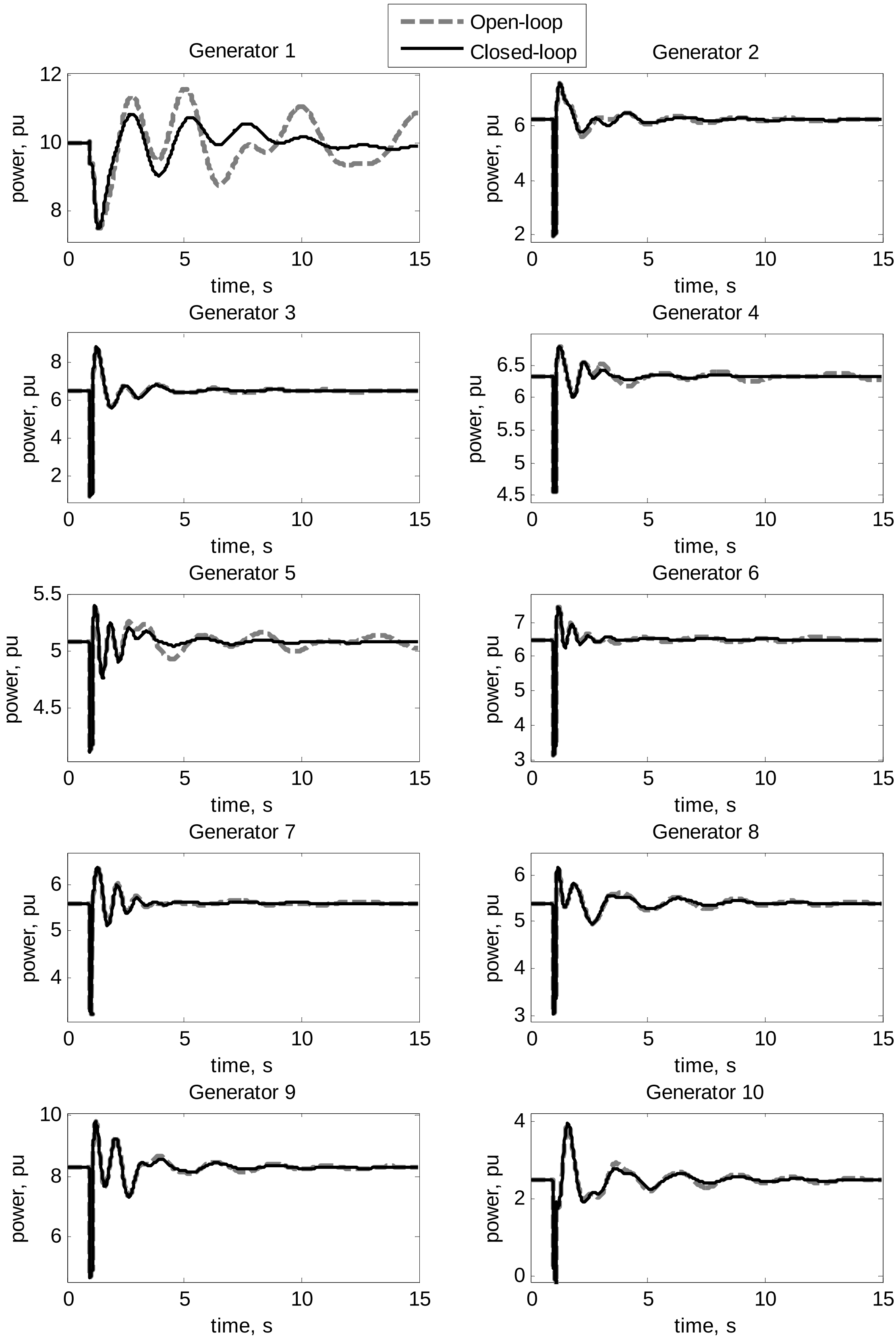

Figure 8-14: Active power responses for a large disturbance at bus 14 (OC-A2)

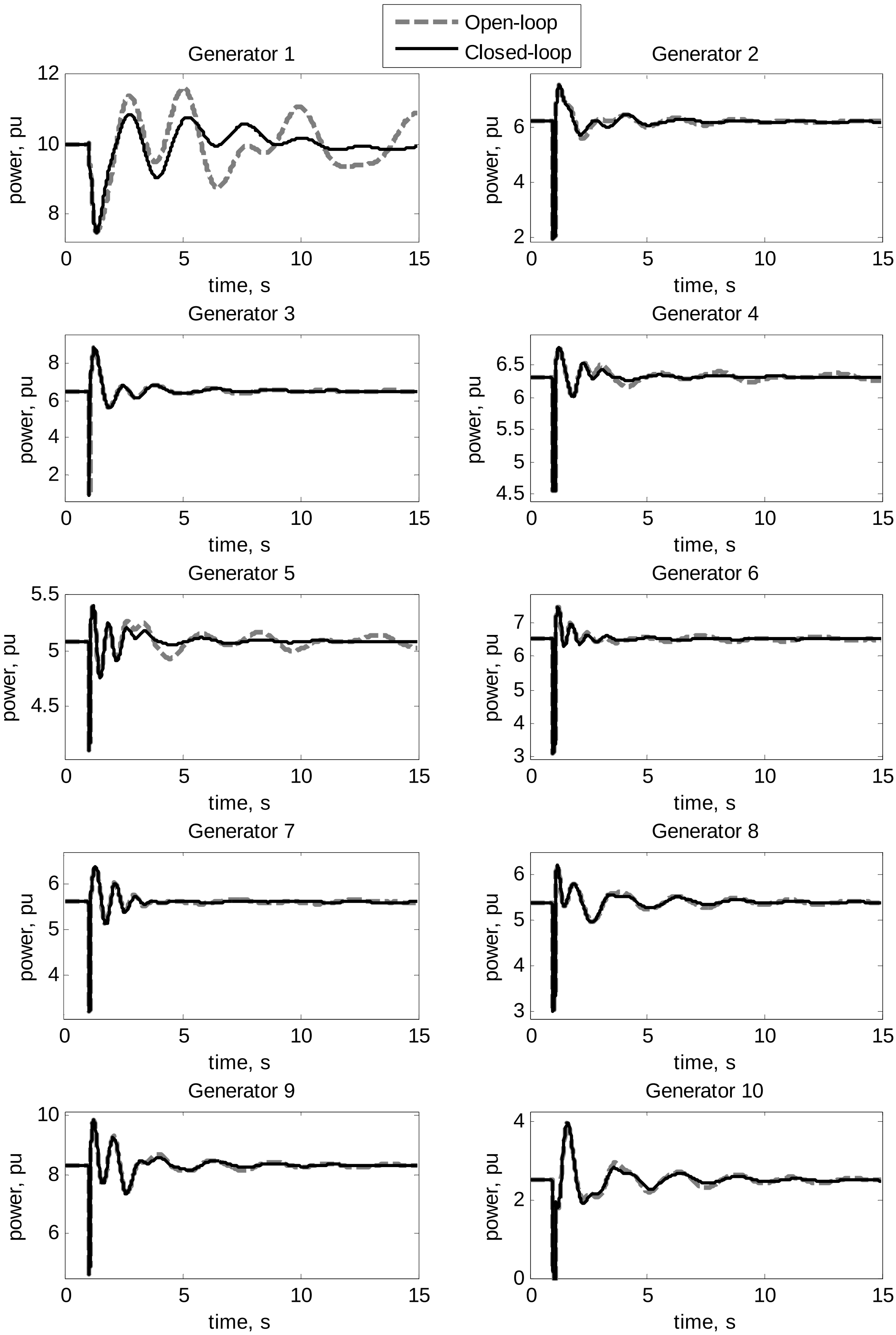

Figure 8-15: Active power responses for a large disturbance at bus 14 (OC-A3)

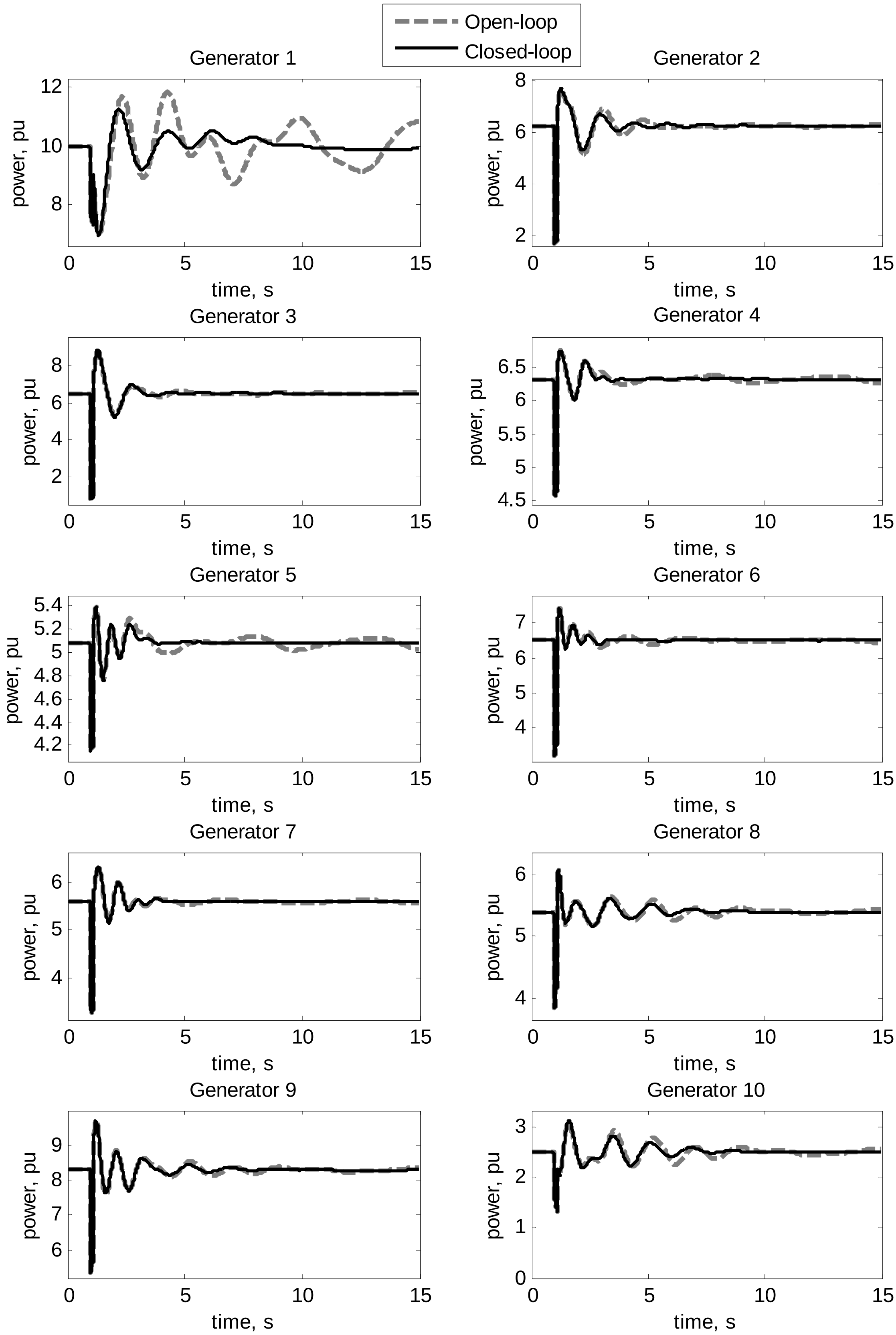

Figure 8-16: Active power responses for a large disturbance at bus 14 (OC-A4)

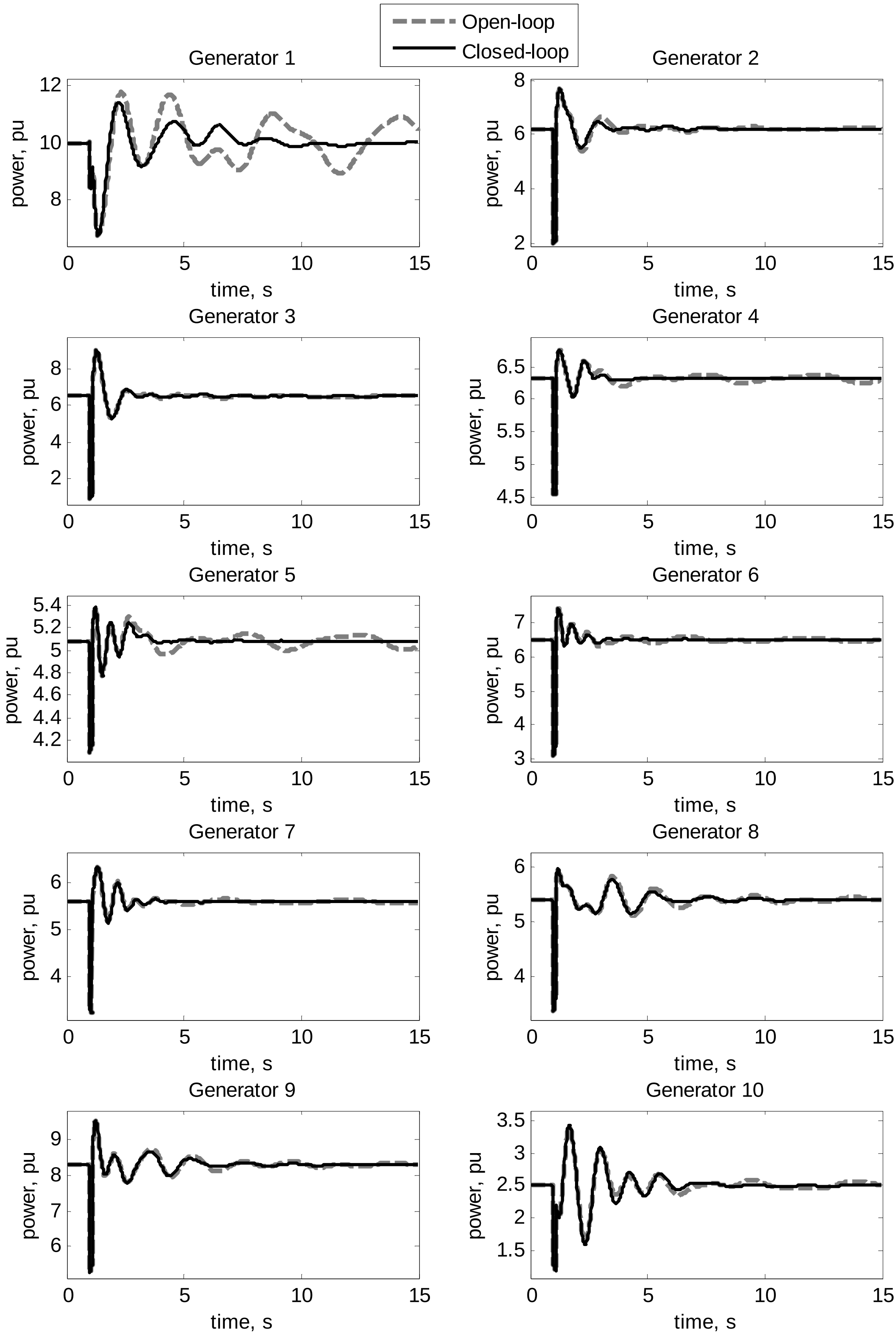

Figure 8-17: Active power responses for a large disturbance at bus 14 (OC-A5)

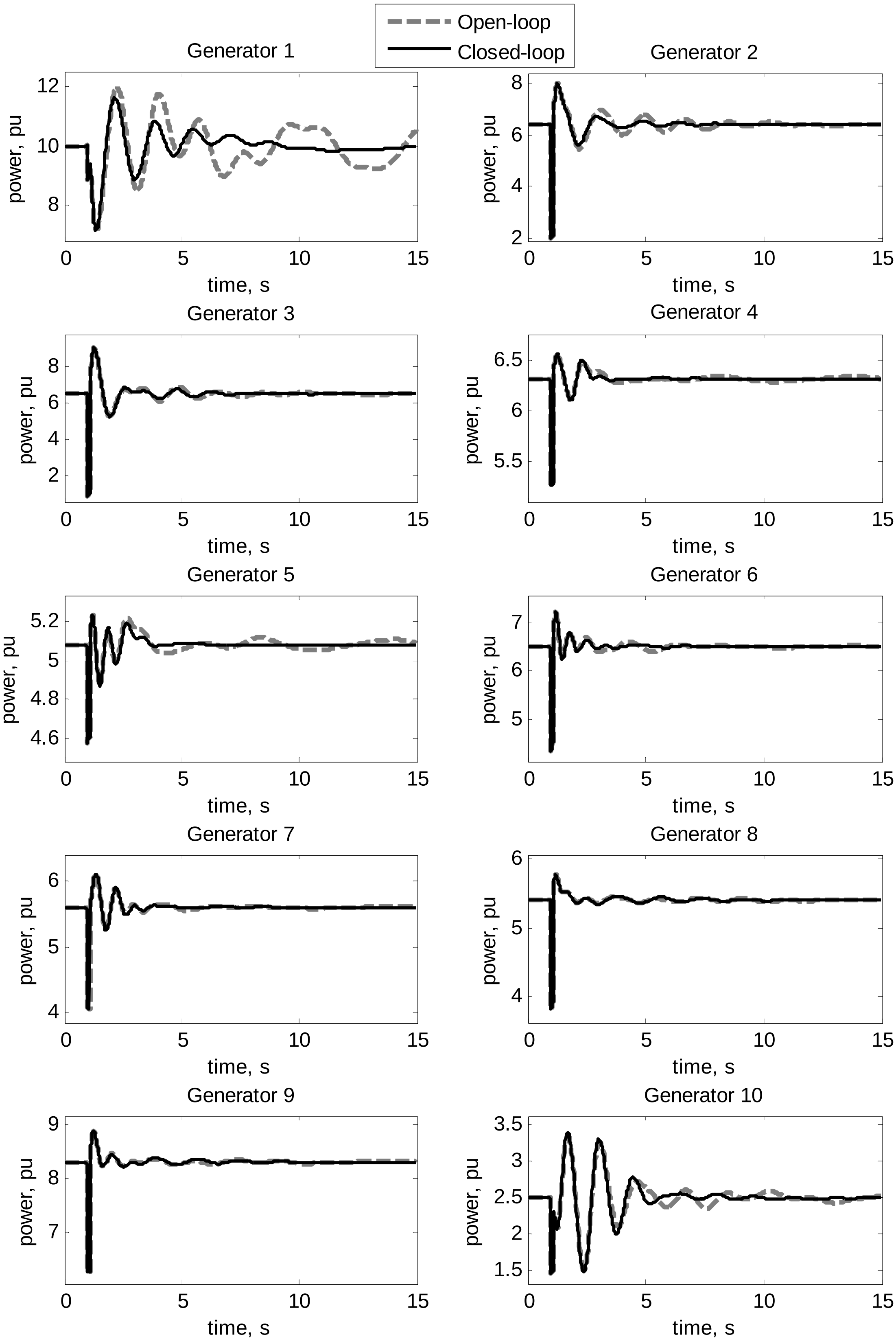

Figure 8-18: Active power responses for a large disturbance at bus 14 (OC-A6)

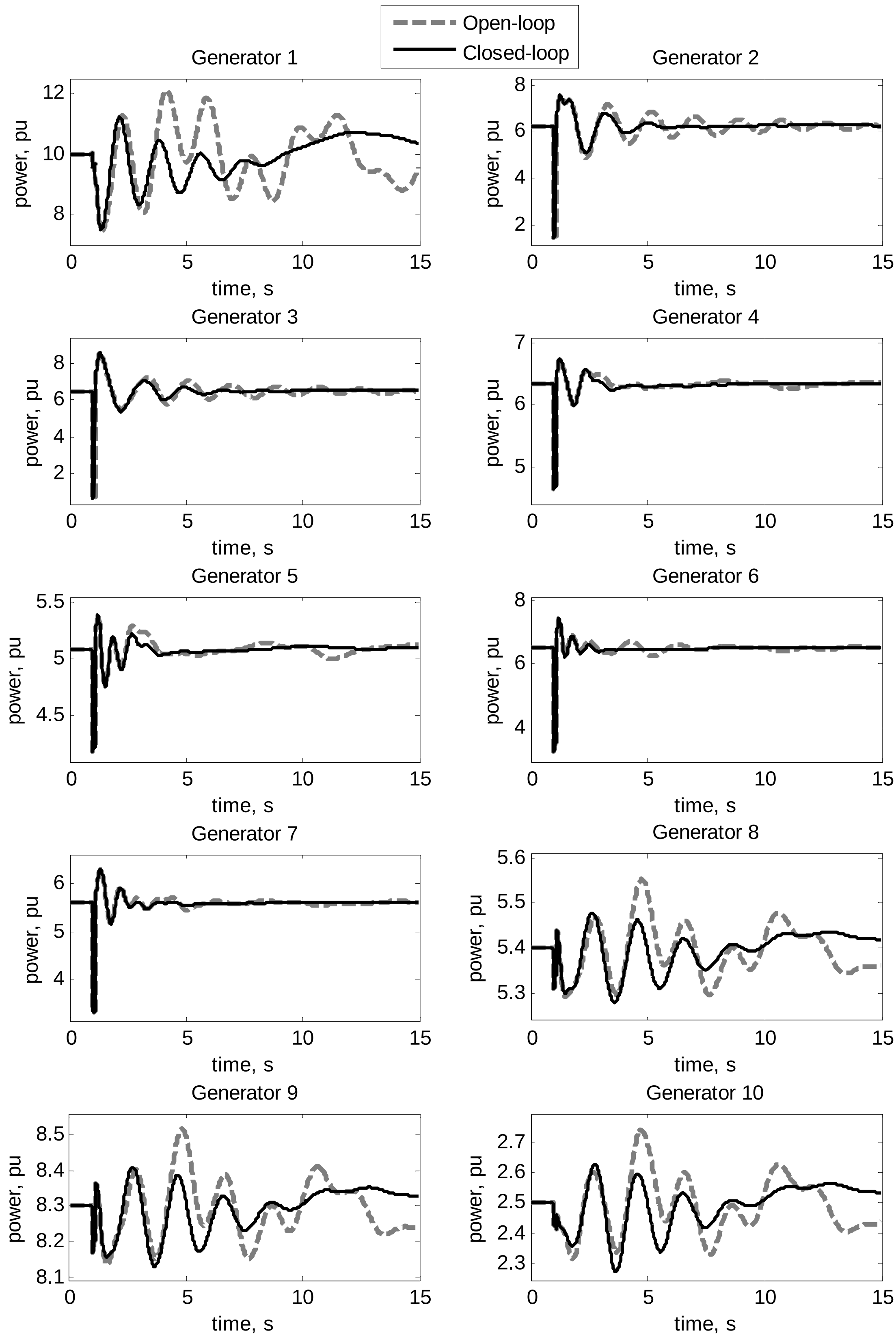

Figure 8-19: Active power responses for a large disturbance at bus 14 (OC-A7)

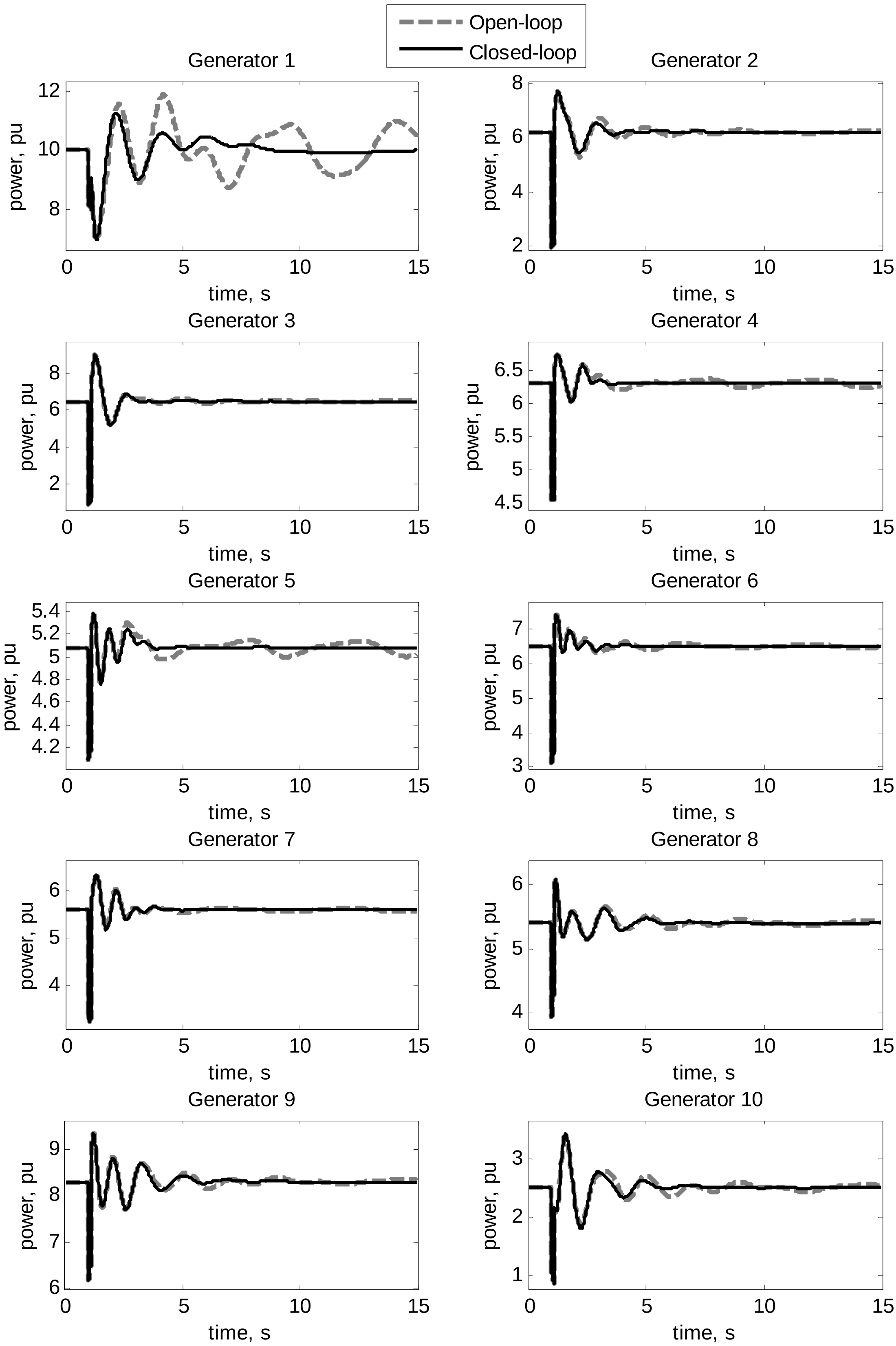

Figure 8-20: Active power responses for a large disturbance at bus 14 (OC-A8)

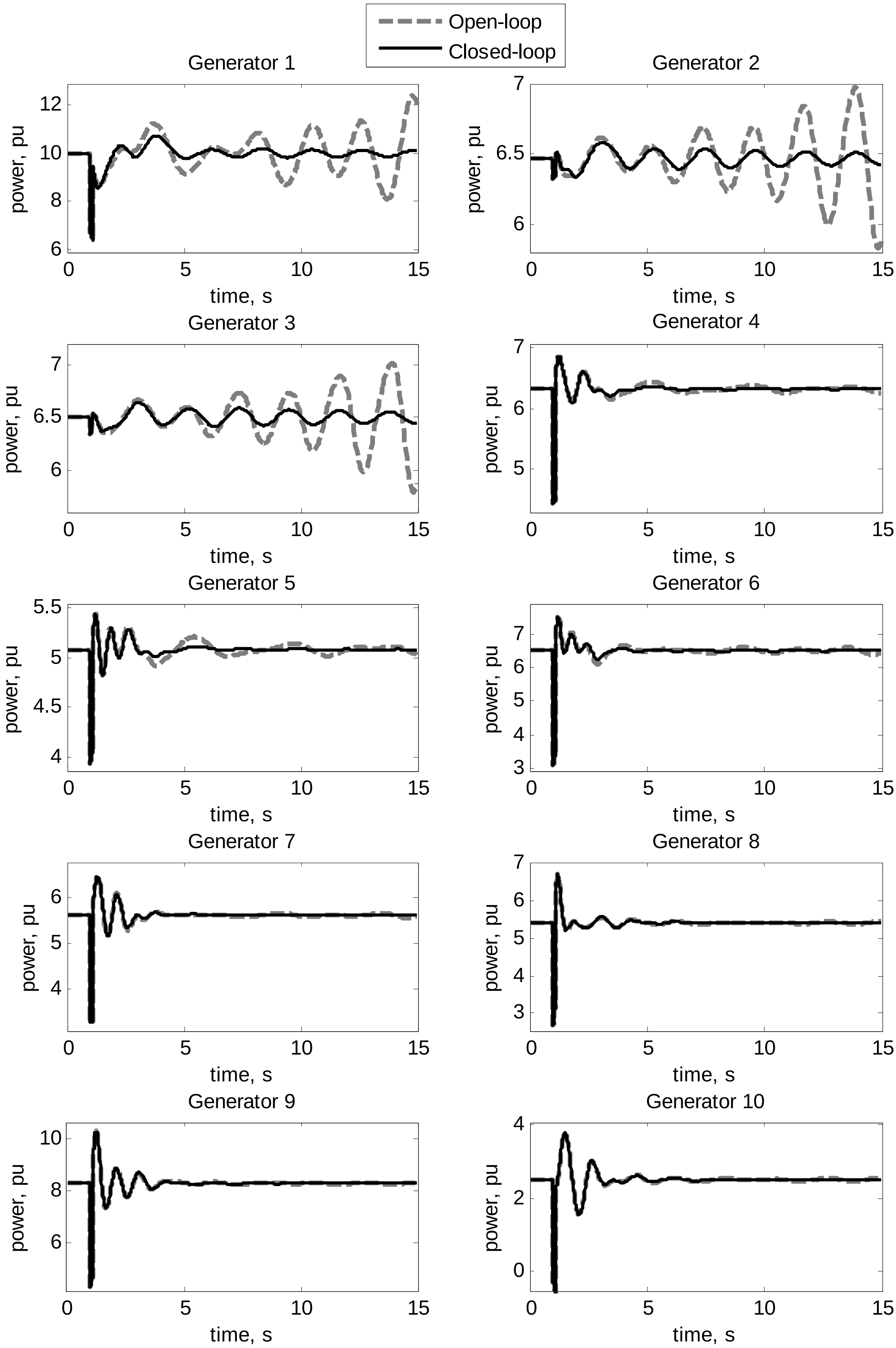

Figure 8-21: Active power responses for a large disturbance at bus 14 (OC-A9)

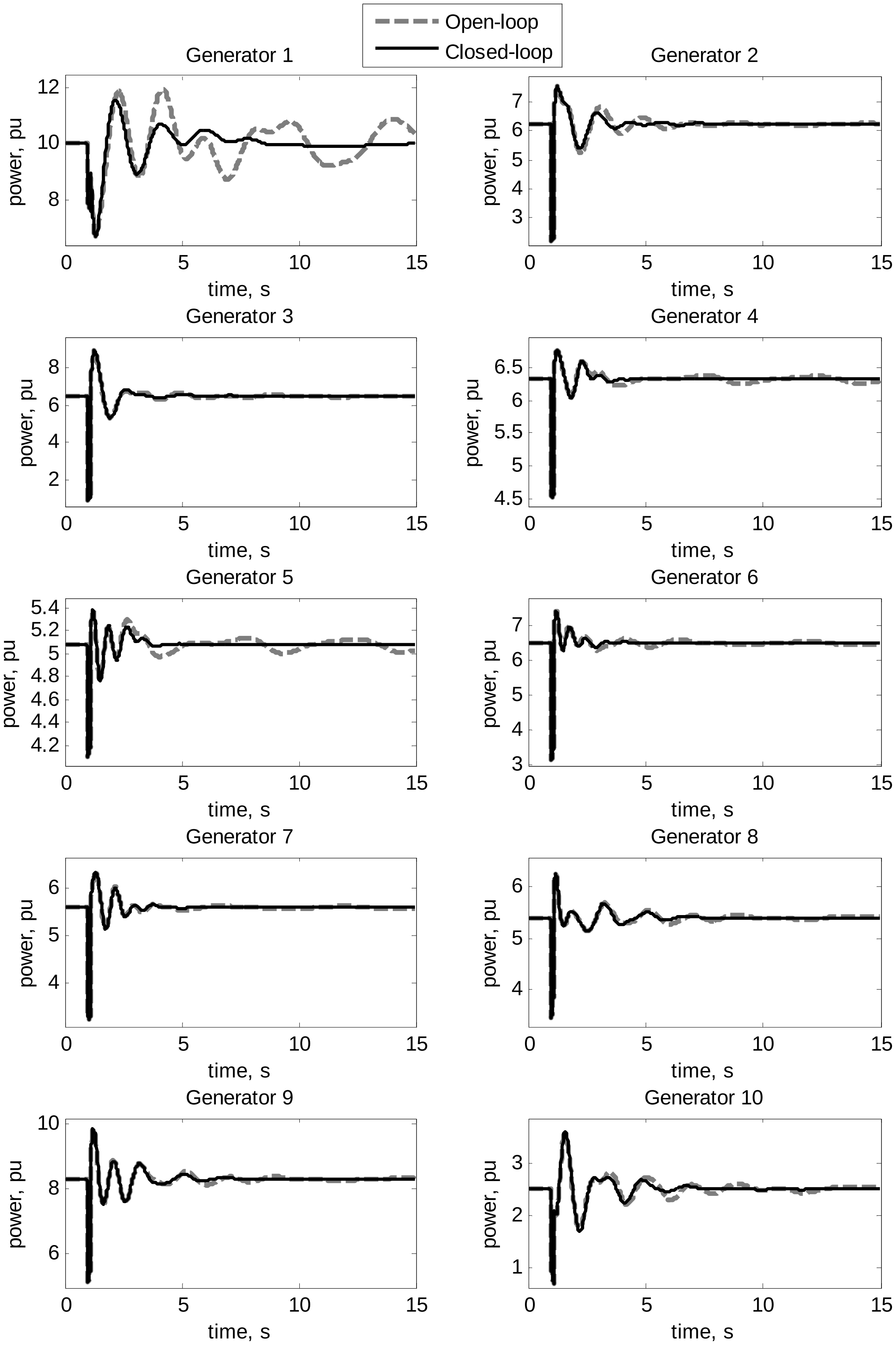

Figure 8-22: Active power responses for a large disturbance at bus 14 (OC-A10)

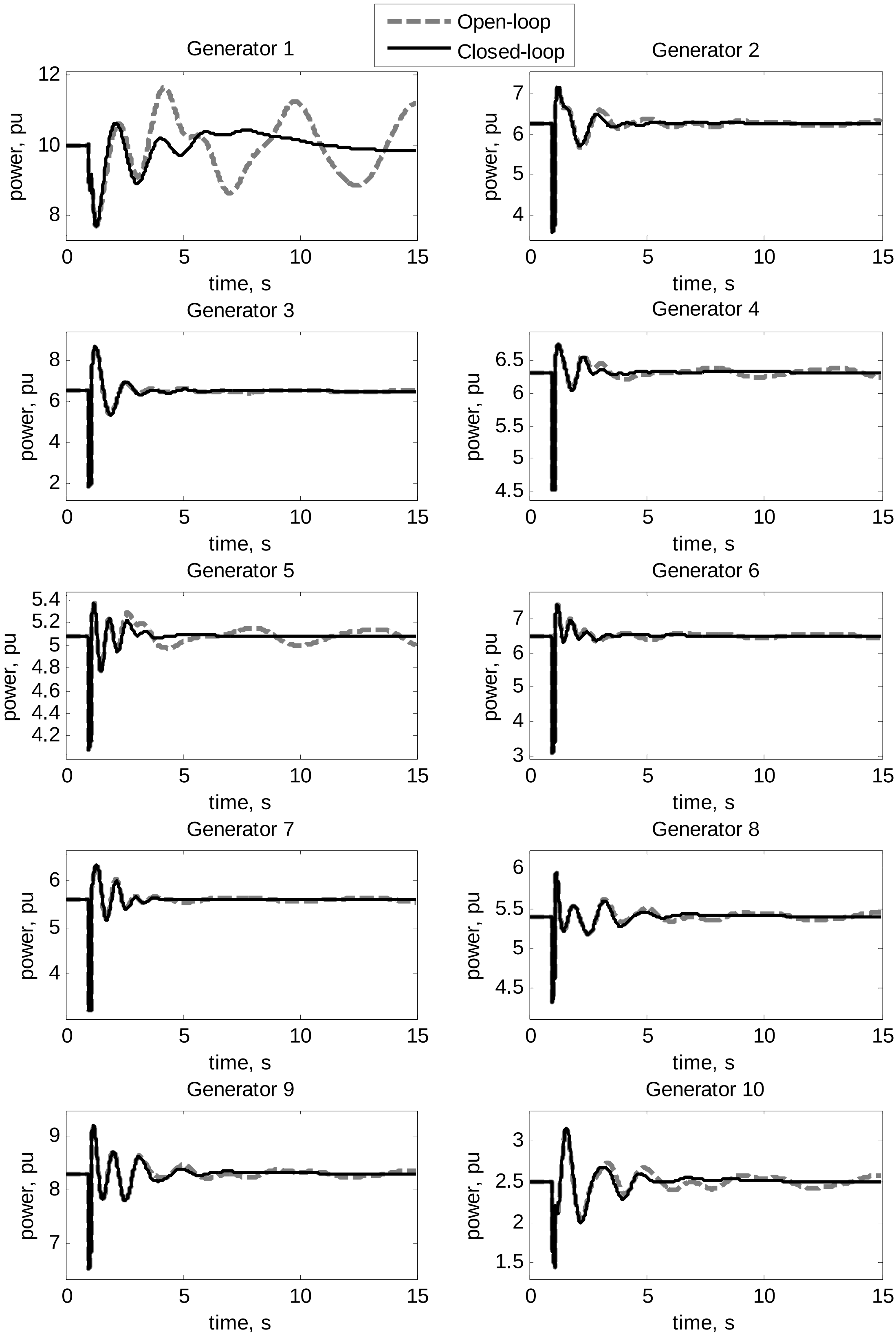

Figure 8-23: Active power responses for a large disturbance at bus 14 (OC-A11)

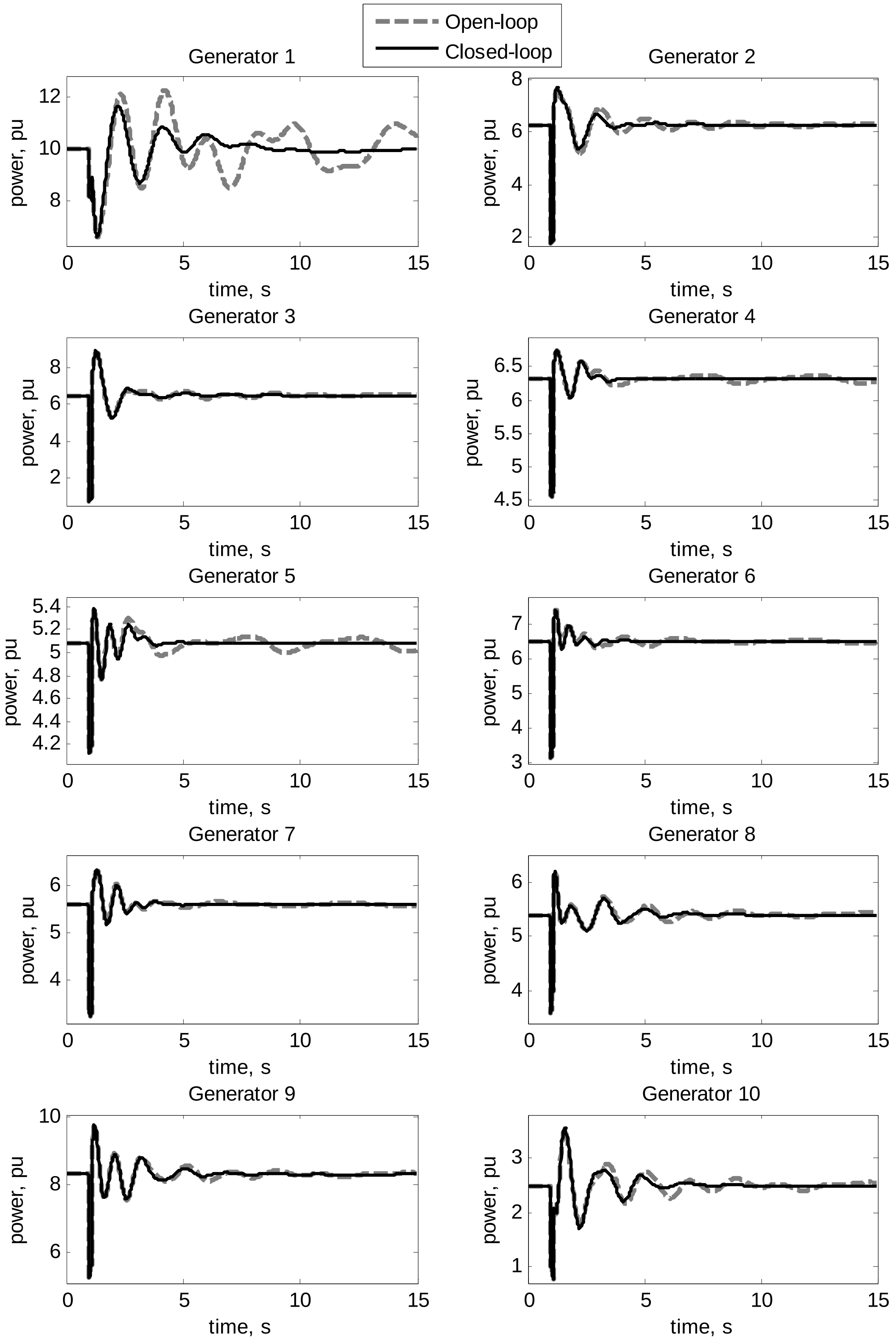

Figure 8-24: Active power responses for a large disturbance at bus 14 (OC-A12)

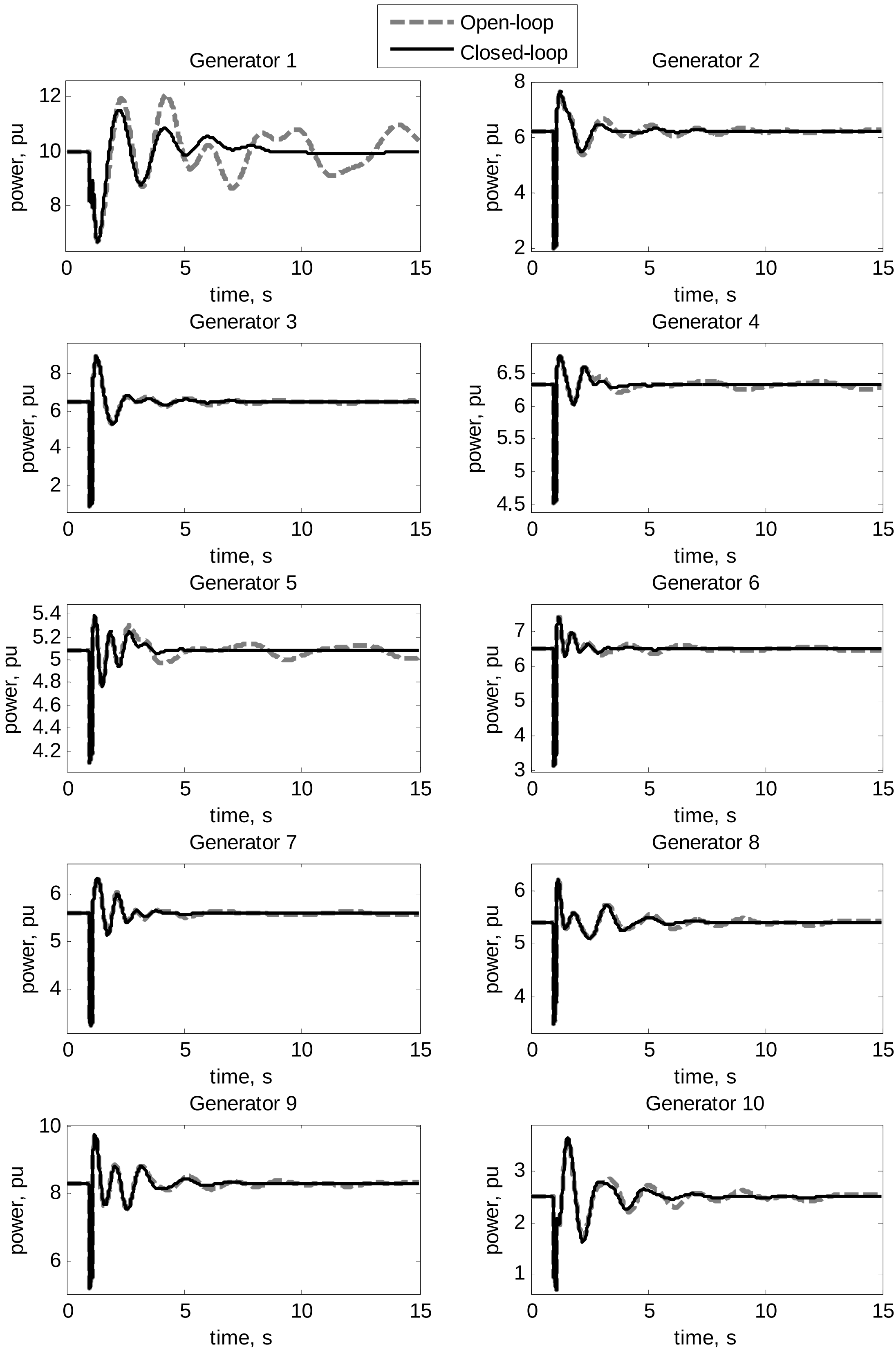

Figure 8-25: Active power responses for a large disturbance at bus 14 (OC-A13)

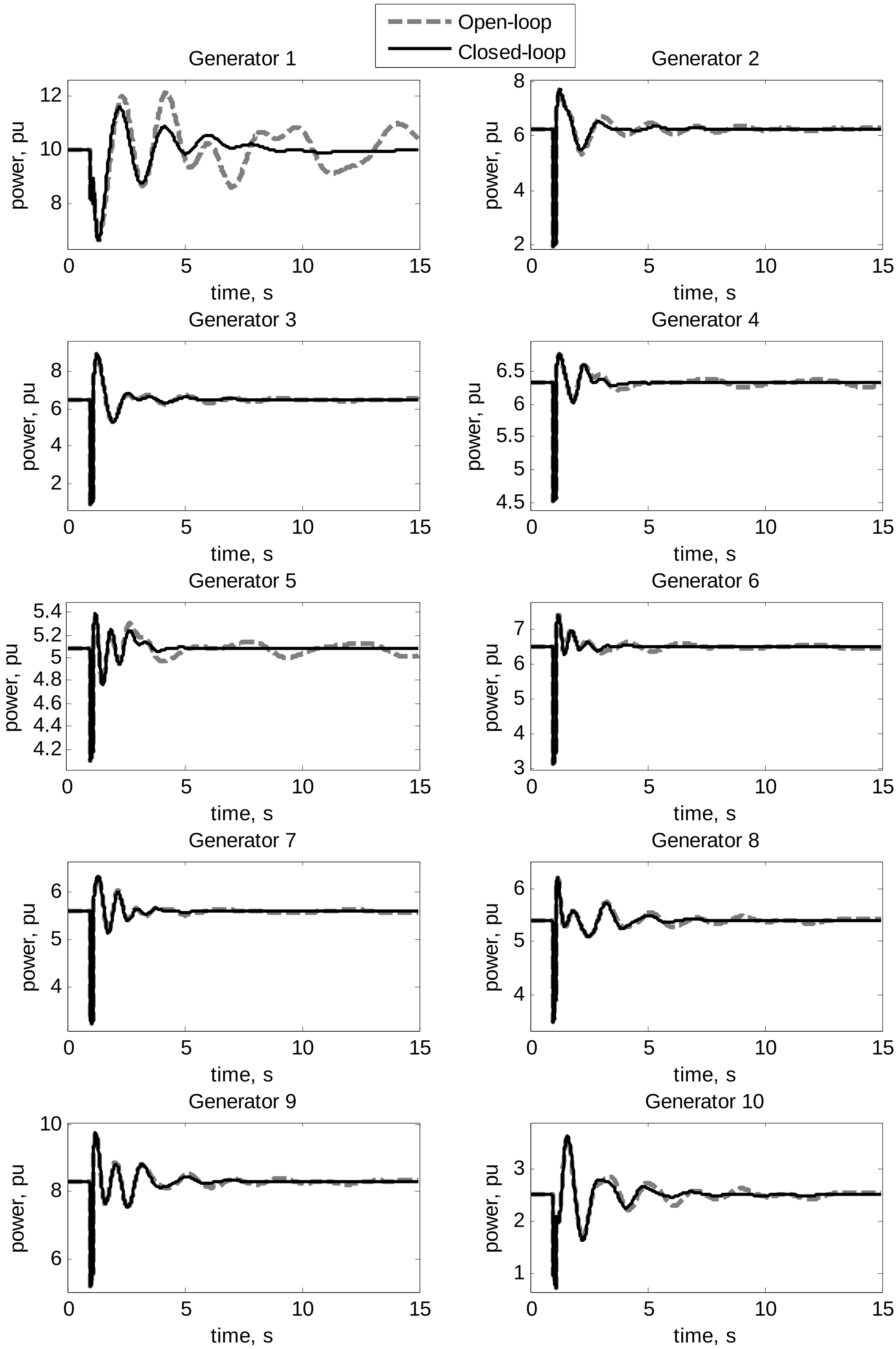

Figure 8-26: Active power responses for a large disturbance at bus 14 (OC-A14)

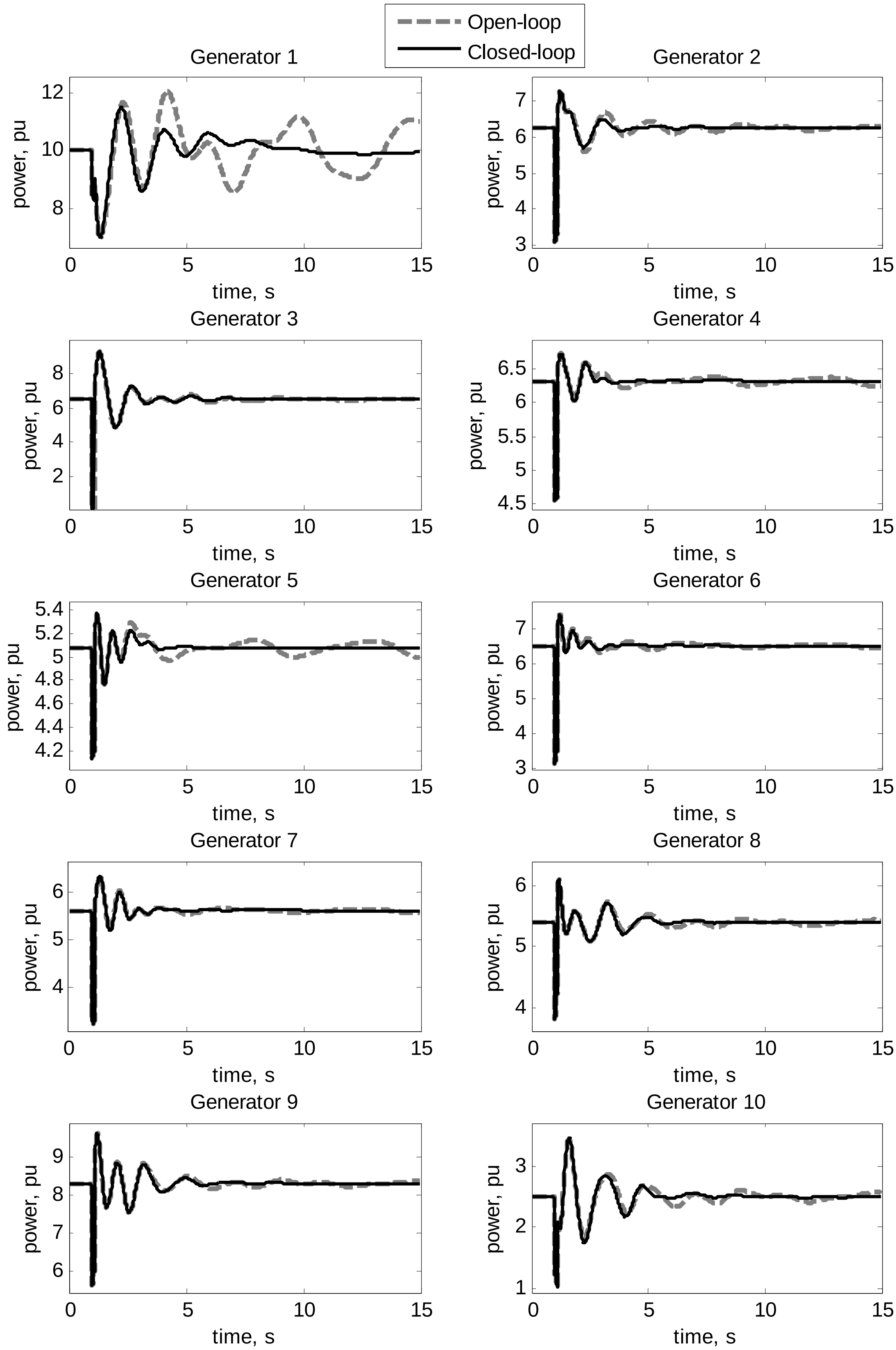

Figure 8-27: Active power responses for a large disturbance at bus 14 (OC-A15)

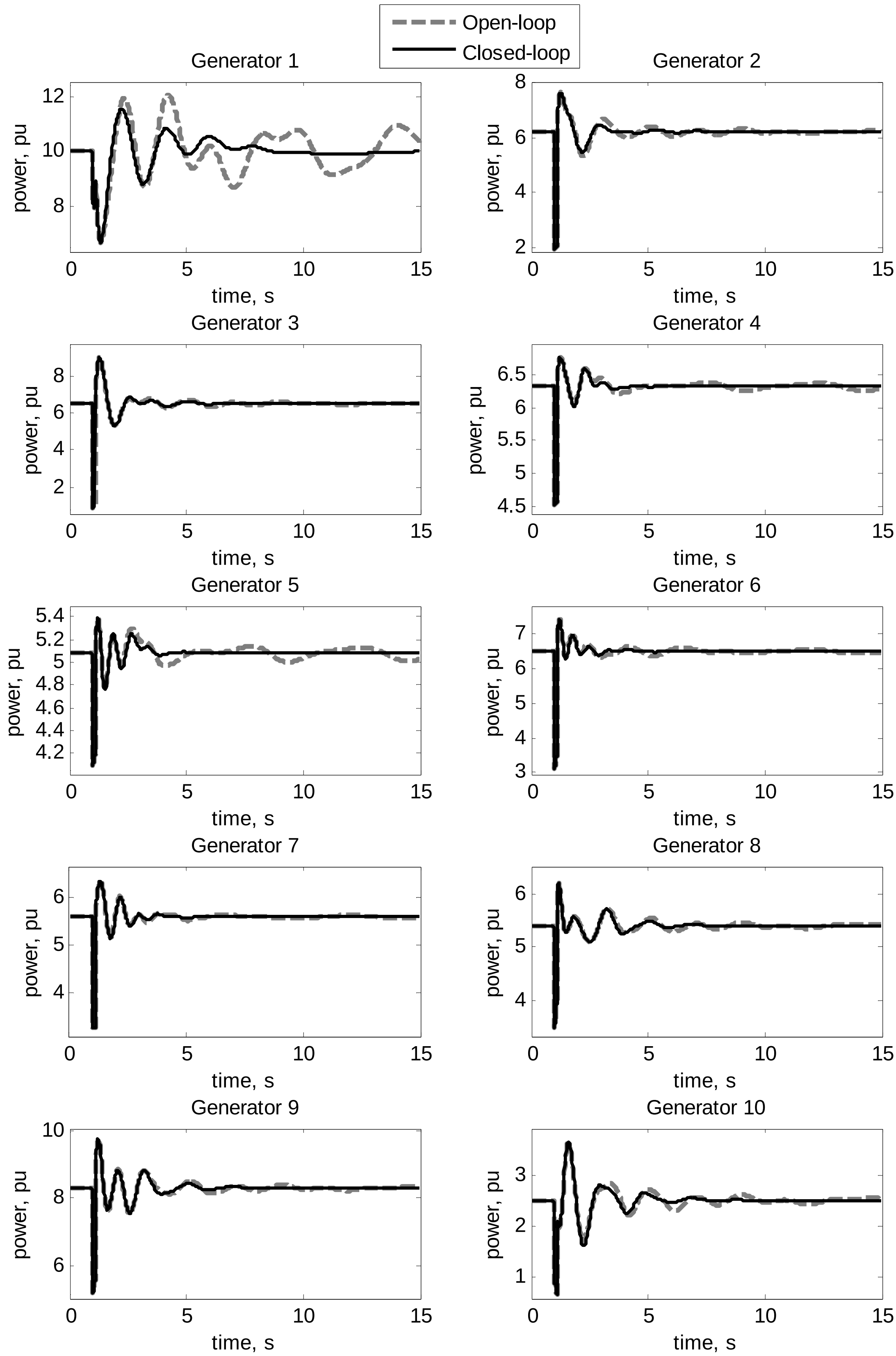

Figure 8-28: Active power responses for a large disturbance at bus 14 (OC-A16)

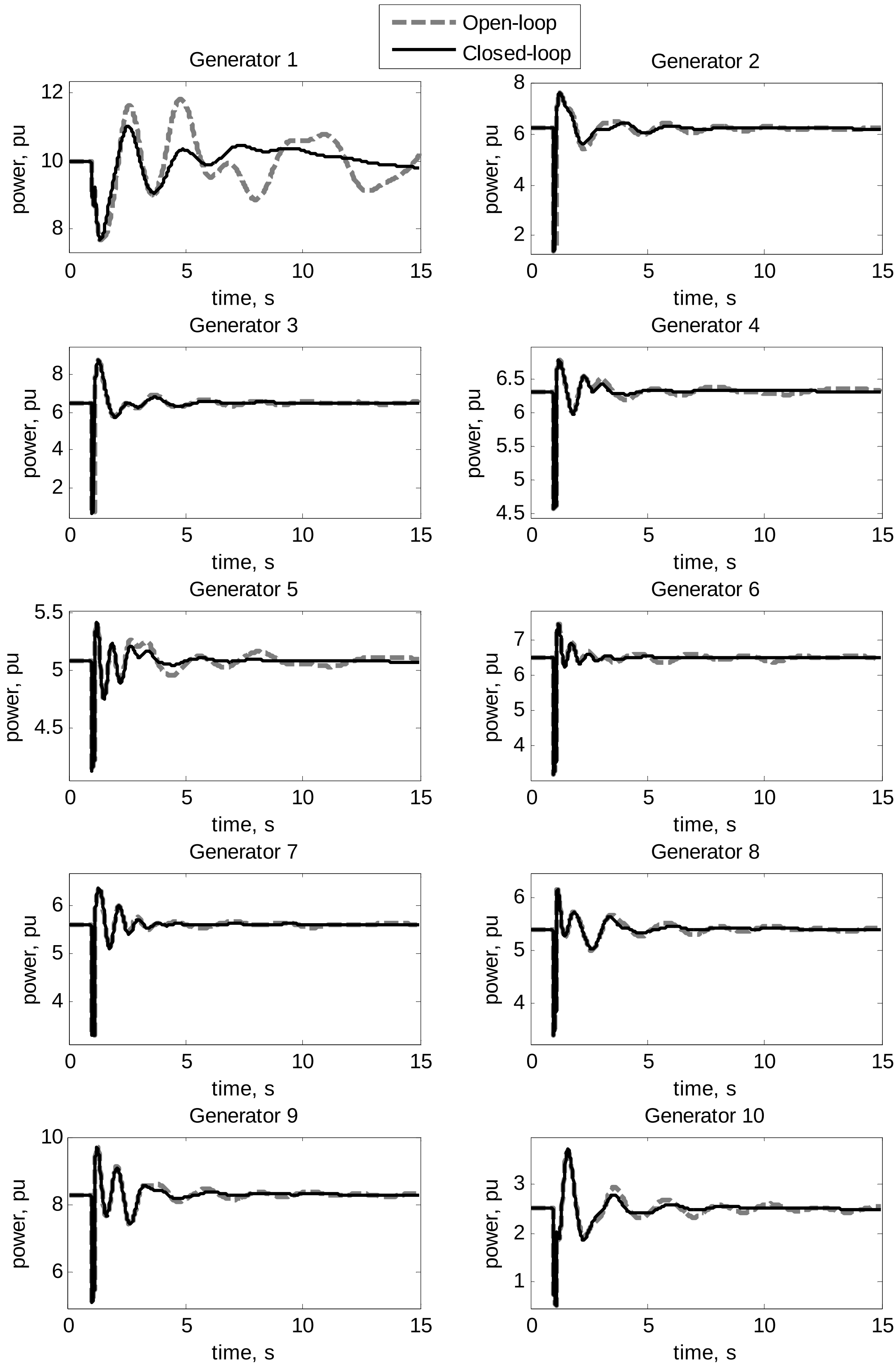

Figure 8-29: Active power responses for a large disturbance at bus 14 (OC-A17)

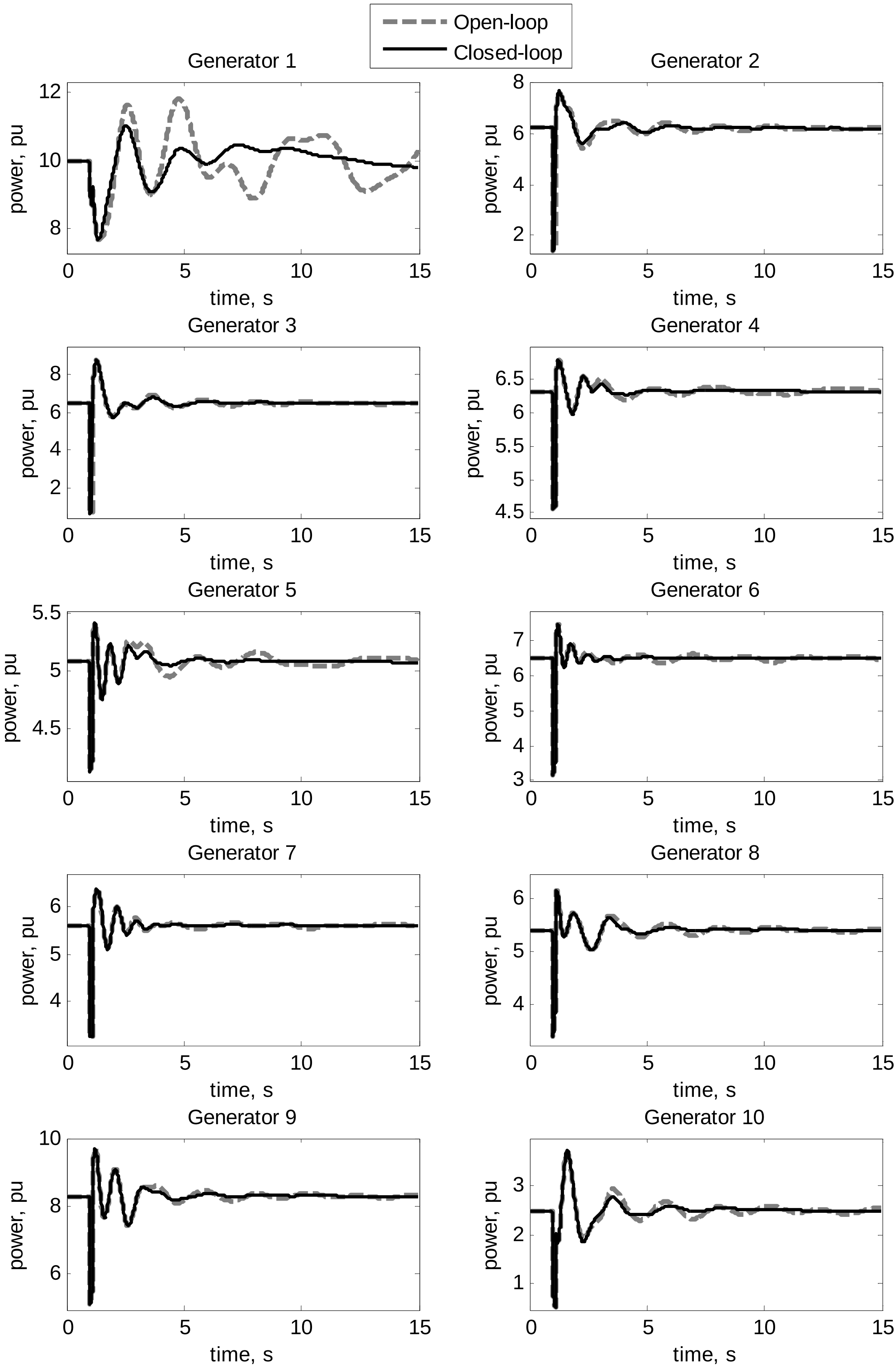

Figure 8-30: Active power responses for a large disturbance at bus 14 (OC-A18)

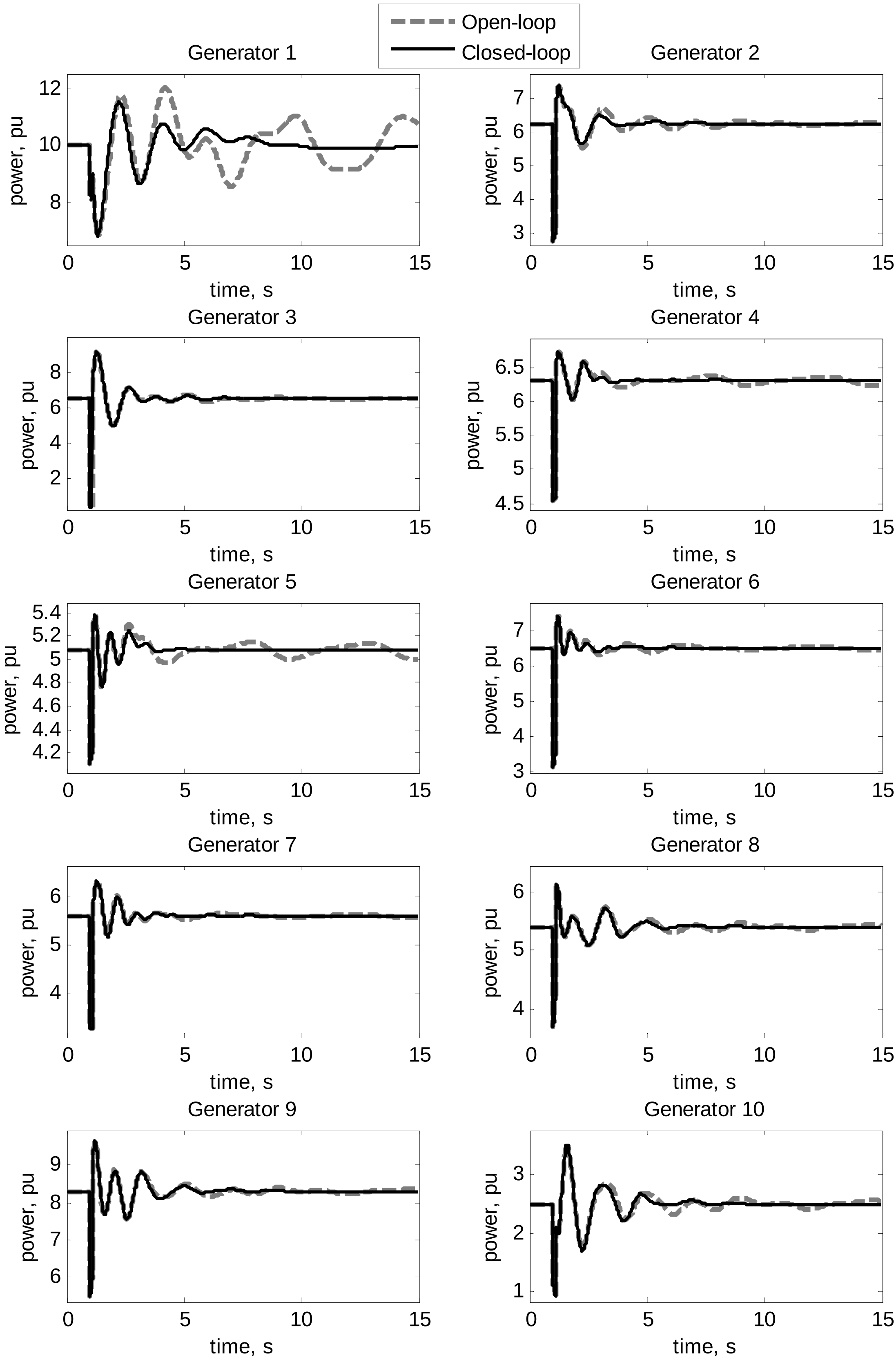

Figure 8-31: Active power responses for a large disturbance at bus 14 (OC-A19)

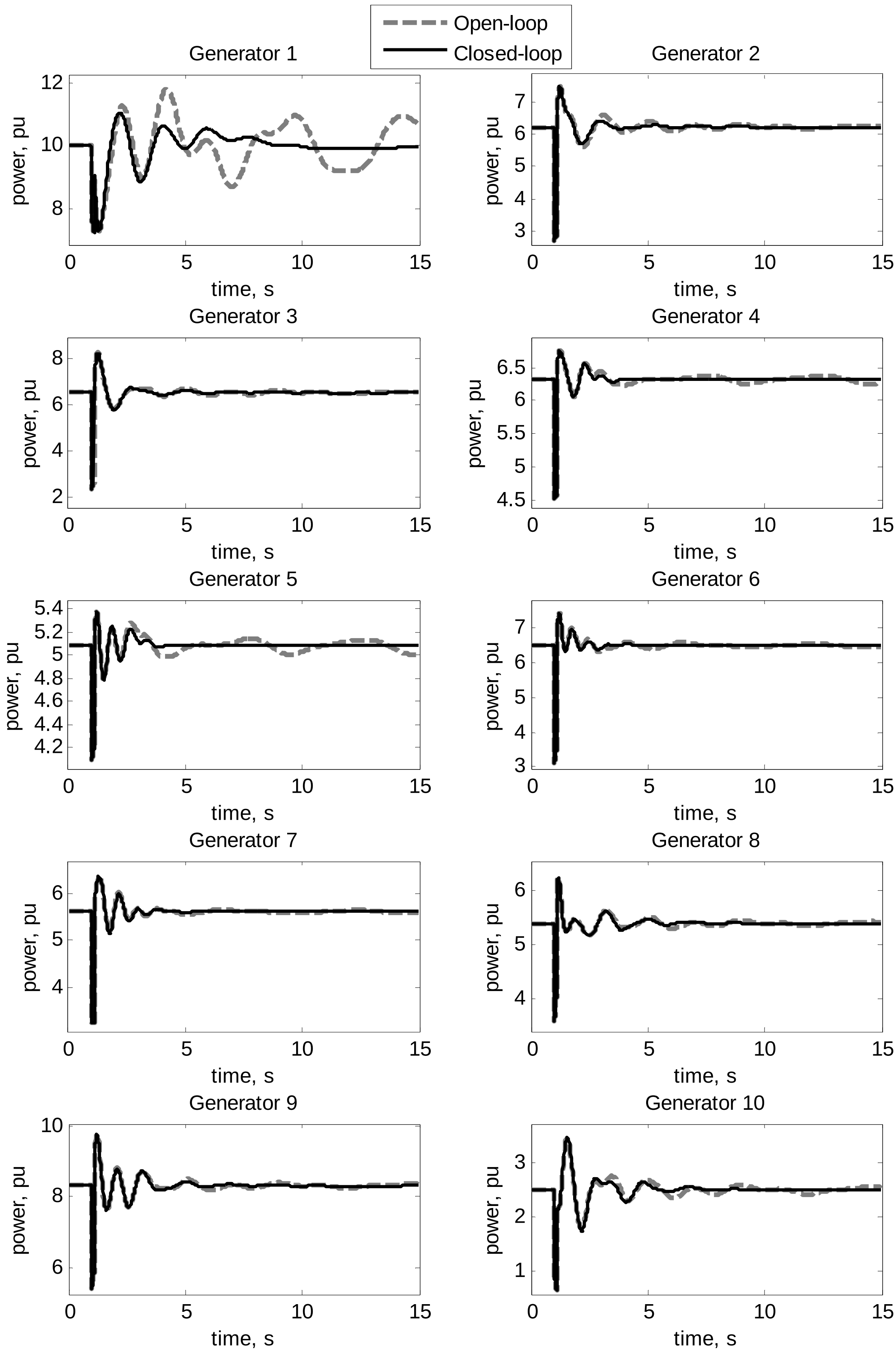

Figure 8-32: Active power responses for a large disturbance at bus 14 (OC-A20)

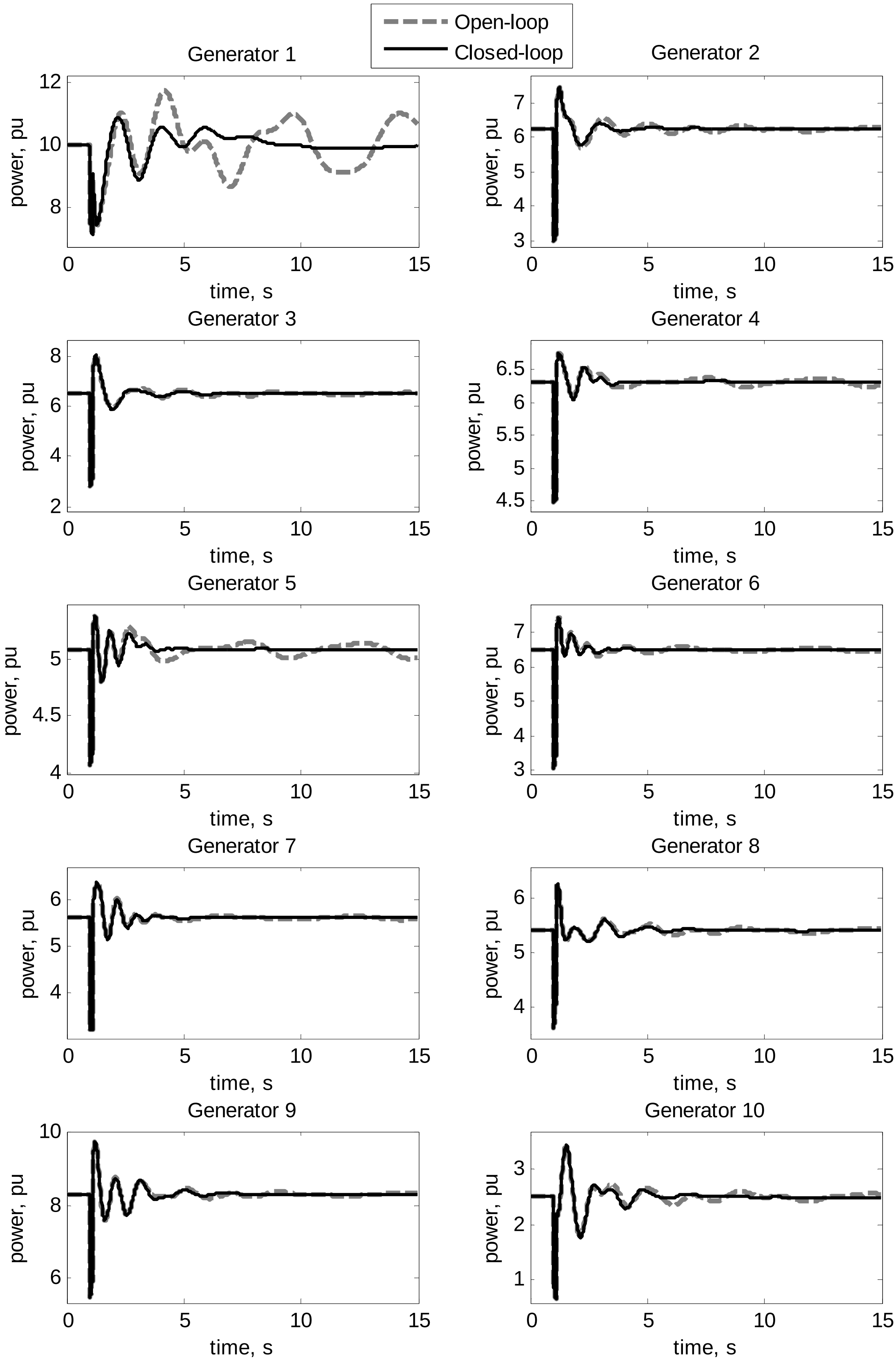

Figure 8-33: Active power responses for a large disturbance at bus 14 (OC-A21)

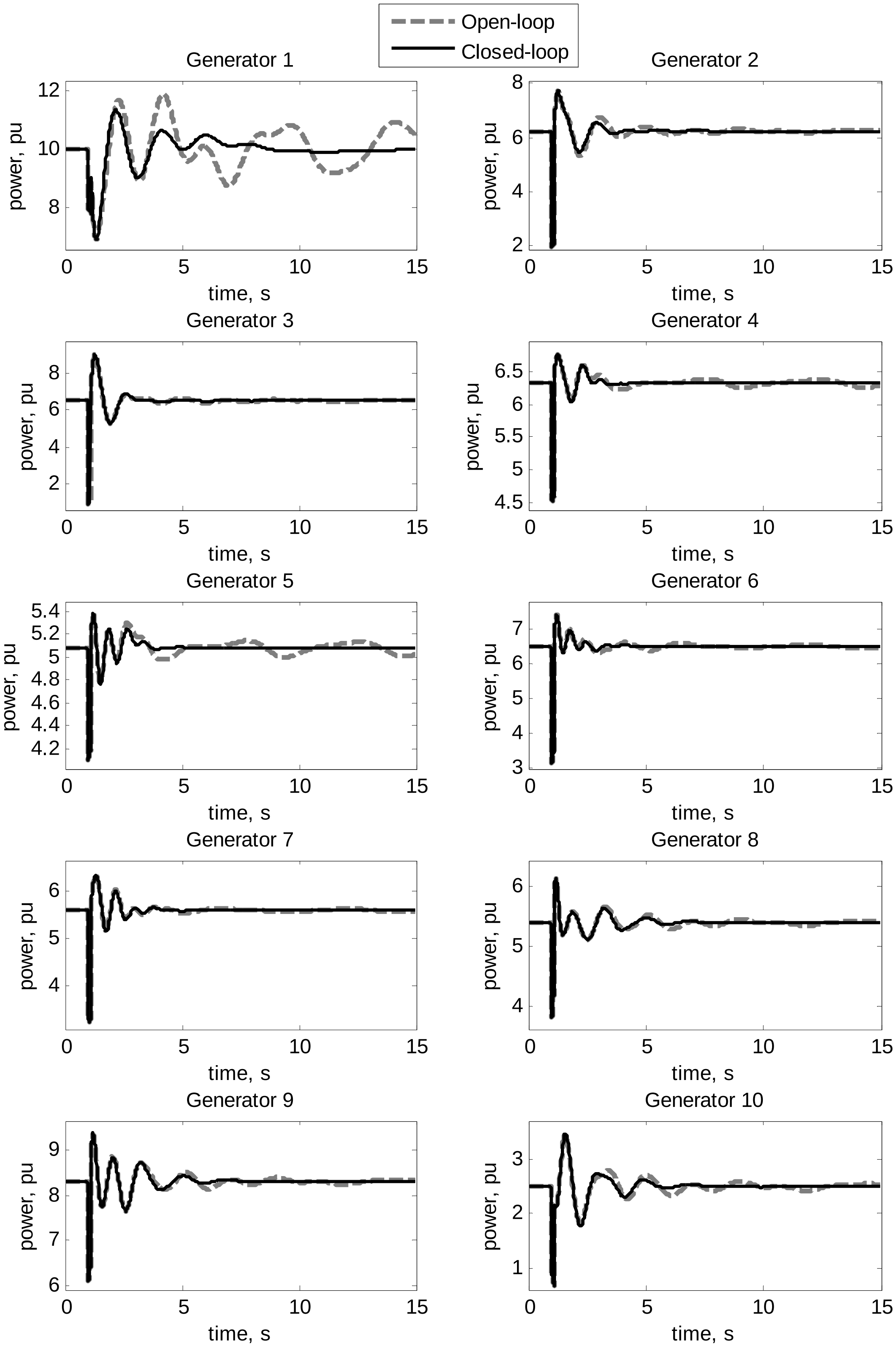

Figure 8-34: Active power responses for a large disturbance at bus 14 (OC-A22)

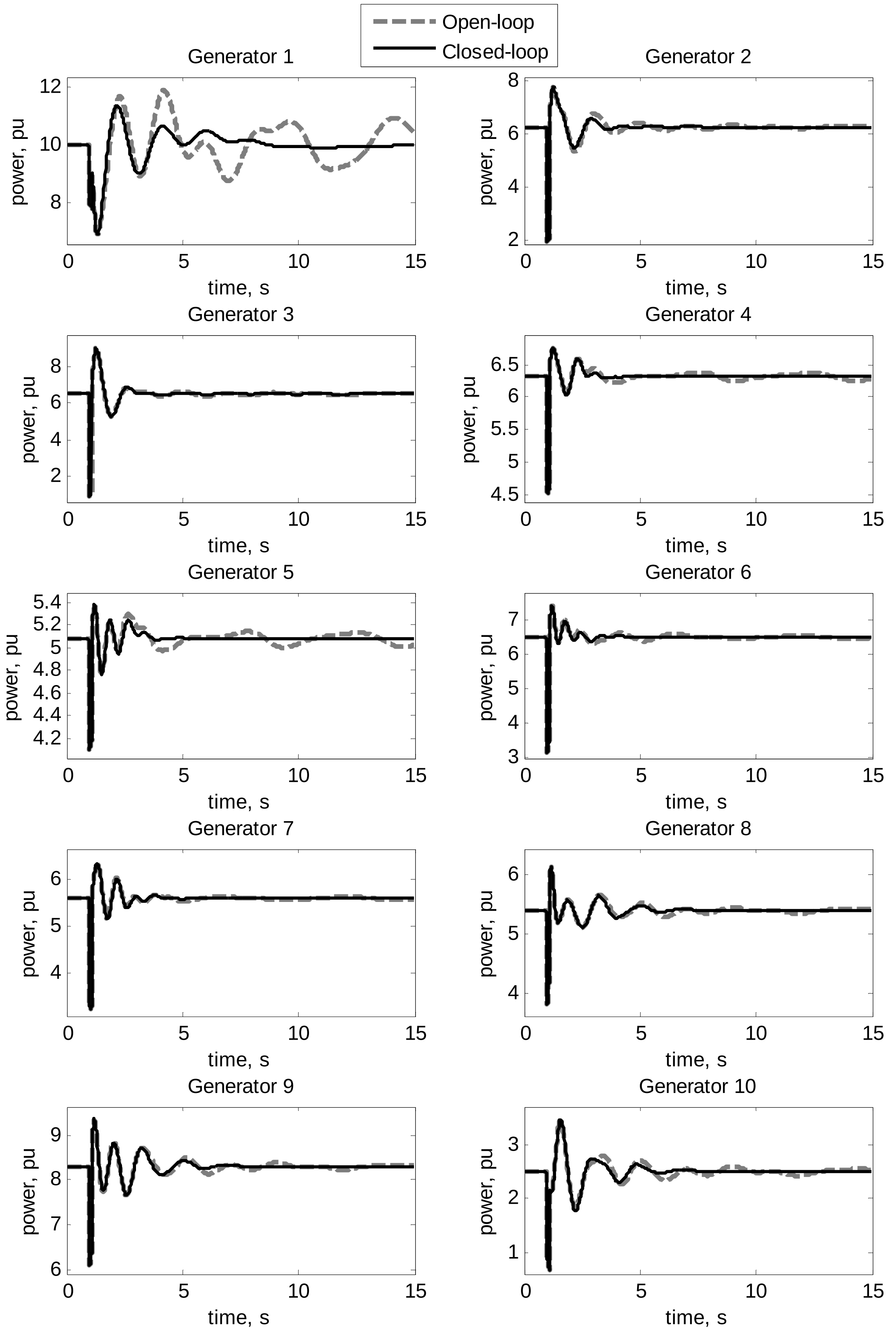

Figure 8-35: Active power responses for a large disturbance at bus 14 (OC-A23)

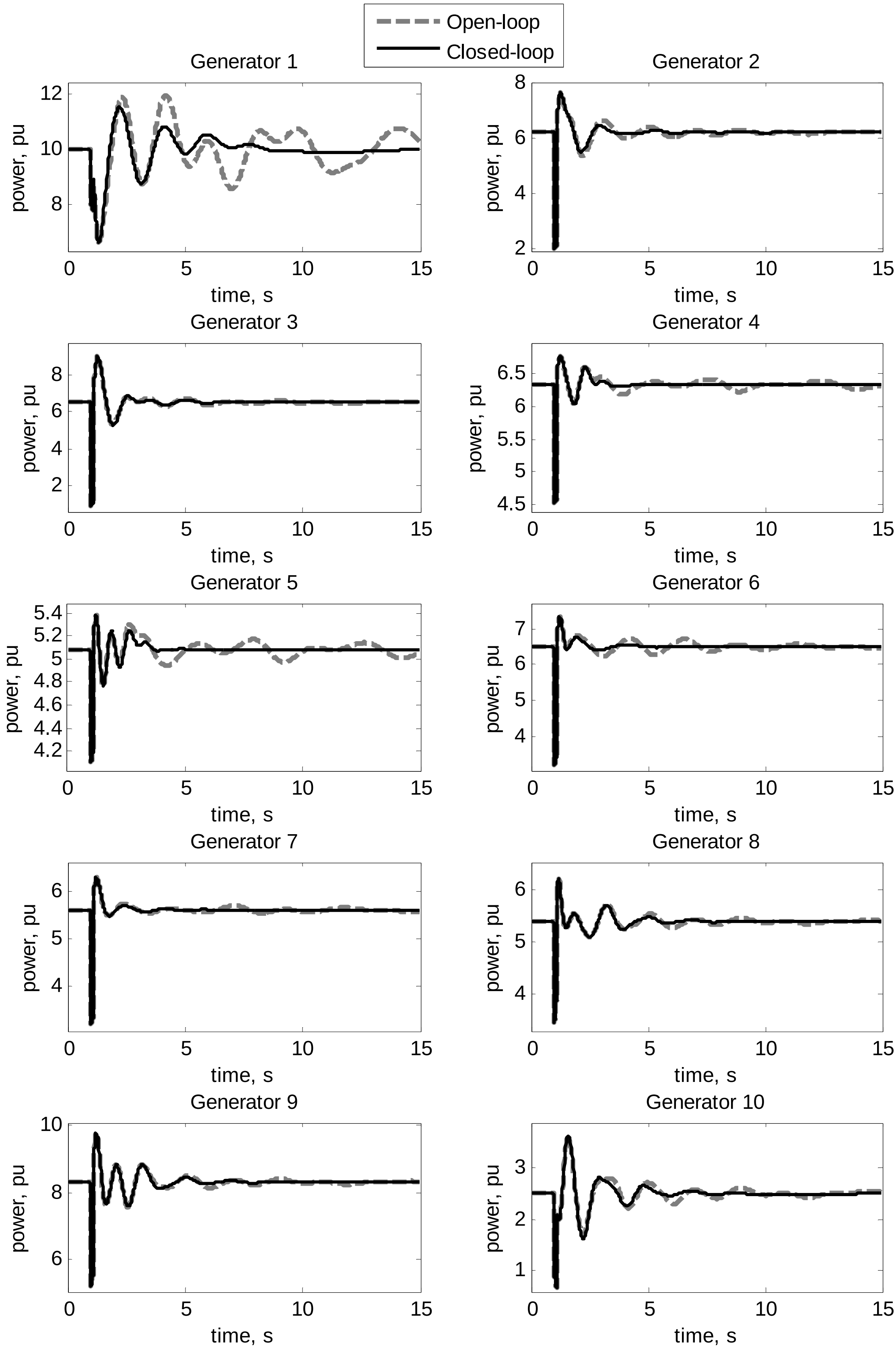

Figure 8-36: Active power responses for a large disturbance at bus 14 (OC-A24)

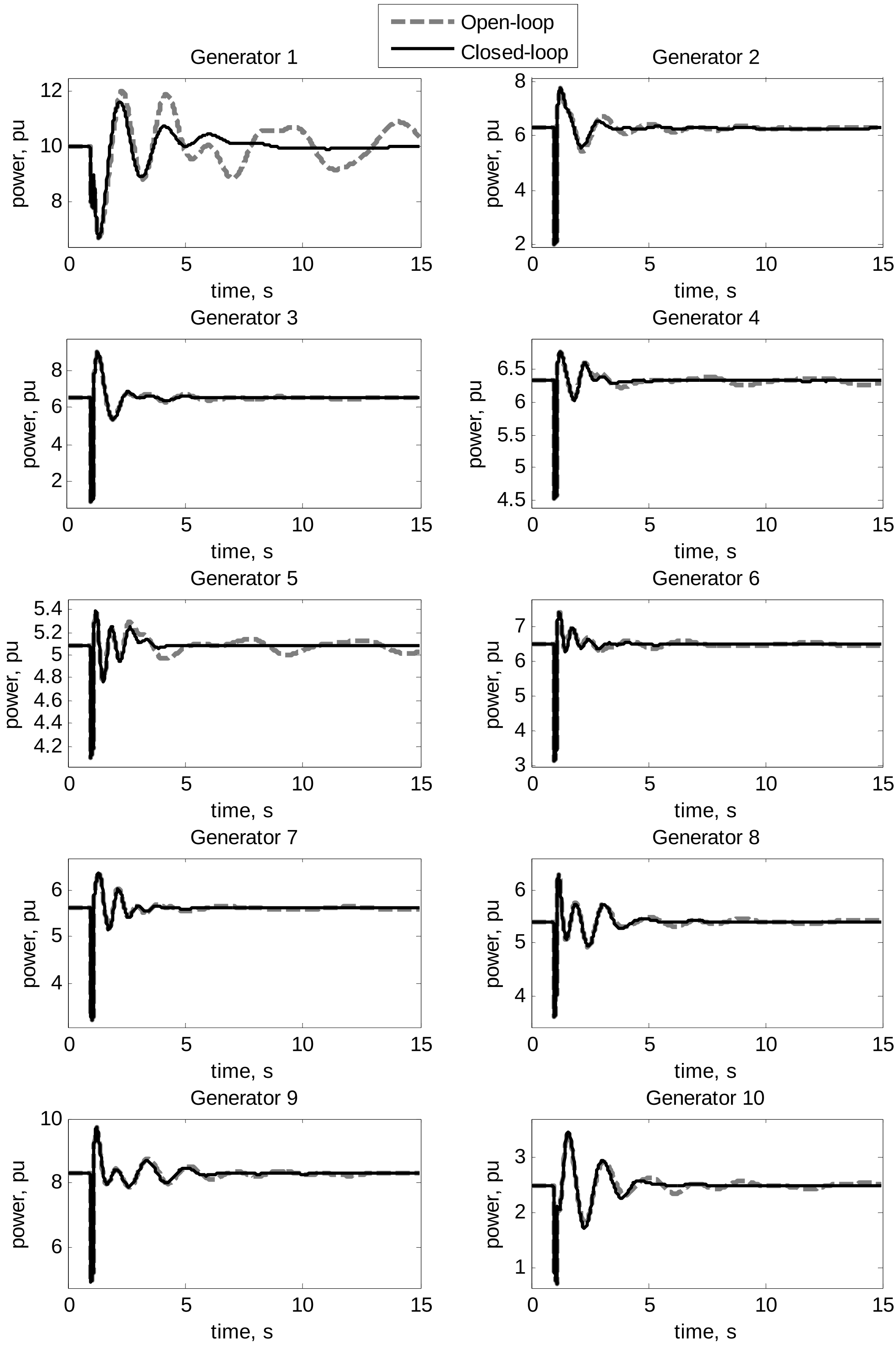

Figure 8-37: Active power responses for a large disturbance at bus 14 (OC-A25)

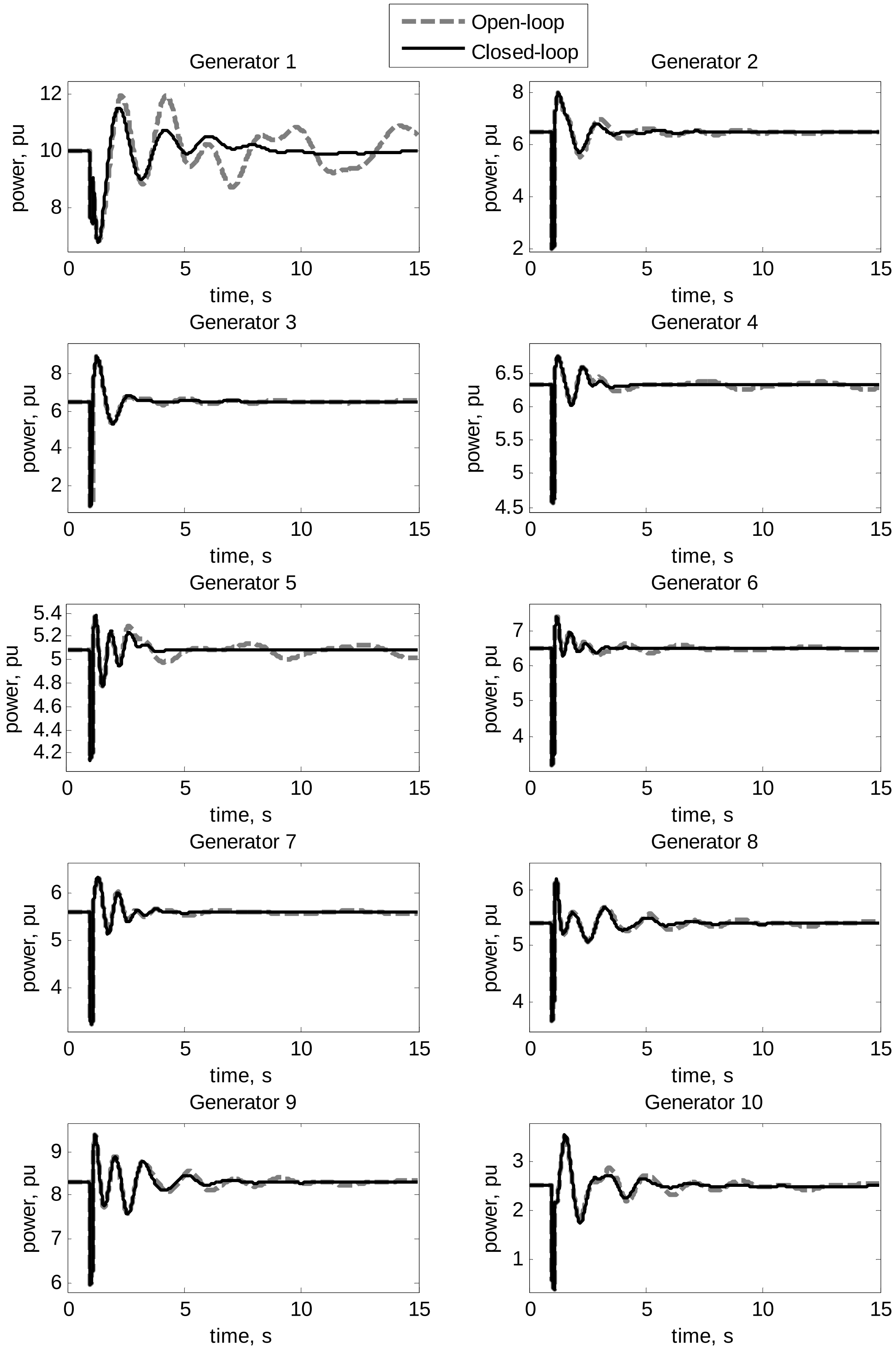

Figure 8-38: Active power responses for a large disturbance at bus 14 (OC-A26)

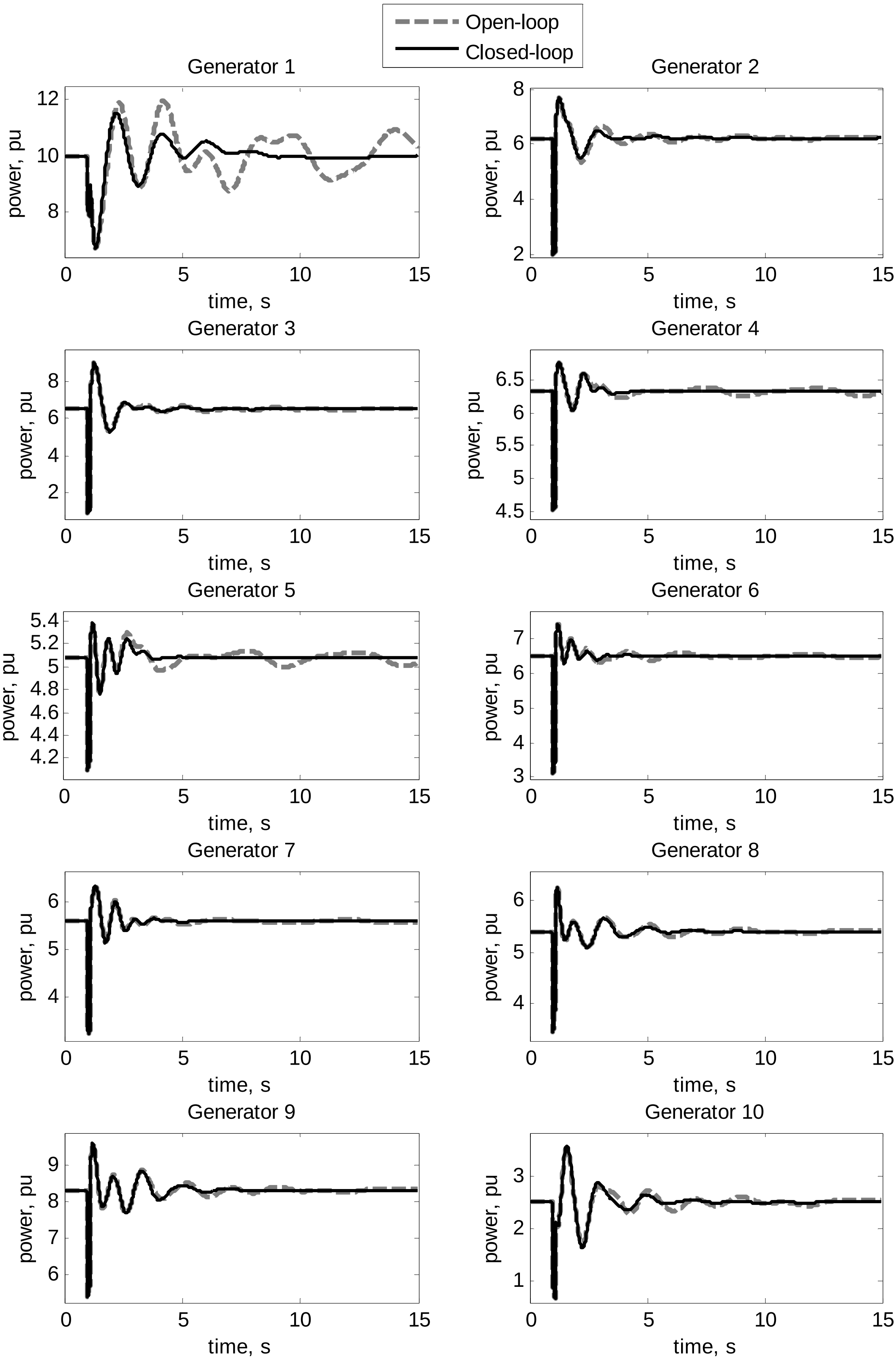

Figure 8-39: Active power responses for a large disturbance at bus 14 (OC-A27)

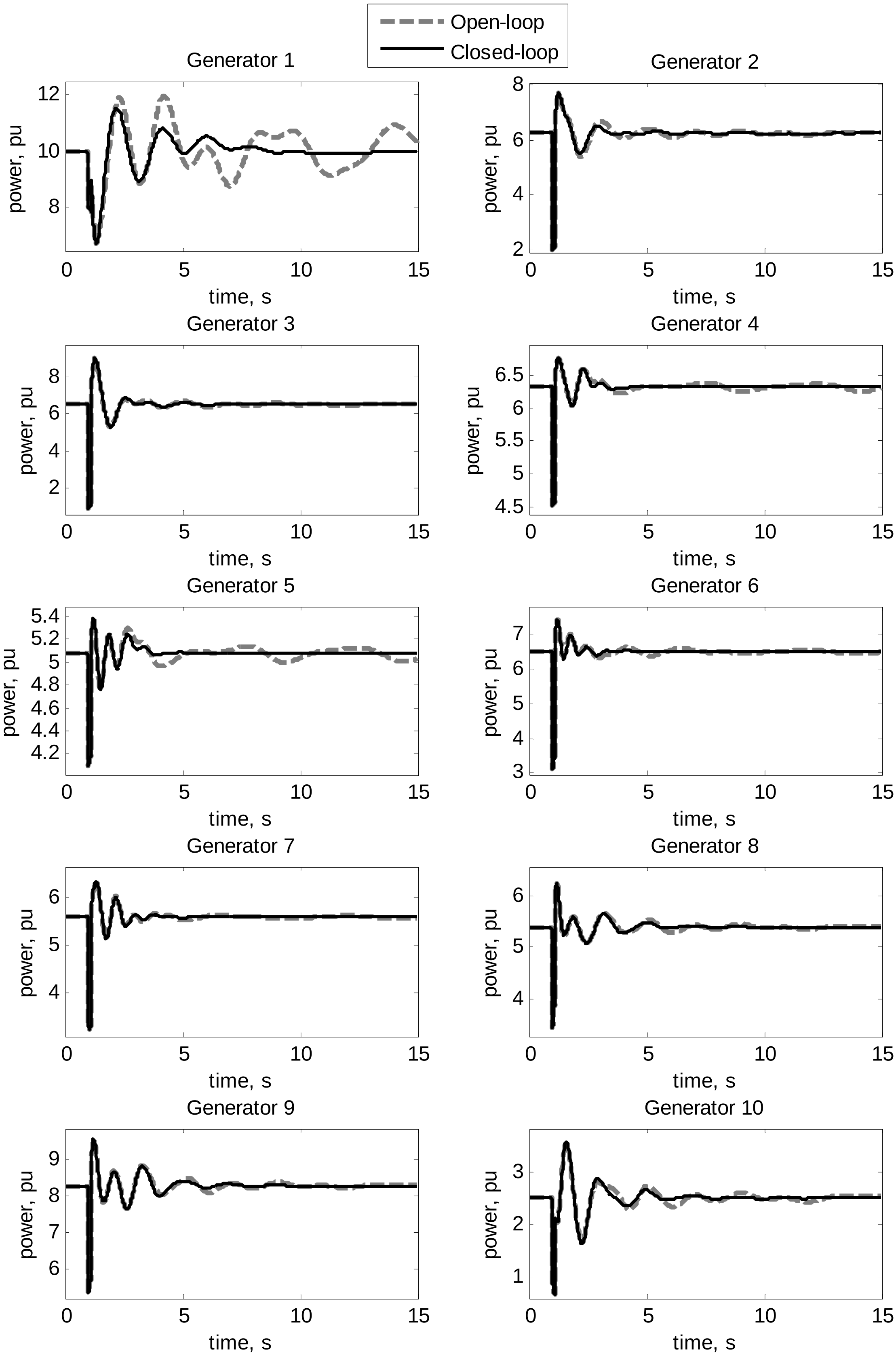

Figure 8-40: Active power responses for a large disturbance at bus 14 (OC-A28)

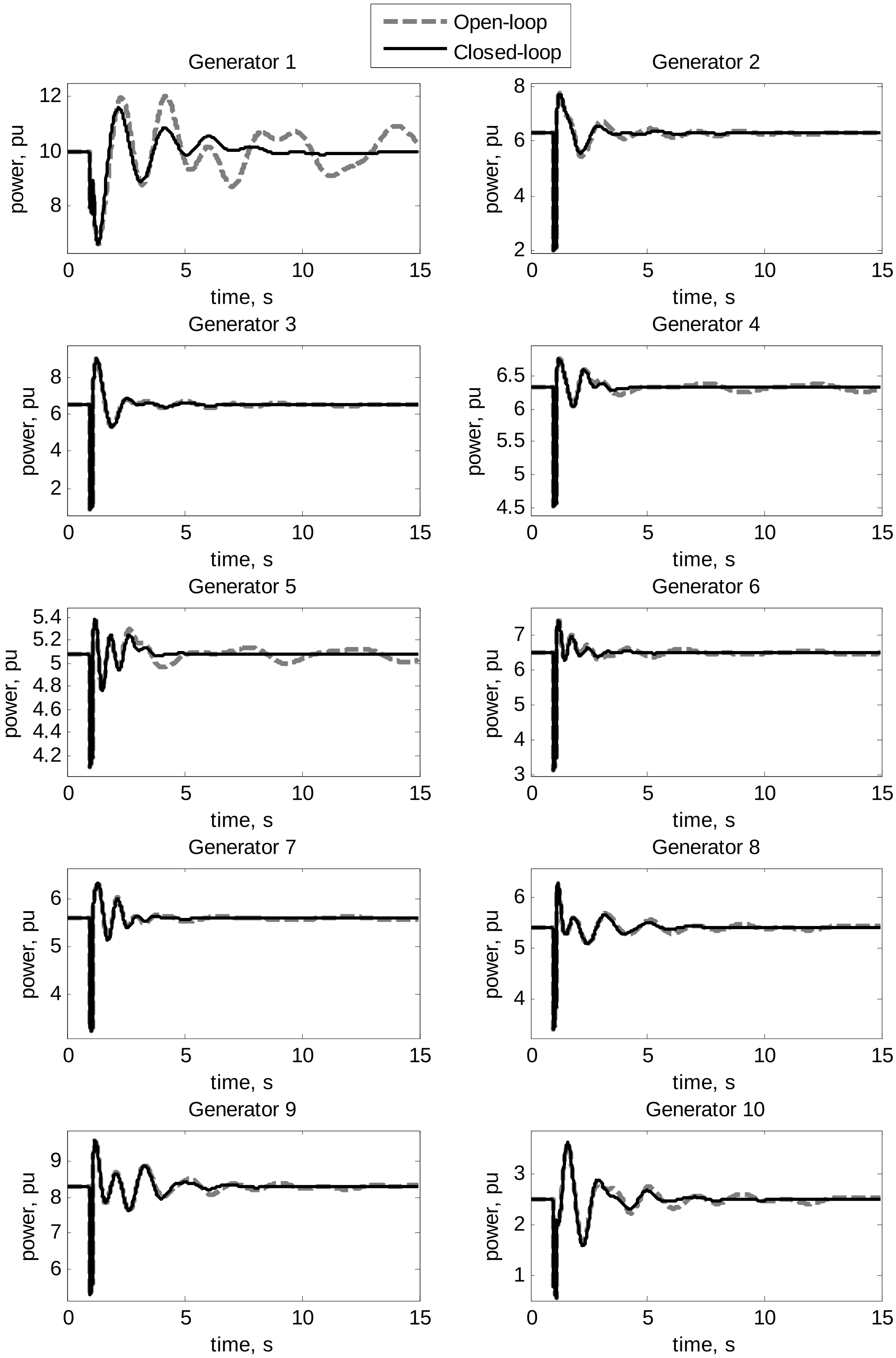

Figure 8-41: Active power responses for a large disturbance at bus 14 (OC-A29)

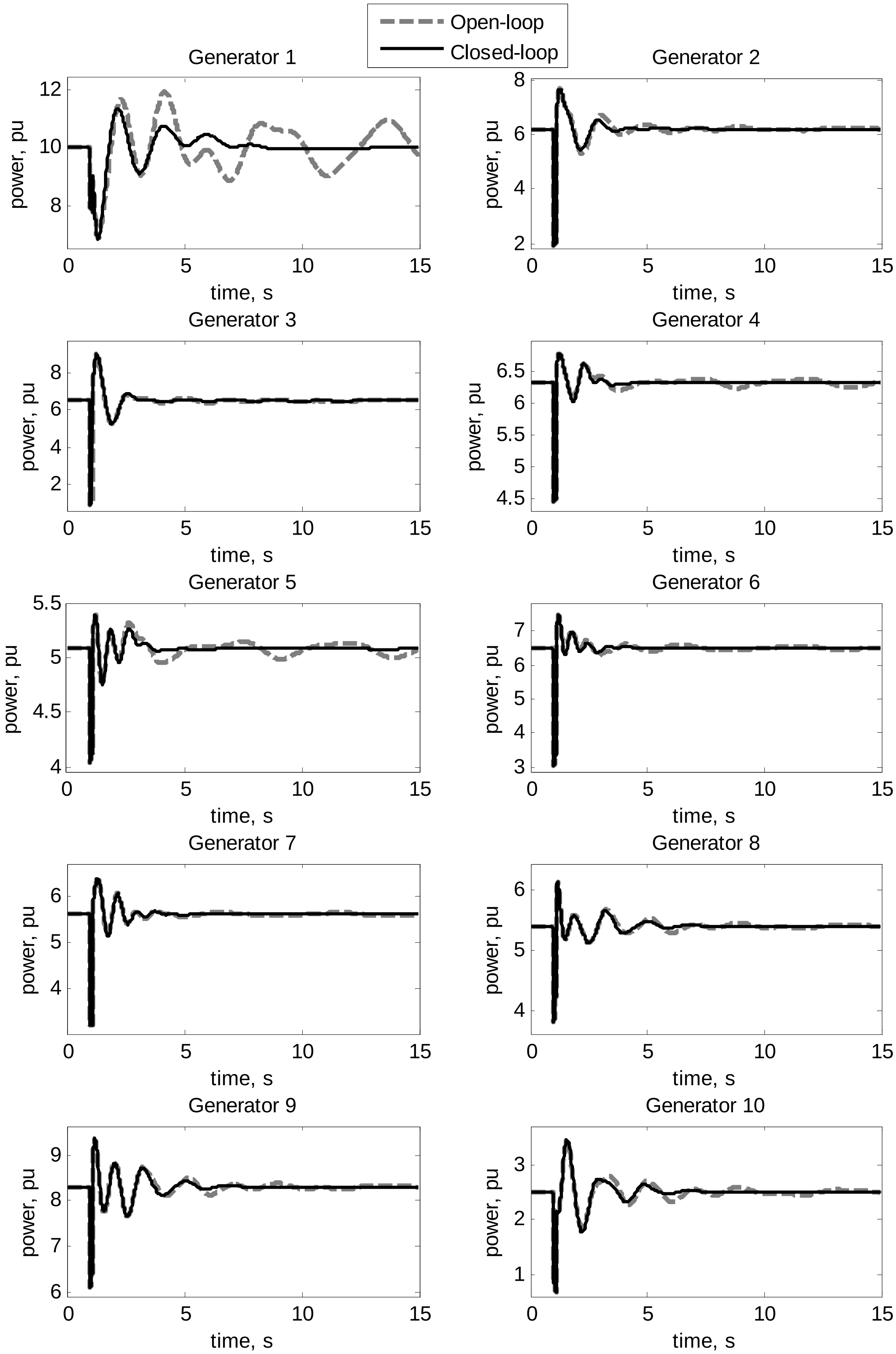

Figure 8-42: Active power responses for a large disturbance at bus 14 (OC-A30)

8.5 Appendix E

8.5.1 Thesis Based Publications

a) International Journal Papers (submitted):

E1. A. M. Almutairi, O. Marjanovic, and J. V. Milanovic, "Design of WAMS based modal LQG controller for damping interarea oscillations," submitted to *Electric Power System Research*.

E2. A. M. Almutairi, O. Marjanovic, and J. V. Milanovic, "Robust stabilization of power system using WAMS based modal LQG controller," submitted to *Electric Power System Research*.

E3. A. M. Almutairi, O. Marjanovic, and J. V. Milanovic, "Hierarchical WAMS based control for robust damping of inter-area oscillations," submitted to *Electric Power System Research*.

b) International Conference Papers (published):

E4. A. M. Almutairi, S. K. Yee, and J. V. Milanovic, "Identification of coherent generators using PCA and cluster analysis," in *Proc. Power Systems Computation Conf. (PSCC08)*, Glasgow, UK, 2008.

E5. A. M. Almutairi and J. V. Milanovic, "Comparison of different methods for optimal placement of PMUs," in *Proc. IEEE PowerTech Conf.*, Bucharest, 2009.

E6. A. M. Almutairi and J. V. Milanovic, "Optimal input and output signal selection for wide-area controllers," in *Proc. IEEE PowerTech Conf.*, Bucharest, 2009.

E7. A. M. Almutairi and J. V. Milanovic, "Comparison of different methods for input/output signal selection for wide area power system control," in *Proc. IEEE Power & Energy Society General Meeting*, Calgary, Canada, 2009.

c) International Conference Papers (submitted):

E8. R. Preece, A. M. Almutairi, O. Marjanovic, and J. V. Milanovic, "Damping of electromechanical oscillations by VSC-HVDC active power modulation with supplementary WAMS based modal LQG controller," submitted to the *IEEE Power & Energy Society General Meeting*, 2011.

E9. R. Preece, A. M. Almutairi, O. Marjanovic, and J. V. Milanovic, "Damping of electromechanical oscillations using WAMS based supplementary LQG controller installed at VSC based HVDC line," submitted to the *IEEE PowerTech Conf.*, Trondheim, 2011.